

**Dielectric properties of atomic-layer-deposited  
 $\text{La}_y\text{Zr}_{1-y}\text{O}_x$  and  $\text{Er}_y\text{Hf}_{1-y}\text{O}_x$  thin films**

**DISSERTATION**

**to obtain  
the doctor's degree at the University of Twente,  
on the authority of the rector magnificus,  
Prof. dr. H. Brinksma,  
on account of the decision of the graduation committee,  
to be publicly defended  
on Wednesday 06<sup>th</sup> of October 2010 at 16.45**

**By**

**Jinesh Kochupurackal Balakrishna Pillai**

**born on 01 June 1978  
in Kapickad, Kerala, India**

# Dielectric Properties of Atomic-Layer-Deposited $\text{La}_y\text{Zr}_{1-y}\text{O}_x$ and $\text{Er}_y\text{Hf}_{1-y}\text{O}_x$ Thin Films

Jinesh Kochupurackal Balakrishna Pillai

This dissertation has been approved by Promotor Prof. dr. J. Schmitz, University of Twente.

VOORZITTER ( <i>Chairman</i> ):	Prof.dr.ir. J. van Amerongen	University of Twente,
PROMOTOR ( <i>Supervisor</i> ):	Prof.dr. J. Schmitz	University of Twente
REFERENTEN ( <i>Referees</i> ):	Dr.ir. W.F.A. Besling Dr.ir. J.H. Klootwijk	NXP Semiconductors Philips Research
LEDEN ( <i>Members</i> ):	Prof.dr. R.A.M. Wolters Prof.dr.ing. D.H.A. Blank Prof.dr. S. Hall Prof.dr.ir. G. Groeseneken	University of Twente / NXP Semiconductors University of Twente University of Liverpool Katholieke University / IMEC Leuven

**ISBN: 978-90-889-1196-5**

The work described in this thesis was performed at NXP Semiconductors, Eindhoven. This work received partial financial support from the European Consortium, REALISE (Project Number: IST-NMP- 016172).

*To Devi*





## **Table of contents**

<b>Chapter 1 Introduction to this Thesis.....</b>	<b>1</b>
1.1 Introduction .....	1
1.2 Concepts of this Thesis: targeted problems .....	2
1.3 Concepts of this Thesis : solutions to the integration issues.....	3
1.4 Outline of this Thesis .....	7
1.5 References .....	9
<b>Chapter 2 Physical characterization of atomic-layer-deposited <math>\text{La}_y\text{Zr}_{1-y}\text{O}_x</math> thin films .....</b>	<b>11</b>
2.1 Introduction .....	11
2.2 Details of the sample preparation.....	14
2.3 Material analysis techniques .....	14
2.4 Spectroscopic ellipsometry studies .....	15
2.5 Stoichiometric studies .....	16
2.6 X-ray Diffraction analyses .....	17
2.7 High Resolution Transmission Electron Microscopy and Energy dispersive X-ray spectrometry analyses .....	23
2.8 Discussion & Conclusions .....	36
2.9 References .....	42
<b>Chapter 3 Electrical characterization of atomic-layer-deposited <math>\text{La}_y\text{Zr}_{1-y}\text{O}_x</math> thin films .....</b>	<b>43</b>
3.1 Introduction .....	43
3.2 Experimental details.....	44
3.3 Atomic force microscope studies: surface roughness of the films .....	44
3.4 Capacitance-Voltage ( $C-V$ ) measurements .....	46
3.5 Current–Voltage ( $I-V$ ) measurements .....	63
3.6 Discussion and Conclusions.....	93
3.7 References .....	96
<b>Chapter 4 Silicon out-diffusion in atomic-layer-deposited <math>\text{La}_y\text{Zr}_{1-y}\text{O}_x</math> thin films .....</b>	<b>99</b>

---

4.1 Introduction.....	99
4.2 Case study on La <sub>2</sub> O <sub>3</sub> with TOFSIMS .....	99
4.3 Conclusions from TOFSIMS data of La <sub>2</sub> O <sub>3</sub> films.....	104
4.4 Si out-diffusion in La <sub>y</sub> Zr <sub>1-y</sub> O <sub>x</sub> films with Al top electrodes.....	106
4.5 Conclusions.....	111
4.6 References.....	113
<b>Chapter 5 Dielectric properties of La<sub>y</sub>Zr<sub>1-y</sub>O<sub>x</sub>-SiO<sub>2</sub> bilayer stacks.....</b>	<b>114</b>
5.1 Introduction.....	114
5.2 Experimental details .....	115
5.3 Thickness measurements: HRTEM.....	116
5.4 Electrical properties of TiN/ La <sub>y</sub> Zr <sub>1-y</sub> O <sub>x</sub> /SiO <sub>2</sub> /Si stack .....	117
5.5 Lifetime measurements of the SiO <sub>2</sub> /LaZrO <sub>x</sub> stacks.....	134
5.6 Conclusions.....	144
5.7 References.....	145
<b>Chapter 6 Electrical characterization of atomic-layer-deposited Er<sub>2</sub>O<sub>3</sub> and Er<sub>y</sub>Hf<sub>1-y</sub>O<sub>x</sub> thin films .....</b>	<b>147</b>
6.1 Introduction.....	147
6.2 Dielectric properties of Er <sub>2</sub> O <sub>3</sub> films.....	147
6.3 Dielectric properties of Er <sub>y</sub> Hf <sub>1-y</sub> O <sub>x</sub> films.....	157
6.4 Conclusions.....	172
6.5 References.....	173
<b>Chapter 7 High-density capacitors using high-<i>k</i> dielectric thin films – Towards industrial needs.....</b>	<b>175</b>
7.1 Introduction: Passive Integration Connecting Substrates.....	175
7.2 High-density capacitors realized with Al <sub>2</sub> O <sub>3</sub> : illustration of the feasibility	176
7.3 High-density capacitors using La <sub>y</sub> Zr <sub>1-y</sub> O <sub>x</sub> layers.....	178
7.4 Conclusions and outlook .....	184
7.5 References.....	187
<b>Chapter 8 Summary of this Thesis .....</b>	<b>188</b>
<b>Samenvatting .....</b>	<b>192</b>
<b>List of publications .....</b>	<b>197</b>

**Curriculum Vitae ..... 205**



# Chapter 1

## Introduction to this Thesis

### 1.1 Introduction

The functions in electronic devices such as mobile phones are increasing, while their dimensions are shrinking every year. To comply with this trend, the number of components on the integrated circuits (IC's) is drastically increasing and their performance such as the switching speed are improving every year as was observed by Gordon Moore in 1965 [1]. Moore suggested that the number of active components on an IC will double every 18 months [2]. Cramping more components into integrated circuits necessitates the lateral and vertical shrinkage of the component dimensions. The International Technology Roadmap for Semiconductors (ITRS) foresees several challenges in complying with Moore's law in future semiconductor devices [3], among which two reasons are worth noting. Firstly, the calculations of tunnel current through the dielectric layers by Hirose et al., based on multiple-scattering theory show that the transconductance fluctuations will be problematic when the gate oxide thickness is scaled down to 0.8 nm [4]. This sets the fundamental limit for thinning down the gate oxide ( $\text{SiO}_2$ ) in complementary metal-oxide-semiconductor (CMOS) devices to 0.7 nm, beyond which the spill-over of the silicon conduction-band wave-functions into the oxide generates interface states that will generate unacceptably large power consumption [5]. Secondly, every bit of data processed in a CMOS logic gate consists of a thermodynamically irreversible process, which is given by the Landauer limit  $k_B T \ln 2 = 17.9 \text{ meV}$  [6], which might set the noise limit beyond which the CMOS technology may not be possible unless another smart technology is developed [7].

Nevertheless, Moore's law deals only with the downscaling of the active elements inside integrated circuits (ICs). The microchips that follow Moore's law are only 10 percent of the systems, where the rest consists of large passive components such as capacitors, inductors, sensors, antennas and resistors. Technologists are currently looking towards the integration of systems, such as cell phones, digital television receivers, health monitoring systems and sensors, which are functioning based on a different technological basis. Integration of large systems into one system has led to two complementary directions. One is

the “*More Moore*” concept with the urge towards extremely small device dimensions and thus the development of system-on-chip (SoC) concepts. Second is the “*More than Moore*” concept, pursuing the integration of the passive elements that are excluded from the domain of Moore’s law, which lead to the System-in-Package (SiP) solution [8].

## 1.2 Concepts of this Thesis: targeted problems

This Thesis is a contribution to the development of SiP solutions, where the integration of high-density capacitors is targeted. Integrating the capacitors and inductors with the IC’s is quite a challenging task, because the device area is a crucial parameter in determining their values.

The basic quest of this Thesis is simple: from the standard expression of the capacitance of a parallel plate capacitor given by [9],

$$C = \frac{\epsilon_0 k A}{d} \quad (1.1)$$

it is clear that the capacitance can be increased by 1) increasing the dielectric constant  $k$ , 2) increasing the area of electrodes  $A$ , and 3) reducing the thickness  $d$  of the dielectric layer. The challenges to integrate the capacitors into the *More than Moore* concept are the following: firstly, increasing the area within a chip is normally nonnegotiable, since the total silicon area on a chip is reducing and the number of component processed over it is increasing every year as per Moore’s law.

Secondly, reducing the dielectric thickness has certain limits, beyond which the charge carriers (electrons or holes) tunnel through the dielectric. This causes increase in leakage currents as the thickness reduces. Leakage current dissipates power as heat, thus heating up the whole chip, which can lead to the failure of different active and passive components on the chip. The tolerance limit of the leakage through a MOS device is  $1 \text{ A/cm}^2$  as per ITRS specifications. For the thickness limit of an ideal dielectric layer (without traps), leakage currents due to tunnelling (direct or Fowler-Nordheim) is the determining factor [10,11,12].

Thirdly, the parameter that can be tuned to achieve a large capacitance density is the dielectric constant  $k$  of the material, hence the research for high- $k$  dielectric materials with  $k$  values several times larger than the conventional  $\text{SiO}_2$  ( $k \sim 3.9$ ). The search for a large- $k$  material opens up plenty of possibilities of different material combinations, starting from  $\text{Si}_3\text{N}_4$  ( $k \sim 5.6 - 6.3$ ) [13],  $\text{Al}_2\text{O}_3$  ( $k \sim 9$ ) [14],  $\text{ZrO}_2$  ( $k \sim 22$ ) [15],  $\text{HfO}_2$  ( $k \sim 25$ ) [16], rare-earth

metal oxides including the oxides of Lanthanide series ( $k \sim 11-27$ ),  $\text{TiO}_2$  ( $k \sim 80$ ) and tertiary metal oxides such as  $\text{SrTiO}_x$  with  $k > 200$  (for a review on high- $k$  materials see Ref. [17]).

The requirements for a reliable high- $k$  material are 1) thermodynamic stability with Si, 2) band offsets larger than 1 eV with Si and the electrode material in order to limit the leakage current through the devices, 3) good electrical interface with Si (to minimize the interfacial traps) and 4) few electrically active defects [17]. The interface formed between the Si and the high- $k$  materials has attracted a lot of attention recently [18], because it determines the interface state density in the band-gap of silicon. Usually a thin interfacial  $\text{SiO}_2$  layer and/or a mixed silicate layer forms at the interface between Si and the high- $k$  film. But, around the year 2010, an interfacial  $\text{SiO}_2$  layer that forms during the deposition of the high- $k$  layers on Si will no longer be tolerable for CMOS downscaling [18].

Even when an optimized high- $k$  layer is achieved on silicon, there are several reliability issues of the high- $k$  material itself related to the thermodynamic stability, defect generation and other phenomena such as asymmetric gate band structure and charge trapping within the oxides (for a review, see Ref. [19]). Another issue is related to the breakdown voltage of the high- $k$  materials. An empirical model states that the breakdown electric field ( $E_{BD}$ ) of the high- $k$  materials is related to the dielectric constant  $k$  by [20]

$$E_{BD} = \frac{20}{\sqrt{k}} [\text{MV/cm}] \quad (1.2)$$

and several binary oxides have shown to fall below the “best-can-do” limit of  $E_{BD}^2 \times k = 400 (\text{MV/cm})^2$  given by this empirical model. Thus, a high- $k$  layer of  $k \sim 100$  would have a breakdown field less than 2 MV/cm, and for a 10 nm thick film, this corresponds to a maximum breakdown voltage as low as 2 V.

### 1.3 Concepts of this Thesis : solutions to the integration issues

The solutions to the issues concerning the integration of the high-density capacitors described in the previous section are three-fold:

1. Enhance the area of the device by micro-patterning the bare-silicon area in a chip.
2. Deposit very thin dielectric layers with reduced leakage current using nanolaminated approaches or multicomponent “ternary” mixed oxides.
3. Explore new metal oxide combinations that give good dielectric strength and high- $k$

values.

These three solutions together are expected to give the capacitance density required by the industrial needs.

In order to enhance the area available in a chip, the idea of micro-patterned silicon has been put forward by *Lehmann et al* [21], where deep pores with high aspect ratios (10-20) are etched in silicon either by deep reactive ion etching (DRIE) or by wet chemical etching. By forming an array of such deep pores etched in silicon, the total area of the capacitor can be enhanced by 10-15 times [22]. Fig. 1.1 shows the micro-pores thus etched in silicon.

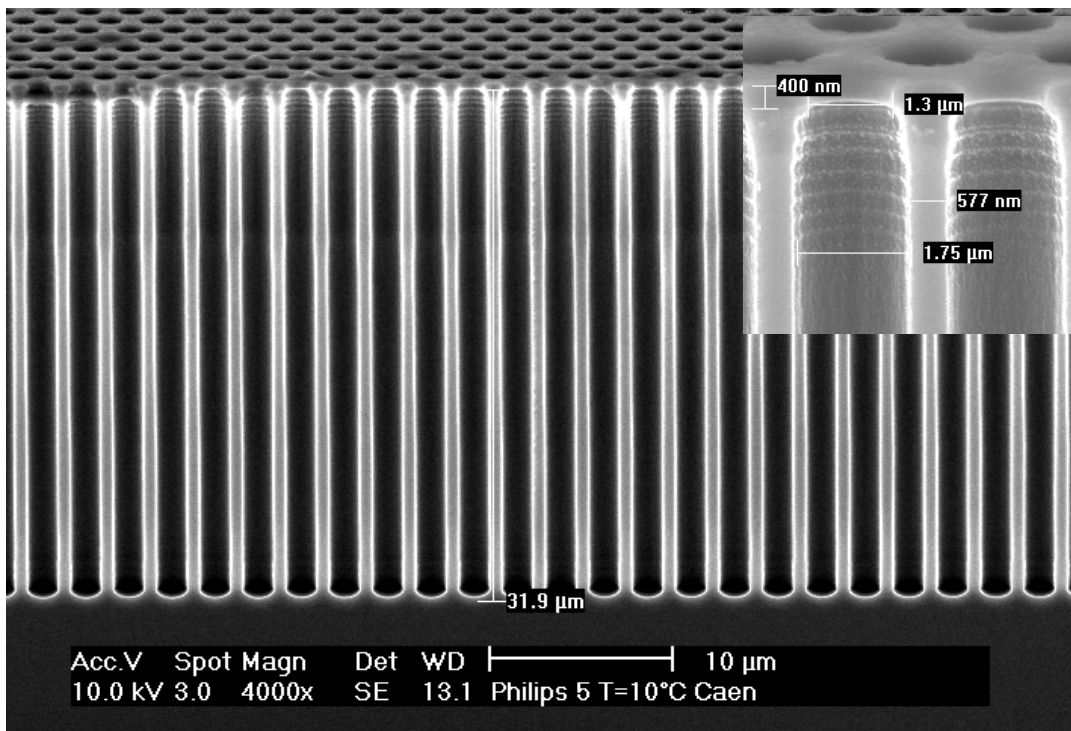


*Fig. 1.1. High-aspect-ratio micro-pores etched in silicon using DRIE process to realize the area enhancement. The scallop structures on the sidewalls shown in the inset are due to repetitive Bosch process.*

The etching of these micro-pores was carried out with the Bosch process that involved ion etching together with  $\text{SF}_6/\text{O}_2$  gas mixture, then a subsequent surface passivation step using  $\text{C}_4\text{F}_8$  (without ions) to protect the sidewalls. Repetition of these steps yields high-aspect-ratio pores. The pores are normally positioned in a hexagonal lattice and separated far enough such that individual pores will not make contact with each other through the silicon substrate. The typical diameter of the pores is 1.5-2  $\mu\text{m}$  with spacing of 0.5-1  $\mu\text{m}$  creating a pitch of 2-3  $\mu\text{m}$ .



In order to achieve very uniform and thin (8 nm – 32 nm) high- $k$  layers within the three dimensional structure, the atomic layer deposition (ALD) technique was employed. ALD or CVD (chemical vapour deposition) is a prerequisite for the fabrication of high density capacitors with micro-pores, because of the well-known step-coverage of films deposited using these techniques [23, 24,25]. For the characterization of the high- $k$  layers described in different Chapters of this Thesis, planar devices (without micro-pores) were utilized, where the high- $k$  films were deposited by means of ALD and electrode materials (Al or TiN) were deposited by physical vapour deposition (PVD) technique. Micro-pore devices were fabricated with both the high- $k$  layers and the TiN electrodes deposited by ALD, due to the requirement of uniform step-coverage over the entire three dimensional area of the capacitors.

As high- $k$  materials, binary and tertiary oxides of Lanthanum (La) and Erbium (Er) from the rare-earth series together with Zirconium (Zr) and Hafnium (Hf), which form  $\text{La}_y\text{Zr}_{1-y}\text{O}_x$  and  $\text{Er}_y\text{Hf}_{1-y}\text{O}_x$ , were examined in this Thesis. The dielectric properties such as  $k$ -values of the combinations together with the breakdown fields are characterized in different Chapters.

The results of this Thesis summarize the work done in two years (2007-2009) during the course of the European project namely “*Rare Earth oxide Atomic Layer deposition for InnovationS in Electronics*” abbreviated to “REALISE” (project number IST-NMP- 016172), in which the development of ALD-processed high- $k$  materials were investigated focusing on rare-earth metal oxides. The choice of the dielectric materials described in this Thesis comes from the current status of the materials used in industrial research conferred through REALISE meetings. Among the lanthanide series in rare-earth metals,  $\text{La}_2\text{O}_3$  is an emerging dielectric material with a large band-gap (5-6 eV) [17,26] and a dielectric constant of ~ 20-30.  $\text{La}_2\text{O}_3$  has a relatively stable interface with silicon, but is highly hygroscopic in nature, thus absorbing water from the ambient, it forms its low- $k$  phase of  $\text{La}(\text{OH})_3$  [27]. Albeit, *in situ* electrode deposition subsequent to the  $\text{La}_2\text{O}_3$  deposition has been suggested to avoid moisture absorption [26], it is not a permanent solution, since moisture diffusion can still occur through the periphery of the electrodes, thus gradually degrading the device. When mixing with other metal oxides, for instance,  $\text{Al}_2\text{O}_3$  to form tertiary metal oxides (like  $\text{LaAlO}_x$ ), La gives a thermodynamically stable dielectric material that is less sensitive to moisture [28,29]. However, despite the thermal stability of the films, alloying with Al gives comparatively

lower dielectric constant. In this regard, considering the thermodynamic stability and high dielectric permittivity of dielectric materials,  $\text{ZrO}_2$  is known to stabilize rare-earth metal oxides [30,31,32], which triggered the study of  $\text{La}_y\text{Zr}_{1-y}\text{O}_x$  as a potential high- $k$  material in this Thesis. Fig. 1.2 shows the variation of the capacitance when  $\text{La}_2\text{O}_3$  is exposed to different percentages of relative humidity and the stabilization of the capacitance value when doped with Zr.

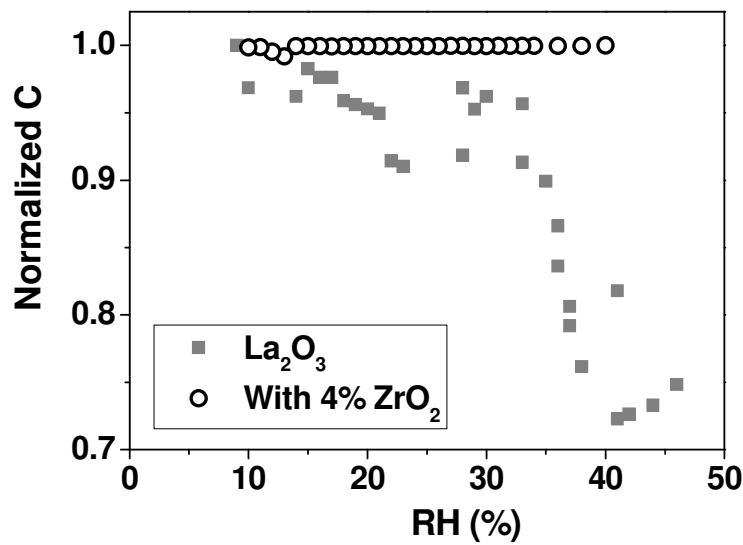


**Fig. 1.2.** Capacitance of MIS devices comprising  $\text{La}_2\text{O}_3$  and  $\text{La}_y\text{Zr}_{1-y}\text{O}_x$  (with 4 at.% Zr) layers exposed to environment of different relative humidity. Capacitance of  $\text{La}_2\text{O}_3$  changes due to its hygroscopicity, while  $\text{La}_y\text{Zr}_{1-y}\text{O}_x$  layer is stable in humid environments.

Despite the hygroscopicity,  $\text{La}_2\text{O}_3$  has the largest ionic radius among the metal oxides in the lanthanide series. Because of this large bond length, silicon from the substrate and metallic species (for instance, Al) from the top electrodes diffuse into the dielectric layer [33,34,35], deteriorating the dielectric layer. This happens in  $\text{La}_y\text{Zr}_{1-y}\text{O}_x$  as well, suggesting that an alternative metal oxide with lower ionic radius in the lanthanide series should be a better material in terms of stability. For this reason,  $\text{Er}_2\text{O}_3$  was studied, together with another promising and industrially important dielectric material,  $\text{HfO}_2$ . Advantageously,  $\text{Er}_y\text{Hf}_{1-y}\text{O}_x$  films do not exhibit silicon out-diffusion and provide  $k$ -values as high as the  $\text{La}_y\text{Zr}_{1-y}\text{O}_x$  films.

## 1.4 Outline of this Thesis

The scope of the Thesis has been discussed in this Introduction Chapter. The ALD processing details and the material characterization of  $\text{La}_y\text{Zr}_{1-y}\text{O}_x$  thin films are discussed in Chapter 2. The major result of this chapter is that  $\text{ZrO}_2$  undergoes phase segregation to tetragonal nanocrystals above 30% Zr content in the film. A model based on the surface free energy of the nanocrystals is presented to account for the preference to tetragonal phase segregation of  $\text{ZrO}_2$  from the  $\text{La}_y\text{Zr}_{1-y}\text{O}_x$  film.

Chapter 3 presents the electrical characterization of the MIS devices comprising the  $\text{La}_y\text{Zr}_{1-y}\text{O}_x$  thin films. All the films exhibit dielectric properties surpassing the hypothetical limit suggested by an empirical law relating breakdown field and dielectric constant ( $E_{BD}^2 k \gg 400 (\text{MV}/\text{cm})^2$ ). A model based on the electric field simulations of a dielectric medium with embedded dielectric nanocrystals is presented to explain these enhanced dielectric properties.

Chapter 4 presents novel technical challenge: out-diffusion of silicon from the substrate through the  $\text{La}_y\text{Zr}_{1-y}\text{O}_x$  thin films at room temperature. A gradual siphoning of silicon from the substrate through the high- $k$  layers is observed. This effect is explained as due to the triplet grain boundaries in Al top electrode, through which the diffusion of Si ions is faster. TiN electrodes suppress the siphoning of Si and thus enhance the electric strength and reliability of the devices

Chapter 5 presents the electrical properties of  $\text{SiO}_2/\text{La}_y\text{Zr}_{1-y}\text{O}_x$  stacks with different  $\text{La}_y\text{Zr}_{1-y}\text{O}_x$  layer thicknesses. The asymmetric charge injection through the layers depending on the polarity of the electrodes is explained on the basis of the Maxwell-Wagner effect. An equivalent circuit model is presented to explain the observed asymmetry of charge injection. The Debye and Maxwell-Wagner relaxation timescales of electrons are extracted from fitting the model with experiments. Then, the influences of the Maxwell-Wagner effect on measurement results are described showing charge-to-breakdown ( $Q_{BD}$ ) measurements. Further on, the lifetime extrapolations of the devices are performed using constant voltage stress (CVS) measurements and the activation energy of degradation is estimated from the Arrhenius behavior of time-to-breakdown ( $t_{BD}$ ).

Chapter 6 presents the electrical characterization of ALD processed  $\text{Er}_y\text{Hf}_{1-y}\text{O}_x$  films. As an emerging dielectric material, the electrical properties of ALD processed  $\text{Er}_2\text{O}_3$  films are

discussed in detail in the beginning of this Chapter. Then the effects of adding Hf to  $\text{Er}_2\text{O}_3$  are detailed. The enhancement in dielectric permittivity of  $\text{Er}_y\text{Hf}_{1-y}\text{O}_x$  films is explained as due to the cubic phase stabilization of  $\text{HfO}_2$  in the presence of Er, which is explained on the basis of X-ray diffraction analyses.

Chapter 7 deals with the realization of the high-density capacitors with the high- $k$  layers deposited over the surface area of an  $n^{++}$  Si substrate pre-structured with large aspect ratio ( $>10$ ) micro-pores. Using ALD processed  $\text{Al}_2\text{O}_3$  and TiN layers, multiple metal-insulator-metal (MIM) stacks comprising 3 capacitors on top of each other (a MIMIMIM stack) were realized. These stacks give an ultra-high capacitance density of  $450 \text{ nF/mm}^2$ . Subsequently,  $\text{SiO}_2/\text{Er}_y\text{Hf}_{1-y}\text{O}_x$  stacks were deposited with excellent step coverage in deep pores and the devices were electrically characterized. The early breakdown of the micro-pore devices comparing to the planar devices is due to the sharp edges of the devices and is explained using high resolution transmission electron microscopy (HRTEM) imaging of the breakdown spots.

Chapter 8 summarizes the results of this Thesis.

## 1.5 References

1. G. Moore, *Electronics* **38**, 114 (1965).
2. G.E. Moore, *Tech. Dig. IEEE Int. Electron Device Meeting*, page11, (1975).
3. International Technology Roadmap for Semiconductors (ITRS), 2009 Edition.
4. M. Hirose et al., *Semicond. Sci. Technol.* **15**, 485 (2000).
5. D. A. Muller et al., *Nature* **399**, 758 (1999).
6. R. Landauer, *IBM J. Res. Dev.* **5**, 183 (1961).
7. J. Izydorczyk, *IEEE Trans. Very Large Scale Intergr. (VLSI) Syst.* **18**, 161 (2010).
8. F. Murray et al., *Advanced Electronic Packaging Symposium*, page 3 (2007).
9. J. D. Jackson, *Classical Electrodynamics*, 3rd ed. Wiley, NewYork, (1999).
10. M. Lenzlinger, E.H. Snow, *J. Appl. Phys.* **40**, 278 (1969).
11. G. Pananakakis, et al., *J. Appl. Phys.* **78**, 2635 (1995).
12. . H. C. Lin, P. D. Ye, G. D. Wilk, *Solid-State Electron.* **50**, 1012 (2006).
13. S.A. Awan et al., *Thin Solid Films* **423**, 267 (2003).
14. M.D. Groner et al., *Thin Solid Films* **431**,186 (2002).
15. D.H. Triyoso et al., *Appl. Phys. Lett.* **88**, 222901 (2006).
16. G. D. Wilk, R. M. Wallace, J. M. Anthony, *J. Appl. Phys.*, **87**, 484 (2000).
17. J. Robertson, *Eur. Phys. J. Appl. Phys.* **28**, 265 (2004).
18. C.J. Först et al., *Nature* **427**, 53 (2004).
19. G. Ribes et al, *IEEE T. Device Mat. Re.* **5**, 5 (2005).
20. P. Jain, E. J. Rymaszewski, *IEEE Transactions on Advanced Packaging*, **25**, 454 (2002).
21. V. Lehmann, U. Grüning, *Thin Solid Films* **297**, 13 (1997).
22. F. Roozeboom et al., *Int. J. Microcircuits and Electronic Packaging*, **24**, 182 (2001).
23. R.G. Gordon et al., *Chem. Vapor. Depos.* **9**, 73 (2003).
24. S.O. Kuchayev et al., *Langmuir* **24**, 943 (2008).
25. G.M. Sundaram et al., *Solid State Technol.* **52**, 12 (2009).
26. H. Iwai et al, *Tech. Dig. - Int. Electron Devices Meet.* **625** (2002).
27. Y. Zhao et al., *Appl. Phys. Lett.* **88**, 72904 (2006).
28. S. Van Elshocht et al., *J. Vac. Sci. Technol. A* **26**, 724 (2008).
29. J.H. Jun, J. Jun, D.J. Choi, *Electrochem. Solid St. Lett.* **6**, F37 (2003).

30. J.P. Maria et al., *J. Appl. Phys.* **90**, 3476 (2001).
31. K.B. Jinesh et al., *Appl. Phys. Lett.* **93**, 062903 (2008).
32. D. Tsoutsou et al., *Appl. Phys. Lett.* **94**, 053504 (2009).
33. K. B. Jinesh et al., *Appl. Phys. Lett.* **93**, 192912 (2008).
34. T. M. Pan et al., *Electrochem. Solid-State Lett.* **10**, H101 (2007).
35. H. Ono, T. Katsumata, *Appl. Phys. Lett.* **78**, 1832 (2001).



## Chapter 2

# Physical characterization of atomic-layer-deposited $\text{La}_y\text{Zr}_{1-y}\text{O}_x$ thin films

### 2.1 Introduction

For the deposition of thin  $\text{La}_2\text{O}_3$  and  $\text{ZrO}_2$  films, numerous techniques are commonly used, such as molecular beam epitaxy (MBE) [1], radio frequency magnetron sputtering [2,3], low temperature oxidation [4], physical vapour deposition (PVD) [5], pulsed laser deposition (PLD), metal-organic chemical vapour deposition (MOCVD) [6] and its modified form, and atomic-layer deposition (ALD) [7-11]. As discussed in the previous chapter, the optimal deposition technique for the uniform deposition over structured surfaces is ALD, due to its self-limiting properties that allow monolayer deposition over entire surface [12]. Prior to introducing  $\text{La}_y\text{Zr}_{1-y}\text{O}_x$  deposition in micropores, it is essential to characterize the thin films on well-defined planar surfaces to know the quality of the interface between  $\text{La}_y\text{Zr}_{1-y}\text{O}_x$  and silicon, the relation between the ALD precursor cycles and the eventual film thickness and the stoichiometry of the films compared to the desired atomic ratios of the materials. Therefore, this chapter is dedicated to the physical characterization of the  $\text{La}_y\text{Zr}_{1-y}\text{O}_x$  thin films and this study aims to examine the influence of Zr in chemically and thermodynamically stabilizing the  $\text{La}_2\text{O}_3$  films.

#### 2.1a Atomic Layer Deposition of $\text{La}_y\text{Zr}_{1-y}\text{O}_x$ thin films

ALD is based on alternating pulses of two or more precursors separated from each other by a purge pulse consisting of an inert gas in order to remove excess of adsorbed precursor molecules or even precursor residues like molecular fragments originating from the chemical reaction (such as organic residues, which can contaminate the films if not removed properly). During each pulse the growth is self limiting by occupancy of the active sites and by the reactive adsorption onto the surface. As a result the film growth occurs in a mono-layer by

mono-layer fashion. The consequences are three fold: 1) a very uniform and conformal film growth is obtained; 2) the monolayer by monolayer growth behaviour allows full control over the total stack thickness just by setting the number of cycles, 3) low contamination levels because reaction products are completely removed from the surface during each pulse sequence. The ALD technique is based on the principle that at least two gaseous reactants are made to react with the wafer surface one at the time. Here we use two metal precursors in combination with ozone as an oxidizing agent to obtain a ternary oxide at a deposition temperature of  $300^\circ\text{C}$ . These metal precursors are tris(2,2,6,6-tetramethyl-3,5-heptanedionato) lanthanum or  $\text{La}(\text{thd})_3$  as the La-precursor, and  $\text{Zr}(\text{CH}_3\text{C}_5\text{H}_4)_2\text{CH}_3\text{CH}_3\text{O}$  or ZrD-O4, as the Zr-precursor (more deposition details will be given later in this chapter) The deposition sequence can be described in various steps as follows:

### *Step 1*

In the first step one of the two metal precursors is introduced in the reaction chamber. This precursor reacts with the surface forming a chemical bonding with the substrate atoms. The settings of reaction conditions such as temperature, pressure, etc. are selected such that only one monolayer of the material is grown on the surface; and importantly, condensation or decomposition of additional precursor material does not take place under the chosen conditions. The duration of the precursor flow is maintained long enough such that the chemisorbed monolayer is formed everywhere on the surface including the sidewalls and base of deep vias, around corners, etc. The chemisorbed monolayer results in a new surface termination, characteristic for the specific precursor used. For instance, on surface termination, the surface of silicon dioxide consists of Si–OH groups. When this surface is exposed to ZrD-O4 vapour, Si–O–Zr(+ligands) bonds will be formed and gaseous hydrogenated ligands will be released. These hydrogenated ligands are methane ( $\text{CH}_4$ ), and/or methanol  $\text{CH}_3\text{OH}$ .

### *Step 2*

In the second step a purge of an inert gas is introduced that removes the excess of all gaseous precursor molecules (i.e. ZrD-O4) used in the first step. The purge gas, e.g.  $\text{N}_2$  or Ar, is kept flowing sufficiently long to ensure the complete removal of the first type of precursor. As the monolayer grown in the first step is chemisorbed, the purge gas will not remove this layer.



**Step 3**

Subsequent to step 2, the second precursor is introduced. The type of precursor is selected such that it reacts with the monolayer grown in the first step to form an additional layer. In this example  $\text{O}_3$  will oxidise the ligands that remained attached to the zirconium central atom after the first exposure step. The exposure to ozone leads to bond rupture between the ligands and the zirconium atom. Part of the ligands will get “burned” and transformed into  $\text{CO}_2$  leaving oxygen radical groups or hydroxyl groups on the surface. For sake of clarity it is assumed that the surface becomes terminated by  $-\text{O}-\text{Zr}-\text{OH}$  groups now. Again, the oxidation reaction will proceed until all available cyclopentadienyl/methyl/methoxy ligands on the  $-\text{O}-\text{Zr}(\text{ligand})_3$  surface sites are replaced by  $-\text{Zr}-\text{OH}$  groups. Also in this step, the flow of reactant gas is kept long enough to ensure that all surface sites have reacted; at the same time, the conditions are such that no condensation takes place on the surface of the deposited film.

**Step 4**

The fourth step is another purge with inert gas that removes all excess reaction products remaining from the third step.

In the subsequent step, the first precursor is introduced again (i.e.  $\text{ZrD-O4}$ ). The precursor reacts with the ligands that remained after the chemical reaction in the third step, i.e. with the  $-\text{Zr}-\text{OH}$  groups. This results in the formation of gaseous hydrogenated reaction products (see step 1), and a surface terminated with  $-\text{O}-\text{Zr}(\text{ligand})_x$  groups. In the continuation of the deposition process, each of the four basic steps is repeated many times, until a  $\text{ZrO}_2$  film with the desired thickness has been realized. Typically one deposition cycle consists of the four basic steps when binary compounds are grown.

Also, ternary compounds can be deposited upon replacing one or more zirconium precursor pulses by one or more pulses of another metal precursor. (But it should be mentioned that an ALD process with given precursors works only in a certain temperature window. Therefore, the chosen precursors should show an overlap in this temperature window). For instance, as we follow here, lanthanum can be incorporated using a pulse of La-precursor, tris(2,2,6,6-tetramethyl-3,5-heptanedionato) lanthanum or  $\text{La}(\text{thd})_3$ . After each metal pulse an ozone pulse is needed to strip off the ligands and prepare the surface for

chemisorption of the next metal pulse. Depending on the pulse ratio of the consecutive Zr and La precursor pulses, different compositions of the  $\text{La}_y\text{Zr}_{1-y}\text{O}_x$  layers can be obtained.

In summary, the basic principles are (mainly) two-fold: firstly, each precursor is brought into contact with the surface long enough, to guarantee a uniform growth of one monolayer everywhere on all substrates present in the reactor. Secondly, the gaseous reactants participating in the chemical reaction are never present in the reaction chamber at the same time. This would result in uncontrolled growth due to gas phase reactions and particle formation.

## 2.2 Details of the sample preparation

Thin films of  $\text{La}_2\text{O}_3$ ,  $\text{ZrO}_2$  and  $\text{La}_y\text{Zr}_{1-y}\text{O}_x$  with different La:Zr pulse ratios 1:0 (which gives pure  $\text{La}_2\text{O}_3$  films), 4:1, 1:1, 1:4, 1:9 and 0:1 (which gives pure  $\text{ZrO}_2$  films) were deposited on p-type 200 mm Si (100) substrates (with resistivity of 3-10  $\Omega\text{-cm}$ ) in an ASM hot-wall, cross-flow PULSAR<sup>®</sup> 2000 ALCVD reactor. The wafers were HF-dipped for 1 minute to remove the native oxide, prior to the film depositions. The depositions were done at ASM Microchemistry, Finland. As mentioned in the previous section, Tris(2,2,6,6-tetramethyl-3,5-heptanedionato) lanthanum,  $\text{La}(\text{thd})_3$ , and bis(cyclopentadienyl)methyl methoxy(IV)zirconium, ZrD-04, [both from SAFC Hitec] were used as precursors for the  $\text{La}_2\text{O}_3$  and  $\text{ZrO}_2$  deposition, respectively, with ozone as the oxidizing agent. The deposition temperature was 300 °C. The composition of the  $\text{La}_y\text{Zr}_{1-y}\text{O}_x$  layers was varied by changing the pulse ratio of the  $\text{La}(\text{thd})_3$  and the ZrD-04 precursor. Different deposition rates and nucleation behaviour of  $\text{La}_2\text{O}_3$  and  $\text{ZrO}_2$  on top of each other result in samples with different thickness. (The number of ALD cycles used for different layers is given in Table 2.1).

## 2.3 Material analysis techniques

Once the layers were deposited on blanket wafers, they were analyzed with the following techniques:

- a) Spectroscopic ellipsometry to estimate the mean thickness of the deposited film.
- b) Rutherford back scattering spectroscopy (RBS) and X-ray photoelectron spectroscopy (XPS); both to investigate the composition of the films and in particular the La:Zr ratio.
- c) X-ray diffraction (XRD) to check the crystallinity and crystal structure of the thin

film material.

- d) High resolution transmission electron microscopy (HRTEM) facilitated with High Angle Annular Dark Field (HAADF) detector and Energy dispersive X-ray spectrometry (EDX) to determine the exact thickness of the film and the compositions of different phases in detail. This combination allowed us to check the composition of the desired region of the films with nanometer resolution.

## 2.4 Spectroscopic ellipsometry studies

Ellipsometric studies were useful to estimate the mean thickness of the dielectric films and to know the variation of the thickness along the surface. To estimate the thickness of films of different La:Zr ratios, the measurement program uses a combination of refractive indices of  $\text{La}_2\text{O}_3$  and  $\text{ZrO}_2$ . Fig. 2.1 shows a representative wafer scan that gives the variation in film thickness on the wafer and Fig. 2.2 shows 3D ellipsometric map of film thickness variation on a representative wafer. The reason for this thickness variation across the wafer is the lateral flow of the gases including the precursors as shown in Fig. 2.1.

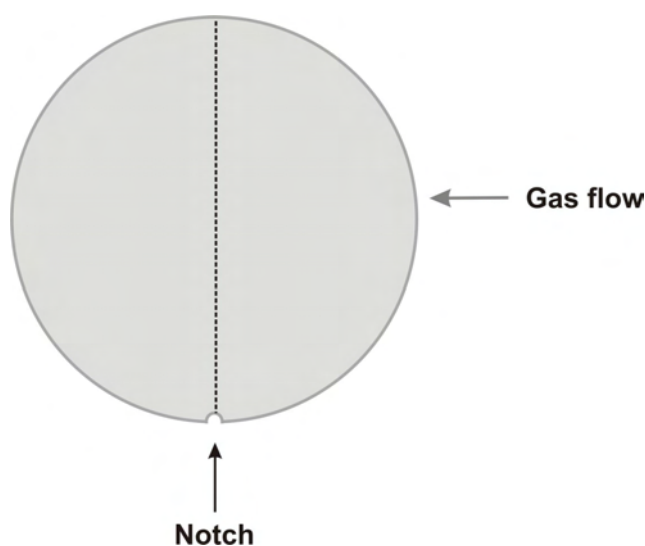


*Fig. 2.1. Schematics of mounting the 8 inch wafer in the reaction chamber and the direction of the gas flow.*

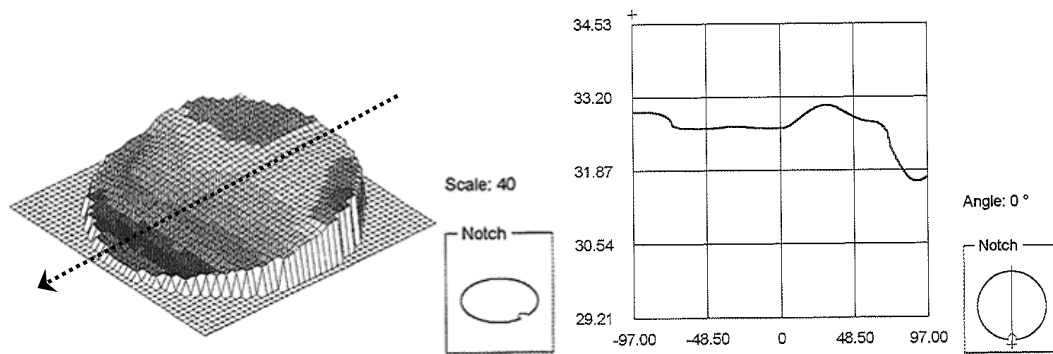


**Fig. 2.2.** Thickness profile of sample 1:4 measured using ellipsometry; (left) 3D and (right) 1D profile of the  $\text{La}_y\text{Zr}_{1-y}\text{O}_x$  film. The dotted arrow in the right image indicates the direction of the gas flow. The average value of the thickness of the film was 32.35 nm.

## 2.5 Stoichiometric studies

A comparison between stoichiometries determined with RBS and XPS and mean thickness estimated with ellipsometry are given in Table 2.1.

La:Zr pulse ratio	Number of ALD cycles	Mean thickness (nm) (Ellipsometry)	RBS La/La+Zr (%)	XPS La/La+Zr (%)
1:0	500	13.64 ± 3.06	100	100
4:1	120	21.42 ± 3.91	58.1	53.40
1:1	480	24.70 ± 2.31	26.4	24.20
1:4	240	32.35 ± 1.4	8.3	8.80
1:9	120	37.10 ± 1.80	1.9	1
0:1	500	22.54 ± 1.08	0	0

**Table 2.1.** Number of ALD cycles, mean ellipsometric film thickness, and stoichiometry (RBS, XPS), measured for different La to Zr precursor pulse ratios.

Ellipsometry data is average thickness of 49 different spots on the wafer. The nonuniformity in the film thickness is larger in films with larger lanthanum content, presumably due to the hygroscopicity of the films. The relation between the actual percentage of La and the La pulse ratio in % is shown in Fig. 2.3.

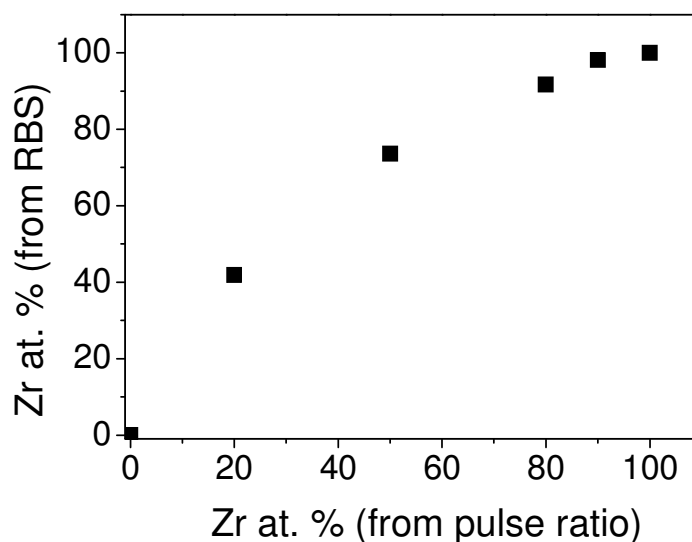


*Fig. 2.3. Relation between the expected Zr composition in the film (from the La:Zr pulse ratio) and the actual zirconium content in the film based on RBS measurements.*

Figure 2.3 shows that the relationship between the theoretical Zr%, estimated from the La:Zr pulse ratio and the actual percentage of Zr in the film does not follow a linear relationship with the intended Zr percentage. This nonlinear behaviour could be due to different growth rates of  $\text{ZrO}_2$  and  $\text{La}_2\text{O}_3$  films and different nucleation behaviour on top of each other. However, such a plot would be useful to deposit  $\text{La}_y\text{Zr}_{1-y}\text{O}_x$  layers with desired Zr% in it.

## 2.6 X-ray Diffraction analyses

This section explains the results of X-ray diffraction (XRD) experiments carried out to know the crystallinity of the films.

### 2.6a $\text{La}_2\text{O}_3$ samples

Figure 2.4 shows XRD patterns of as-deposited and annealed  $\text{La}_2\text{O}_3$  samples. Most of the  $\text{La}_2\text{O}_3$  films are amorphous when deposited by in ALD [13] (especially when deposited with  $\text{La}(\text{thd})_3$  precursor) and remain so even after a post-deposition anneal at  $850^\circ\text{C}$ . However, it

has also been reported that  $\text{La}_2\text{O}_3$  deposited using radio frequency (RF) magnetron sputtering remains amorphous up to a post-deposition anneal at  $500^\circ\text{C}$  and becomes polycrystalline at  $700^\circ\text{C}$  anneal [14].

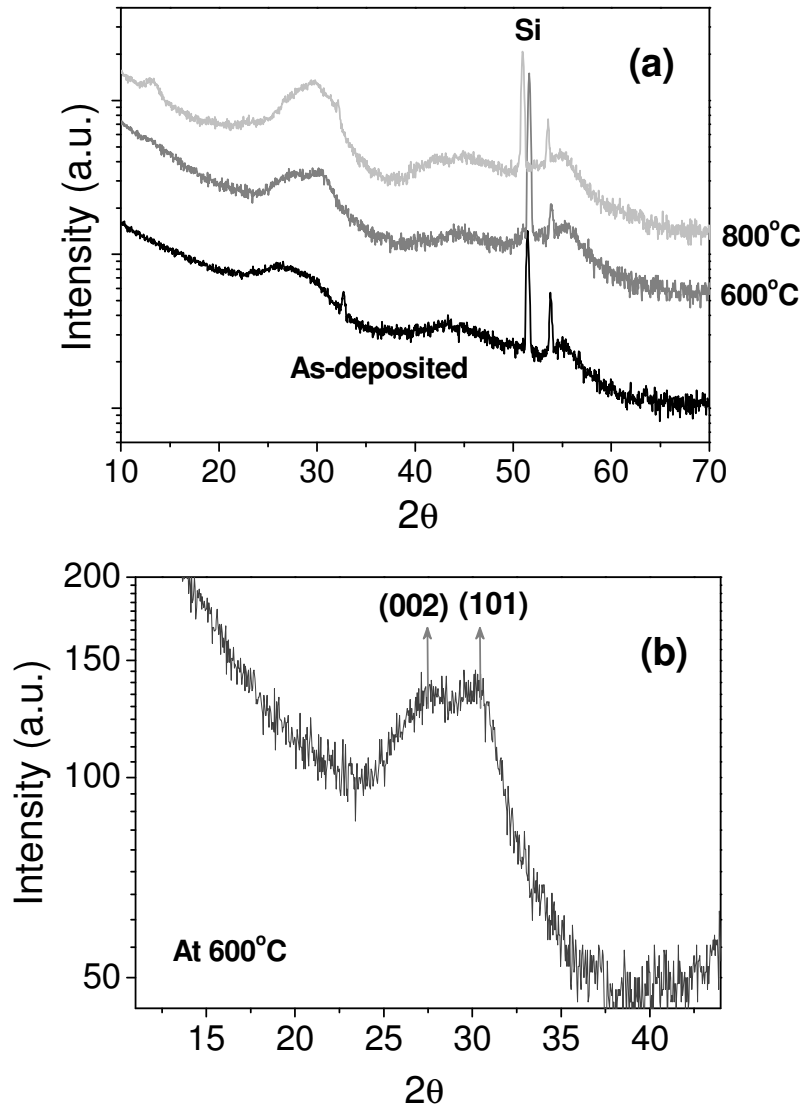


**Fig. 2.4.** (a) XRD patterns of  $\text{La}_2\text{O}_3$  samples as deposited, annealed in nitrogen atmosphere at  $600^\circ\text{C}$  and  $800^\circ\text{C}$ . The sharp peaks around 30 and 50 degree grazing angles are from silicon substrate and the slight relative shifts result from slight variations in grazing angle of X-rays with respect to the sample orientation. (b): Possibility of co-existence of two different nano-crystalline (tetragonal) phases of  $\text{La}_2\text{O}_3$  in the sample annealed at  $600^\circ\text{C}$ .

As becomes evident from Fig. 2.4 (a), the as-deposited  $\text{La}_2\text{O}_3$  films are amorphous and the onset of crystallization (short-range ordering) into hexagonal phase can be vaguely recognized

at 600 °C, as seen in Fig. 2.4 (b). Upon post-deposition anneal at 800°C, these  $\text{La}_2\text{O}_3$  films become more crystalline (in the form of nanocrystallites, judging from the appearance of small-angle peaks close to 14°), but the bulk part of the films remains amorphous. This short-range order is increasing on annealing at higher temperatures, as suggested by the increasing XRD relative intensities of the broad peaks with respect to that from the as-deposited sample.

Table 2.2 gives the identification of peaks in the XRD pattern on comparison with the standard peaks of  $\text{La}_2\text{O}_3$  from literature [15].

$\text{La}_2\text{O}_3$ Sample	Position of the peaks ( $2\theta$ °)	Crystallographic plane
As deposited	26.8	(100)
	45	(110)
	55	(112) and (201)
Annealed at 600°C	30.3	(101)
	55.3	(112) and (201)
	29.8	(101)
Annealed at 800°C	45	(110)
	55	(112) and (201)

**Table 2.2.** Diffraction angles and corresponding planes of as-deposited and annealed  $\text{La}_2\text{O}_3$  samples as per Ref [15].

The diffraction patterns we get for 600°C annealed  $\text{La}_2\text{O}_3$  film emerge seemingly from trigonal A-type  $\text{La}_2\text{O}_3$  with lattice parameters  $a = 0.39$  nm and  $b = 0.62$  nm (however keeping in mind that XRD patterns of nanocrystals usually shift to lower grazing angles due to size effects). This could be considered as the onset of the commonly observed hexagonal phase of  $\text{La}_2\text{O}_3$  upon annealing at higher temperatures than 800°C [15].

### 2.6b Effects of adding Zr to $\text{La}_2\text{O}_3$

The primary intention of mixing Zr with  $\text{La}_2\text{O}_3$  was to synthesize a uniform solid solution to yield  $\text{La}_y\text{Zr}_{1-y}\text{O}_x$  thin films. After deposition, the blanket wafers with the mixed oxide films were subjected to XRD analyses and Fig. 2.5 (a) and (b) depicts the XRD patterns of the as-deposited samples with different Zr content. Interestingly, the XRD patterns shown in Fig. 2.5 indicate that crystalline phases start to appear in the films upon mixing Zr into the sample. The black and grey lines protruding from the  $2\theta$ -axis are the respective theoretical positions

of the tetragonal and monoclinic phases of  $\text{ZrO}_2$ . This suggests that  $\text{ZrO}_2$  undergoes phase segregation in the film where  $\text{ZrO}_2$  forms hexagonal or monoclinic crystals in an amorphous  $\text{La}_2\text{O}_3$  medium, rather than forming a uniform  $\text{La}_y\text{Zr}_{1-y}\text{O}_x$  film.

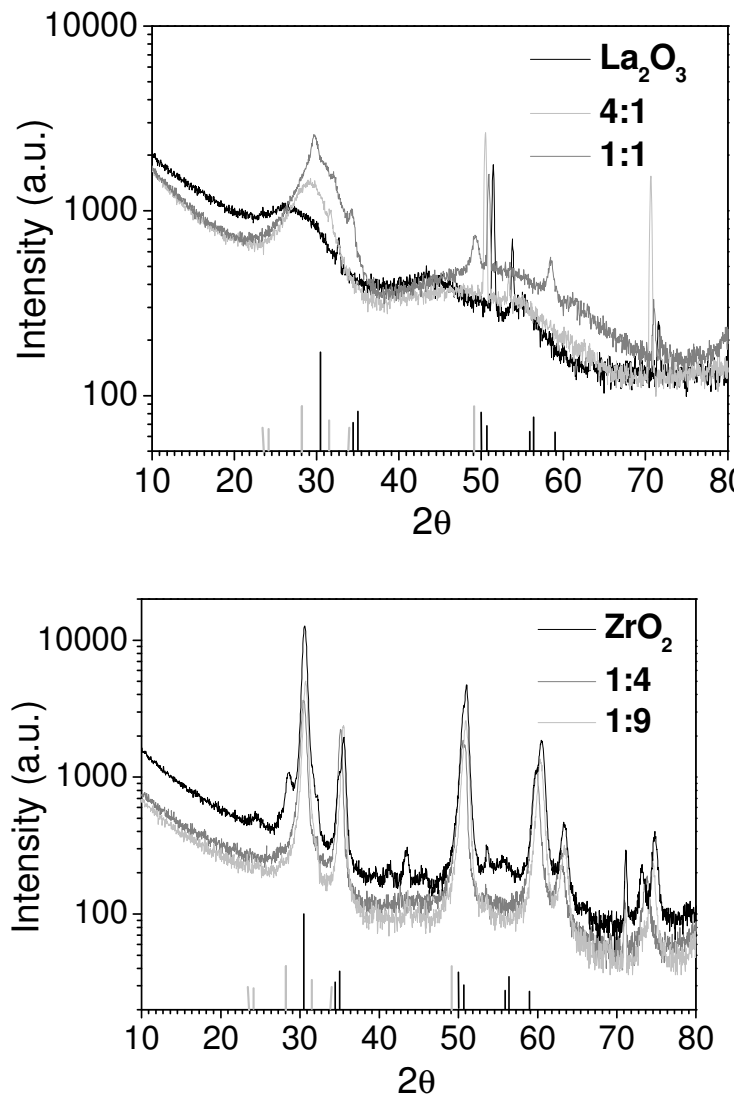


**Fig. 2.5.** (a): XRD patterns of  $\text{La}_2\text{O}_3$ ,  $\text{La}/\text{Zr}=4:1$  and  $\text{La}/\text{Zr}=1:1$  pulse ratio samples. The black and grey lines protruding from the X-axis are theoretical positions of XRD peaks of tetragonal and monoclinic  $\text{ZrO}_2$ . (b): XRD patterns of  $\text{La}/\text{Zr}=1:4$ ,  $\text{La}/\text{Zr}=1:9$  and  $\text{ZrO}_2$ .

Comparing the intensities and the peak-widths of XRD patterns of films with different Zr percentage, it is evident that the film becomes more and more crystalline by adding Zr in it and that the  $\text{ZrO}_2$  cluster size is increasing with increasing percentage of Zr in the film. It is



also important to notice that the phase segregation to tetragonal or a mixed phase of tetragonal and monoclinic form depends on the Zr content in the films. A discussion on the details of the crystal phase will be given later in this chapter.

A crude estimation of the  $\text{ZrO}_2$  cluster size in the samples can be derived from the full-width-at-half-maximum (FWHM) of the XRD peaks (employing a Gaussian fit to the selected curve), using the Debye-Scherrer formula [16], which gives the grain size of the clusters normal to the reflecting plane of the X-rays in terms of the half-width  $\beta$  (the width of the diffraction peak at which the intensity has fallen to half the maximum intensity) as

$$D = \frac{0.94\lambda}{\beta \cos \theta} \quad (2.1)$$

Here  $\theta$  is half the grazing angle where the highest diffraction peak appears. Fig. 2.6 shows the estimated cluster size of the  $\text{ZrO}_2$  as a function of the Zr % in the film. (The experimental Zr% mentioned throughout this chapter is from RBS measurements).

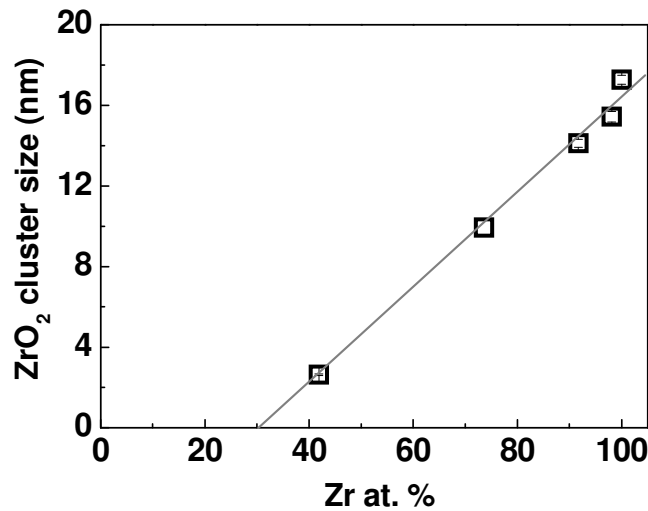


**Fig. 2.6.**  $\text{ZrO}_2$  cluster size estimated using Debye-Scherrer formula, as a function of the Zr% (from RBS measurements) in the films.

The  $\text{ZrO}_2$  cluster size increases linearly with the Zr content of the film (regardless of its phase) as Fig. 2.6 shows. It is important to note that the cluster sizes are much lower than the film thickness. Since the Debye-Scherrer formula gives an estimate of the cluster size normal to the angle of incidence of the X-rays, the crystal sizes estimated here are not a function of the thickness of the films. A linear extrapolation of the data suggests that there is no cluster

formation in the film when the Zr content in the film is less than 30%. Therefore, the solid-solubility limit of  $\text{ZrO}_2$  in  $\text{La}_2\text{O}_3$  is 30% in these films.

To check this hypothesis, films with 20% Zr in the films were deposited with the La:Zr precursor pulse ratio of 12:1. Fig. 2.7 shows the XRD patterns of this film together with a reference pattern of 4:1 films for comparison. The intensity of the 12:1 sample is lesser than that of 4:1 and the absence of small angle peaks suggests that the existence of nanocrystallites in the film is very unlikely and any plausible short-range order in the film is beyond the detection limit of the X-ray diffractometer.

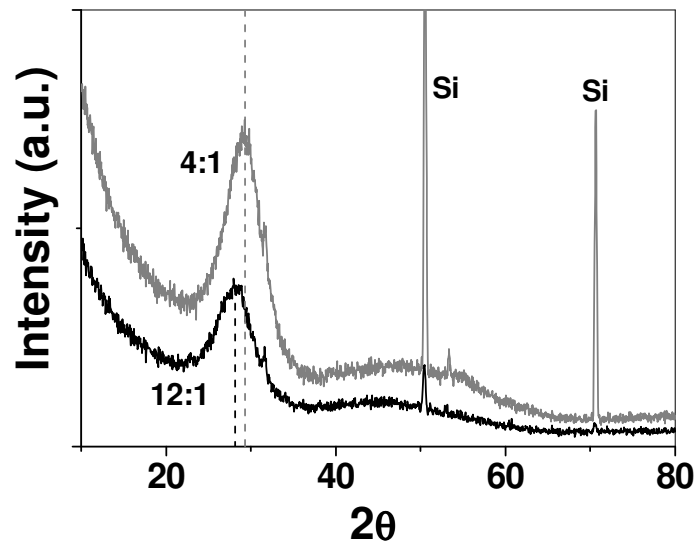


*Fig. 2.7. XRD of La:Zr pulse ratio=12:1 (black) and  $\text{ZrO}_2$  (grey) samples. The dotted lines indicates the position of the diffraction peak (maximum of the Gaussian) of the films.*

The signature peak of the Si substrate also is shown in Fig. 2.7; the positions of the diffraction peaks from the silicon substrate in both the spectra coincide within the accuracy of the experiments. Referring to the previous XRD results reported, the peak position  $2\theta = 28.7$  of the 12:1 sample corresponds to the  $d(222)$  interplanar spacing of the mixed  $\text{La}_y\text{Zr}_{1-y}\text{O}_x$  phase in the film [5], if there exists any short-range ordering at all. The diffraction peak of the 4:1 film corresponds more to the tetragonal  $\text{ZrO}_2$  phase. However, it is worth noting that the mixed phase boundary of  $\text{La}_y\text{Zr}_{1-y}\text{O}_x$  to a phase segregation is very close to 4:1 film. Assuming that film with La:Zr = 12:1 is a mixed solid-solution, its stoichiometric form with 20% La should be  $\text{La}_{0.2}\text{Zr}_{0.8}\text{O}_{1.9}$ .

## 2.7 High Resolution Transmission Electron Microscopy and Energy dispersive X-ray spectrometry analyses

In order to further validate the conclusion from the XRD analyses that above 30 at% Zr in the film, the film has a phase-separation into nanocrystalline  $\text{ZrO}_2$  and amorphous  $\text{La}_y\text{Zr}_{1-y}\text{O}_x$  rather than a uniform  $\text{La}_y\text{Zr}_{1-y}\text{O}_x$  thin film, further morphological studies are necessary. Obviously, the next analysis to identify these nanoclusters and their distribution in the film is High Resolution Transmission Electron Microscope (HRTEM). Together with HR-TEM, Energy Dispersive X-ray spectrometry was used to identify the stoichiometry of the desired regions in the films with nanometer resolution. For instance, EDX allows us to identify the amorphous regions or if the clusters are composed of  $\text{ZrO}_2$  or metallic Zr or otherwise.

For the HR-TEM inspection, the  $\text{La}_y\text{Zr}_{1-y}\text{O}_x$  thin films on silicon wafers were prepared using a FIB200 (FIB stands for Focussed Ion Beam) and a Nova Nanolab200 SDB (Small Dual Beam). Before FIB preparation an aluminium layer was deposited on the samples as protection layer. Subsequently a thin Pt layer is deposited in a sputter coater on the sample. After this deposition a 1.5  $\mu\text{m}$  Pt layer is deposited in the FIB on the region of interest to protect the sample during FIB milling. For the final thinning and the removal of the damage of the high-energy (30 keV) ion milling steps, the SDB is used and operated at 5 keV. TEM studies were performed using a TECNAI F30ST TEM operated at 300kV.

The HAADF (High Angle Annular Dark Field) detector uses the electrons scattered over large angles for imaging. The HAADF detector is therefore mass sensitive, which means that higher brightness in the image corresponds to the presence of (a larger concentration of) heavier atoms.

Using an Energy Dispersive X-ray detector it is possible to detect element characteristic X-rays. In the EDX spectrum the detected signal is plotted as a function of the (characteristic) energy. Chemical compositions can be obtained by quantification of the data. However, quantification of the light elements does not necessarily lead to the right concentrations since other parts of the sample partially absorb the X-ray signals of these elements.

### 2.7a Results of TEM & EDX inspection

Table 2.3 gives a comparison between the dielectric layer thicknesses measured using ellipsometry and TEM. Table 2.4 gives the stoichiometry comparison between the RBS, XPS (X-ray Photoelectron Spectroscopy), EDX and TEM (EDX) measurements. This confirms the

accuracy of other stoichiometry measurements once again, though EDX is not as accurate as RBS or XPS. Apparently, unlike RBS, EDX together with HRTEM gives the stoichiometry of a very narrow region of the film.

TEM gives comparable results with the other techniques utilized. Thickness of layer 4:1 measured with TEM seems to be lower than the ellipsometry estimation, but TEM has shown slightly varying thickness in different parts of the wafer, which is because of the slight thickness variation across the blanket film on the wafer akin to the case seen in Fig. 2.2.

<b>La:Zr pulse ratio</b>	<b>Thickness ellipsometry (nm)</b>	<b>Thickness TEM (nm)</b>
1:0	13	14
4:1	22	16
1:1	24	30
1:4	32	35
1:9	37	40
0:1	22	23

**Table 2.3.** A comparison between the thicknesses of different  $\text{La}_y\text{Zr}_{1-y}\text{O}_x$  films measured using ellipsometry and TEM.

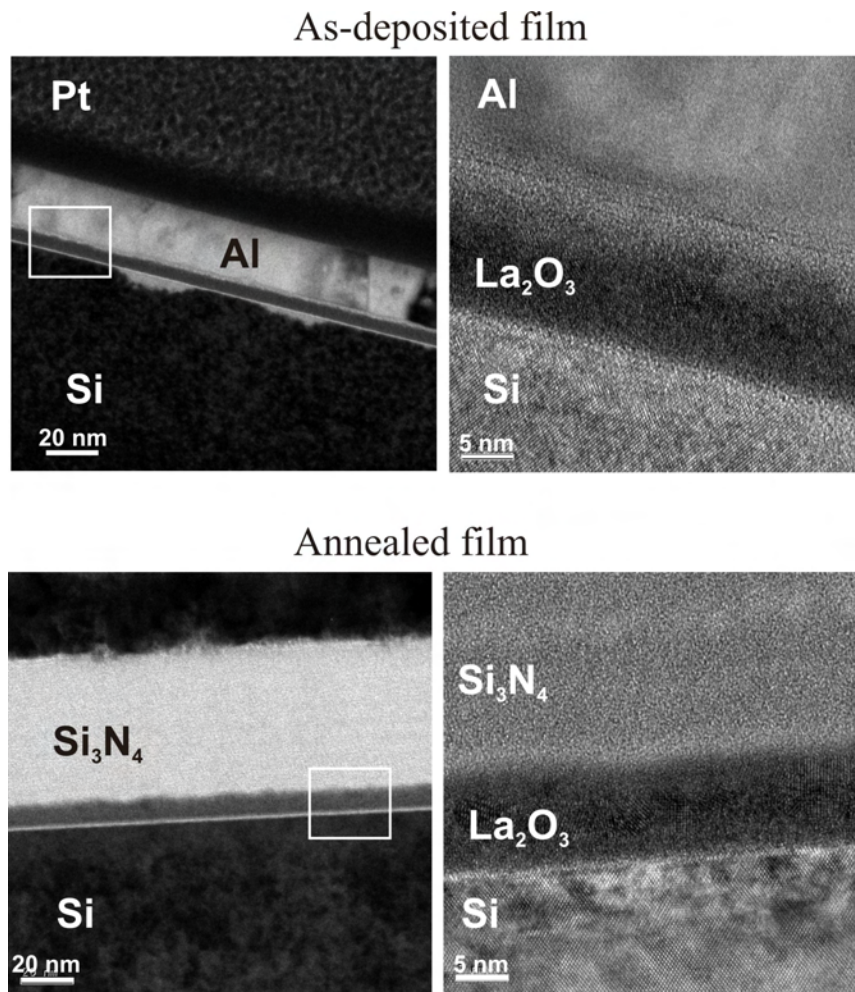
<b>La:Zr</b>	<b>La/La+Zr</b>		<b>EDX La/La+Zr</b>	<b>Amorphous/ crystalline</b>
	<b>RBS</b>	<b>XPS</b>		
1:0	100%	100%	99%	Amorphous / beam-induced crystallization
4:1	58.1%	53.4%	62%	Amorphous
1:1	26.4%	24.2%	17%	Amorphous with crystalline clusters
1:4	8.3%	8.8%	10%	Crystalline with a 3-6 nm thick amorphous bottom part
1:9	1.9%	-	1%	Crystalline
0:1	0%	0%	0%	Crystalline

**Table 2.4.** Comparison between the stoichiometries measured with RBS, XPS and TEM (EDX).

In conclusion, local stoichiometry estimation using EDX is in close agreement with RBS and XPS measurements. TEM and ellipsometry measurements of the dielectric thickness also are comparable. In the next section, a comparison between results obtained using HR-TEM on as-deposited samples and samples annealed at 400°C for 30 minutes in nitrogen atmosphere is discussed.

### 2.7.a.1 HR-TEM of lanthanum oxide

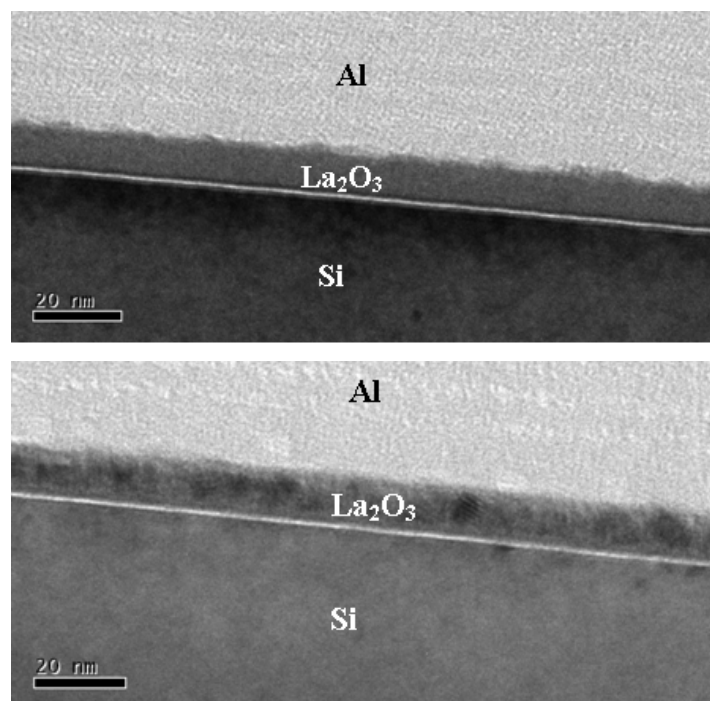
Figure 2.8 gives a general impression on the interfacial details of the as-deposited and annealed  $\text{La}_2\text{O}_3$  thin films on silicon with HR-TEM images. In the as-deposited films, aluminium and platinum were deposited as protection layers for the focused ion beam (FIB) preparation of the sample. In a detailed image at a higher magnification as shown in Fig. 2.8, the  $\text{La}_2\text{O}_3$  film appears polycrystalline, and most often with clear Moiré patterns in it, meaning that there is more than one crystal with different crystal orientation in the film. Strikingly, the interface between  $\text{La}_2\text{O}_3$  and Al appears very fuzzy, though the interface can be identified as a line in the upper right image. Apparently, the grey region in the  $\text{La}_2\text{O}_3$  film, below the interface line with aluminium is due to aluminium in-diffusion to the  $\text{La}_2\text{O}_3$  film. This would adversely influence the inspected film qualities, especially after annealing, where the in-diffusion will be enhanced. Therefore, for the experiments with annealed films,  $\text{Si}_3\text{N}_4$  was used as the FIB protection layer, which makes a better interface with the  $\text{La}_2\text{O}_3$  film. Annealing of the films was performed in forming gas (10%  $\text{H}_2$  + 90%  $\text{N}_2$ ) at 430 °C for 30 minutes. HR-TEM inspection indicates that there is no crucial change with forming gas anneal (FGA). The interfacial oxide thickness in the as-deposited film was  $0.8 \pm 0.1$  nm, which remains nearly the same ( $0.7 \pm 0.1$  nm) upon FGA.



**Fig. 2.8.** HR-TEM images of as-deposited and annealed (FGA)  $\text{La}_2\text{O}_3$  on silicon. (Top left): Al and Pt protection layers deposited on top of the oxide film. The amorphous-like parts appearing in silicon lattice close to the Si-  $\text{La}_2\text{O}_3$  interface is damage in silicon due to the ion beam. (Top right): Zoomed-in version of the rectangular portion of the film, where the interface between Si/ $\text{La}_2\text{O}_3$  and  $\text{La}_2\text{O}_3$ /Al are clearly seen. (Lower left):  $\text{La}_2\text{O}_3$  thin film after forming-gas anneal for 30 minutes; (Lower right): Zoomed-in image of the rectangular part of the image.

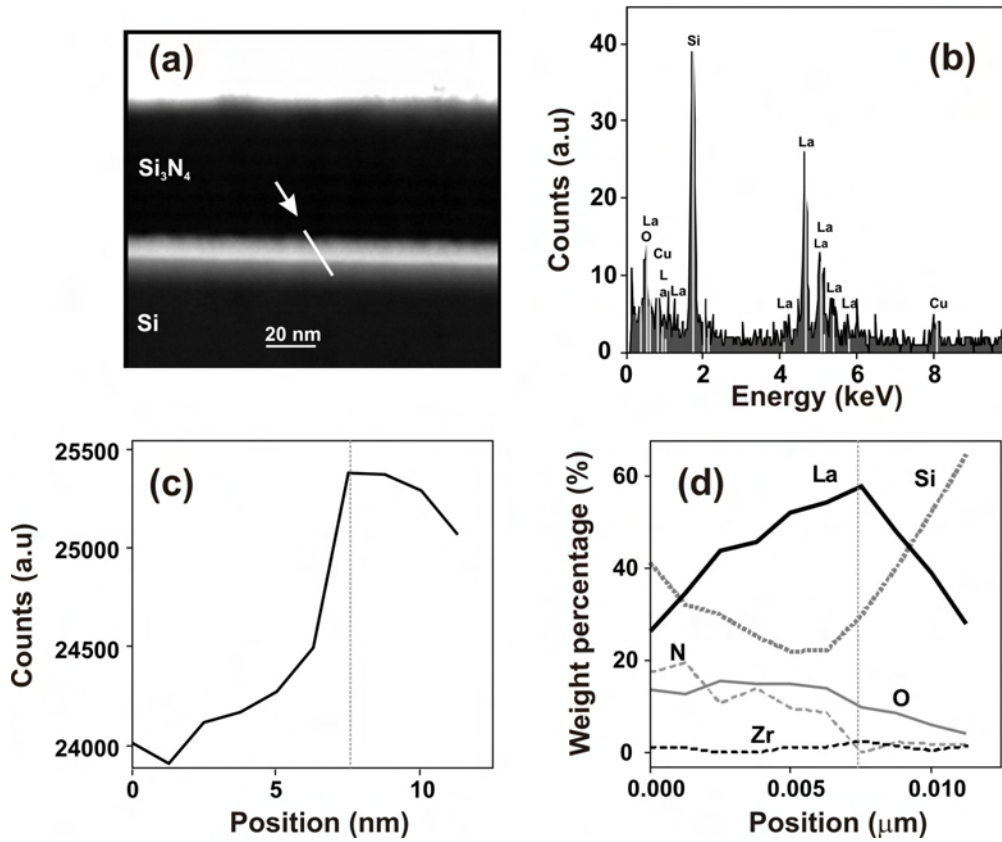
The polycrystalline nature of  $\text{La}_2\text{O}_3$  films observed in HR-TEM is contradicting to the XRD results, which indicates that the  $\text{La}_2\text{O}_3$  film is completely amorphous. Therefore, much attention was given to the HR-TEM inspection and more detailed experiments were performed, where the film was exposed to the electron beam for different durations. From this, it was found that this crystallization is an electron-beam-induced phenomenon. The films exposed to the electron beam of the TEM for a few seconds ( $< 10$  s) were amorphous and the

nucleation was observed to set in gradually. Fig. 2.9 shows the HR-TEM images of a quick imaging and image of the same area after a few seconds (which took more than 10 seconds).



**Fig. 2.9.** (Above) HR-TEM image of  $\text{La}_2\text{O}_3$  film with a rapid scan, where the film appears amorphous; (below) nanocrystals of  $\text{La}_2\text{O}_3$  nucleating as a result of the electron beam from the TEM after a few seconds.

As discussed in section 3.2.1, crystallization in amorphous  $\text{La}_2\text{O}_3$  sets in at 800 °C (though an onset of crystallization appears already at 600 °C), but the electron beam is powerful enough to initiate a strong annealing effect resulting in the nucleation of nanocrystals. Occasionally, the e-beam induced damage can be observed even in silicon substrate, for instance the white patches appearing in Si in Fig. 2.8 (a) that are amorphous regions created by e-beam damage. However, this is an important observation that if one relies on HRTEM alone, that will lead to the erroneous conclusion that as-deposited  $\text{La}_2\text{O}_3$  films are polycrystalline. An instance for such a confusion can be seen in Ref. [17], where the ALD processed 35 nm  $\text{La}_2\text{O}_3$  layers appears to have nanocrystals embedded in the film, but the XRD spectra up to 700 °C show no trace of crystallization. An added complexity is that in films thinner than 5 nm, identifying nanocrystals with X-ray diffraction is rather difficult. Therefore, imaging techniques should be carefully performed to derive conclusions about the crystallinity of such layers.



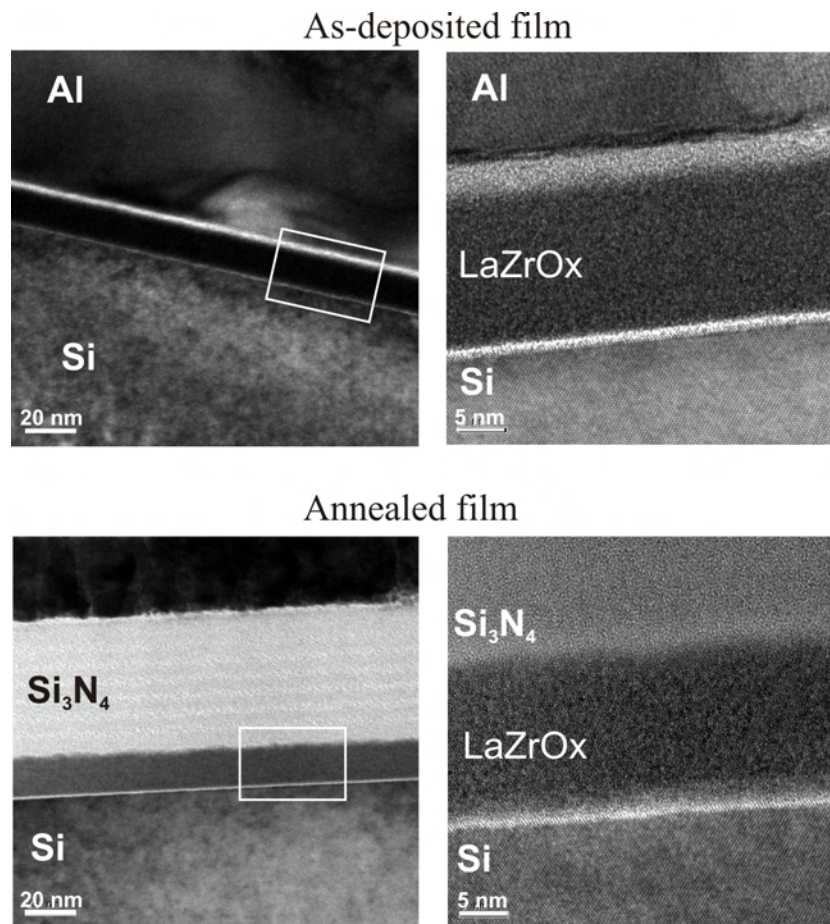
**Fig. 2.10.** (a) TEM image of a  $\text{Si}_3\text{N}_4/\text{La}_2\text{O}_3/\text{Si}$  stack, where the bright region is the  $\text{La}_2\text{O}_3$  film. (b) EDX of  $\text{La}_2\text{O}_3$  film from a selected area of the film cross-section. (c) HAADF detector signal for La along the white line in (a), across the  $\text{La}_2\text{O}_3$  film. The dotted line is roughly the  $\text{La}_2\text{O}_3$ -Si interface. (d) Atomic weight percentage of different elements in the film according EDX along the white line across the film in (a).

Figure 2.10 shows the EDX analysis on the annealed  $\text{La}_2\text{O}_3$  film performed together with HAADF detector. The line scan was carried out across the film, as the line in the TEM image shows and the corresponding stoichiometric information obtained is plotted in the right-side image of Fig. 2.10. Besides a very thin native oxide ( $\text{SiO}_x$ ) at the interface with silicon, the lanthanum content is increasing considerably towards the  $\text{SiO}_2$ - $\text{La}_2\text{O}_3$  interface, as evident from the HAADF signal shown in Fig. 2.10 (c). In addition, the EDX signals given as atomic weight percentage shown in Fig. 2.10 (d) gives the same conclusion. The small  $\text{La}_2\text{O}_3$  peak width (i.e. the thickness range where  $\text{La}_2\text{O}_3$  is only present) indicates the formation of either  $\text{La}_y\text{Si}_{1-y}\text{O}_x$  usually forming when  $\text{La}_2\text{O}_3$  reacting with  $\text{SiO}_x$  upon annealing at temperatures  $>600^\circ\text{C}$  [5, 18] and/or the formation of silicide ( $\text{LaSi}_2$ ) due to lanthanum diffusion to the  $\text{La}_2\text{O}_3$ -Si interface [19].



### 2.7.a.2 TEM of the sample with La:Zr = 4:1

HR-TEM images of the as-deposited and annealed thin film with La:Zr = 4:1 (containing 58% La) is shown in Fig. 2.11, crystalline structures cannot be observed in the  $\text{La}_y\text{Zr}_{1-y}\text{O}_x$  layer, though it seems to contain  $\text{ZrO}_2$  nanocrystals of  $\sim 3\text{nm}$  size from the XRD studies. Such small crystallites are usually not seen in TEM and therefore, the sample looks amorphous. An interesting observation here is that inclusion of Zr in the film prevents the sample from crystallizing under electron bombardment, even after longer exposure to the electron beam. Interfacial oxide thickness seems to remain constant ( $\sim 1\text{ nm}$ ) upon FGA.



**Fig. 2.11.** TEM of as-deposited La:Zr = 4:1 thin film at different magnifications (scale bar is 20 nm in the left and 5 nm in the right image). The sample looks amorphous.

To perform the compositional analysis, HAADF overview images were used, by selecting a small area from the cross-section of the annealed  $\text{La}_y\text{Zr}_{1-y}\text{O}_x$  film as shown as a white rectangular box in Fig. 2.12 (a). Fig. 2.12 (b) shows the EDX spectrum of the highlighted

region, where Zr and La signals can be clearly identified. This analysis provides a measure of 53.4 at% of La in the film measured, which is comparable with the RBS estimation of 58.1 at. %. Fig. 2.12 (d) shows the weight percentage of different elements across the film, along the white line shown in (c).

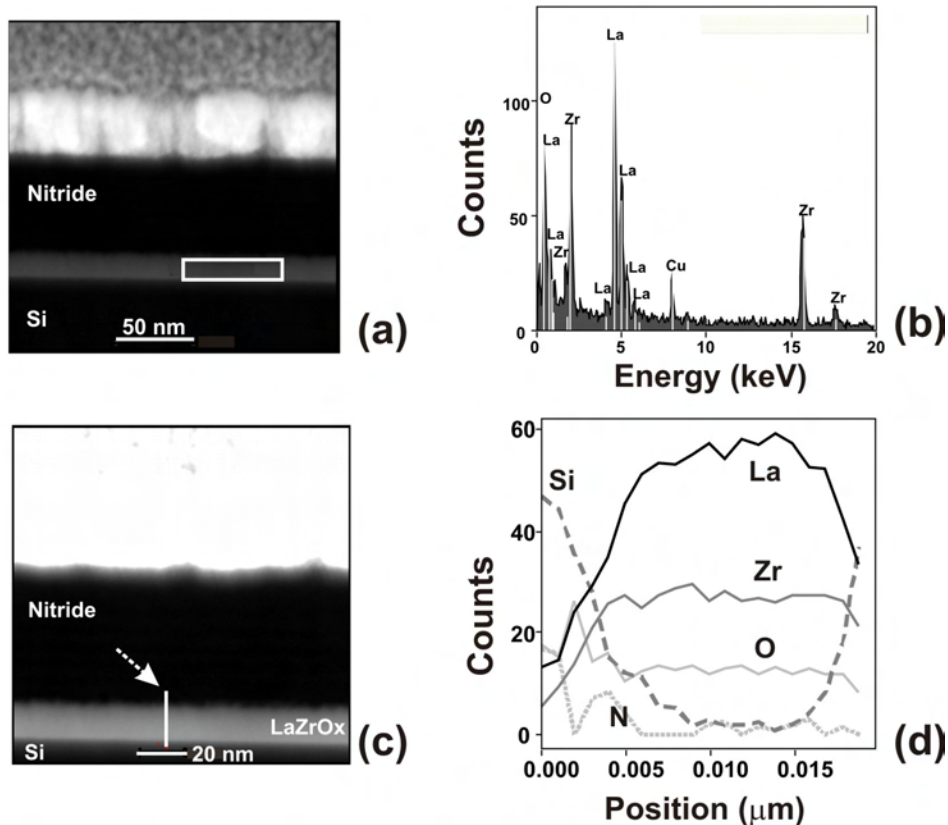


**Fig. 2. 12.** (a) HAADF image; the grey band with the white box is the  $\text{La}_y\text{Zr}_{1-y}\text{O}_x$  film. 4:1 (b) EDX spectrum of the film enclosed in the rectangle in the HAADF image (c) HAADF overview image of the sample and the white line across the high-k film is the EDX line scan performed across the stack, which yielded the EDX weight percentage of different species shown in (d).

### 2.7.a.3 TEM of the sample with La:Zr = 1:1

Sample with La:Zr = 1:1 (containing 26% La) shows clear cluster formation as indicated in Fig 2.13. Different embedded clusters could be observed in the bright-field image as well. Since XRD analyses were performed on thin films deposited on Si substrate before the electrode deposition, this clustering cannot be due to the influence of the  $\text{Si}_3\text{N}_4$  layers deposited on top.

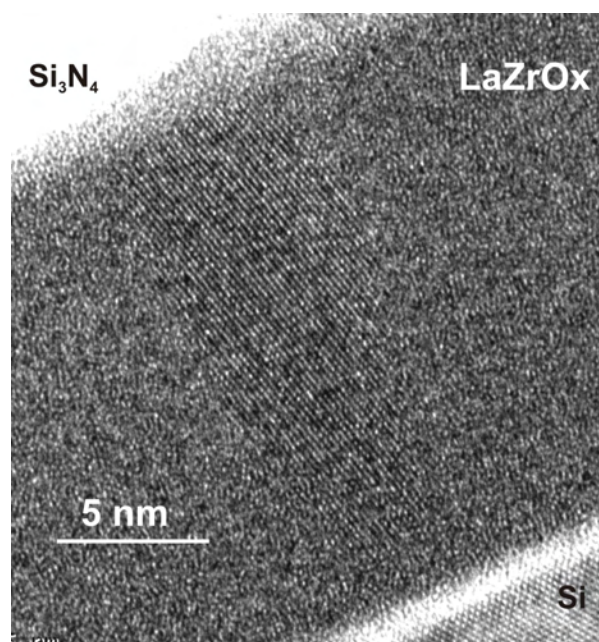


**Fig. 2.13.** HR-TEM image of 1:1 sample. A columnar nanocluster of  $\text{ZrO}_2$  can be seen embedded in amorphous  $\text{La}_2\text{O}_3$ . The interfacial oxide thickness is 1.5 nm.

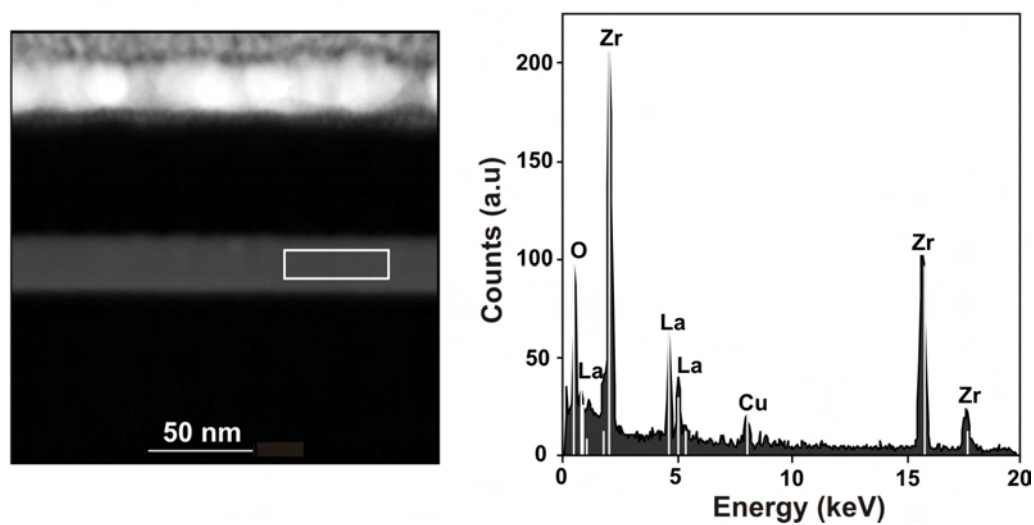


**Fig. 2.14 (a).** (left) TEM with (High angle annular dark field - HAADF) detector image of the layer and the area inside the red square chosen was selected to study the composition with EDX. (Right) EDX spectrum of the film in the selected region of the film.

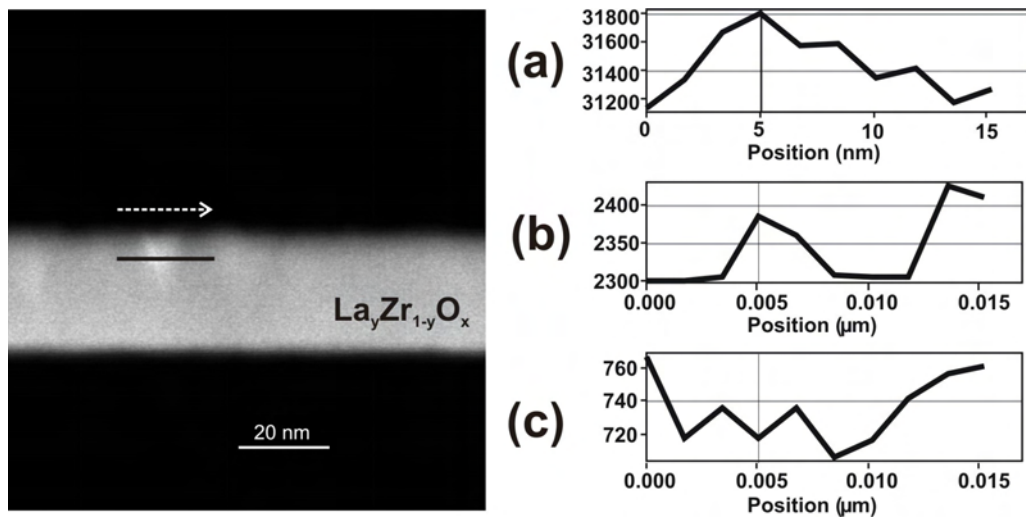


**Fig. 2.14 (b).** (Left) HAADF image of the same film where a nanocrystal is seen very vaguely. The white arrow indicates the scan direction. (Right) a) HAADF detector signal, b) Zr signal in the cluster, c) La signal in the cluster.

The high angle annular dark field (HAADF) image shown in Fig. 2.14(b) shows very vague bright clusters embedded in the oxide thin film. At the bright location in the HAADF image a crystalline  $\text{ZrO}_2$  grain is present. A line-scan across this cluster (Fig. 2.14(a) - (a)) shows an enhanced HAADF signal, which suggests that the bright spot contains a different stoichiometry than the surrounding region. A detailed inspection shows that at this location the Zr-signal is higher, as shown in (b). At the end of the line scan both the Zr and La signal increase. The reason for this signal increase is unknown: if the material were denser on that location, one would expect an intensity increase on the HAADF-detector too. However, this is very improbable here.

#### 2.7.a.4 TEM of the sample with La:Zr = 1:4

With increasing Zr content in the film, larger cluster formation is observed as shown in Fig. 2.15, the HR-TEM image of sample containing La:Zr = 1:4 (with only 8.3% La in the film). Even though the film is largely crystalline, the first 3-6 nm on the bottom part of the film is amorphous. From our EDX inspection, it is not clear whether the composition in the crystalline and the amorphous parts are different, but XRD shows mainly tetragonal  $\text{ZrO}_2$  clusters in the film.

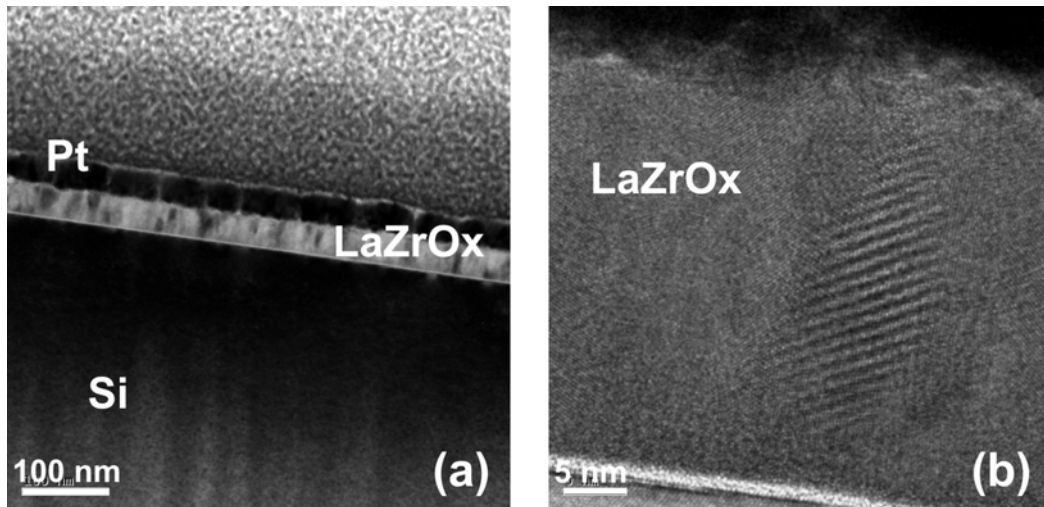


**Fig. 2.15.** (a) Bright field HRTEM image of 1:4 sample, where the dark spots in the oxide film are nanoclusters embedded in the film. (b) HRTEM image of the nanoclusters, exhibiting a Moiré pattern resulting from the differently oriented crystals behind the projected crystal. The film is 35 nm thick.

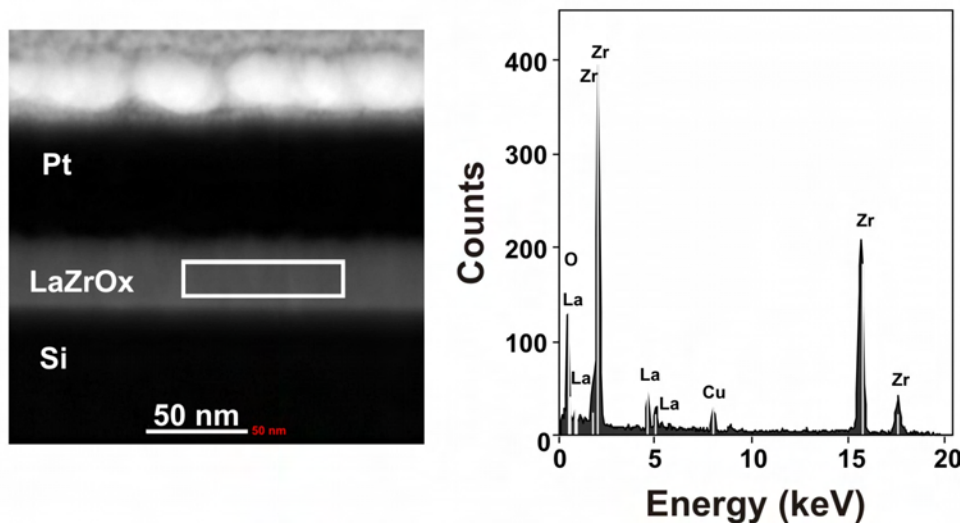


**Fig. 2.16.** HAAFD image (left) and EDX of the selected area of the film (right).

The native oxide thickness in these layers was  $\sim 1.5$  at the silicon- high- $k$  interface and there is no change in this native oxide thickness after forming gas annealing. Fig. 2.15 (a) shows that the layer has a large distribution of the  $\text{ZrO}_2$  clusters (which appear as dark dots in the film). From EDX, La content of 8.8 at% was estimated, while the RBS measurements give 8.3 at.% of La in the film (as shown in Table 2.1).



### 2.7.a.5 TEM of the sample with La:Zr = 1:9

A much higher cluster density is seen in the TEM images of the 1:9 sample, where the Zr content is dominating (98.2%), which appear as columnar black regions in Fig. 2.17 (a). Moiré patterns of nanocrystallites can be clearly seen in Fig. 2.17 (b). The thickness of the native oxide layer here also is  $\sim 1$  nm. EDX analysis gives a measure of 1% La in the film (RBS gives 1.9%).

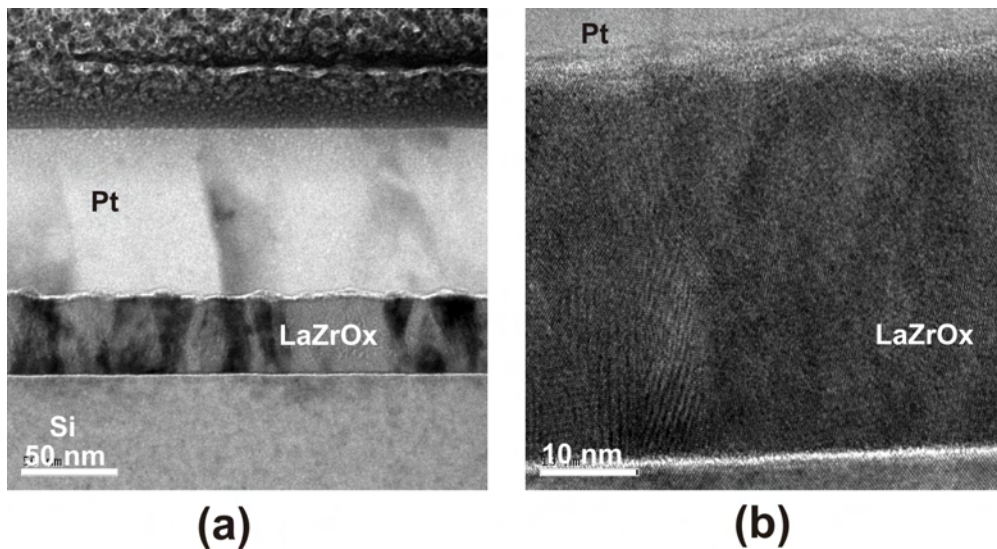


**Fig. 2.17.** (a) Bright field TEM image of the as-deposited sample with La:Zr = 1:9; (b) Zoomed-in version of the film, where Moiré patterns due to the diffraction of electrons from crystals of different orientation is visible.

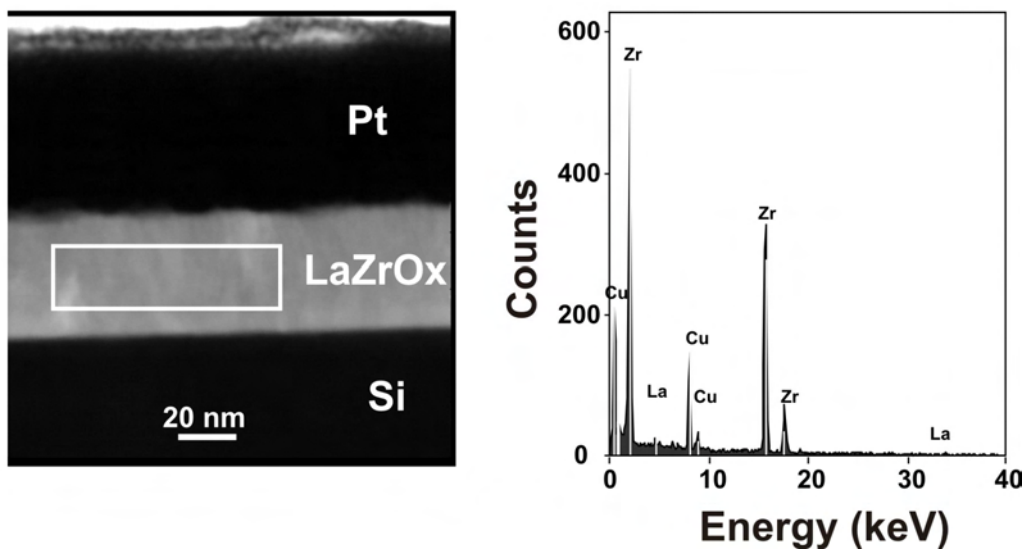


**Fig. 2.18.** HAADF image of the sample with La:Zr = 1:9 and the EDX spectrum of the highlighted area. The peaks of Cu in the spectra are from the X-ray source of the EDX spectrometer.

### 2.7.a.6 TEM of the sample with La:Zr = 0:1 – $\text{ZrO}_2$ films

As evident from XRD studies,  $\text{ZrO}_2$  film is polycrystalline, with a mix of tetragonal and monoclinic phases. As deposited samples exhibit an interfacial oxide thickness of 0.5 nm,

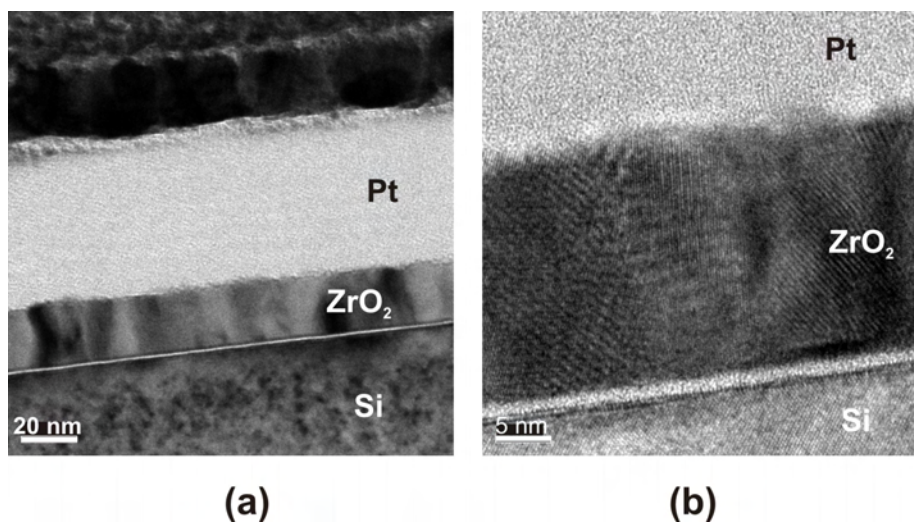


**Fig. 2.19.** (a) Bright field TEM image of  $\text{ZrO}_2$  sample, showing polycrystalline  $\text{ZrO}_2$  in the film. The film is 22 nm thick. (b) A closer look at the grains - Moiré patterns due to crystals of different orientation in the film. Columnar grain growth of  $\text{ZrO}_2$  can be identified from this image.

which becomes 1 nm upon forming gas annealing. Fig. 2.19 shows the HRTEM images of  $\text{ZrO}_2$  films, in which polycrystalline film with columnar  $\text{ZrO}_2$  grains can be identified. Fig. 2.20 shows the HAADF image and the EDX spectrum of the film.

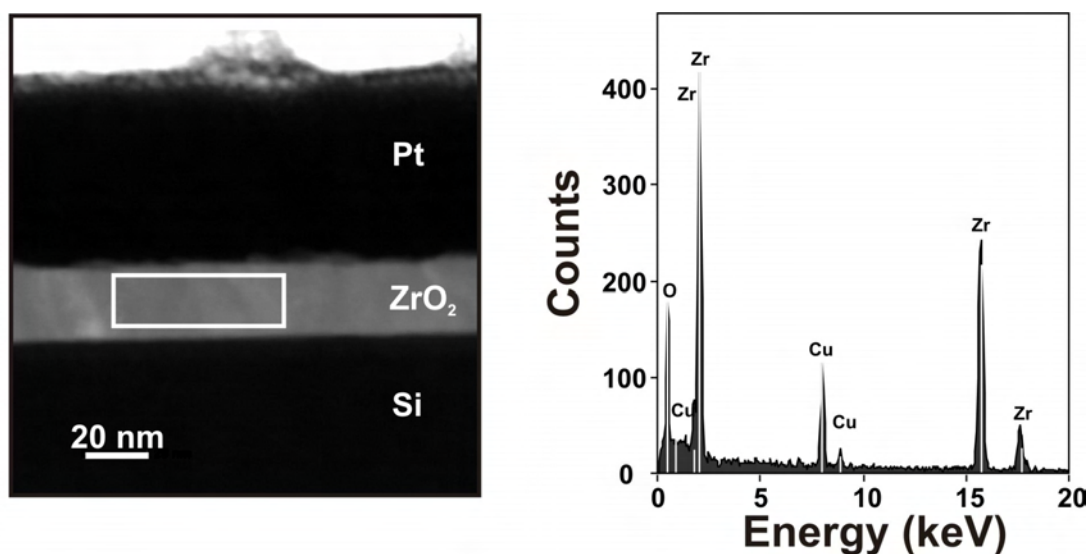


**Fig. 2.20.** HAADF image of annealed  $\text{ZrO}_2$  thin film and the EDX spectrum of the highlighted area.

## 2.8 Discussion & Conclusions

### 2.8a Structure and interfaces of the films

This chapter concludes the results of the material analysis of atomic layer deposited  $\text{La}_y\text{Zr}_{1-y}\text{O}_x$  thin films, deposited by alternating precursor pulses of La and Zr. This is an intrinsically interesting system, because ALD processed  $\text{La}_2\text{O}_3$  is always amorphous and  $\text{ZrO}_2$  is crystalline. Therefore, obtaining a uniform  $\text{La}_y\text{Zr}_{1-y}\text{O}_x$  thin film is rationally challenging. X-ray diffraction analyses clearly prove that  $\text{ZrO}_2$  undergoes a phase-separation when the film contains more than 30 at% Zr in it, which sets the thermodynamically stable solid solubility limit of  $\text{ZrO}_2$  in  $\text{La}_2\text{O}_3$  / $\text{LaZrO}_x$  films when deposited using atomic layer deposition technique using the particular precursor used in these experiments.

From our HR-TEM experiments, a number of conclusions can be drawn.  $\text{La}_2\text{O}_3$  forms a thin layer of silicate at the  $\text{La}_2\text{O}_3$ -Si interface, as evidenced by EDX line scans together with HAADF imaging. As-deposited  $\text{La}_2\text{O}_3$  films are amorphous and the onset of crystallization starts at  $800^\circ\text{C}$ , though short-range order in the films appears already at  $600^\circ\text{C}$ . However, the electron beams from TEM induces crystallization in  $\text{La}_2\text{O}_3$  films. On the contrary, the sample with 58% La is stable and shows no e-beam induced crystallization. Forming gas anneal at  $430^\circ\text{C}$  has no effect on the morphology of the films. Table 2.5 summarizes the major parameters of the films extracted from HRTEM measurements.

La:Zr	Mean thickness (Ellipsometry) [nm]	High- <i>k</i> thickness HR-TEM [nm]		Native oxide thickness HR-TEM [nm]	
		Before FGA	After FGA	Before FGA	After FGA
1:0	13	14-15	9-10	0-0.8	0-0.7
4:1	22	16	17	0.4-0.5	0.4-0.5
1:1	24	30	26-28	0.9-1.2	0.9-1.0
1:4	32	35	32-35	0.7-1.0	0.8
1:9	37	40	38-42	0.6-0.7	0.5-0.7
0:1	22	23	22-24	0.5	0.8-1.0

**Table 2.5.** Thickness of the  $\text{La}_y\text{Zr}_{1-y}\text{O}_x$  films and the native  $\text{SiO}_x$  films thickness measured with HR-TEM and compared with ellipsometry measurements.



### 2.8b Thermodynamic model of $\text{ZrO}_2$ phase segregation

The nucleation of  $\text{ZrO}_2$  during the deposition of  $\text{La}_y\text{Zr}_{1-y}\text{O}_x$  film or upon a post-deposition anneal can be precursor-specific; for instance, Tsoutsou *et al.*, reports that  $\text{La}_y\text{Zr}_{1-y}\text{O}_x$  films deposited using completely different La and Zr precursors do not have  $\text{ZrO}_2$  phase segregation even when the film contains 75% of Zr in it; the film was identified to be amorphous [20]. This contrast in result sheds light on the thermodynamic and the kinetical aspects of  $\text{ZrO}_2$  phase segregation. The thermal budget of the thin film deposition in our experiments and in the experiments of Tsoutsou *et al.* is the same, since the deposition temperatures are set at 300 °C in both cases. Therefore, the difference has to do with the orientation and/or mobility/moveability of the Zr atoms and its ligands on the hydroxylized surface after each precursor purge. Most probably the orientation and size of the ligands result in a slightly different growth rate of the Zr planes which could result in preferential growth of tetragonal  $\text{ZrO}_2$  planes when depositing with the ZrD-O4 ( $\text{Zr}(\text{CH}_3\text{C}_5\text{H}_4)_2\text{CH}_3\text{CH}_3\text{O}$ ) precursor than with the  $(\text{MeCp})_2\text{ZrMe}(\text{OMe})$  or ZrD-04 precursor used in the experiments by Tsoutsou *et al.* Remarkably, the phase-separation of  $\text{ZrO}_2$  into tetragonal or cubic  $\text{ZrO}_2$  occurs in their experiments after a rapid-thermal anneal (RTA) at 600°C, whereas in our case this takes place during deposition at a deposition temperature of 300°C itself. Therefore, it may be concluded that the phase-segregation of  $\text{ZrO}_2$  is kinetically favoured when the Zr percentage is above a certain threshold value. This conclusion supports the major discovery of this chapter that above 30% Zr content in the film, the formation of crystalline  $\text{ZrO}_2$  occurs in  $\text{La}_y\text{Zr}_{1-y}\text{O}_x$  thin films. There is hardly any change in the morphology of the film upon forming gas anneal in our experiments, which means that these films are thermodynamically stable at least until 450°C. Supporting this argument, studies on  $\text{HfLaO}_x$  thin films have shown that with increasing La content in  $\text{HfO}_2$  film, the crystallization temperature of the film increases [21].

When comparing with similar systems that have been studied earlier, in homogeneous aluminium zirconium oxide ( $\text{AlZrO}_x$ ) films deposited by ALD, such phase segregation was not observed [22]. These films remained amorphous even after prolonged anneals at elevated temperatures. However, pure  $\text{ZrO}_2$  films are usually polycrystalline regardless of the deposition techniques or the precursors, and nucleation of crystallites are triggered when the film thickness is larger than 3nm. Phase segregation to crystalline phase can be either as  $\text{ZrO}_2$  or even as metallic Zr clusters [23].

The X-ray diffraction experiments indicate that the pure  $\text{ZrO}_2$  contains a large fraction of monoclinic and a small fraction of the tetragonal phase. With reducing cluster size,  $\text{ZrO}_2$  tends to crystallize solely to tetragonal phase, which is similar to the observed tetragonal phase stabilization in  $\text{HfO}_2\text{-ZrO}_2$  [9].

Figure 2.21 shows the phase-diagram of  $\text{ZrO}_2\text{-La}_2\text{O}_3$  system; the maximum solubility of  $\text{ZrO}_2$  in  $\text{La}_2\text{O}_3$  is found to be 30% at  $1900^\circ\text{C}$ . This value correlates with the solubility of  $\text{ZrO}_2$  in  $\text{La}_2\text{O}_3$  at  $300^\circ\text{C}$  deposition temperature in ALD process as well, which confirms the conclusion that the phase segregation in these thin films is a thermodynamically driven phenomenon.

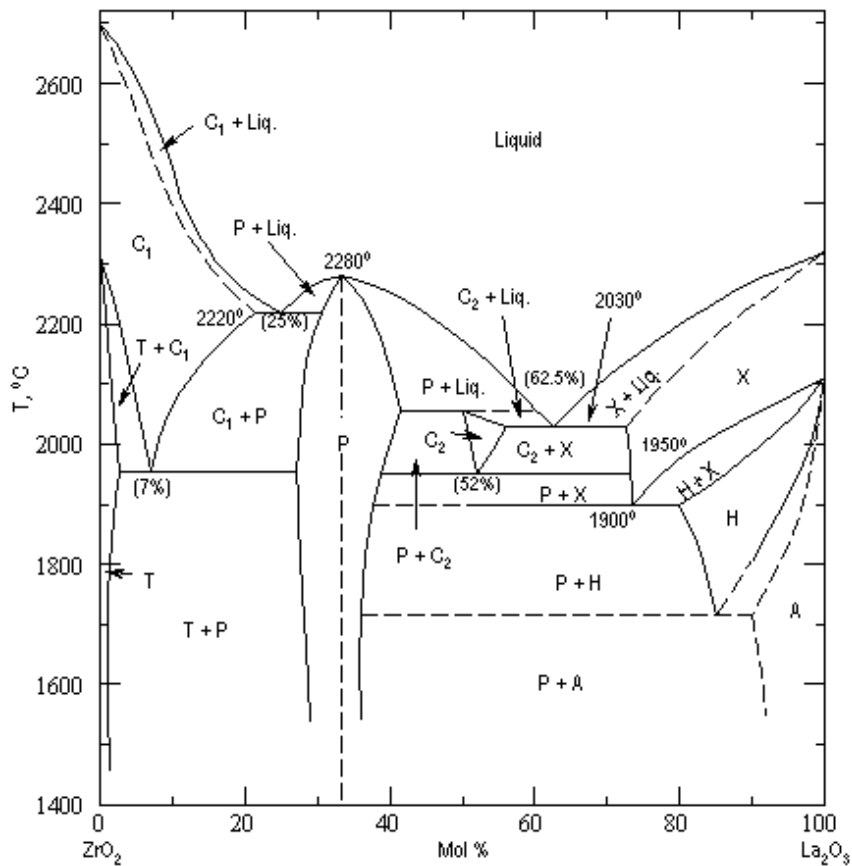


**Fig. 2.21.** Phase diagram of  $\text{La}_2\text{O}_3\text{-ZrO}_2$  system, taken from Ref [24]. Nomenclature in the figure: P – Pyrochlore, H – Hexagonal, T – Tetragonal, C – cubic.

A careful analysis of this phase-diagram suggests that addition of  $\text{ZrO}_2$  into  $\text{La}_2\text{O}_3$  causes the transition of amorphous  $\text{La}_2\text{O}_3$  into the pyrochlore-type compound and with higher percentage of  $\text{ZrO}_2$ , the mixture turns into a tetragonal phase around  $1800^\circ\text{C}$  [24]. The XRD peak of the  $\text{La}_{0.2}\text{Zr}_{0.8}\text{O}_{1.9}$  (with La:Zr = 12:1) shown in Fig. 2.7 corresponds to the pyrochlore phase [25].

In the pure  $\text{ZrO}_2$  thin film, a combination of monoclinic and tetragonal phases are present.  $\text{ZrO}_2$  has a strong preference towards tetragonal phase by the addition of  $\text{La}_2\text{O}_3$  in the film. The tetragonal phase is a high temperature meta-stable phase of  $\text{ZrO}_2$  crystals, which appears at temperatures above  $1100^\circ\text{C}$  [26]. However, it has been found that when zirconia powder is prepared by precipitation or calcination, it forms tetragonal crystallites at room temperature. A quenching at  $800^\circ\text{C}$  converts the hexagonal zirconia to pure monoclinic crystals. Looking in detail to the thermodynamics of this intriguing result, Garvie reported in 1965 that the room-temperature stabilization of the tetragonal phase of  $\text{ZrO}_2$  is closely related to the surface free energy of the crystals. With diminishing dimensions, the excess free energy (relative to large single crystals) increases dramatically. If two phases of a crystal coexist in a system at equilibrium, their free energies must be the same. Therefore, if  $G_m$  and  $G_t$  are the molar free energies of  $\text{ZrO}_2$  in monoclinic and tetragonal form, then at equilibrium,

$$G_m + \gamma_m A_m = G_t + \gamma_t A_t \quad (2.2)$$

where  $\gamma_m$  and  $\gamma_t$  are the surface free energies and  $A_m$  and  $A_t$  are the molar surface area (represented in units of  $\text{cm}^2/\text{mole}$ ) of monoclinic and tetragonal phases respectively. The surface free energy ( $\gamma$ ) of monoclinic phase is larger than that of the tetragonal phase, thus  $\gamma_m A_m \gg \gamma_t A_t$ . This difference with the large molar surfaces associated with them, the molar free energies of the system becomes equal when the crystal diameter is approximately 30 nm for  $\text{ZrO}_2$ . That means, below 30 nm cluster size, the molar free energy of the tetragonal phase is much larger than that of the monoclinic phase (i.e.,  $G_t \gg G_m$ ) and apparently, the tetragonal phase stabilization occurs at room temperature.

The largest  $\text{ZrO}_2$  cluster size estimated in thin films reported here being 17 nm, this explanation correlates adequately with our observation that the  $\text{ZrO}_2$  clusters are stabilized with tetragonal phase in these thin films. In addition, the solid-solubility limit of  $\text{ZrO}_2$  in  $\text{La}_2\text{O}_3$  is 30%, which associates properly with the high-temperature phase diagram of the  $\text{La}_2\text{O}_3$ - $\text{ZrO}_2$  system. This suggests that even though atomic layer deposition is a non-equilibrium process, the thermal budget of the deposition is sufficient to stabilize the composition and morphology of the films thermodynamically. A similar observation has been reported for nanolaminates composed of ALD processed  $\text{ZrO}_2$  and  $\text{HfO}_2$  layers, where a phase transition from tetragonal to monoclinic phase occurs in films thicker than 14 nm [27].

The phase-diagram of  $\text{ZrO}_2$ - $\text{La}_2\text{O}_3$  system shown in Fig. 2.21 depicts that the melting

point of  $\text{La}_2\text{O}_3$ -mixed  $\text{ZrO}_2$  system gradually decreases with increasing  $\text{La}_2\text{O}_3$  content in it, and has a minimum at  $\sim 70$  molar percent of  $\text{La}_2\text{O}_3$  at  $1900^\circ\text{C}$ . This suggests that the lattice energy of the mixed phase ( $\text{La}_y\text{Zr}_{1-y}\text{O}_x$ ) has a minimum when the La content is  $\sim 70\%$  or the Zr content is roughly  $30\%$ . With increasing Zr percentage, the lattice energy of the  $\text{La}_y\text{Zr}_{1-y}\text{O}_x$  film also increases almost linearly. Generally, the activation energy  $\Delta E$  of nucleation from an amorphous phase is related to the free energy of amorphous  $\rightarrow$  crystalline phase transition and the surface free energy of the interface between  $\text{ZrO}_2$  nanoclusters and the amorphous  $\text{La}_2\text{O}_3$  by the relationship [21]:

$$\Delta E = \frac{\sigma^3}{\Delta G^2} \quad (2.3)$$

where  $\Delta G$  is the free energy gain per unit volume in the amorphous  $\rightarrow$  crystalline phase transition and  $\sigma$  is the amorphous-crystalline interface energy per unit area. Two reasons increase the free energy of the  $\text{La}_y\text{Zr}_{1-y}\text{O}_x$  system here: one is the increase in lattice energy when there is more than  $30\%$  Zr in the film. In a mixed solution,  $\Delta G$  defines the gain in lattice energy of the system by incorporating La atoms in  $\text{ZrO}_2$  lattices. As evident from the phase diagram,  $\Delta G$  increases above  $30\%$  Zr in the film, meaning that the activation energy of nucleation (phase segregation) reduces linearly with Zr content in the film. Therefore the film becomes gradually stable with the phase-segregation of  $\text{ZrO}_2$  during the atomic-layer deposition process.

Second reason is the excess free energy of the  $\text{ZrO}_2$  nanocrystals comparing to the large single crystals. The thermodynamic model of Garvie and experiments reported in Ref. [26] indicate that the excess free energy gain for a  $100\text{ nm}$   $\text{ZrO}_2$  nanocrystallite is  $1\text{ kcal/mole}$ , which increases to as high as  $7\text{ kcal/mole}$  for a cluster of  $25\text{ nm}$  diameter. The tetragonal phase of  $\text{ZrO}_2$  has lower interface energy than the monoclinic phase. The phase-stability of the crystallites can be understood from Eqn (2.3): a high value of  $\Delta G$  and a low  $\sigma$  together make the activation energy  $\Delta E$  small enough to initiate the nucleation of tetragonal  $\text{ZrO}_2$  crystallites in the films with Zr content larger than  $30\%$ .

The process of crystallization based on these explanations together with the results of various experiments discussed in this chapter can be summarized into a physical cross section of the  $\text{La}_y\text{Zr}_{1-y}\text{O}_x$  system as function of composition given in Fig. 2.22:

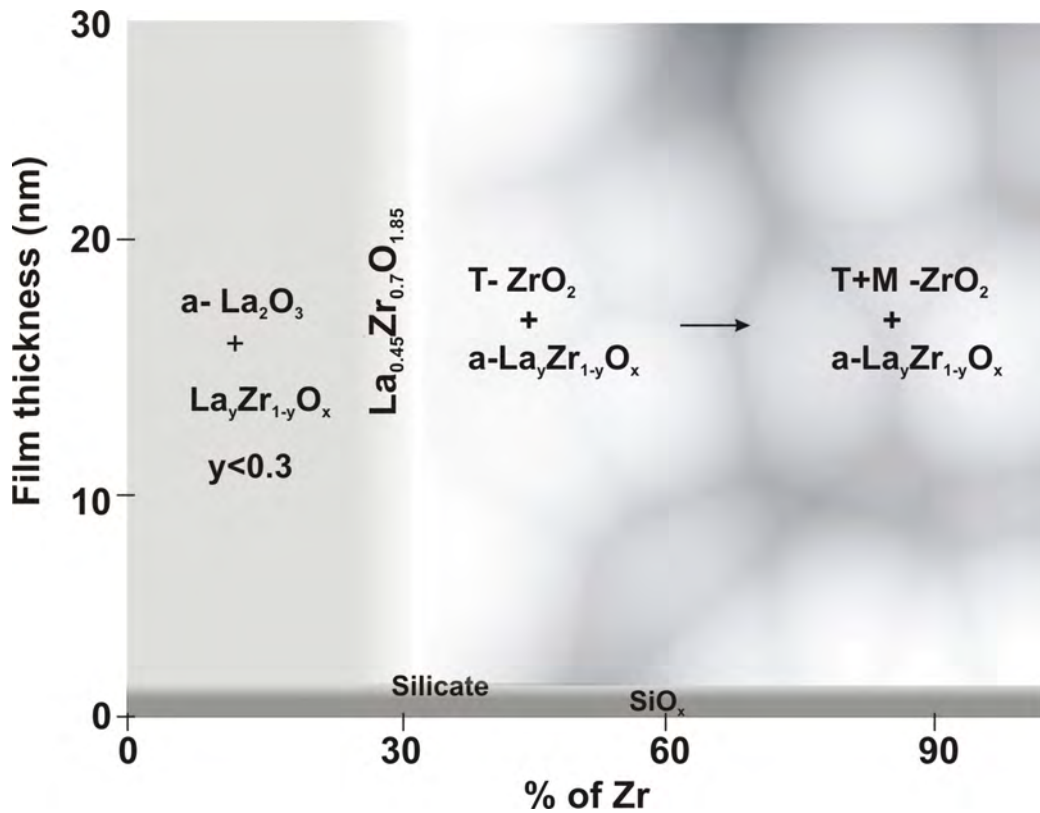


*Fig. 2.22. Room-temperature phase diagram of  $\text{La}_y\text{Zr}_{1-y}\text{O}_x$  system studied in this chapter.  $\text{T-ZrO}_2$  and  $\text{M-ZrO}_2$  represent tetragonal and monoclinic phases of  $\text{ZrO}_2$ ,  $\text{a-La}_2\text{O}_3$  and  $\text{a-La}_y\text{Zr}_{1-y}\text{O}_x$  represent amorphous  $\text{La}_2\text{O}_3$  and  $\text{La}_y\text{Zr}_{1-y}\text{O}_x$  films.*

The thermodynamic stability of these films is crucial in determining their dielectric behavior for the application as high- $k$  materials. Therefore, a more or less comprehensive understanding of the composition and morphology of the films is necessary as this chapter attempts to describe. The characteristic electrical behavior of the devices fabricated with these films is presented in detail in the next chapter.

## 2.9 References

1. V. Capodieci et al., *Microelectronics Reliability* **45**, 937 (2005).
2. C.H. Hsu, M.T. Wang, J.Y. M. Lee, *J. Appl. Phys.* **100**, 074108 (2006).
3. P.V. Aleskandrova et al., *Eur. Phys. J. B* **52**, 453 (2006).
4. Y. H. Wu et al., *Electron Device Lett.* **21**, 341 (2000).
5. S. Stemmer, J.-P. Maria A. I. Kingon, *Appl. Phys. Lett.* **79**, 102 (2001).
6. J.B. Cheng et al., *Appl. Surf. Sci.* **233**, 91 (2004).
7. K.B. Jinesh et al., *Appl. Phys. Lett.* **93**, 062903 (2008).
8. D.H. Triyoso et al., *J. Vac. Sci. Technol. B* **23**, 288 (2005).
9. D.H. Triyoso et al., *Appl. Phys. Lett.* **88**, 222901 (2006).
10. R. Inman et al., *Mat. Chem. Phys.* **104**, 220 (2007).
11. S. J. Yun et al., *Electrochem. Solid-State Lett.* **10**, H90 (2007).
12. M. Ritala et al., *Science* **288**, 319 (2000).
13. D.H. Triyoso et al., *J. Vac. Sci. Technol. B* **22**, 2121 (2004).
14. F.C. Chiu, H.W. Chou, J. Y. Lee, *J. Appl. Phys.* **97**, 103503 (2005).
15. A.A. Dakhel, *J. Mat. Chem. Phys.* **102**, 266 (2007).
16. L. V. Azároff, *Elements of X-ray crystallography*, TechBook publications, Ed.1 (1968), p. 552.
17. S.J. Jo et al., *Thin Solid Films* **513**, 253 (2006).
18. J.-P. Maria et al., *J. Appl. Phys.* **90**, 3476 (2001).
19. C. R. Ashman, C. J. Först, K. Schwarz, P. E. Blöchl, *Phys. Rev. B* **70**, 155330 (2004).
20. D. Tsoutsou, et al., *Appl. Phys. Lett.* **94**, 053504 (2009).
21. Y. Yamamoto, K. Kita, K. Kyuno, A. Toriumi, *Appl. Phys. Lett.* **89**, 032903 (2006).
22. W.F.A. Besling et al., *J. Non-Cryst. Solids* **303**, 123 (2002).
23. T. Kauerauf, *Degradation and breakdown of MOS gate stacks with high permittivity dielectrics*, PhD Thesis, Katholieke Universiteit, Leuven. (2007), p. 98.
24. A. Rouanet, *Rev. Int. Hautes Temp. Refract.* **8**, 161 (1971).
25. J.W. Seo et al., *Appl. Phys. Lett.* **83**, 5211 (2003).
26. R.C. Garvie, *J. Phys. Chem.* **69**, 1238 (1965).
27. H. Kim, K.C. Saraswat, P.C. McIntyre, *J. Mater. Res.* **2**, 3125 (2005).

# Chapter 3

## Electrical characterization of atomic-layer-deposited $\text{La}_y\text{Zr}_{1-y}\text{O}_x$ thin films

### 3.1 Introduction

With the information we have on the morphology, stoichiometry and the interfacial properties of  $\text{La}_y\text{Zr}_{1-y}\text{O}_x$  films investigated in the previous chapter, this chapter examines the electrical behaviour of these high- $k$  layers fabricating metal-insulator-silicon (MIS) capacitor structures. The standard ways of evaluating a dielectric material involves the measurement of static and dynamic charge properties, where the former gives the capacitance and the latter gives the current through the device. Capacitance being strongly dependent on the polarizability of the insulating layer, gives the dielectric permittivity ( $\epsilon_r$ ) represented as the relative dielectric constant  $k$ . The  $k$ -value determines the applicability of a material as a high- $k$  dielectric [1], which is usually expressed in a more standard measure namely the equivalent oxide thickness (EOT), also known as the capacitance equivalent thickness (CET) as will be discussed later in this Chapter. The current measurements provide the leakage currents through the device, which should be as low as possible comparing to the limit of  $1 \text{ A/mm}^2$  set by the technology roadmaps (ITRS) [2]. In addition, another technologically important parameter derived from the current measurements is the dielectric breakdown electric field ( $E_{bd}$ ) that determines the reliability of the devices at normal operational voltages.

From the physics point of view, capacitance-voltage measurements give information about the electrode dielectric interfaces, trapped charges and type of defects in the material, while current-voltage measurements provide information on the band-diagram of the material, the type of charges responsible for leakage (mostly whether it is electrons, holes or both). In addition, the type of defects in the dielectric and their energy levels also can be estimated from current measurements. The details of these measurements will be given later in this chapter.

### 3.2 Experimental details

For the electrical measurements, the  $\text{La}_y\text{Zr}_{1-y}\text{O}_x$  films described in chapter 2 were used. These films were deposited on 200 nm p-type Si (100) substrates with resistivity of 3–10  $\Omega \cdot \text{cm}$ . All the ALD depositions were carried out on the native silicon oxide of about 1.2 nm -1.5 nm thickness. Either 500 nm aluminium or 100 nm TiN was sputter deposited on the cleaned layers. The electrodes were fabricated using standard lithography and subsequent selective etching, which yielded capacitor structures with electrode area ranging from  $100 \times 100 \mu\text{m}^2$  to  $3000 \times 3000 \mu\text{m}^2$ . Selected pieces from each composition were subjected to a 30 minutes rapid thermal anneal (RTA) at  $450^\circ\text{C}$  after electrode deposition for comparison with as-deposited samples. The major electrical results mentioned in this chapter are from devices with TiN electrode on top of the  $\text{La}_y\text{Zr}_{1-y}\text{O}_x$  films, because, the devices with aluminium electrode on top suffers from various reliability issues as mentioned in Chapter 4. The electrical measurements employed an HP 4275A Multi-frequency LCR meter, an HP 4194A impedance analyzer, an Agilent 4155C Semiconductor Parameter Analyzer and an Agilent B1500A Semiconductor Device Analyzer.

### 3.3 Atomic force microscope studies: surface roughness of the films

Prior to the electrode deposition onto the ALD films, three selected samples were analyzed with atomic force microscope (AFM) in order to obtain information on the surface roughness of the films. The selected samples were with La:Zr pulse ratios of 12:1, 4:1 and 1:1. The 12:1 sample was a uniform  $\text{La}_y\text{Zr}_{1-y}\text{O}_x$  film with no phase segregation, 4:1 has small  $\text{ZrO}_2$  nanoclusters in it and 1:1 has even bigger clusters. The measurements were performed in intermittent contact (tapping) mode with a Veeco Dimension 3100 scanning probe microscope, using conductive Co/Cr-coated (Veeco MESP) Si probes. The results, showing the topography of  $2 \times 2 \mu\text{m}^2$  areas, are presented in Fig. 3.1. Table 3.1 gives the average and root mean square (RMS) values of the surface roughness.



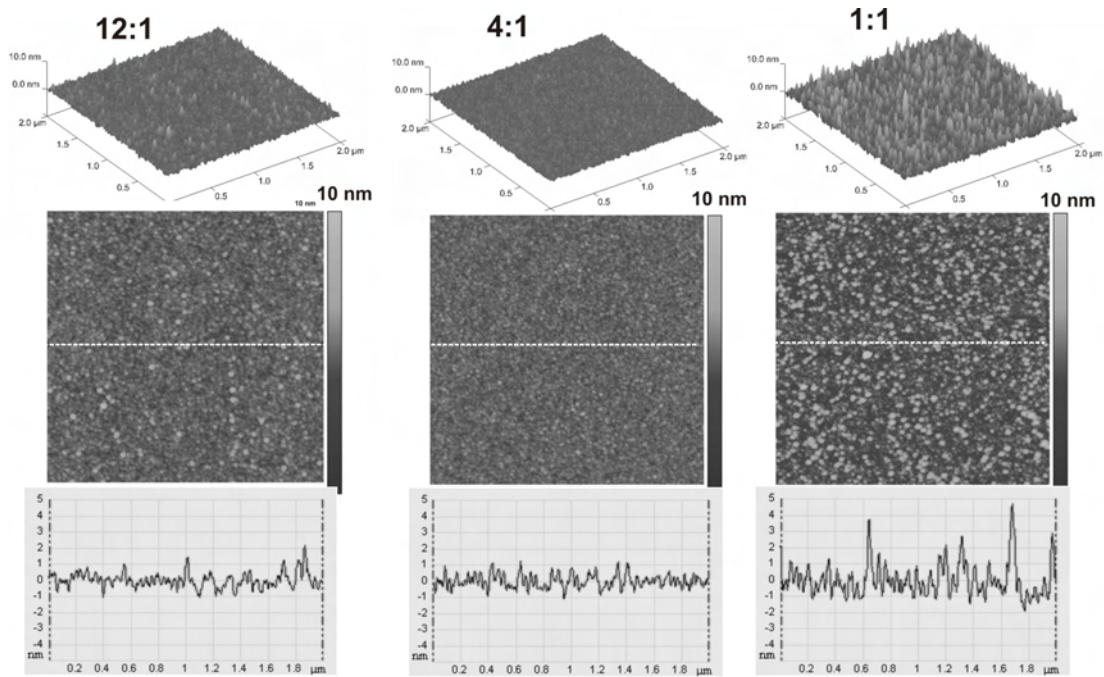


**Fig. 3.1.** Tapping mode AFM images of the surface of thin films with La:Zr pulse ratios 12:1, 4:1 and 1:1. The bottom panel is the topographical variations along the dotted line in the topographical image in middle panel. The images span the surface area of  $2 \times 2 \mu\text{m}^2$ .

Sample	$R_a$ (nm)	$R_q$ (nm)
La:Zr = 1:1	0.77	1.04
La:Zr = 4:1	0.32	0.41
La:Zr = 12:1	0.39	0.52

**Table. 3.1.** The average roughness ( $R_a$  in nm) and the RMS roughness ( $R_q$  in nm) of the three samples investigated. The RMS instrumental noise is 0.05 nm.

The major conclusion from this analysis is that increasing Zr content increases the film roughness, which might be due to  $\text{ZrO}_2$  cluster formation in films with larger Zr content (lower La content). Additionally, surface potential scans were recorded, using scanning Kelvin probe microscopy (SKPM) with the same instrument setup, to detect possible charging of the  $\text{ZrO}_2$  nanoclusters. The results are presented later in section 3.5.9. Aluminium or TiN was sputter deposited to form electrodes after these measurements.

### 3.4 Capacitance-Voltage ( $C$ - $V$ ) measurements

A known difficulty in obtaining a clean electrical behaviour is the interface the high- $k$  material makes with silicon [1]. Even when the layers are fabricated epitaxially in clean environment [3], lattice mismatching with silicon leads to interface trap levels [4] and charge disproportionation effects [5] resulting in hysteresis in  $C$ - $V$  measurements and  $1/f$  noise in these devices [6]. These interface trap levels can be studied using parallel conductance measurements [7], which will be discussed later in this chapter.

#### 3.4a $C$ - $V$ measurements

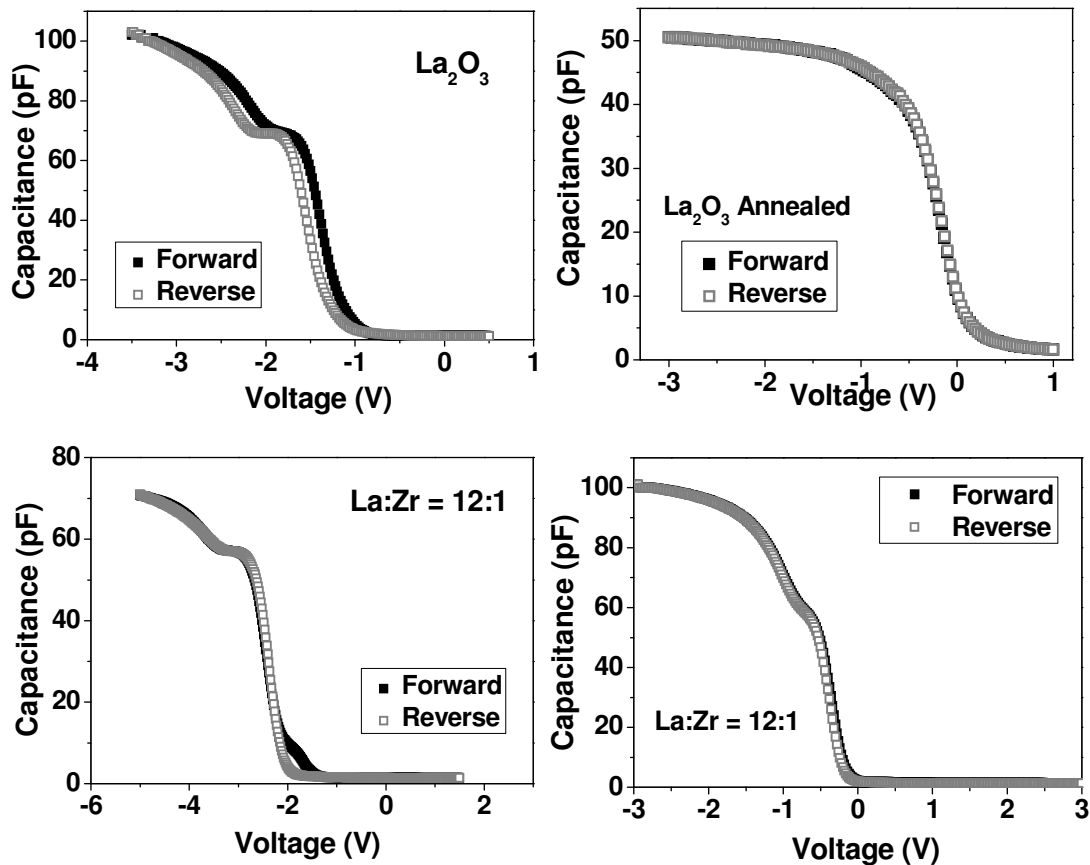
In a metal-insulator-semiconductor (MIS) device, there are mainly four types of trapped charges. They are categorized as follows [8]:

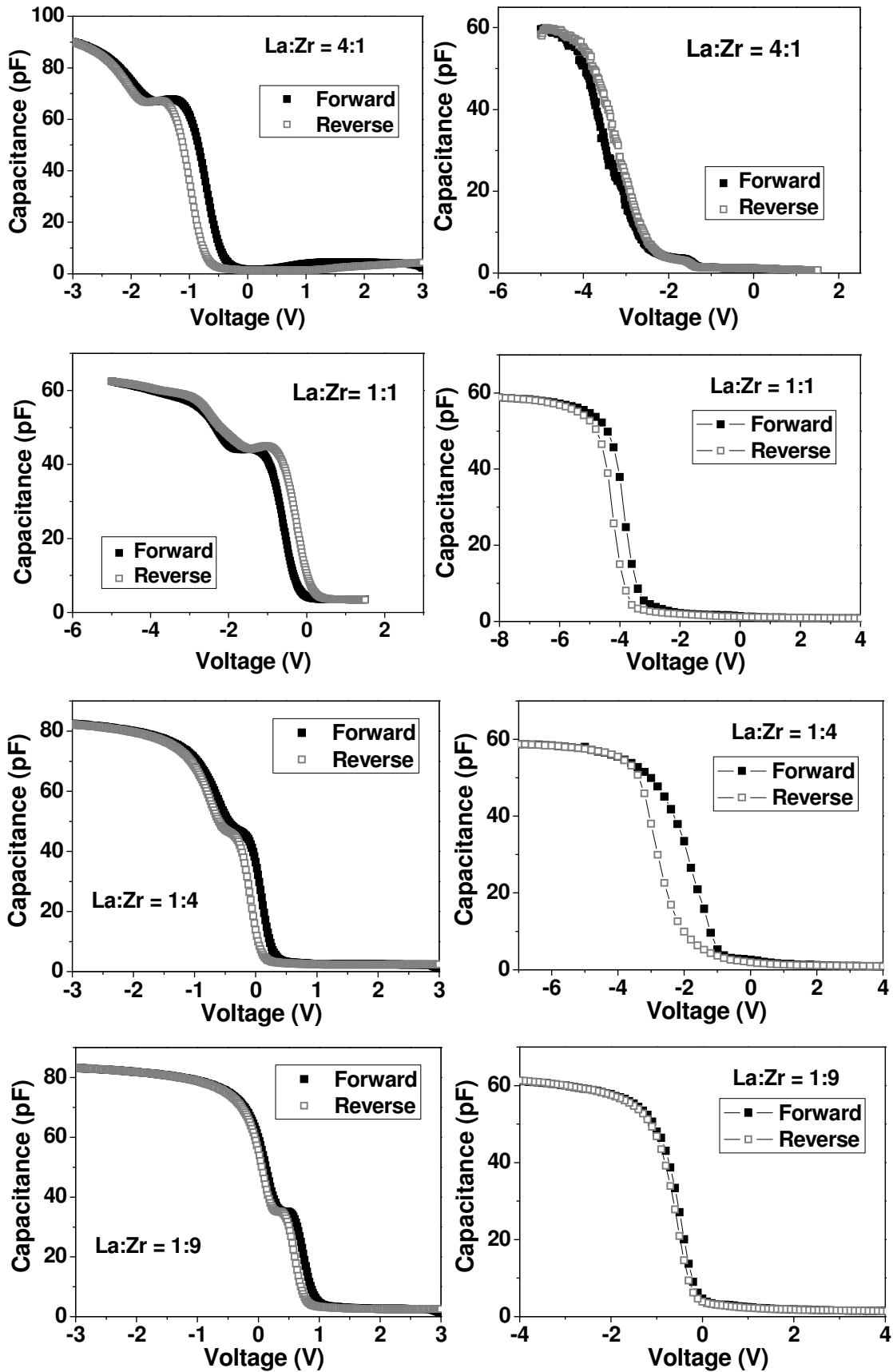
1. Interface trap charges ( $Q_{it}$ ) – positive or negative charges at the interface, originating mainly from the imperfections at the Si-dielectric interface. These are surface charges that communicate electrically with the silicon substrate unlike other oxide charges. These charges are usually coming from dangling bonds at the interface, lattice mismatching between Si and the crystalline oxides, oxidation induced structural defects at the Si-oxide interface, metal impurities close to the interface, broken electronic bonds due to radiation damage, hot charge carrier injection etc. Most of these imperfections can be healed out usually with a forming gas anneal (FGA) or a rapid thermal anneal (RTA). Interface trap density ( $D_{it}$ ) and trapped charge density ( $N_{it}$ ) are experimentally extractable device parameters.
2. Fixed oxide charges ( $Q_f$ ) – trapped charges within the dielectric layer, arising due to different oxidation conditions of the dielectric layer.
3. Oxide trap charges ( $Q_{ot}$ ) – charges originating from the trapped electrons or holes in the oxide. Trapping of these charges could be due to avalanche charge injection or hot carrier injection into the oxide.
4. Mobile charges ( $Q_m$ ) – mainly ionic charges such as  $\text{Na}^+$ ,  $\text{Li}^+$ ,  $\text{K}^+$  and  $\text{H}^+$  ions.

The capacitance-voltage ( $C$ - $V$ ) characteristics of the MIS devices are useful in quantifying these charges using various parameters that can be extracted from the  $C$ - $V$  curves. Secondly,  $C$ - $V$  measurements employ an applied frequency modulation, which allows distinguishing between different types of charges, since the relaxation timescales of these charges differ

from each other. The presence of these four charges in the MIS device generate mirror charges segregating close to the silicon-oxide interface, which causes the conduction and valence bands of silicon to distort near the interface. This is generally called band bending and this excess electron energy increases or decreases according to the nature of dopants in the silicon (which makes it either p-type or n-type) and the doping level. The voltage needed to neutralize the electric field that causes band bending is termed as the flat-band voltage ( $V_{fb}$ ), which can be estimated from the  $C$ - $V$  measurements of the devices.

The  $C$ - $V$  curves of the MIS devices with as-deposited  $\text{La}_y\text{Zr}_{1-y}\text{O}_x$  films as dielectric layer and TiN electrodes are shown in Fig. 3.2. The experiments were done at 10 kHz, at an oscillation voltage of 30 mV. The as-deposited films exhibit characteristic humps in the depletion region indicating interfacial states, suggesting that there is significant charge trapping at the  $\text{La}_y\text{Zr}_{1-y}\text{O}_x/\text{Si}$  interface. [9,10]. These humps disappear up on rapid thermal annealing (RTA) of the samples at 450°C for 30 minutes. The left panel are the  $C$ - $V$  characteristics of the as-deposited and the right panel are that of the annealed samples.





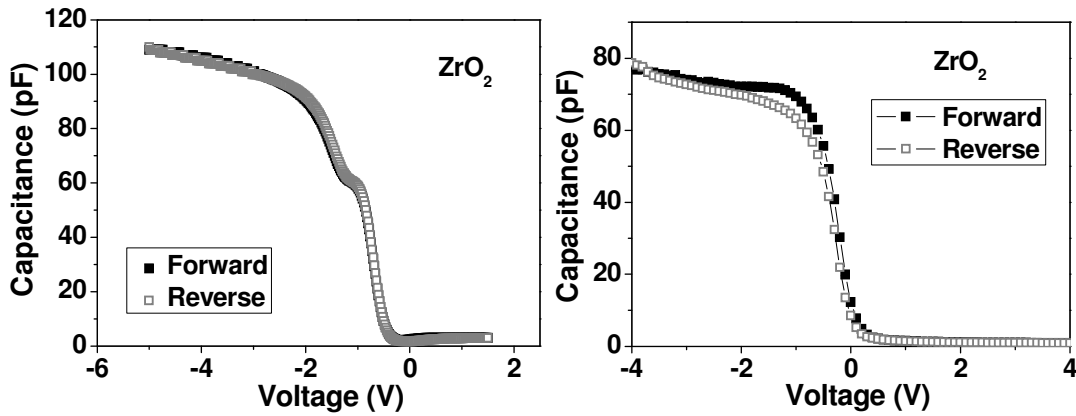


*Fig. 3.2. C-V characteristics of the  $\text{TiN}/\text{La}_y\text{Zr}_{1-y}\text{O}_x/\text{p-Si}$  capacitors. The left panel is the C-V plots of the devices with as-deposited films and the figures at the right-hand-side are devices undergone rapid thermal anneal (RTA).*

The striking differences between the  $C$ - $V$  curves of the fresh and annealed devices are that the latter have smoother and steeper  $C$ - $V$  curves indicating that the interfaces states are less, and that the accumulation capacitance after RTA is smaller than those of the fresh devices. The flat-band voltages of these devices also change upon RTA. A detailed analysis of these features will be given in the coming sections.

### 3.4b Analysis of the $C$ - $V$ curves

An LCR meter that measures the capacitance of the device measures the ac current amplitude and the phase difference between the applied voltage sinus and the measured current sinus. The impedance of the device is given in terms of the measurement (angular) frequency  $\omega$  by

$$Z = R_S + R_P(1 - j\omega C R_P) / [1 + \omega^2 C^2 R_P^2] \quad (3.1),$$

where  $R_P$  is the parallel resistance (resistance offered by the dielectric) and  $R_S$  is the series resistance, which is the frequency dependent resistances of the electrode and the substrate. In terms of the capacitance  $C$  and dissipation  $D$  of the device, the impedance becomes

$$Z = (D - j) / \omega C(1 + D^2) \quad (3.2),$$

where  $D = 1/\omega R C$ .  $D$  is the tangent of the angle between the real and imaginary parts of the impedance (represented as  $\tan(\delta)$ ). Therefore, it should be noted that the impedance measurements are less accurate when  $D$  is larger and thus, the capacitance measurements

become increasingly erroneous with increasing dissipation. However, Lønnum and Johannessen reported in 1986 that the presence of both parallel and series resistances requires measurements to be done at two different frequencies to obtain the correct depletion capacitance value [11]. By measuring the capacitance and dissipation of the devices at two different frequencies  $f_1$  and  $f_2$ , the *actual* capacitance of the device can be estimated using the following expression [11]:

$$C = [f_1 C_1 (1 + D_1^2) - f_2 C_2 (1 + D_2^2)] / (f_1^2 - f_2^2) \quad (3.3).$$

The  $C$ - $V$  characteristics of rapid thermal annealed  $\text{Al}/\text{La}_2\text{O}_3/\text{Si}$  device are shown in Fig. 3.3 for different frequencies. The curves do not exhibit considerable dispersion in a frequency span of 1–100 kHz.

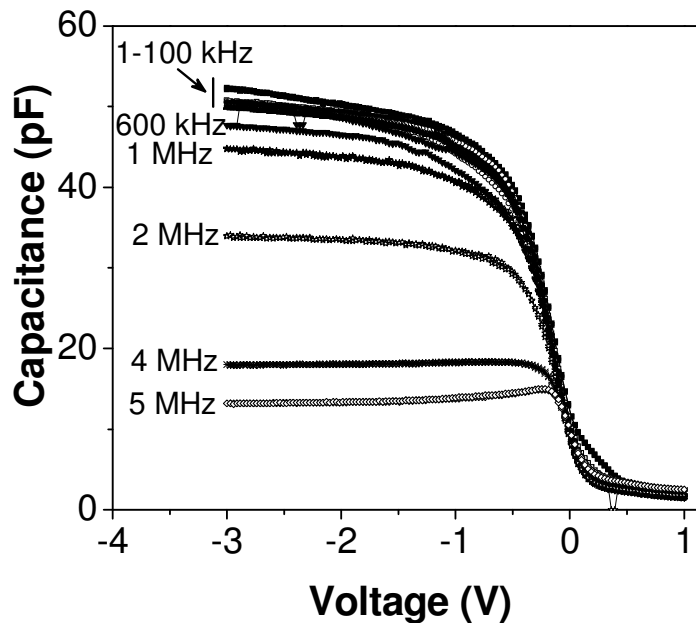


**Fig. 3.3.** Frequency dependence of  $C$ - $V$  characteristics of  $\text{Al}/\text{La}_2\text{O}_3/\text{Si}$  device after annealing measured using the  $R_s$  circuit model.

From Fig. 3.3, combination of two  $C$ - $V$  curves at different frequencies were selected to check the capacitance correction using Eqn. 3.3. An example of dissipation of the capacitors measured at 10 kHz and 1 MHz frequencies are given in Fig. 3.4, where the dissipation at 1 MHz is high in accumulation as expected from Fig. 3.3.

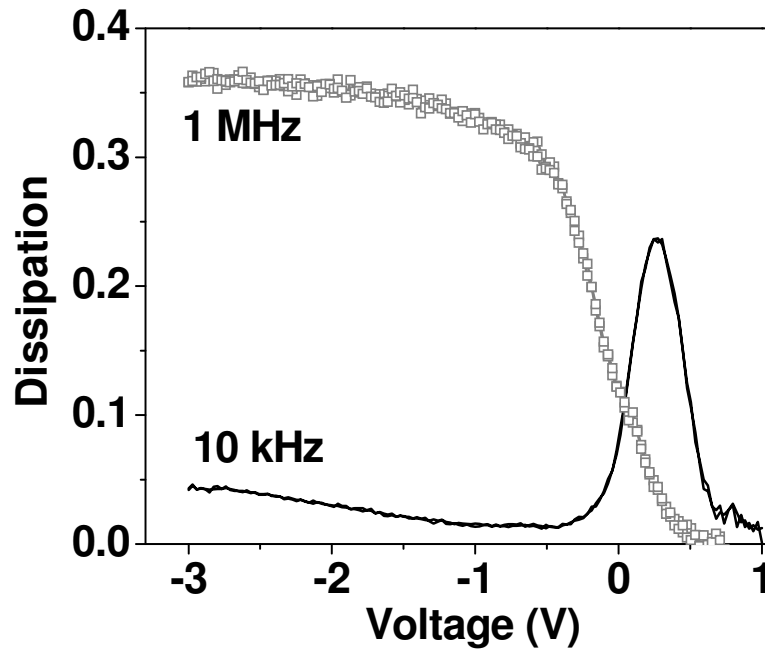


*Fig. 3.4. Dissipation of the annealed Al/La<sub>2</sub>O<sub>3</sub>/Si device at 10 kHz and 1 MHz frequency.*

However, dissipation in the range of frequencies from 1 to 100 kHz remains less than 5% in accumulation capacitance, indicating that the tunnelling current through these layers is negligible and that dissipation correction due to quantum tunnelling effects, is not required. This argument is confirmed by evaluating Eqn. 3.3, as shown in Fig. 3.5.

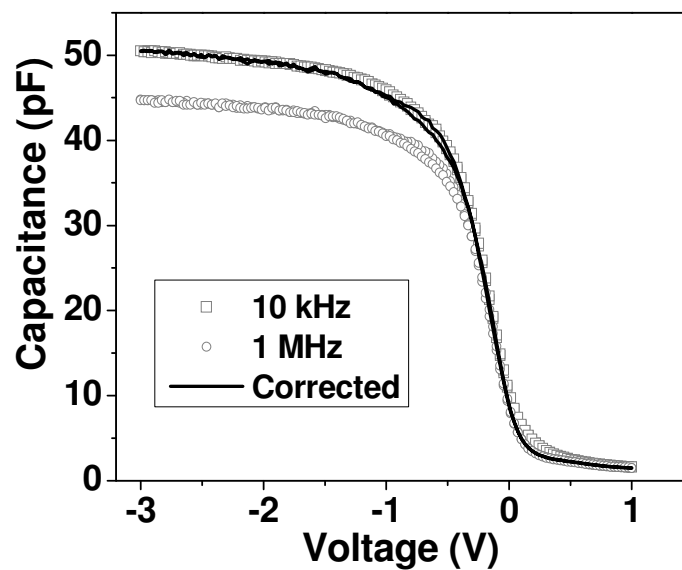


*Fig. 3.5. Capacitance of the annealed Al/La<sub>2</sub>O<sub>3</sub>/Si device at 10 kHz and 1 MHz frequencies (symbols) and the corrected capacitance using Eqn. 3.3 (solid line).*

Figure 3.5 shows that the capacitance corrected for excessive dissipation related to high tunnelling currents goes perfectly in line with the capacitance measured at 10 kHz, suggesting that when measuring at these low frequencies, an additional leakage correction is not necessary. In other words, the usage of 10 kHz frequency to measure  $C$ - $V$  curves of these films is quite appropriate and the influence of  $R_S$  and  $R_P$  on the depletion capacitance is negligible. Quantum mechanical corrections are generally applicable for high- $k$  layers with thickness less than 3 nm [12,13]. Therefore, in the measurements reported in this thesis, any quantum mechanical correction for the leakage current has not been applied.

### 3.4c Interface states: parallel conductance measurements

Interface states are surface states originating from dangling bonds or interfacial imperfections. Interface states contribute to the leakage current through thin high- $k$  films, with direct tunnelling of electrons through the native or stress-induced interface states in silicon [14]. As discussed in the previous section, while sweeping the bias voltage, electrons are trapped in these levels and appear as a hump in  $C$ - $V$  measurements. Since these charges contribute enormously to the flat-band shifts and thus to the threshold voltage of the CMOS devices, great attention has been given to reduce interface states as much as possible.

Interface trap levels of the MIS devices are distributed throughout the band-gap of silicon. They have a small trapping and de-trapping time of the order of tens of microseconds. Therefore, characteristic humps appear typically in  $C$ - $V$  measurements performed at lower frequencies. Measuring the equivalent parallel conductance ( $G_P$ ) is a widely accepted way of extracting the interface state density in silicon band-gap. The interface states can be probed measuring  $G_P$  as function of the frequency, since  $G_P$  represents the energy loss of the majority charge carriers during the capture-emission process at the interface states. Since the interface states are distributed over the band-gap of silicon, a positive bias will shift the conduction band towards the Fermi level and more filled states are occupied below the Fermi level with average electron energy equal to that of the free electrons in silicon. This happens during the positive half cycle of the applied frequency. During the negative half cycle, the conduction band shifts away from the Fermi level and more states appear above the Fermi energy, with average energy higher than that of the free electrons. Both these capture processes release energy as heat in the form of phonons, which can be measured using parallel conductance measurements. At very low frequencies, all the traps are filled, and therefore the dissipation is



low. So is at high frequencies, where the charges do not respond to the frequencies and very few traps are filled and emptied. At the intermediate frequencies, continuous trapping and de-trapping occurs, which causes energy loss of the charges. This means that the trap levels have characteristic timescales of charge capture and release. Therefore, in terms of the time constant  $\tau_{it}$  of the carries at the interface traps, the normalized conductance  $G_p/\omega$  is related to the interface trap density  $D_{it}$  by the relation [8]

$$\frac{G_p}{\omega} = \frac{q\omega\tau_{it}D_{it}}{1 + (\omega\tau_{it})^2} \quad (3.4).$$

Generally  $G_p$  is measured as a function of frequency  $f$  (or  $\omega = 2\pi f$ ) and  $(G_p/\omega)$  is plotted as a function of  $\omega$ , resulting in distributions similar to Fig. 3.6 (a), where the two curves belong to two different  $D_{it}$  values, both assuming a fixed time constant of  $\tau_{it} = 8 \mu\text{s}$ . Fig. 3.6 (b) compares between the theoretical value of  $G_p/\omega$  with experimental data for La:Zr = 1:1 sample. This experiment was done at 0.3 V, in depletion, and the theoretical curve employed  $\tau_{it} = 0.13 \mu\text{s}$  obtained from experimental curve and  $D_{it} = 4.2 \times 10^{13} \text{ cm}^{-2} \cdot \text{eV}^{-1}$ .

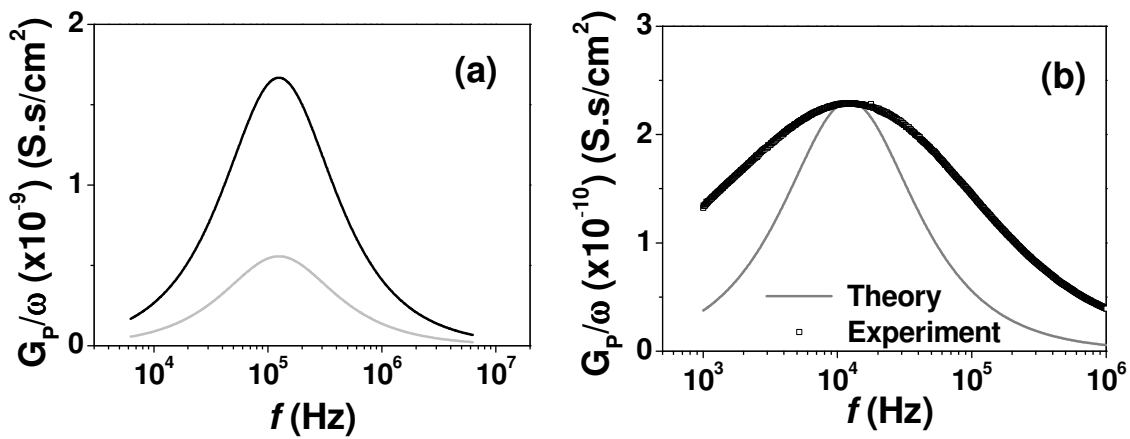


**Fig. 3.6.** (a) Theoretical curves of  $G_p/\omega$  estimated using Eqn. 3.6 using  $\tau_{it} = 8 \mu\text{s}$  for two interface state densities of  $D_{it} = 3 \times 10^{10} \text{ cm}^{-2} \cdot \text{eV}^{-1}$  (black curve) and  $1 \times 10^{10} \text{ cm}^{-2} \cdot \text{eV}^{-1}$  (grey curve) for  $120 \times 120 \mu\text{m}^2$  capacitors. (b) Comparison between theoretical ( $G_p/\omega$ ) curve with experimental data for device comprising thin film with La:Zr = 1:1.

Equation 3.4 is an expression for single level interface trap distribution in the silicon band-gap. But in reality, the interface surface potential fluctuates due to non-uniformities in the oxide charge and interface traps and the doping density of the substrate, which causes

dispersion in interface trap time, because different interface traps have different capture-emission times and thus they respond to different frequencies. This causes broadening of the curves, which explains why the experimental curve shown in Fig. 3.6 (b) appears broader than the theoretical curve. Therefore, a statistical model that integrates  $D_{it}$  over the probability distribution of the surface potential fluctuation has to be used in order to model the broad experimental curves accurately. However, the parameter important within the scope of this thesis is an approximate expression for the interface trap density, as given by

$$D_{it} \approx \frac{2.5}{q} \left( \frac{G_p}{\omega} \right)_{\max} \quad (3.5),$$

where,  $(G_p / \omega)_{\max}$  is the maximum value at the peak of  $(G_p/\omega)$  versus  $\omega$  curve. To estimate the  $D_{it}$  values of the devices with different Zr contents, high resolution  $(G_p/\omega)$  curves were measured for each device. Prior to  $G_p$  measurements, the  $C$ - $V$  curves of the devices were analyzed and the parallel conductance ( $G_p$ ) was measured as a function of frequency at a bias voltage around the transition voltage from deep depletion to depletion region. Fig. 3.7 depicts  $(G_p/\omega)$  measured as a function of  $\omega$  for fresh and rapid-thermal-annealed TiN/La<sub>2</sub>O<sub>3</sub>/p-Si devices of area  $120 \times 120 \mu\text{m}^2$ .

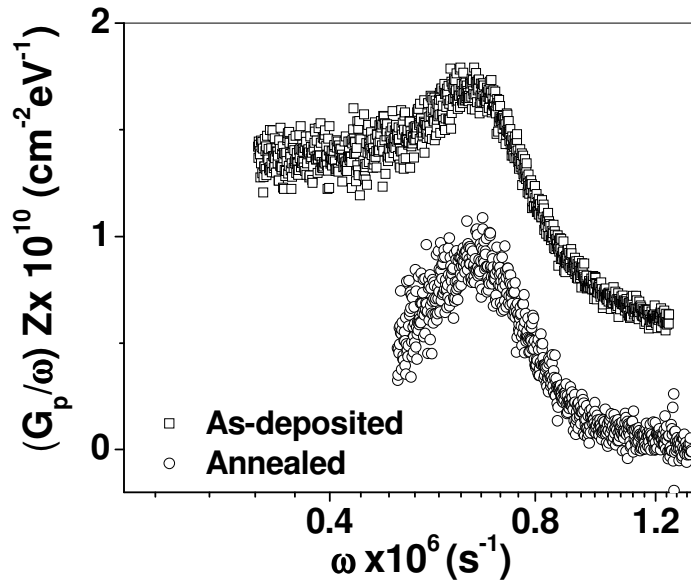


*Fig. 3.7.  $(G_p/\omega)$  of fresh and annealed TiN/La<sub>2</sub>O<sub>3</sub>/Si devices measured as the function of frequency. The maxima of the curves give the interface state density of the device. The term  $Z = 2.5/qA$ , where  $q$  is the electronics charge and  $A$  is the area of the capacitor.*

Wu et al. reported  $D_{it}$  values on 5 nm  $\text{La}_2\text{O}_3$  films using low temperature oxidation and subsequent annealing at  $900^\circ\text{C}$  upon using quasi-static  $C$ - $V$  measurements and found  $D_{it}$  of  $3 \times 10^{10} \text{ cm}^{-2} \text{ eV}^{-1}$  [15]. Fig. 3.7 shows that the as-deposited  $\text{La}_2\text{O}_3$  samples have  $1.67 \pm 0.05 \times 10^{10} \text{ cm}^{-2} \text{ eV}^{-1}$ , which reduces to  $8.83 \pm 0.08 \times 10^9 \text{ cm}^{-2} \text{ eV}^{-1}$  on RTA. Likewise, the  $D_{it}$  of  $\text{ZrO}_2$  deposited using plasma-enhanced ALD (PEALD) technique has been reported to be  $5\text{-}6 \times 10^{12} \text{ cm}^{-2} \text{ eV}^{-1}$  [16], whereas, the  $D_{it}$  in our samples is  $1.67 \pm 0.08 \times 10^{12} \text{ cm}^{-2} \text{ eV}^{-1}$  for the as-deposited  $\text{ZrO}_2$  films, which reduces to  $3.54 \pm 0.06 \times 10^{11} \text{ cm}^{-2} \text{ eV}^{-1}$  upon annealing. It is also worth noting that the data becomes more symmetrical up on RTA. The broadening of the data in the case of the devices with as-deposited films indicates larger dispersion in the interface trap time constants arising from the surface potential fluctuations due to non-uniformities in oxide charge distribution and interface traps [Ref. 8, page 348].

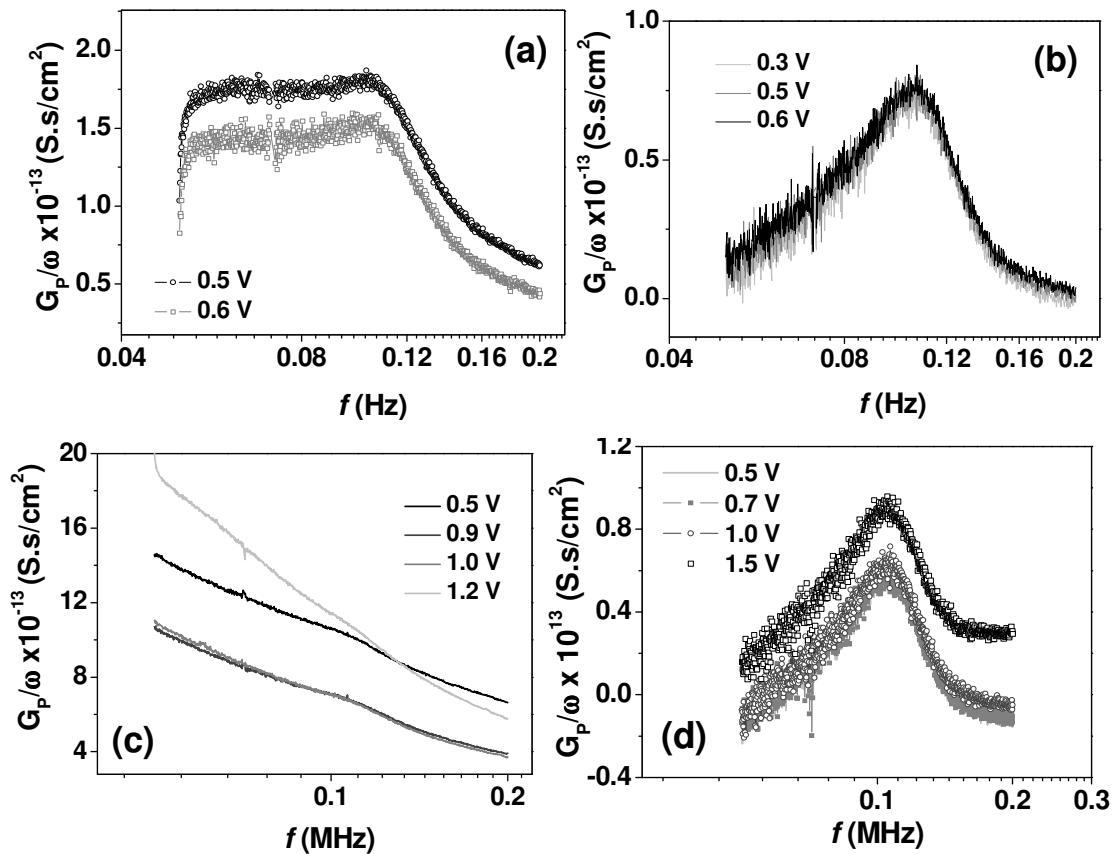
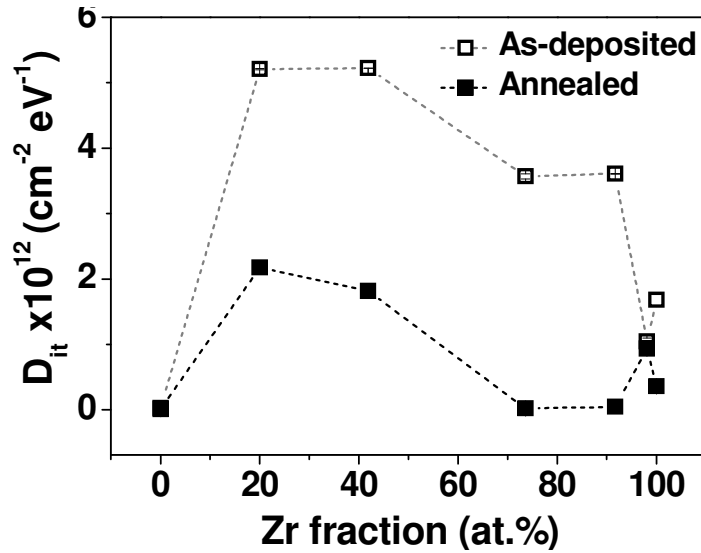


Fig. 3.8. ( $G_p/\omega$ ) of as-deposited devices with (a)  $\text{La:Zr} = 12:1$  and (b)  $\text{La:Zr} = 4:1$  at different bias conditions. (c) ( $G_p/\omega$ ) measured for as-deposited and (d) annealed films with  $\text{La:Zr} = 1:1$ .

Figure 3.7 is plotted in terms of  $(G_P/\omega) \times Z$  versus  $\omega$ , where  $Z = 2.5/qA$ , where  $q$  is the electronics charge and  $A$  is the area of the capacitor. This allows reading  $D_{it}$  directly from the curves as the maximum of these curves give the actual interface density of the devices. Fig. 3.8 is a collection of  $G_P$  measurements on different samples, where samples with La:Zr = 12:1 shows stronger dependence on the bias voltage than La:Zr = 4:1, which indicates that the bulk trap density varied with depth, where the deeper trap levels also start responding. Fig. 3.8 (c) and (d) depict  $G_P$  measured for as-deposited and annealed samples with La:Zr = 1:1. Significant improvement in the interface quality is evident from the clear frequency response upon annealing the films.



*Fig. 3.9. gives the  $D_{it}$  values of as-deposited and annealed devices as a function of the Zr content in the high-k films.*

The  $D_{it}$  values measured for different films are plotted together in Fig. 3.9 as a function of the Zr content in the films. The general trend in this experiment is that the interface states reduce considerably for the mixed oxides after annealing the samples.

#### 3.4d Flat-band voltage and oxide charges

As mentioned in section 3.4.1, flat-band voltage depends on four types of charges in the device. The general expression for flat-band voltage is given by

$$V_{fb} = \phi_{MS} - (Q_f + Q_{it}) \frac{d}{\epsilon_0 k} - \frac{1}{\epsilon_0 k} \int_0^d [\rho_m(x) + \rho_{ot}(x)] x dx \quad (3.6)$$

Where  $\phi_{MS}$  is the work-function difference of the electrodes (TiN and p-Si here),  $(Q_f + Q_{it})$  is the sum of the fixed oxide charge and interface trap charges. The integral sums up the mobile charge densities  $\rho_m$  and the oxide trap charge densities  $\rho_{ot}$  in the films over the oxide thickness. In annealed devices, the interface states and the mobile charges are assumed to be negligible based on the analysis of  $C$ - $V$  curves with a forward and reverse voltage sweep at 10 kHz. The temperature and duration of the RTA process also should be long enough to ensure that the Si/high- $k$  interface anomalies have been cured out. Vanishing of interface states can be identified from the absence of the characteristics humps at low frequencies ( $\leq 10$  kHz) that are generally observed in the freshly deposited films. This will be discussed in more detail in section 3.4., where the measurements and results of the interface states are discussed. The absence of the mobile charges can be noticed from the collapse of the  $C$ - $V$  hysteresis upon RTA. Under these conditions, it is safe to assume that the oxide film contains only fixed oxide charge. Therefore, the expression for the flat-band voltage approximately shrinks to

$$V_{fb} = \phi_{ms} - \frac{Q_f}{C} \text{ or } Q_f = (\phi_{ms} - V_{fb}) \times C \quad (3.7).$$

The flat-band voltages of the devices were estimated using Mott plots, by plotting  $1/C^2$  against the voltage [Ref. 8, page 329] as shown in a typical example shown in Fig. 3.10.

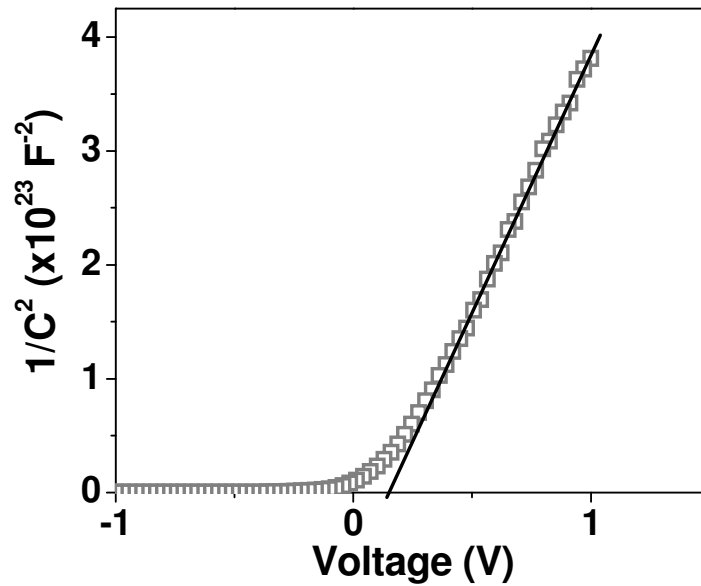


**Fig. 3.10.** Mott plot of the annealed  $\text{Al}/\text{La}_2\text{O}_3/\text{Si}$  device measured at 10 kHz frequency. The linear extrapolation to the horizontal axis gives a flat-band voltage of 0.13 V.

The flat-band voltages estimated using Mott plots for different films with different Zr content are plotted together in Fig. 3.11. The grey symbols represent  $V_{fb}$  of devices with as-deposited  $\text{La}_y\text{Zr}_{1-y}\text{O}_x$  films and the black symbols are of the devices that have undergone RTA.

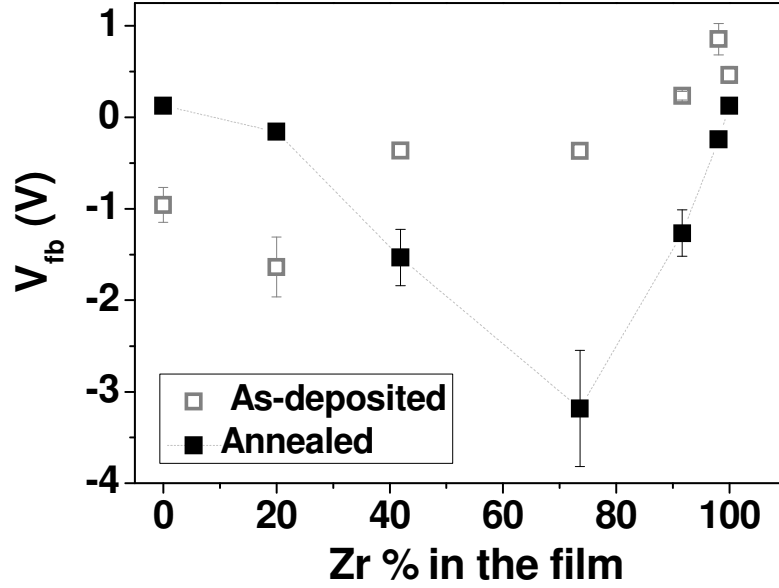


**Fig. 3.11.** Flat-band voltage estimated from Mott plots for samples as a function of the Zr content of the film. Black symbols are the values for annealed (RTA) and grey open symbols are values of as-deposited thin films.

The flat-band voltages of the devices with as-deposited films and the annealed films show no correlation at all, indicating that the band-bending in the as-deposited films are dominated by all the charges, i.e. the interface and oxide trap charges and the interface states and mobile charges that have not been passivated yet. The flat band voltage shifts of the annealed films, however, are depending on the fixed oxide trap charges only. If there are no charges at all in the oxide, then the theoretical flat-band voltage of the device should be  $V_{fb} = \phi_{ms} = \phi_{TiN} - \phi_{Si}$ . The work function of p-type silicon is 4.85 eV [17] and that of TiN is 4.5 eV [18], which means that the ideal-case flat-band shift should be  $\phi_{ms} = -0.35$  V. Using this value, the fixed oxide charge densities of the films estimated using Eqn. 3.7 are plotted in Fig. 3.12.

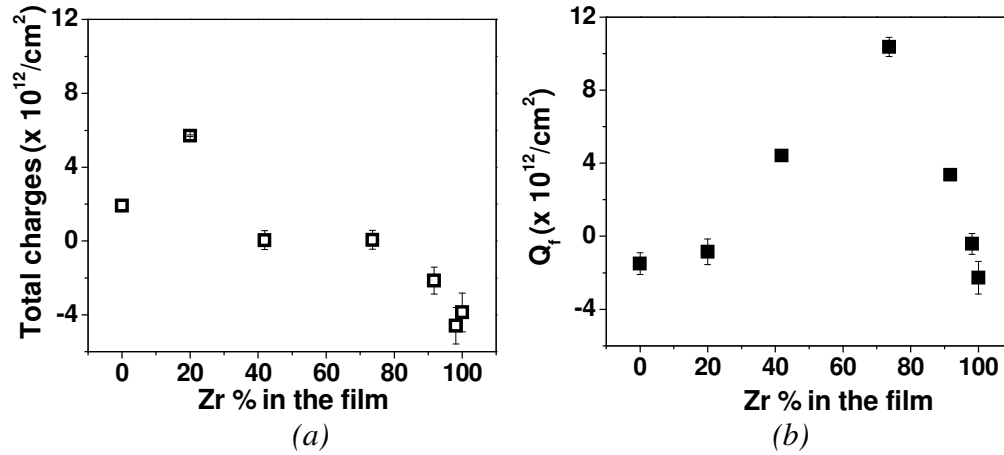


**Fig. 3.12.** (a) Total charges in the as-deposited devices and (b) the fixed oxide charges of the thin films estimated from the flat-band shifts, as a function of the Zr% in the films.

As seen from Fig. 3.12, the devices with as-deposited films have net positive charges in the La-rich films, whereas Zr-rich films have net negative charges in it. On annealing, the La-rich films also exhibit net negative charges in the film, while the samples with 42%, 74% and 92% Zr have positive net charges in the film. Again, the Zr rich films with 98% and 100%  $\text{ZrO}_2$  have negative fixed oxide charges. Since it is assumed that the annealed samples have only negligible interface trap charges, the net charges in the annealed devices are fixed oxide charges. Since the samples are not yet annealed, it is possible that the interface trap charges and mobile charges contribute significantly to the total charges that influence the flat-band shift.

On annealing the devices, several non-ideal phenomena could occur in the film and its interfaces with silicon and TiN. After annealing,  $\text{La}_2\text{O}_3$  forms  $\text{LaSiO}_x$  at the  $\text{La}_2\text{O}_3/\text{Si}$  interface, as evident from the Energy dispersive X-ray (EDX) spectroscopy studies in Chapter 2. At the TiN/ $\text{La}_2\text{O}_3$  interface, possibilities of Ti in-diffusion and oxidation of Ti also can not be entirely ruled out, though it is less severe than in the case of aluminium (see next paragraph). However, the (fixed) oxide charge density in  $\text{La}_2\text{O}_3$  on annealing the device is  $-1.5 \times 10^{12} / \text{cm}^2$ , which is  $1.9 \times 10^{12} / \text{cm}^2$  in the fresh device. In contrast, the oxide charges in  $\text{ZrO}_2$  remain negative and fairly stable: in the as-deposited films the total oxide charges were  $-3.9 \times 10^{12} / \text{cm}^2$ , which became  $-2.3 \times 10^{12} / \text{cm}^2$  upon annealing the film.

In Fig. 3.12, it is worth noting that the fixed oxide charge  $Q_f$  of the mixed films has been increased after annealing, whereas for pure  $\text{La}_2\text{O}_3$  and pure  $\text{ZrO}_2$  samples,  $Q_f$  reduced. This

enlargement in the mixed oxide layers could be due to the charges accumulated at the interface between  $\text{ZrO}_2$  clusters and the amorphous  $\text{La}_y\text{Zr}_{1-y}\text{O}_x$  dielectric surrounding them. It can be further explained as follows: La has a higher electron affinity (50 kJ/mole) than Zr (41.1 kJ/mole), which means the possibility of the presence of oxygen vacancies at the  $\text{La}_y\text{Zr}_{1-y}\text{O}_x$ - $\text{ZrO}_2$  interface, which possess positive interface cluster charges within the oxide layer. The films have  $\text{ZrO}_2$  clusters above  $\text{La}:\text{Zr} = 4:1$ . This could explain the large number of positive charges appearing in films with  $\text{Zr} > 30$  at.%, in particular, after rapid thermal annealing, when the oxygen transfer is more likely from  $\text{ZrO}_2$  to  $\text{LaZrO}_{x-1}^+$  vacancies.

### 3.4e Dielectric constant and Equivalent oxide thickness

When an oxide is deposited by means of atomic layer deposition, the formation of 0.5–1.5 nm thick interfacial  $\text{SiO}_x$  layer is inevitable [19]. Due to this additional  $\text{SiO}_x$  layer in addition to the high- $k$  oxide layer, the total capacitance measured (as shown in Fig. 3.3) is the effective capacitance of two capacitors in series – one with the low- $k$   $\text{SiO}_x$  layer and the other with the high- $k$  oxide. The dielectric constant estimated using the parallel plate approximation given by  $k = d \times C / \epsilon_0 A$  gives the effective dielectric permittivity of the stack including high- $k$  and  $\text{SiO}_2$  layers. In order to extract the  $k$ -value of the high- $k$  layers, a widely accepted method is to plot equivalent oxide thickness as a function of the total film thickness. The interfacial oxide thickness can be extracted from the linear fit of the data extrapolating to the EOT axis. From the slope of this linear fit, the  $k$ -value of the high- $k$  layer without the interfacial oxide layer also can be extracted. This is more or less a theoretical approach, where two assumptions have to be correct. Firstly, the interfacial oxide should be same for all film thicknesses. Secondly, the dielectric constant of the films should be independent of the film thickness at least in the studied range. The approach adopted in this chapter is to estimate the film thickness and the interfacial oxide thickness accurately using high-resolution transmission electron microscopy (HRTEM) data detailed in the previous chapter (see Table 2.5) and use individual dielectric and interfacial oxide thickness to estimate the dielectric constants of individual layers. The permittivities of the films were derived from the accumulation capacitance shown in Fig 3.2. A capacitance-in-series model was employed for this, with  $k = 3.9$  for the interface oxide and the individual thickness of high- $k$  and interface oxide layers measured with HR-TEM:



$$k_{\text{High-k}} = \frac{d_{\text{High-k}}}{\left( \frac{A \cdot \epsilon_0}{C_{\text{tot}}} - \frac{d_{\text{SiO}_2}}{3.9} \right)} \quad (3.8)$$

Fig. 3.13 shows the dielectric constant of the as-deposited films as a function of the Zr content in these films, using Al and TiN as the top electrodes. A consistent increase in the dielectric constant with increasing Zr percentage in the film is observed here. While the estimated  $k$ -value of  $\text{La}_2\text{O}_3$  is in between 18-22 and of  $\text{ZrO}_2$  is 30-32, the mixed oxide films have dielectric constants peaking up to 35-42 for films that contain up to 93 at % Zr. For comparison, the  $k$ -values of ALD-synthesized  $\text{La}_2\text{O}_3$  have been reported to be 14–27 and that of ALD  $\text{HfO}_2$  is 18–30 depending on the crystallographic phases. [20]

The dielectric constant of the films with Al top electrode is less than that of the devices with TiN electrode, which is probably due to the formation of  $\text{Al}_2\text{O}_3$  and  $\text{LaAlO}_x$  formation at the interface, when Al is used as the top electrode. This is consistent with the observation by Pan et al. [21] that the capacitance of Al/ $\text{La}_2\text{O}_3$ /Si devices is less than that of the Al/TaN/ $\text{La}_2\text{O}_3$ /Si devices electrodes. This was attributed to the enhanced silicon diffusion to the Al/ $\text{La}_2\text{O}_3$  interface, rather than due to the formation of  $\text{LaAlO}_x$ . A detailed Time of Flight Secondary Ion Mass Spectroscopy (TOFSIMS) study on this effect will be given in Chapter 4.

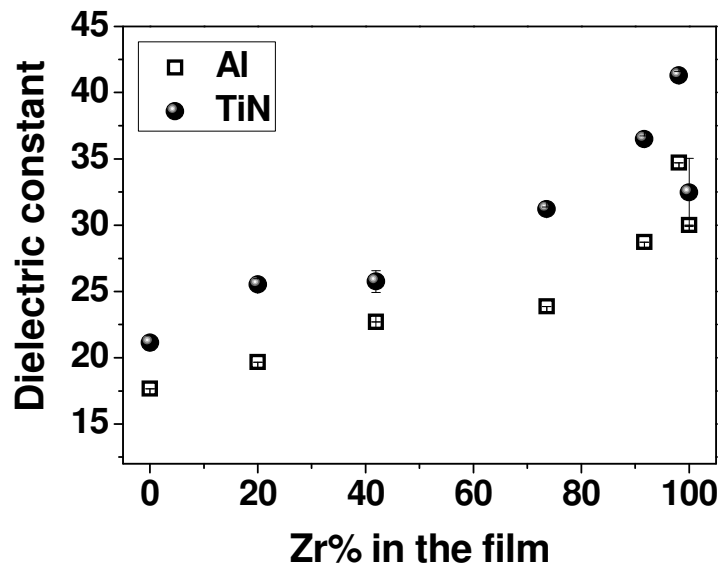


**Fig. 3.13.** Dielectric constant of the as-deposited  $\text{La}_y\text{Zr}_{1-y}\text{O}_x$  films with Al and TiN as top electrodes, as a function of Zr content in the film.

Upon RTA, there is significant change in the  $k$ -values for all of the compositions indicating poor stability against interfacial oxide growth at these annealing conditions. This finding is supported by HRTEM analysis (see Chapter 2). The formation of  $\text{LaAlO}_x$  and  $\text{Al}_2\text{O}_3$  are enhanced upon annealing the sample with Al electrodes on top of the films. In addition,  $\text{La}_2\text{O}_3$  forms silicate at the interface with silicon, which also has a lower dielectric constant than  $\text{La}_2\text{O}_3$ . This causes a further reduction in  $k$ -values measured for the annealed samples. Similar is the case with the lowering of  $k$ -value is the strongest for  $\text{ZrO}_2$ , which is more likely due to  $\text{AlZrO}_x$  or  $\text{ZrSiO}_x$  formation, As Fig. 3.14 shows, a comparable reduction of the dielectric constant is observed for the  $\text{La}_y\text{Zr}_{1-y}\text{O}_x$  mixed oxide films with TiN and Al electrodes but the relative reduction for the pure  $\text{ZrO}_2$  film is larger with an Al top electrode.

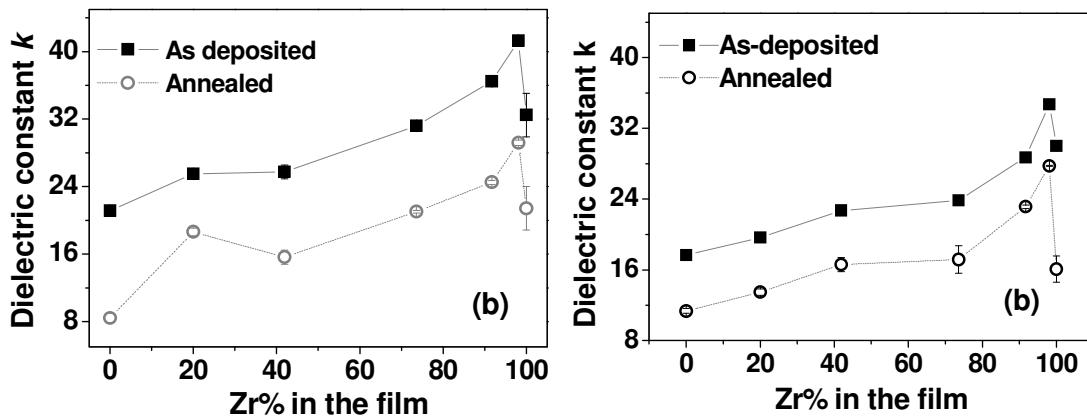


**Fig. 3.14.** Dielectric constant of as-deposited and rapid-thermal-annealed  $\text{La}_y\text{Zr}_{1-y}\text{O}_x$  films with (a) TiN electrode and (b) Al electrode, shown as a function of Zr content in the film.

The estimated dielectric constant of  $\text{La}_2\text{O}_3$  is 17.3 and is relatively low compared to the value of 27 reported earlier [22]. This low dielectric constant is possibly due to the amorphous character of the film and the instability of the oxide-hydroxide phase, since the film had been already exposed to normal ambience. Fig. 3.14 shows that the dielectric constant of the films increases linearly with the Zr content in the film. Similar enhancement in dielectric permittivity has been shown in homogeneous  $\text{Al}_y\text{Zr}_{1-y}\text{O}_x$  films, where the dielectric constant linearly increases with the Zr content in the film [23]. Besling et al. used  $\text{ZrCl}_4$  and  $\text{H}_2\text{O}$  as precursors and have observed the formation of the monoclinic  $\text{ZrO}_2$  phase which has a lower dielectric constant of around 22. On the other hand, the reasonably high dielectric constant of 30 for the pure  $\text{ZrO}_2$  layers indicates that the choice of  $\text{ZrD-O4}$  as Zr precursor has a significant impact on the dielectric properties of the film, compared to chlorine-based

precursors. This is nicely supported by XRD analysis that the  $\text{ZrO}_2$  clusters are predominantly found in the tetragonal phase which is known to exhibit a much larger dielectric permittivity than the monoclinic phase [24]. In this respect the peaking up to 35-42 for the  $\text{La}_y\text{Zr}_{1-y}\text{O}_x$  mixed oxide films is remarkable because the  $k$ -value is higher than the best ever reported permittivities for tetragonal  $\text{ZrO}_2$ .

The equivalent oxide thickness (EOT), also called the capacitance equivalent thickness (CET) can be estimated using the expression:

$$EOT = 3.9 \times \frac{\epsilon_0 A}{C} = 3.9 \times \frac{d_{\text{high-}k}}{k} + d_{\text{SiO}_2} \quad (3.9),$$

where  $A$  is the area and  $C$  is the capacitance of the device. The EOT estimated for the as-deposited layers is shown in Fig. 3.15.

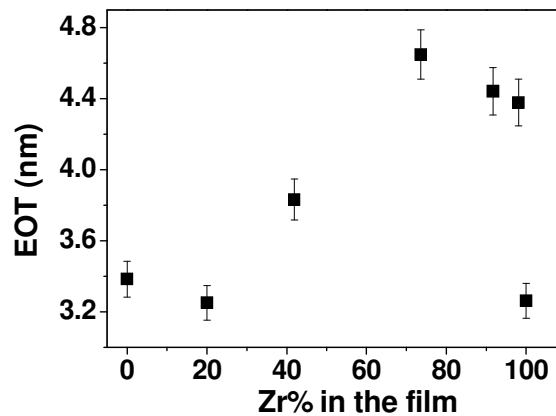


*Fig. 3.15. EOT of as-deposited  $\text{La}_y\text{Zr}_{1-y}\text{O}_x$  films as a function of the Zr content in the films.*

### 3.5 Current–Voltage ( $I$ - $V$ ) measurements

Capacitance measurements give ample information about the interfaces and polarizability of the dielectric layer, which determines the eventual usage of the material as a high- $k$  layer. However, a parameter equally important as that of the dielectric permittivity is the leakage current through the device, which exponentially increases with reducing the thickness of the layer. Leakage current contributes to the parallel resistance of the capacitor (and thus influences the capacitance measurements) and increases the power consumption of the device. In addition, height of the leakage current determines the long term reliability of the device. As

per the CMOS specifications of ITRS, the limit of leakage current density is  $1 \text{ A/mm}^2$ , which comes in the nano-Ampere range for the structures of the forthcoming CMOS technological nodes.

Comparing to the  $C$ - $V$  measurements, current-voltage ( $I$ - $V$ ) measurements are simpler to understand and interpretations of the data is less ambiguous. While  $C$ - $V$  measurements are heavily influenced by the interfacial states,  $I$ - $V$  measurements are sensitive to the properties of the oxide layer, such as its band-gap, band offsets with the electrodes, defect levels and tunnelling probabilities. Therefore, the leakage current characteristics are more important to identify the electrical quality of the layers, as well as to study the transient effects due to charge or defect accumulation in the oxide.

In this section, several standard leakage current measurement techniques will be addressed such as thermal activation of shallow traps in the oxide, analysis of  $I$ - $V$  curves for various conduction regimes, for instance, Ohmic conduction, space-charge limited conduction or trap ionization. In addition, different conduction mechanisms will be addressed among them quantum tunnelling of the charge carriers through the conduction band of the oxide and Poole-Frenkel thermal charge hopping.

### 3.5a Arrhenius behavior of leakage current

Interface state density extractions discussed in section 3.4c are helpful in identifying the interface trapped charges and their influence on the flat-band shifts. These energy levels are distributed over the band-gap of the silicon substrate. However, lattice mismatching and bonding imperfections at the silicon/oxide interfaces do have effects on the band diagram of the oxide as well. Another class of trap levels appears due to the intrinsic defects in the oxide layer, such as vacancies and grain boundaries. These imperfections appear as shallow trap levels close to the conduction band of the oxide and they are thermally excitable electronic states. Different from normally studied high- $k$  oxide layers, the  $\text{La}_y\text{Zr}_{1-y}\text{O}_x$  thin films investigated here have a phase-segregated  $\text{ZrO}_2$  clusters in amorphous  $\text{La}_y\text{Zr}_{1-y}\text{O}_x$  matrix. As discussed in Section 3.4d, there are clear indications that the positive charges in the sample have been increased upon annealing, which is attributed to the increased oxygen vacancies at the  $\text{ZrO}_2$ - $\text{La}_y\text{Zr}_{1-y}\text{O}_x$  interface. This complicates the normal band-diagram of the device, with additional trap levels originating from the surface states of  $\text{ZrO}_2$  clusters as shown in Fig. 3.16.

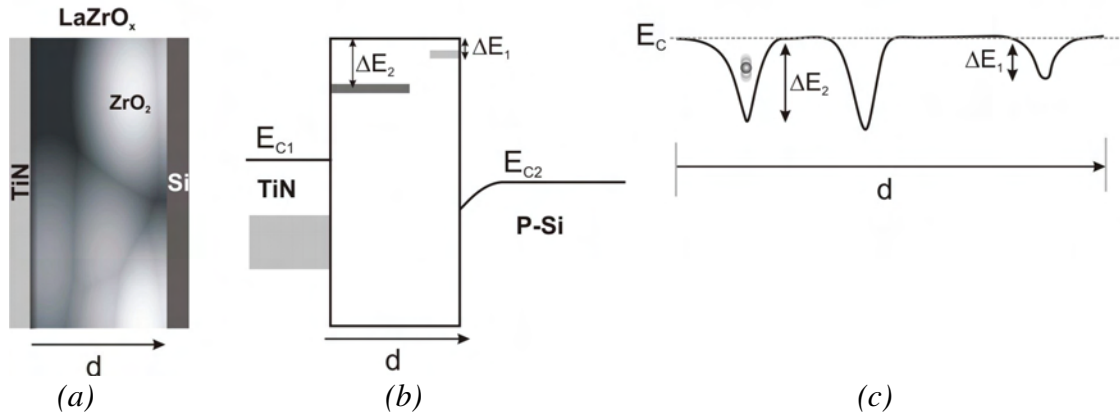


**Fig. 3.16.** (a) Cartoon of the  $\text{La}_y\text{Zr}_{1-y}\text{O}_x$  dielectric layer, with embedded  $\text{ZrO}_2$  nanocrystals in amorphous  $\text{La}_y\text{Zr}_{1-y}\text{O}_x$  matrix. (b) Band-diagram of the device with trap levels  $\Delta E_1$  and  $\Delta E_2$  representing the shallow traps and the traps at the  $\text{ZrO}_2$ -  $\text{La}_y\text{Zr}_{1-y}\text{O}_x$  interface, respectively. (c) Trap levels close to the conduction band of the oxide at zero applied bias voltage.

Fig. 3.16 (a) shows the model of the dielectric layer with  $\text{ZrO}_2$  nanocrystals embedded in  $\text{La}_y\text{Zr}_{1-y}\text{O}_x$  matrix. Case (b) shows the schematic band-diagram of this oxide, with trap energies  $\Delta E_1$  and  $\Delta E_2$  representing the shallow traps that belong to the interfacial imperfections such as dangling bonds and the traps at the  $\text{ZrO}_2$ -  $\text{La}_y\text{Zr}_{1-y}\text{O}_x$  grain boundaries. Since these trap levels are close to the conduction band of the oxide, there is a non-zero probability that the wave-function of these electrons overlap with the conduction band and appear as free electrons. The probability of these electrons to traverse the energy barrier to reach the conduction band exponentially increases with the temperature of the system. This thermally activated process can be described using an Arrhenius law: the rate of successful jumps of electrons from the trap levels to the conduction band depends on the energy barrier height  $\Delta E$  and the temperature of the ensemble by the expression [25]

$$r = r_0 \exp\left(-\frac{\Delta E}{k_B T}\right) \quad (3.10),$$

where  $r_0$  is the attempt frequency of an electron in the potential well shown in Fig. 3.16 (c),  $r$  is the rate of successful jumps and  $k_B$  is the Boltzmann constant. This expression tells that the number of thermally activated electrons reaching the conduction band and contributing to the leakage current increases with temperature for a given trap level. Therefore, it is safe to

assume that  $r_0 \propto J_0$  and  $r \propto J$ , where  $J_0$  and  $J$  are current densities in a-thermal (infinite temperature) and thermally activated regimes of charge conduction. Thus expression 3.10 becomes

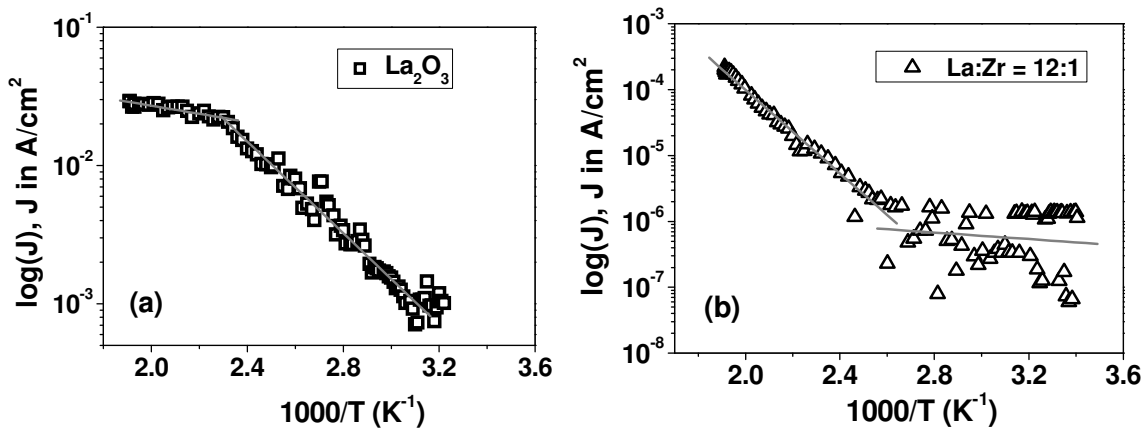
$$J = J_0 \exp\left(-\frac{\Delta E}{k_B T}\right) \quad (3.11).$$

Therefore, the slope of the Arrhenius plot where  $\ln(J/J_0)$  is plotted against  $1/T$  gives the activation energy  $\Delta E$  of the trap levels. From Eqn. (3.11),  $\Delta E$  can be derived independent of  $J_0$  as

$$\Delta E = -\frac{k_B}{e} \frac{\log \frac{J_2}{J_1}}{\left(\frac{1}{T_2} - \frac{1}{T_1}\right)} \quad (3.12)$$

in units of electron volts (eV).

Figure 3.17 shows the Arrhenius behaviour of the  $\text{La}_y\text{Zr}_{1-y}\text{O}_x$  films, where the leakage current was measured at a fixed electric field of 2 MV/cm for all the films (electric field is defined as the applied voltage divided by the thickness of the layers measured by HRTEM). The choice of the electric field ensures that the leakage current measured is the thermally stimulated current through the system rather than the temperature-assisted tunnelling current mentioned later on in this Chapter.



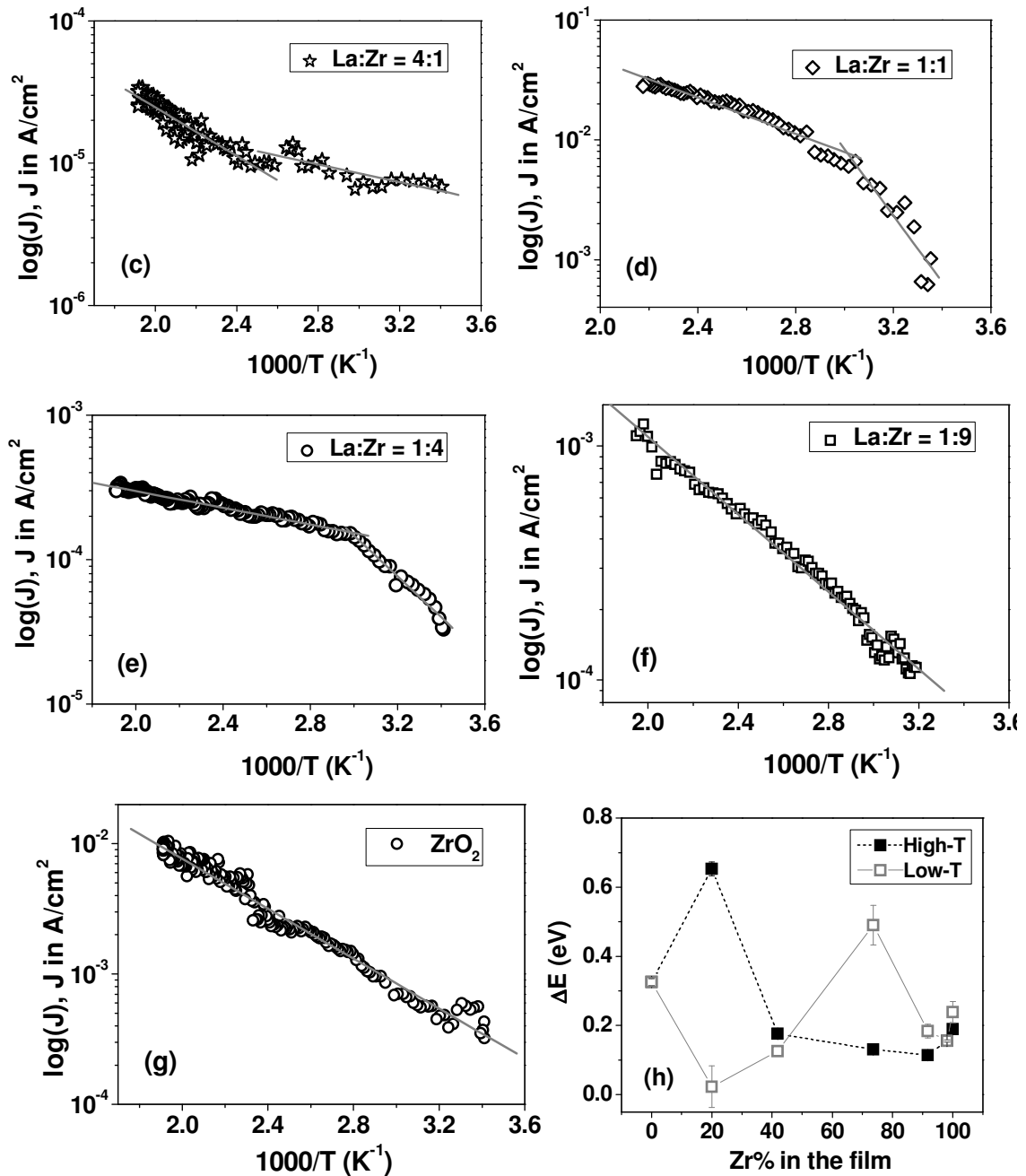


**Fig. 3.17.** Arrhenius plots of the films with different La:Zr compositions: (a)  $\text{La}_2\text{O}_3$ , (b) La:Zr = 12:1, (c) La:Zr = 4:1, (d) La:Zr = 1:1, (e) La:Zr = 1:4, (f) La:Zr = 1:9, (g)  $\text{ZrO}_2$ , and (h) shows the activation energy estimated for the low-temperature branch and high-temperature branch of the Arrhenius plots.

Figure 3.17 shows that most of the oxide films with mixed stoichiometries have two branches in the Arrhenius behaviour with different slopes indicative of two different activation energies. They are termed as high-T and low-T branches for convenience. Noticeably, the

behaviour of the high-T and low-T branches change with Zr content in the sample. Samples with 20% and 42% Zr has a higher slope for the high-T branch than the low-T branch (see Fig. 3.17 (b) and (c)), while samples with 74% and 92% of Zr have lower slope for high-T branch than low-T branch. In these samples, the activation energy of  $\text{La}_2\text{O}_3$  (0.33 eV) is almost twice than that of  $\text{ZrO}_2$  (0.19 eV). This explains the different behaviour of the films at low and high temperature branches. Higher activation energy levels respond to higher temperatures in La-rich samples, where lower activation energy levels emerge at high temperatures in Zr-rich films.

Generally, when using the slope of the  $\ln(J_0)$  versus  $1/T$  linear distribution,  $J_0$  is an unimportant parameter. But this parameter gives indications about the Arrhenius behaviour of traps levels. Since the Arrhenius equation (Eqn. 3.11) deals only with the energy barrier between the trap energy  $E_t$  and the conduction band  $E_C$ , so that  $\Delta E = E_C - E_t$ , the pre-exponential factor  $J_0$  is purely the current due to the trapped electrons at infinite temperature, where all the trap levels are filled with thermal energy and electrons are evacuated completely from these traps. Therefore,  $J_0$  represents the maximum capacity of the trap levels continuously trapping and releasing electrons. Thus  $J_0$  should have similar behaviour as of the fixed traps in the oxide.

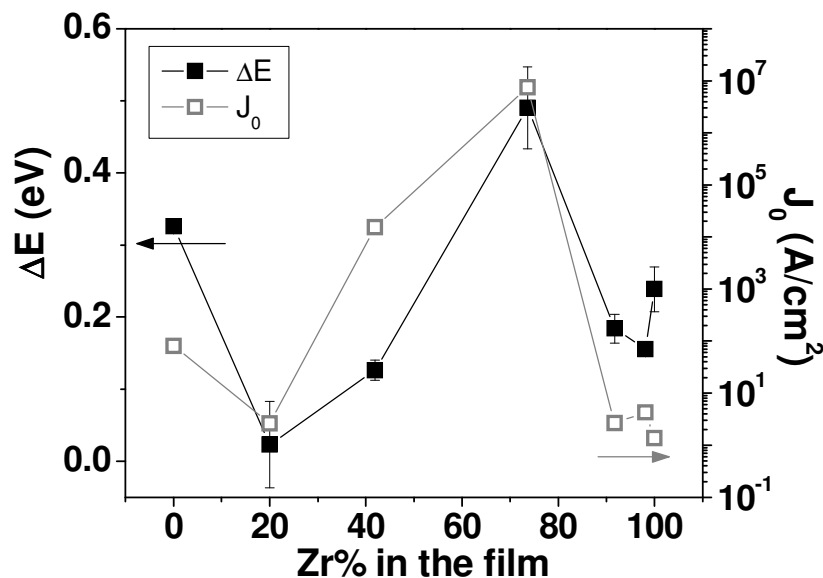


**Fig. 3.18.** Activation energy of the low-T branch and the corresponding  $J_0$  as a function of the Zr content in the films.

In order to illustrate this, Figure 3.18 shows the resemblance between the activation



energy of the lower temperature branch with the Arrhenius exponential pre-factor  $J_0$ . In addition, if one compares the similarity between the positive fixed oxide charges given in Fig. 3.12 and the  $J_0$  one finds a remarkable similarity, because they might be originating from the same trap level – the oxygen vacancies at the  $\text{ZrO}_2$ -  $\text{La}_y\text{Zr}_{1-y}\text{O}_x$  interface.

### 3.5b Different regimes of electrical conduction in a dielectric

When a voltage is applied across the electrodes of a MIS device, usually with the metallic electrode (here TiN) negatively biased, majority electrons accumulate at the metal-oxide interface and mirror charges (holes) accumulate at the oxide-silicon interface. This image force along the dielectric thickness is given by  $q^2/16\pi\epsilon x^2$ , where  $\epsilon$  is the dielectric permittivity of the oxide. At flat-band condition, the free electrons in the conduction band of the metal have to traverse the energy barrier  $\phi_{b0} = E_{C\text{-Oxide}} - E_{C\text{-metal}}$  in order to reach the conduction band of the silicon. Due to the image force of the mirror charges, the conduction band of the oxide bends towards the silicon conduction band, as shown in Fig. 3.19. This phenomenon is generally called Schottky barrier lowering [26,27]. This barrier lowering,  $\Delta\phi_b$ , is a function of the electric field and is given by  $q\Delta\phi_b = q\phi_{b0} - q\phi_b = (q^3 E_{ox}/4\pi\epsilon)^{1/2}$ , where  $E_{ox}$  is the electric field inside the oxide.

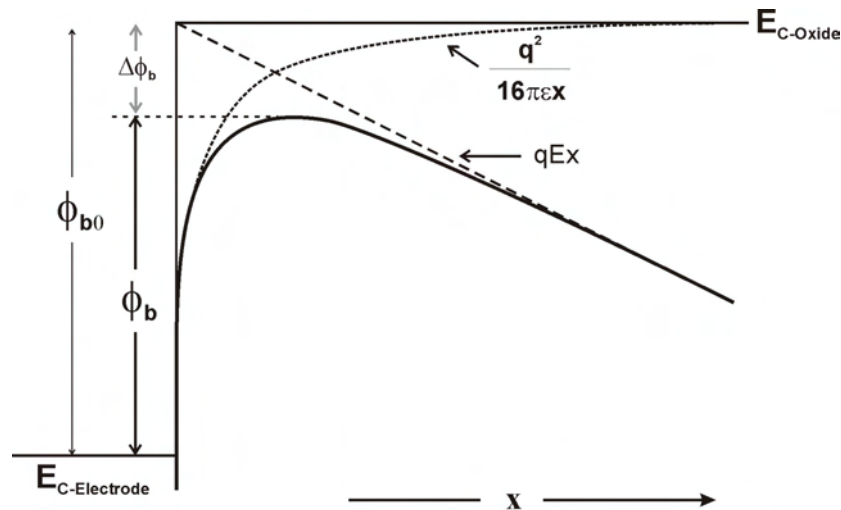


**Fig. 3. 19.** Schottky barrier lowering due to image force. The thick line is the resulting conduction band of the oxide under an applied bias, which is the sum of the actual conduction band, the image force and the applied electric field ( $= qEx$ ).

The actual picture of the conduction band is even more complex if one includes defects levels also associated with it. With increasing bias voltage, different charge transport mechanisms emerge. At sufficiently low bias voltages (corresponding to 0 to  $\sim 1$  MV/cm) when the band bending is negligible, a very minute fraction of the available electrons in the conduction band of the metal resistively passes through the oxide. This current through the oxide follows Ohm's law and is proportional to the bias voltage ( $I_{Ohm} \propto V$ ).

Increasing the voltage further causes the electrons to trap in the oxide, whose electric field limits the further flow of electrons. The current in this regime is termed as space-charge limited current (SCLC) and follows Child's law [28], which states that the leakage current is proportional to the square of the bias voltage and inversely proportional to the cube of the dielectric thickness ( $I_{Child} \propto V^2/d^3$ ).

The leakage current in the SCLC regime is sensitive to the temperature, because the *shallow* traps liberate free electrons to the conduction band, which is a thermally activated process that follows Arrhenius law. Therefore, SCLC regime is the correct bias range for the temperature-dependent leakage current measurements to draw Arrhenius plots, since the trap levels are filled in these bias voltages. At even higher voltages, the charges trapped in the oxide begin to de-ionize and start contributing to even higher leakage currents through the dielectric.

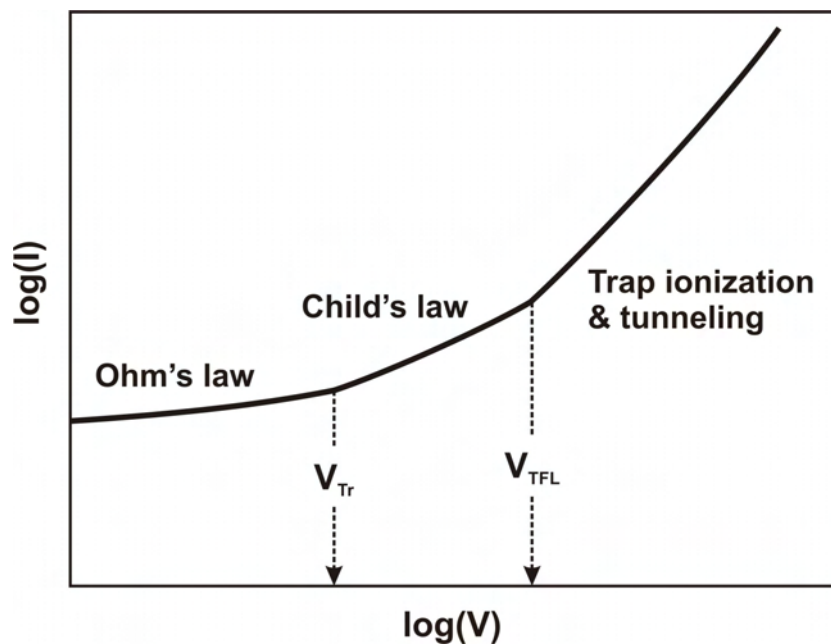


**Fig. 3.20.** *I-V* curve in log-log plot showing different conduction regimes that follow different voltage power laws.

From the slopes of the data in  $\log(I) - \log(V)$  form of the  $I$ - $V$  plot, these different regimes of conduction are clearly identified as Fig. 3.20 illustrates. In Fig. 3.20,  $V_{Tr}$  represents the transition voltage at which the transition from Ohmic conduction to SCLC regime occurs. From the *trap-filled limit voltage* ( $V_{TFL}$ ), i.e. the voltage at which the transition from the SCLC regime to trap-free conduction occurs, the trap concentration  $N_t$ , which is the volume trap density in the semiconductor, can be estimated as

$$V_{TFL} = qN_t d^2 / 2\epsilon_0 \epsilon_r \quad (3.12).$$

Here,  $\epsilon_r$  is the dynamic dielectric constant and  $d$  is the thickness of the film [29]. The current in the SCLC regime follows the Child's law where the current density is given by

$$J_{Child} = 9\mu\epsilon_0\epsilon_r V^2 / 8d^3 \quad (3.13).$$

Therefore, the intersect of the SCLC regime in the  $J$ - $V$  plot in Fig. 3.20 gives the electronic mobility  $\mu$ . Using this value, the free carrier density  $n_0$  at room temperature can be calculated from the Ohmic current in the first regime as

$$J_{Ohm} = qn_0\mu V / d \quad (3.14)$$

When the bias voltage rises beyond  $V_{TFL}$ , the charge carriers undergo trap-free conduction and the traps begin to ionize, liberating electrons to the conduction band of the oxide.

At electric fields lower than  $\sim 3$  MV/cm, the leakage current is resulting from the electrons that have sufficient energy to cross the metal-oxide barrier  $\phi_b$ . This thermal electron emission resembles the thermionic emission of electrons from a metallic surface at high temperature and therefore, they follow the Schottky thermionic emission given by

$$J_s = AT^2 \exp\left(\frac{-\phi_b + q\sqrt{qE/4\pi\epsilon_0\epsilon_r}}{kT}\right) \quad (3.15)$$

where  $\phi_b$  is the Schottky barrier height and  $A$  is the effective Richardson constant [28]. The intersect of the data on the  $\ln(J_s / AT^2)$  axis is given by  $\phi_b / kT$ , from which the effective barrier height  $\phi_b$  can be estimated. But, the conduction band of the oxide bends at sufficiently high electric fields (beyond  $V_{TFL}$ ), as illustrated in Fig. 3.19, and the charge carriers (electrons through the conduction band or holes through the valence band of the oxide) tunnel from the conduction band of the metal to the trap levels in the oxide band-gap and thermally hop through the trap levels to reach the silicon valence band. This electric field assisted thermal hopping of charges is known as Poole-Frenkel (FP) charge injection. The current density due

to PF charge injection is therefore similar to the Schottky emission current density, and can be written as

$$J_{PF} = CE \exp\left(\frac{-\phi_t + q\sqrt{qE/4\pi\epsilon_0\epsilon_r}}{kT}\right) \quad (3.16).$$

Here,  $C$  is a constant and  $\phi_t$  is the ionization energy of the deep traps. Generally in modelling Poole-Frenkel charge injection,  $\Delta E = \phi_t$ , where  $\Delta E$  is the trap level estimated from the Arrhenius plots.

It is worth noting that the equations 3.13, 3.15 and 3.16 employ the dynamic dielectric constant  $\epsilon_r$ , instead of static low-frequency dielectric constant. This is because, in the Schottky emission picture, the electrons reside at the metallic surface only for a very small time. Similarly, the pre-exponential factor in Arrhenius law (Eqn. 3.10), which is the attempt frequency of the electrons in a potential well set by the traps, is  $\sim 10^{13} \text{ s}^{-1}$ . This high-frequency dielectric constant (the optical dielectric permittivity) is related to the refractive index of the material by  $\eta = \sqrt{\epsilon_r}$  and thus, the refractive index of the oxide also can be deduced *if* it exhibits PF charge injection [30].

At higher electric fields, the conduction band of the oxide bends towards the silicon to the extent that it triggers electron tunnelling through the oxide. This type of charge conduction is called Fowler-Nordheim (FN) tunnelling, and is extensively used in field emission from sharp metallic tips. FN tunnelling is purely a quantum mechanical tunnelling of electrons through a rounded triangular potential energy barrier of the oxide. This tunnelling takes place from the conduction band of the TiN through the oxide to the conduction band of the p-type silicon substrate in the case of electrons and from the valence band of the silicon through the oxide to the valence band of TiN for holes. Whether the charge carrier is electrons or holes depends primarily on the conduction and valence band offsets of silicon with that of the oxide. The current density due to FN tunnelling is given by [31]

$$J_{FN} = \frac{q^3 m}{16\pi^2 \hbar m_{ox} \phi_b} E^2 \exp\left(-\frac{4}{3} \frac{\sqrt{2m_{ox}}}{q\hbar E} \phi_b^{3/2}\right) \quad (3.17)$$

where  $\phi_b$  is the tunnelling barrier height and  $m_{ox}$  is the electron effective mass in the oxide. The tunnel barrier height can be estimated from the slope of the FN plots, which is a plot with  $\ln(J/E^2)$  plotted against  $1/E$  yielding a straight line.

The major conduction mechanisms described in this section are summarised in Fig. 3.21.

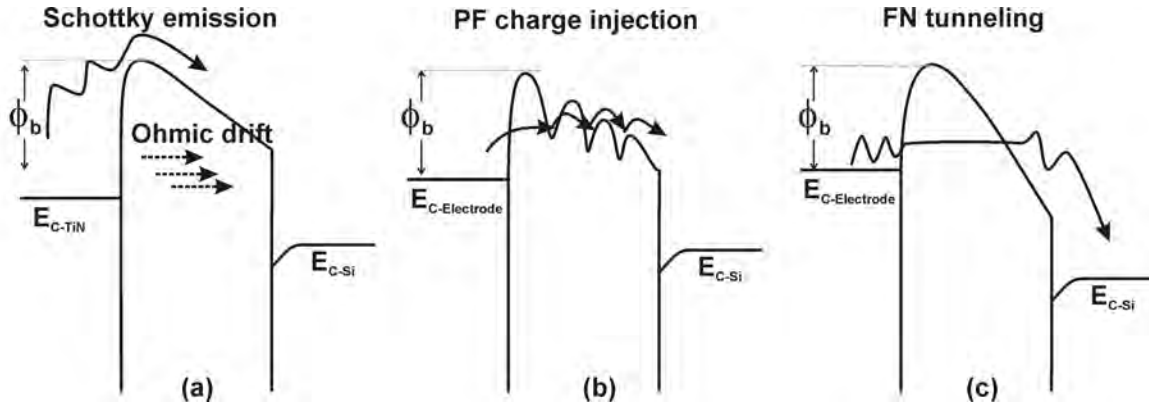


**Fig. 3.21.** Major conduction mechanisms through the oxide at (a) low electric fields, (b) medium electric field (2-4 MV/cm) and (c) high electric fields (>4 MV/cm).

### 3.5c Trap density and charge mobility

The results of  $I$ - $V$  measurements (represented in terms of the current density  $J$  and electric field  $E$ ) of different TiN/ $\text{La}_y\text{Zr}_{1-y}\text{O}_x$ /Si devices are shown in Fig. 3.22.

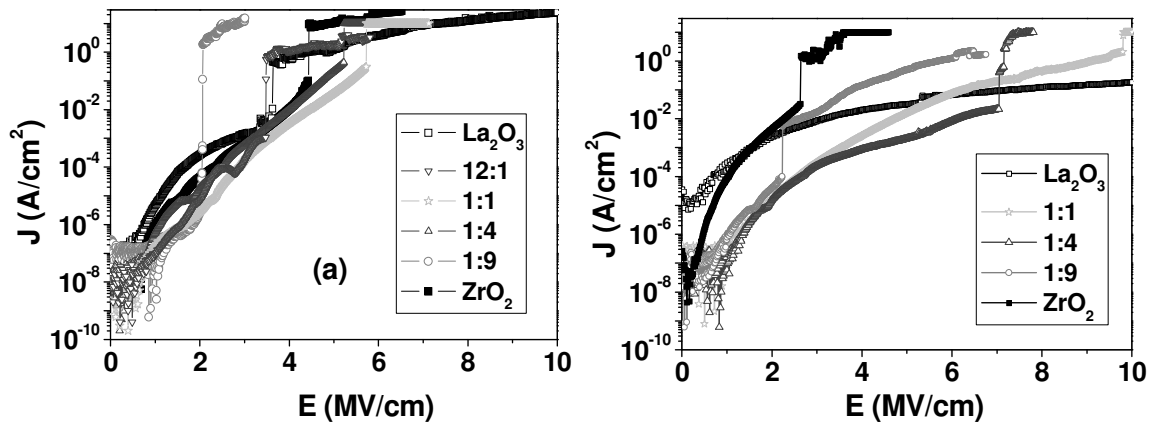


**Fig. 3.22.**  $J$ - $E$  characteristics of (a) as-deposited and (b) annealed TiN/ $\text{La}_y\text{Zr}_{1-y}\text{O}_x$ /Si devices.

The leakage of the devices seems to have deteriorated upon annealing. The devices show better breakdown fields, but the tunnelling behaviour after annealing has lower slope, which is a signature of degradation of the film quality in terms of the bulk defects in the oxide. To understand the origin of this leakage behaviour and the resulting change after RTA, a careful analysis of the individual  $I$ - $V$  characteristics is necessary.

By plotting the  $I$ - $V$  curves as  $\log(I)$ - $\log(V)$  plots, the different regimes of conduction can be recognized. Fig. 3.23 shows a typical log-log plot of  $I$ - $V$  curve of a film with  $\text{La}:\text{Zr} = 1:1$ .

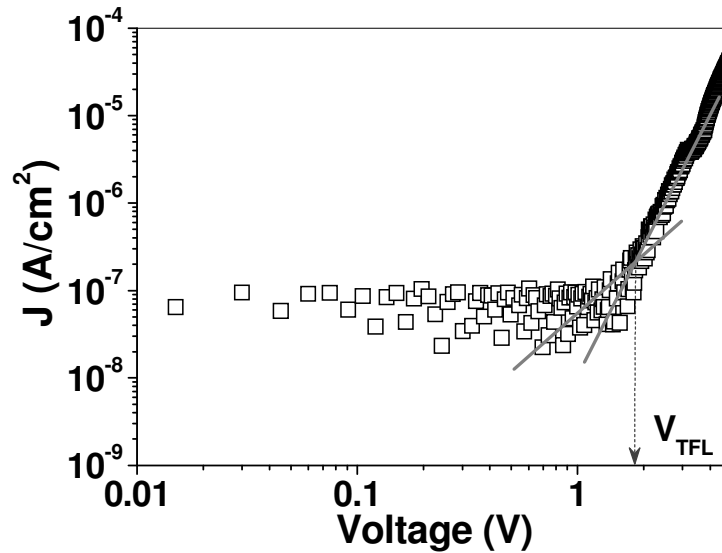


Fig. 3.23. A typical log-log plot of  $I$ - $V$  curve of a film with  $\text{La}:\text{Zr} = 1:1$ .

The plot above gives the SCLC regime where the current follows Child's law, and the trap-filled limit voltage ( $V_{TFL}$ ) where the transition from trap-filling to trap ionization occurs.

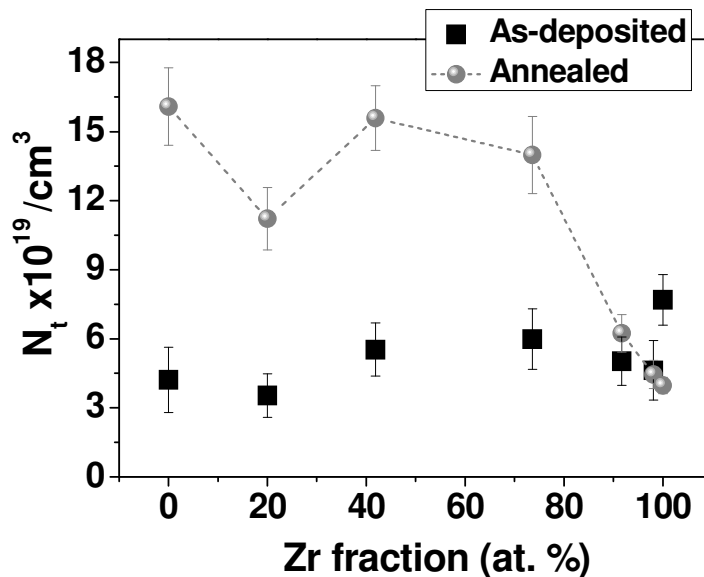
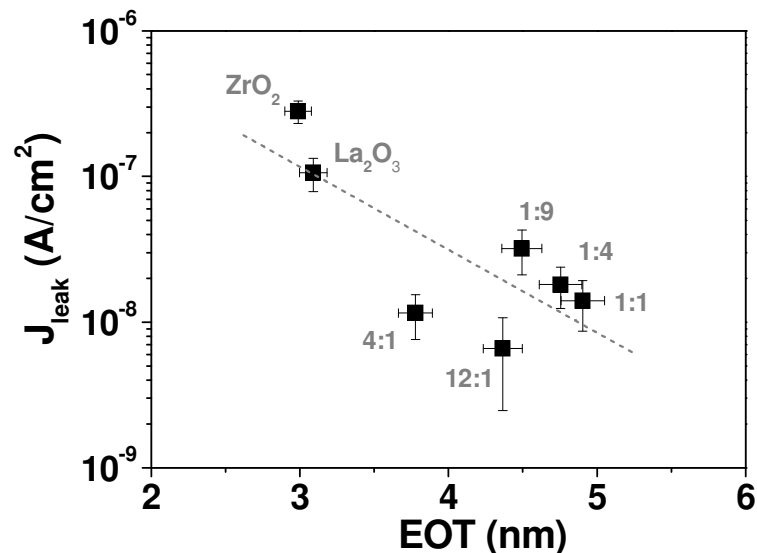


Fig. 3.24. Trap density of the as-deposited and annealed films as a function of the Zr content in the films. To estimate these values, the value of dynamic permittivity of individual layers was used, which was obtained from Poole-Frenkel analyses described in the next section.

Employing equations 3.12 and 3.13, the trap density in these materials can be estimated. The trap density  $N_t$  of the films increases upon annealing as is shown in Fig. 3.24 (top), especially in the films with noticeable La content. This could be due to the formation of  $\text{LaSiO}_x$  at the interface or due to charge trapping at the  $\text{La}_y\text{Zr}_{1-y}\text{O}_x\text{-ZrO}_2$  grain boundaries. The latter possibility has already been evidenced in the fixed oxide charge measurements of the annealed samples depicted in Fig. 3.12 (b), where the charges were assumed to originate from the  $\text{La}_y\text{Zr}_{1-y}\text{O}_x/\text{ZrO}_2$  interfaces in the nanoclustered thin films.

### 3.5d Leakage current density

The leakage current density is a key parameter that determines the quality of a high- $k$  material. Normally, different technological nodes have different specifications of leakage currents and it is therefore crucial that it should be mentioned together with the EOT of the films. Since the thicknesses of these samples are different, the more informative way of presenting the leakage would be plotting the leakage current density against the EOT of the films. Fig. 3.25 gives such a  $J$ -EOT plot of the films measured at 1 MV/cm electric field. Although the slope has not been determined for each composition, the offset between some of  $\text{La}_y\text{Zr}_{1-y}\text{O}_x$  films is significant enough to state that the La-rich films (12:1 and 4:1) are outperforming the Zr-rich films.



**Fig. 3.25.** Leakage current density of the as-deposited films as a function of the EOT. The dotted line is the linear fit to the data and is purely to guide the eye because for each composition the slope could be different.

### 3.5e Poole-Frenkel charge injection through the $\text{La}_y\text{Zr}_{1-y}\text{O}_x$ films

In section 3.5a, the Arrhenius behaviour of leakage currents in the SCLC conduction regime was discussed in detail. Leakage current in SCLC regime follows Child's law, were the trap levels close to the conduction band of the oxide are filled. At higher voltages, the filled traps start ionizing, liberating the trapped electrons to the conduction band of the oxide. The energy levels of these traps are lowered upon applying an external electric field and thus electric field-assisted thermal hopping of charges occurs, which is Poole-Frenkel (PF) charge injection. As per Eqn. 3.16, PF curves are plotted as  $\ln(J/E)$  versus  $E^{1/2}$ , which yields a straight line, as Fig. 3.26 shows.

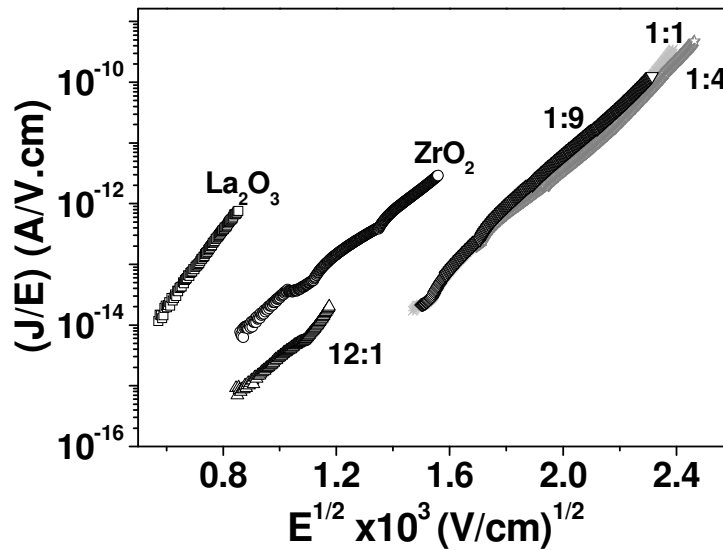


**Fig. 3.26.** Poole-Frenkel plot of as-deposited  $\text{TiN}/\text{La}_y\text{Zr}_{1-y}\text{O}_x/\text{Si}$  devices. For clarity, only the linear section of the  $J$ - $E$  curve is shown here.

The intersect of these straight lines is  $\ln(\phi/k_B T)$ , from which the trap ionization energy can be derived. From the slopes of the curves, the high-frequency (dynamic) dielectric permittivity of these layers can be estimated. These two extracted parameters are plotted against the Zr fraction of the films in Fig. 3.27.



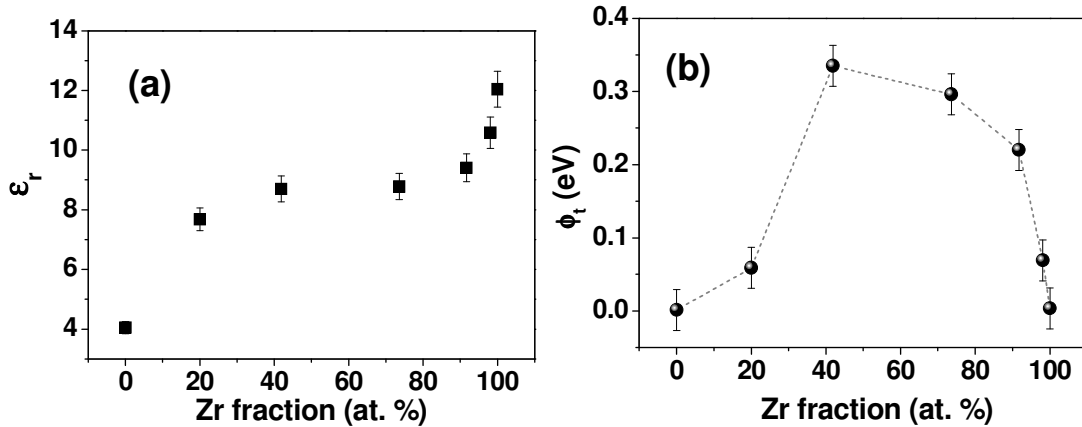


*Fig. 3.27. (a) The dynamic permittivity and (b) the trap ionization energy estimated from PF fitting, as a function of the Zr fraction of the films.*

Different refractive indices of  $\text{ZrO}_2$  thin films have reported in literature, for instance 1.6 by Ramanathan et al. [30] and 2.5 by Chiu et al [23]. The refractive index of  $\text{ZrO}_2$  estimated from our PF analysis is 3.46 (from the square root of the dynamic dielectric permittivity plotted in Fig. 3.27 (a)). Generally, the trap ionization energy (plotted in Fig. 3.27 (b)) should have the same characteristics of the activation energy of the traps estimated from the Arrhenius plots (Fig. 3.17(h)), but they appear to show a different trend. The range of the trap activation energy from the Arrhenius plots is higher than that from the PF plots suggesting that in these samples PF charge injection occurs from the more shallow trap levels whereas the deeper trap levels obtained from the Arrhenius plots can be related to the interface defects of the  $\text{La}_y\text{Zr}_{1-y}\text{O}_x/\text{ZrO}_2$  interface. The bending of the oxide conduction band on the application of the voltage across the film also causes a reduction in the energy levels between the trap levels and the conduction band of the oxide. This also results in a smaller estimated value of the trap ionization energy from PF modelling.

### 3.5f Fowler-Nordheim tunnelling through the $\text{La}_y\text{Zr}_{1-y}\text{O}_x$ films

The main high electric field leakage current mechanism through  $\text{La}_2\text{O}_3$  films grown using different techniques is mostly Fowler-Nordheim (FN) tunnelling [30,32], although Poole-Frenkel conduction also has been assigned as a reason [33].  $\text{La}_2\text{O}_3$  has a conduction band offset (CBO) of 2.3 eV with silicon, and therefore the valence band offset (VBO) with silicon is 2.6 eV [34]. The band-offset conditions for  $\text{ZrO}_2$  and  $\text{La}_2\text{O}_3$  are illustrated in Fig. 3.28.

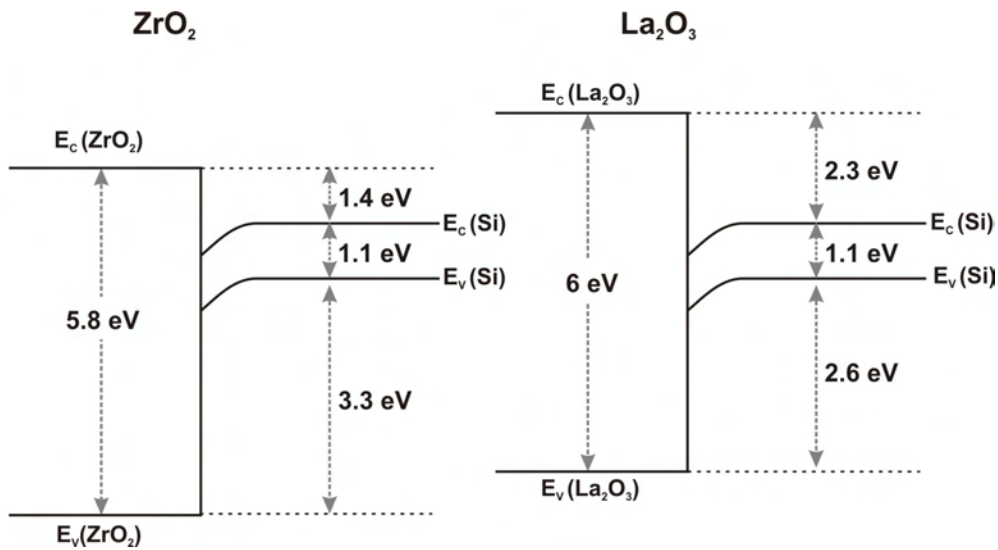


**Fig. 3.28.** Conduction and valence band offsets of  $\text{ZrO}_2$  and  $\text{La}_2\text{O}_3$  with silicon. This figure illustrates only the band offsets of the oxide with silicon, without taking the oxide band bending into account.

Since the CBO is lower than VBO in both  $\text{La}_2\text{O}_3$  and  $\text{ZrO}_2$ , the leakage currents at higher electric fields is more due to the Fowler-Nordheim (FN) tunnelling of electrons than by the tunnelling of holes. FN plots for  $\text{Al}/\text{La}_y\text{Zr}_{1-y}\text{O}_x/\text{Si}$  devices are given in Fig. 3.29.

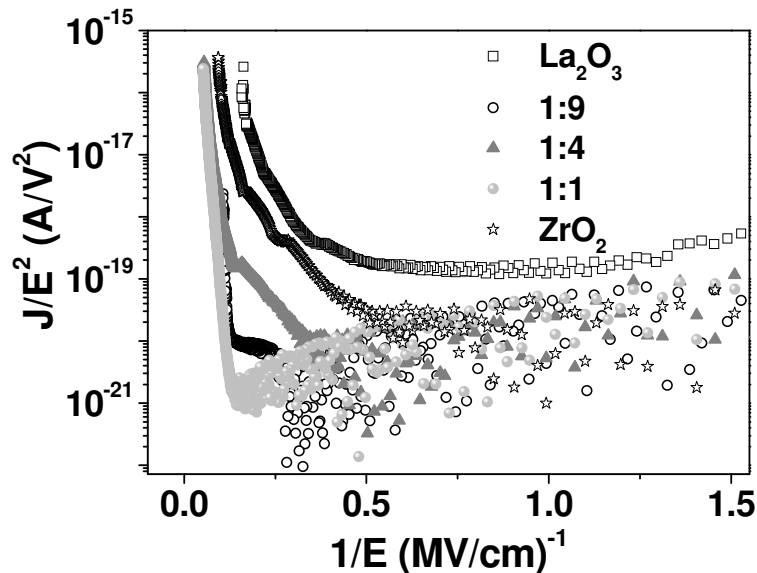


**Fig. 3.29.** FN plots of  $\text{Al}/\text{La}_y\text{Zr}_{1-y}\text{O}_x/\text{Si}$  as-deposited devices.

The leakage behaviour in these films appears to follow Fowler-Nordheim behaviour. But to estimate the barrier heights accurately, one has to employ an effective electron mass ( $m^*$ ) in

the oxide. The discussion about the accuracy of barrier heights obtained from the slopes of normal FN plots is rather conflicting because of two reasons which are explained below.

Firstly, the effective mass can be estimated accurately only for a crystalline material, since the apparent mass of an electron arises due to the interaction with a periodic crystal lattice and therefore influenced by the phonon drag and the interaction with other electrons in the system. The material system considered in this chapter is far from being ideal to derive a consistent effective mass:  $\text{La}_2\text{O}_3$  and  $\text{La}_y\text{Zr}_{1-y}\text{O}_x$  are amorphous, and  $\text{ZrO}_2$  is polycrystalline. The barrier height estimation in literature uses effective masses of (single) crystalline materials. There is a certain uncertainty in literature values as well. For instance,  $m^* = 0.15 m_0$  [30], and  $0.26 m_0$  [35, 36] are reported for  $\text{La}_2\text{O}_3$  thin films. With the band-offset picture given in Fig. 3.25, and considering the work function of TiN to be 4.5 eV at room temperature, the TiN- $\text{La}_2\text{O}_3$  barrier height should theoretically be 2.75 eV. Using this value in the FN equation, the effective mass of electron will be  $0.01 m_0$ . Following the same arguments, TiN- $\text{ZrO}_2$  barrier height should be 1.85 eV, which yields an effective mass of  $0.14 m_0$  in  $\text{ZrO}_2$ .

Second reason is that for a given electric field, the effective barrier height is always lower by a factor of  $\sqrt{q^3 E_{ox} / 4\pi\epsilon_0\epsilon_r}$  as shown in Fig. 3.19, due to Schottky barrier lowering. That implies that the barrier height decreases continuously with the applied field. There is an additional barrier lowering due to temperature, which is in fact not included in the original FN equation.

The leakage current through the dielectric is determined by the tunnel barrier height and the electric field together. This can be explained using a single parameter called the tunnel width, the distance to which the electrons are injected into the oxide. The tunnel width (which is the effective thickness for tunnelling due to the bending of the oxide conduction band) is given by  $d_{eff} = \phi_b / qE_{ox}$ , [37]. For the TiN/ $\text{La}_2\text{O}_3$  system,  $\phi_b = 2.75$  eV and for the TiN/ $\text{ZrO}_2$  system  $\phi_b = 1.85$  eV. But the effective tunnel width is estimated to be  $\sim 8$  nm for both 13 nm  $\text{La}_2\text{O}_3$  and 22 nm  $\text{ZrO}_2$  thin films at the same applied bias of 5 V, which means that the leakage due to tunnelling would be much higher for the TiN/ $\text{ZrO}_2$ /Si devices comparing to TiN/ $\text{La}_2\text{O}_3$ /Si devices. Leakage will be even higher with Al electrodes, since the Al work-function of 4.25 eV is lower than TiN (4.5 eV) [38, 39].

### 3.5g Electrical Breakdown and Stress Induced Leakage Current characteristics of the $\text{La}_y\text{Zr}_{1-y}\text{O}_x$ thin films

One of the main characteristic properties of dielectric materials, which is as important as the dielectric constant or leakage current behaviour, is the breakdown voltage ( $V_{bd}$ ) or the breakdown field ( $E_{BD}$ ). As discussed in Chapter 1, an empirical law exists between the dielectric breakdown field and the dielectric permittivity ( $k$ ) given by

$$E_{BD} = \frac{20}{\sqrt{k}} [MV / cm] \quad (3.19).$$

Though this is an empirical model, several binary oxides have been shown to obey a similar trend [40], which means that the usage of a dielectric with a higher  $k$ -value has the disadvantage of early breakdown.

In order to understand the breakdown phenomena of oxides under an applied electric field, several models have been proposed in the past. The hard breakdown of oxides is usually avalanche breakdown induced by the hot electrons or holes passing through the oxide. When electrons pass through the oxide layer under an applied electric field, defects such as traps, interface states, and positively charged donor-like states etc. accumulate gradually in the oxide, until a critical defect density is reached, when the oxide destructively breaks down. This critical defect density is approximately  $5 \times 10^{13} / \text{cm}^2$  in oxides thicker than 5 nm [41]. At these defect densities, nanometre-long conductive filaments – percolation paths – form in the oxide initiating the final breakdown of the device. When the oxide thickness is diminished to the typical defect size for that material, generation of a single defect in the oxide is sufficient to cause electrical breakdown of the entire film. For the oxide breakdown, Degraeve et al. report a typical defect diameter of 0.5 nm [42] and Nicollian et al. report the defect size of the order of 0.4 nm [43].

The dominant charge transport mechanism at electric fields larger than  $\sim 3$  MV/cm is Fowler-Nordheim tunnelling. Quantum mechanical tunnelling is a non-destructive mechanism in principle, but it often generates defects in the oxide. The charge transport from one electrode to the other can be either tunnelling, or transport through the conduction band of the oxide. Tunnelling is an elastic process by definition. Charge transport through the conduction band can be either elastic or inelastic, or ballistic tunnelling, without losing the energy of the charges. In a ballistic process, the net energy of the charges can be higher than the initial

energy when they reach the anode, since the transported carriers do not have collisions with atoms or lattices under an applied electric field.

In an inelastic process, this charge scattering primarily excites the longitudinal phonon modes of the (crystalline) oxide lattice [44,45]. At higher electric fields, the energy gained by the charge carriers by accelerating through the electric field is balanced by the energy lost into the acoustic phonon modes of the oxide.

Apparently, inelastic tunnelling, also known as *steady-state FN tunnelling*, is a dissipative charge transport process that can initiate oxide degradation. However, several breakdown models have been proposed to explain the oxide degradation and time dependent dielectric breakdown (TDDB) experiments are regarded as standard ways to test these models. Two important field-based models in this category are the  $I/E$  model and the E-model.  $I/E$  model assumes that the major cause of oxide breakdown is generation of holes and the breakdown occurs when a critical hole-fluence has passed through the oxide [46]. These holes are generated by the impact ionization [44] in the oxide due to tunnelling of electrons through it, or due to the energy release of the tunnelling electrons at the oxide-anode interface. In the latter case, the holes generated at the interface tunnel back to the oxide, degrading the oxide.

The E-model is basically a thermochemical model and was originally an empirical model proposed by Anolick in 1979 [47]. This was later on described on the basis of thermodynamics [48,49]. In this model, the time taken for 50% of the device breakdown (termed as  $t_{50}$ ) can be expressed as

$$t_{50} = A \exp(-\gamma E) \exp\left(-\frac{\Delta E}{kT}\right) \quad (3.20)$$

Here,  $\gamma$  is the acceleration parameter in the accelerated breakdown experiments (the slope of the  $\log(t_{BD})-E$  curves),  $A$  is a constant,  $E$  is the electric field in the oxide,  $k$  is the Boltzmann constant and  $\Delta E$  is the activation energy of defect generation.

The electric field models are important to estimate the reliability of the devices in the accelerated tests usually termed as time-dependent dielectric breakdown (TDDB) tests. As mentioned before, the  $I/E$ -models of oxide breakdown assume that dielectric breakdown is a current driven process, caused by tunnelling of the charge carriers such as hot holes injected from the anode (called the Anode Hole Injection model – AHI) due to the energy release of tunnelling electrons at the oxide-anode interface [50]. Since the current driving mechanism is mainly FN tunnelling, the expression for  $t_{50}$  has a  $I/E$  dependence and is given by

$$t_{50} = \tau_0 \exp\left(\frac{G}{E}\right) \exp\left(-\frac{\Delta E}{kT}\right) \quad (3.21)$$

where  $\tau_0$  and  $G$  are constants. [51,52].

In this chapter, we do not concentrate on TDDDB measurements and the validity of the field-based models. However, we will be returning to this discussion later on in this chapter while discussing the stress-induced leakage current (SILC) measurements influencing the dielectric breakdown behaviour.

In  $I$ - $V$  measurements, the leakage current is monitored while the voltage is swept in a given range. This is a comparatively quick experiment, where the accumulation of defects occurs in a short timescale and the average breakdown electric field ( $E_{BD}$ ) can be estimated from the breakdown voltages. The average breakdown electric fields measured for  $\text{La}_y\text{Zr}_{1-y}\text{O}_x$  thin films with different Zr contents are given in Fig. 3.30. The breakdown fields of pure  $\text{La}_2\text{O}_3$  and  $\text{ZrO}_2$  are comparatively lower than the mixed oxide films.

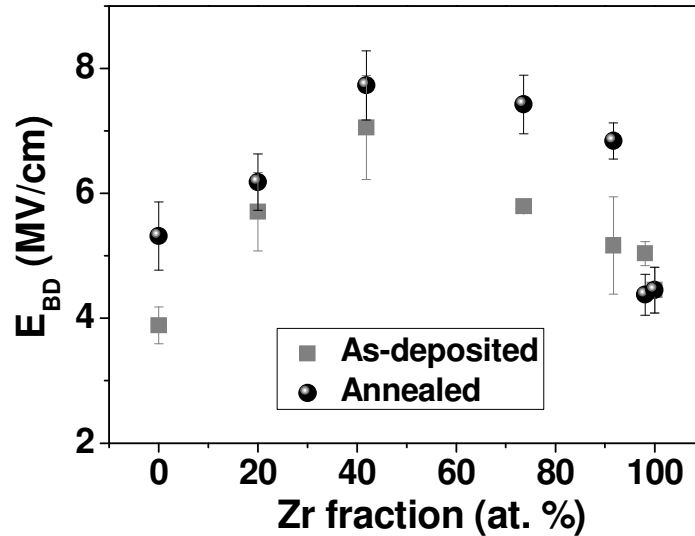


**Fig. 3.30.** Breakdown electric field ( $E_{BD}$ ) of the films as a function of the Zr content in the films.

Upon observing from pure  $\text{ZrO}_2$  films, there appears to be a clear trend of increasing breakdown field with decreasing Zr percentage. This result is puzzling because this trend is not explicitly related to the La% in the film, because the film that contains 80 at.% and 100 at.% La have lower breakdown fields compared to, for instance, a film that contains 60 at.% La. Therefore, it is postulated that this breakdown enhancement of the mixed films is related to the  $\text{ZrO}_2$  cluster formation in the films. Fig. 3.31 demonstrates the relation between

$E_{BD}$  and the  $\text{ZrO}_2$  cluster size in the films (estimated from the XRD experiments using Debye-Scherrer formula described in Chapter 2).

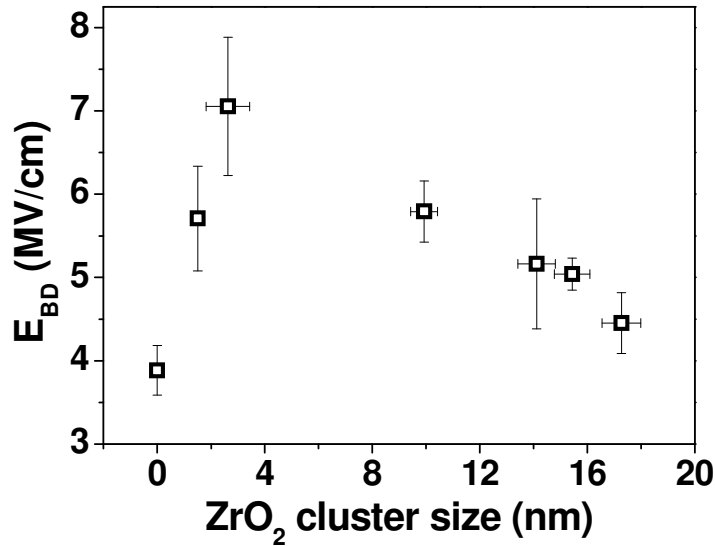


*Fig. 3.31.*  $E_{BD}$  of the as-deposited films as a function of the  $\text{ZrO}_2$  cluster size in the thin films.

An apparent trend in Fig. 3.31 is that the breakdown field ( $E_{BD}$ ) scales linearly with the  $\text{ZrO}_2$  cluster size in the films. The  $\text{La}_2\text{O}_3$  film and the  $\text{La}:\text{Zr} = 12:1$  film with 20 at% Zr do not have a clear crystalline phase, but the cluster size means short-range order in these films. This result illustrates that density of  $\text{ZrO}_2$  crystals embedded in  $\text{La}_2\text{O}_3$  matrix could be the determining factor for breakdown fields of these films.

Two different scenarios that can be proposed to explain the enhancement of  $E_{BD}$  based on the presence of the  $\text{ZrO}_2$  clusters are as follows:

1. The charging of the  $\text{ZrO}_2$  clusters of their interface with  $\text{La}_y\text{Zr}_{1-y}\text{O}_x$ , which screens the electron tunnelling through the films.
2. Increase in the percolation path of defect formed due to the electron tunnelling through the oxide.

It is known that when an electric field is applied across a laminated stack of two different dielectrics with different conductivities, charges accumulate at the interface of the dielectric with lower conductivity; an effect known as Maxwell-Wagner instability [53]. The nanocrystalline  $\text{ZrO}_2$  clusters embedded in an amorphous  $\text{La}_y\text{Zr}_{1-y}\text{O}_x$  matrix forms several interfaces where charges could accumulate, creating partially charged clusters that screen the

incoming electrons due to Coulomb repulsion. Similar charge trapping has been shown to occur at the interface of  $\text{ZrO}_2$  particles artificially embedded in a conducting polymer matrix [54]. Even though  $\text{ZrO}_2$  is more conductive than  $\text{La}_2\text{O}_3$  as evident from the leakage measurements shown in Fig. 3.24, the drop of leakage current in the  $\text{La}_y\text{Zr}_{1-y}\text{O}_x$  films indicates that the embedding of nanocrystalline  $\text{ZrO}_2$  clusters results in less conductive films than bulk  $\text{ZrO}_2$ . Even in Zr-rich  $\text{La}_y\text{Zr}_{1-y}\text{O}_x$  films with elongated  $\text{ZrO}_2$  crystals perpendicularly oriented to the surface the leakage current remains significantly lower than in pure  $\text{ZrO}_2$  films. This could be an indication for electron transport along the grain boundaries and electron trapping at the  $\text{ZrO}_2$  and  $\text{La}_y\text{Zr}_{1-y}\text{O}_x$  interfaces [55].

In order to understand the role of the embedded  $\text{ZrO}_2$  nanoclusters, electric field simulations were carried out using a COMSOL Multiphysics® program [version 3.5a]. The results are depicted in Fig. 3.32(a), where two separate conditions were assumed: Case (A) shows the situation where the dielectric film mimics the film with tetragonal  $\text{ZrO}_2$  clusters embedded in a  $\text{La}_y\text{Zr}_{1-y}\text{O}_x$  matrix. In the simulation program, the dielectric clusters with a dielectric constant of 36 are embedded in a medium of  $k = 27$ . Top electrode is positively biased and bottom electrode is grounded in the simulations. The electric field lines appear to have preferential paths through the  $\text{La}_y\text{Zr}_{1-y}\text{O}_x$  matrix with a tendency to evade the nanoclusters, which is consistent with the hypothesis that the percolation paths are longer in these films than in a regular dielectric film.

To check the consistency of the simulation, the same film morphology with very leaky (*conducting*) clusters were investigated as well. As expected, the electric field lines in these films shortcut through the clusters, as shown in Fig. 3.32 (b). Such films will have a large effective dielectric constant, but will exhibit large leakage currents and relatively lower dielectric breakdown fields than the normal dielectric films.



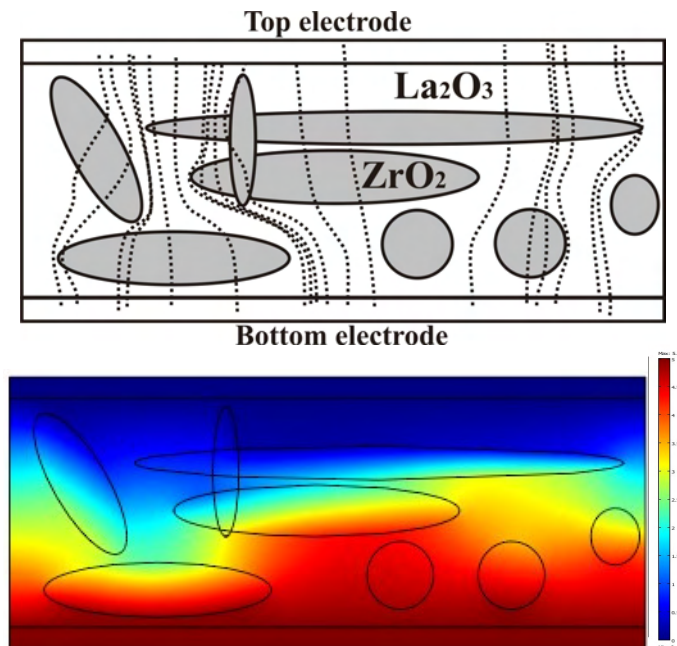


**Fig. 3. 32 (a).** Electric field (above) and potential (below) simulation of a dielectric film with embedded dielectric nanoclusters using COMSOL® program. A dielectric matrix layer ( $k \sim 27$ ) with dielectric clusters of  $k \sim 36$  is used for the simulation. Upper figure is the electric field lines and lower figure shows the electric field distribution in the film. Blue is the minimum and red is the maximum electric field.

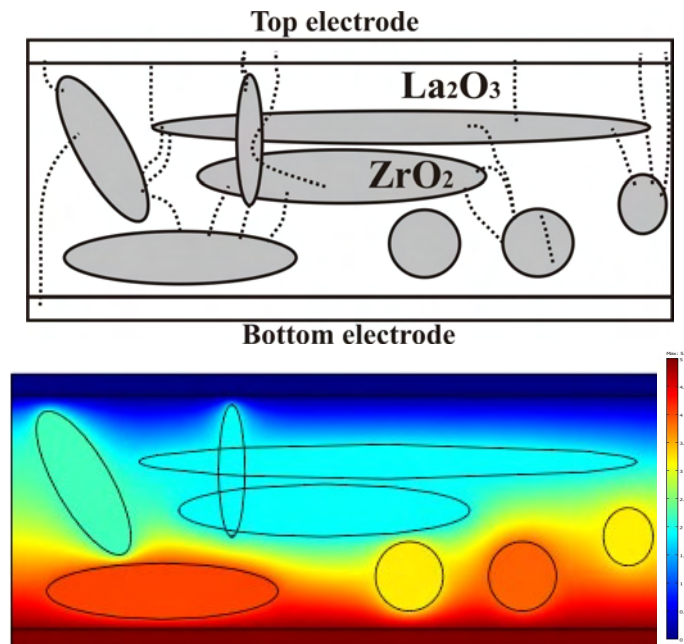


**Fig. 3. 32 (b).** Electric field (above) and potential (below) simulation of a dielectric film with embedded conducting nanoclusters using COMSOL® program. A dielectric matrix layer ( $k \sim 27$ ) with clusters of  $k \sim \infty$  is used for the simulation.

### 3.5h ‘Best-can-do’ performance of the $\text{La}_y\text{Zr}_{1-y}\text{O}_x$ thin films

The breakdown field and the  $k$ -values seem to follow a linear relationship as is shown in Fig. 3.33 which is in contrast to the linear relationship between  $E_{BD}^2$  and  $k$  as predicted by Eqn. 3.19.

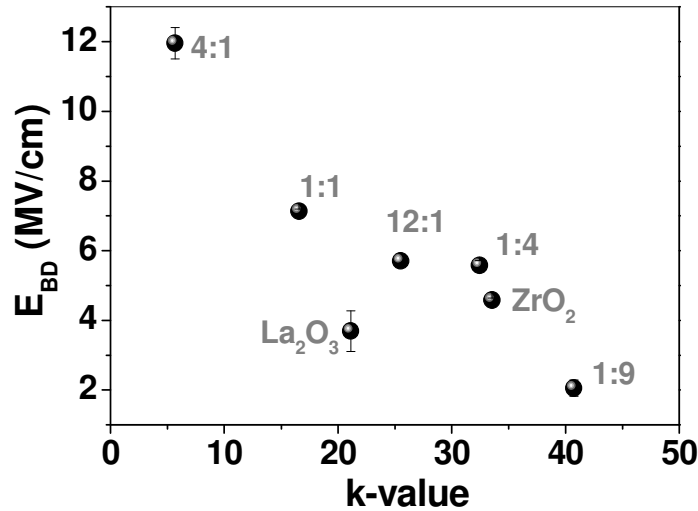


Fig. 3.33. Breakdown electric field versus dielectric permittivity of the devices with  $\text{La}_y\text{Zr}_{1-y}\text{O}_x$  thin films.

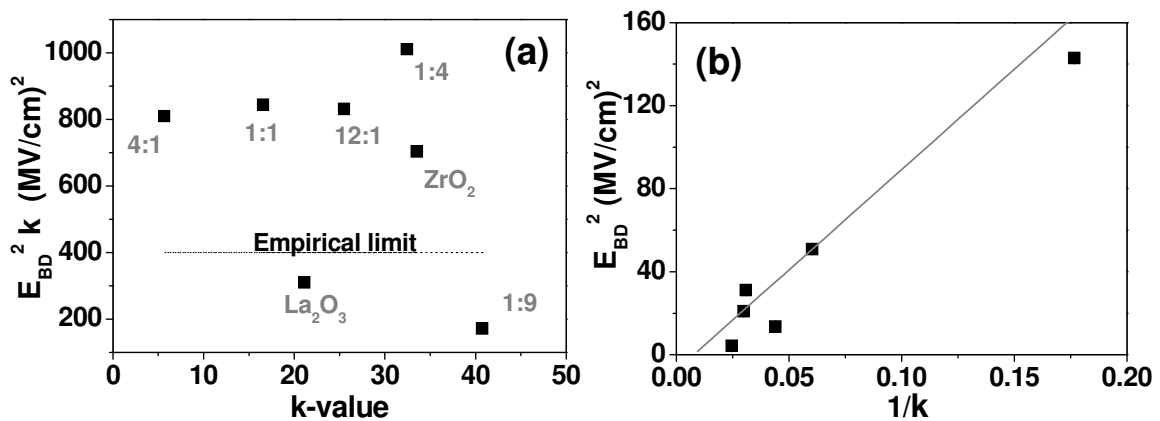


Fig. 3.34. (a) The performance limit set by the empirical law (Eqn. 3.19) and (b) empirical limit obtained for the devices with  $\text{La}_y\text{Zr}_{1-y}\text{O}_x$  thin films.

As per Eqn. 3.19, the maximum empirical performance of a dielectric is at  $E_{BD}^2 k = 400 (\text{MV/cm})^2$ , but Fig. 3.34 (a) shows that all mixed  $\text{La}_y\text{Zr}_{1-y}\text{O}_x$  films exhibit  $E_{BD}^2 k$  values well above  $400 (\text{MV/cm})^2$  except for the film with La:Zr = 1:9. The exact empirical relationship for these samples is depicted in Fig. 3.34 (b), which gives a slope of  $\sim 966 (\text{MV/cm})^2$ . This means that for the ternary  $\text{La}_y\text{Zr}_{1-y}\text{O}_x$  films, the relationship is

approximately  $E_{BD} = 31(MV/cm)/\sqrt{k}$ .

### 3.5i Scanning Kelvin probe microscopy of the $\text{La}_y\text{Zr}_{1-y}\text{O}_x$ thin films: additional evidences

The presence of Zr-rich clusters may result in local differences in surface potential, particularly if they are charged intrinsically or after biasing. The surface potential was measured with scanning Kelvin probe microscopy (SKPM) (also called scanning surface potential microscopy, SSPM, or scanning Kelvin force microscopy, KFM). With this technique a potential (ac + dc) is applied to a conductive probe that is moving above the sample surface. The DC voltage is adjusted such that the force between probe and sample is zero; the resulting DC value equals the surface potential. The measurements were performed with a Veeco Dimension 3100 scanning probe microscope (the same instrument as used for the surface roughness measurements, cf. Section 3.3) placed in a nitrogen-flushed glove box, using conductive Pt/Ir-coated (Veeco SCM-PIT) and Co/Cr-coated (Veeco MESP) Si probes. During the surface potential measurement the probe was kept at a fixed height of 10 nm above the surface. Because of the distance between the probe and the surface during the potential measurement the lateral resolution of this measurement is lower than that of the topography and conductivity measurements. The selected samples were with La:Zr pulse ration of 1:1, 4:1, and 12:1, which have 10 nm and 2.6 nm clusters and 1.5 nm short-range ordering respectively. The choice of the samples also had to be based on comparable thickness of the layers, because the SKPM signal is thickness dependent. The films were kept overnight in nitrogen ambient and were heated to 125°C for 30 minutes in order to remove any water absorbed onto the surface.

The initial Kelvin probe morphological scans were not very conclusive because of the low resolution of the technique in imaging and the low resistivity of the films. Therefore, any surface potential variation was not apparent from the images for these samples. As an additional step, we tried to deliberately charge the clusters by applying an electric field to specific spots. To perform this experiment, a conductive probe was brought into contact with the sample surface and a certain potential (in the range of -12 V to +12 V) was applied for some time (6 s to 600 s depending on the voltage) to the probe. After releasing the probe, the surface potential was measured using the same probe, which yielded the images shown in Fig. 3.35.

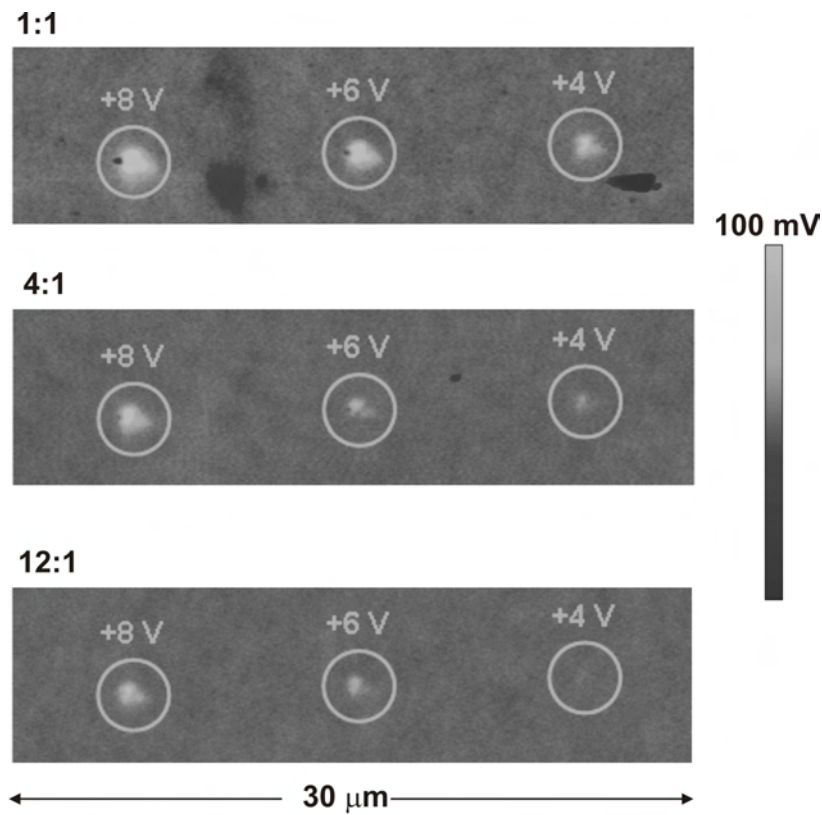


*Fig. 3.35. Surface potential scans after applying the indicated bias voltages on selected areas of the samples with La:Zr = 1:1, 4:1 and 12:1.*

As evident from Fig. 3.35, all samples exhibit noticeable charging (increased surface potential) in the film, which is largest for the sample with La:Zr = 1:1 for the same duration and magnitude of the electric field. Fig. 3.36 shows the variation of the measured surface potential as a function of the applied bias on the probe-tip.

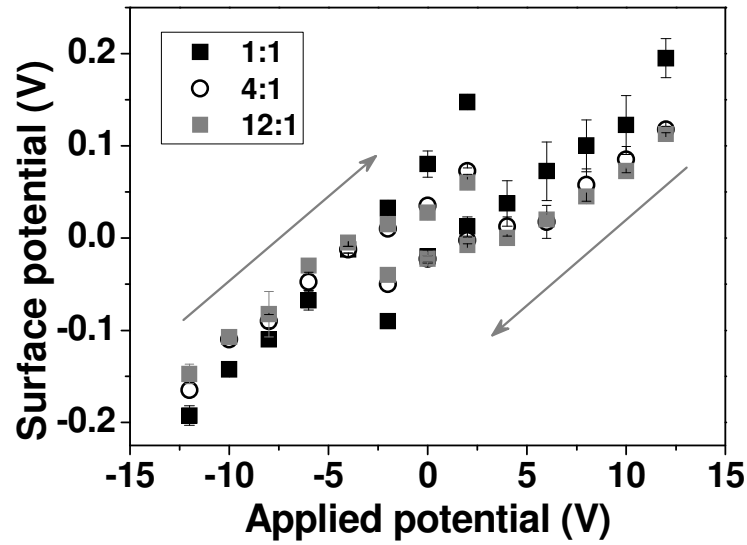


*Fig. 3.36. Surface potential variation of the films as a function of the bias voltage applied on the probe-tip. The arrows give the sweep direction of the applied potential on the probe-tip.*

The surface potential variation with the applied bias has a larger slope for the sample with  $\text{La}:\text{Zr}=1:1$ . The slope of these curves can be called fractional charging of the clusters, since the surface potential variation between two applied voltages gives the number of charges induced in the film.

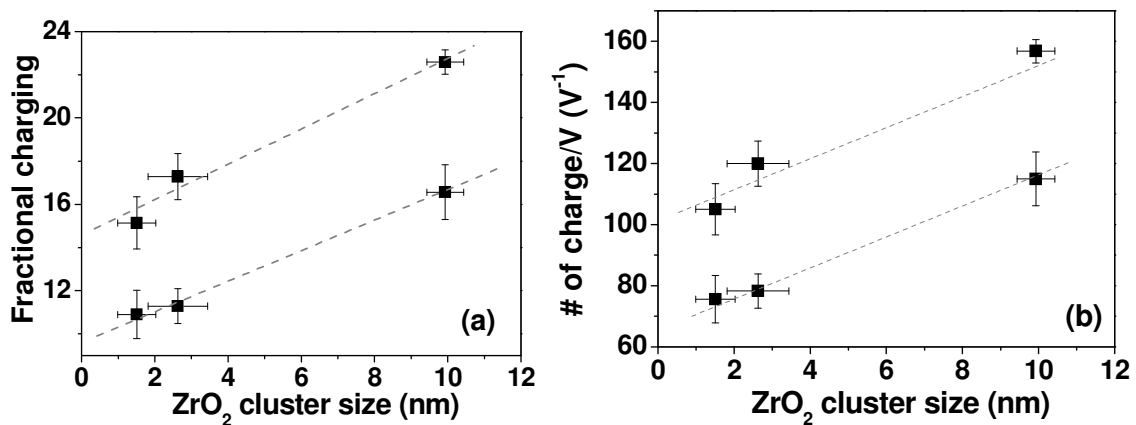


*Fig. 3.37. (a) The (dimensionless) fractional charging defined as the change in surface potential per unit increase in the applied voltage for positive (upper set) and negative bias (lower set) sweeps; (b) estimated number of induced charge per applied bias voltage.*

Fig. 3.37 (a) gives the fractional charging of the films as a function of the  $\text{ZrO}_2$  cluster size and (b) is a crude estimate of the number of charges per unit increase in bias voltage estimated

using Gauss' law ( $Q = \epsilon_0 \oint_S E dA$ ). The fact that the slope of the fractional charge shown in Fig. 3.37 (a) is larger for positive bias sweep and the zero-bias surface potential extrapolated from the positive and negative voltage sweeps is higher for positive sweeps indicates that the induction of the positive charge is easier in these clusters. This correlates well with the interface trapping behaviour of the  $\text{La}_2\text{O}_3$ - $\text{ZrO}_2$  system discussed in this chapter.

This charging behaviour of the clusters can be demonstrated on a global scale using leakage current measurements as well. Fig. 3.38 shows the  $J$ - $E$  characteristics of the film with  $\text{La}:\text{Zr} = 1:1$ , where the leakage current density is plotted as a function of the forward and reverse electric field sweep.

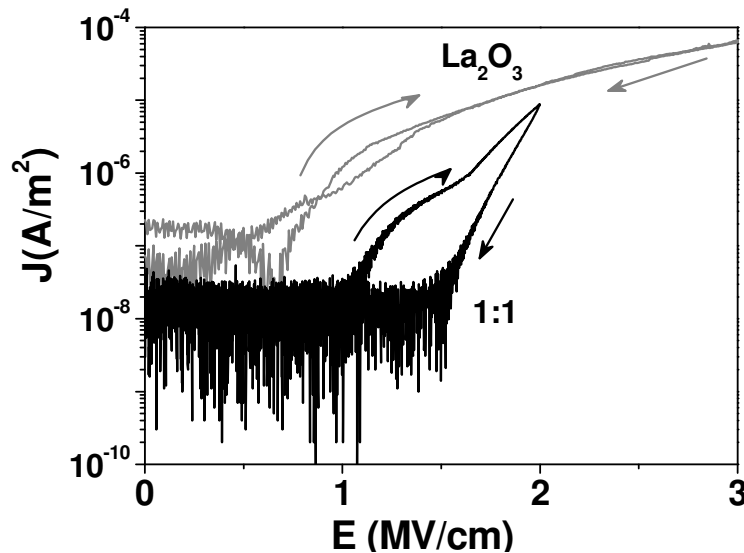


*Fig. 3.38. Hysteresis in  $J$ - $E$  loop observed in the  $\text{La}:\text{Zr} = 1:1$  sample. The  $J$ - $E$  loop of  $\text{La}_2\text{O}_3$  has been given for comparison, which shows no hysteresis.*

The hysteresis observed in the sample with  $\text{La}:\text{Zr} = 1:1$  is presumably due to the charging of the  $\text{ZrO}_2$  nanoclusters or its interface with  $\text{La}_y\text{Zr}_{1-y}\text{O}_x$ , because pure  $\text{La}_2\text{O}_3$  does not exhibit a significant hysteresis. Also, it is worth mentioning that all the mixed films show similar hysteresis behaviour.

### 3.5j Time dependent dielectric breakdown in $\text{La}_y\text{Zr}_{1-y}\text{O}_x$ thin films

As discussed in section 3.5.7, the dielectric breakdown occurs when the defect density in an oxide reaches a critical value. When the electric field in the oxide is high enough, defects accumulate over time and the device finally breaks down. At a given voltage across the

electrodes, the time until the oxide breaks down is known as time-to-breakdown ( $t_{BD}$ ) and the critical defect density for the final breakdown of the device is explicitly linked to the total charge passed through the oxide layer until it breaks down destructively. This total charge passed through the device until the critical defect density is reached is known as the charge-to-breakdown or  $Q_{BD}$  given by

$$Q_{BD} = \int_0^{t_{BD}} I(t) dt \quad (3.22)$$

where  $I(t)$  is the leakage current measured at the fixed stress voltage.  $Q_{BD}$  is usually determined by applying a fixed voltage across the capacitor electrodes and measuring the stress current through the device until it breaks down. This method is generally known as constant voltage stress (CVS) measurement.

Generally,  $Q_{BD}$  has been shown to have strong thickness dependence below 5 nm for silicon oxide, where the electric field models of breakdown do not apply [56], and has strong polarity dependence suggesting that the breakdown in the oxides is determined by the applied voltage-driven maximum energy of the charge carriers, not their electric-field-driven average energy [57]. For the same reason,  $Q_{BD}$  has a strong dependence on the applied voltage across the electrodes. At larger magnitude of the leakage currents (at voltages close to the breakdown voltage), the number of electrons with sufficient energy to induce defects in the oxide are large enough to initiate the avalanche breakdown in the oxide and measurement at these voltages give erroneous  $Q_{BD}$  values. The correct estimation of this parameter would be at voltage low enough to induce defect accumulation instead of avalanche breakdowns. Therefore, if  $Q_{BD}$  is plotted against the leakage current density ( $J$ ), the data points are distributed in two branches, one where the avalanche breakdown dominates and  $Q_{BD}$  vary with  $J$ , and another branch where  $Q_{BD}$  is steady and independent of  $J$ . Fig. 3.39 shows the distribution of  $Q_{BD}$  with  $J$  measured for  $\text{Al}_2\text{O}_3$  [58]

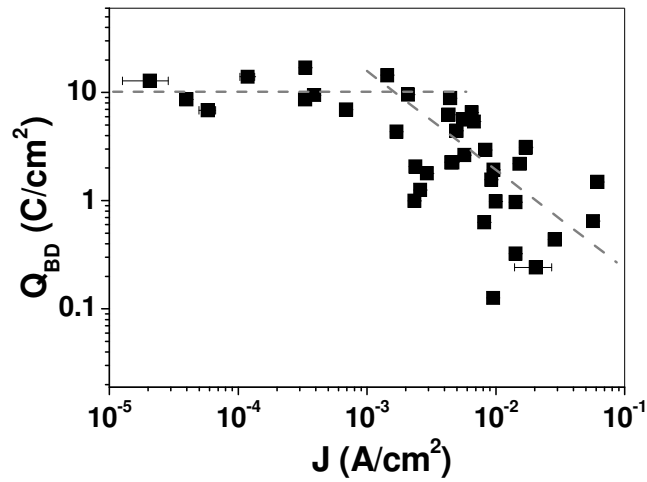


**Fig. 3.39.** Distribution of  $Q_{BD}$  against the leakage current ( $J$ ) at different voltages measured for ALD processed  $\text{Al}_2\text{O}_3$ .

The CVS measurements on the  $\text{La}_y\text{Zr}_{1-y}\text{O}_x$  samples were performed at voltages low enough to measure reliable  $Q_{BD}$  values. The stress current measured for sample with different Zr content is shown in Fig. 3.40.

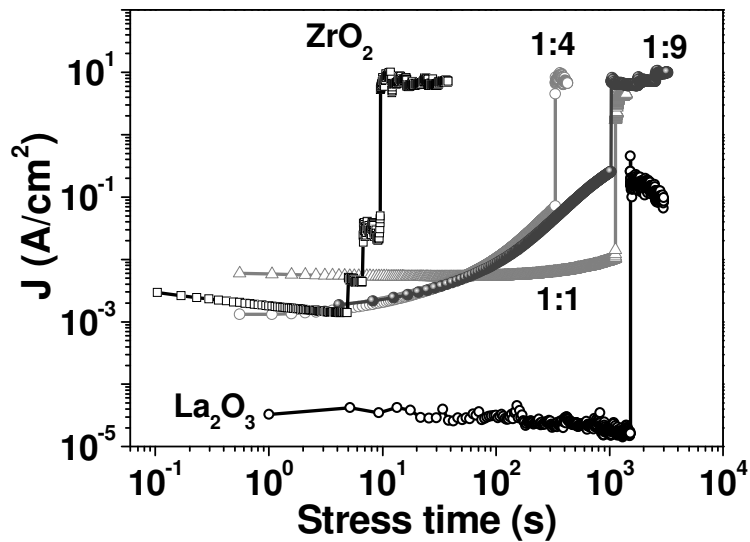


**Fig. 3.40.** Stress current measured for different films at the same electric field of 5 MV/cm.

Figure 3.41 shows the  $Q_{BD}$  values obtained for different as-deposited films as a function of the Zr content.  $\text{La}_2\text{O}_3$  films have the lowest leakage current and the hardest breakdown.



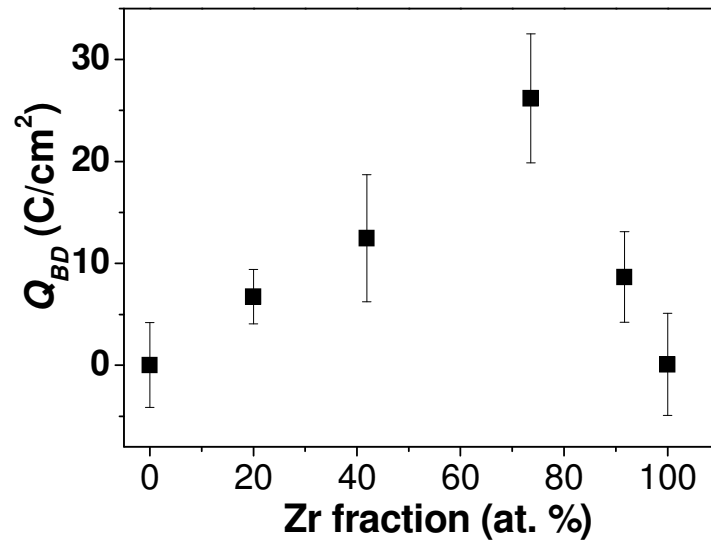


*Fig. 3.41. Charge-to-breakdown ( $Q_{BD}$ ) estimated from SILC measurements for as-deposited films with different Zr fraction.*

In order to estimate the  $Q_{BD}$  values, the leakage current until the first breakdown was integrated over time.  $\text{ZrO}_2$  film exhibit multiple breakdowns as seen in Fig. 3.40, while  $\text{La}_2\text{O}_3$  films has hard breakdown, but still not reaching the measurements limits. CVS studies on ultra thin  $\text{La}_2\text{O}_3$  films deposited using electron-beam-evaporation indicate that such multiple breakdowns are possible in these films as well [32]. But differing from the SILC trends of  $\text{La}_2\text{O}_3$  or  $\text{ZrO}_2$  films, the mixed oxides exhibit a positive slope in leakage current, which indicates the growing charge trapping in the oxide due to the defects generated by the tunnelling electrons. Thus, unlike the  $\text{La}_2\text{O}_3$  or  $\text{ZrO}_2$  films that do not exhibit significant charge trapping in the films, the mixed oxides show significant defect generation and electron trapping in the oxide. We could understand from the electric field simulations that the field lines propagate around the  $\text{ZrO}_2$  nanoclusters, or preferably along the  $\text{ZrO}_2$ -  $\text{La}_y\text{Zr}_{1-y}\text{O}_x$  interface. Therefore, the defects could be originating at the interfaces of the nanoclusters, which are the most likely locations of interface imperfections and charge trapping.

### 3.6 Discussion and Conclusions

This Chapter mainly examines the dielectric characteristics of capacitor devices comprised of as-deposited and annealed  $\text{La}_y\text{Zr}_{1-y}\text{O}_x$  films. The  $C$ - $V$  measurements reveal that the dielectric

constants of the films increases with the Zr content in the film, which is attributed to the stabilization of a high permittivity tetragonal phase of the embedded  $\text{ZrO}_2$  nanoclusters.

The fixed oxide charges in the oxide estimated from the flat-band voltage measurements of the annealed samples indicate that the band bending is due to positive charges in the oxide. Generally the fixed oxide charges are located in the oxide close to the silicon-oxide interface, but on the other hand, the positive charges in these films are more possibly originating from the interface between  $\text{ZrO}_2$  nanocrystals and amorphous  $\text{La}_y\text{Zr}_{1-y}\text{O}_x$  matrix. This hypothesis was supported by the observation that the film with 74% of Zr has the highest charge density in the film, and has the most distinguishable interface with  $\text{La}_y\text{Zr}_{1-y}\text{O}_x$  as per the TEM observations. On annealing, the interface state density of the film reduced to half the value of the fresh devices, meaning that the interfaces between the silicon (or the native oxide) and the  $\text{La}_y\text{Zr}_{1-y}\text{O}_x$  films have improved upon post-deposition anneal. From  $D_{it}$  measurements, it is not clear if the interface improvement is due to the formation of silicates by the reaction with the native silicon oxide, but the lower  $k$ -values of the films after RTA suggests possible silicate formation at the interfaces.

The signature of nanocluster formation was observed in the Arrhenius behaviour of the leakage current of the devices. Two different activation energies could be identified in the mixed oxide films that belong to the oxide material and their interface formation inside the oxide. Despite that the interface properties have been improved upon annealing, the trap density ( $N_t$ ) of the films estimated from the leakage current measurements in SCLC regime shows that the trap density in the films have increased significantly after annealing. This could be due to the diffusion of Ti into the oxide, formation of  $\text{TiO}_x$  at the TiN/  $\text{La}_y\text{Zr}_{1-y}\text{O}_x$  interface etc., but the slight reduction in the charge mobility after annealing shows that the oxide quality has been improved with annealing. The films have appreciable leakage currents at 2 MV/cm electric field and scales with the equivalent oxide thickness of the films as expected. The films exhibit Poole-Frenkel charge injection at voltages larger than the trap-filled limit voltage ( $V_{TFL}$ ), and the dynamic dielectric permittivity and the trap ionization energies could be estimated from the PF data plotting. Besides, the films exhibit Fowler-Nordheim tunnelling at larger electric fields.

The  $\text{La}_y\text{Zr}_{1-y}\text{O}_x$  films exhibit good dielectric breakdown electric fields, which show a fine correlation with the cluster size of the  $\text{ZrO}_2$  nanoparticles. Our electric field simulations

indicates that the electric field lines are curved due to the presence of the  $\text{ZrO}_2$  nanoclusters, and thus the percolation paths for the dielectric breakdown are longer than in normal films with uniform morphology. These films exhibit better dielectric performance than the performance limit set by the empirical rules.

The charge trapping behaviour of these films, especially at the interface between crystalline  $\text{ZrO}_2$  and amorphous  $\text{La}_y\text{Zr}_{1-y}\text{O}_x$  could be identified from various measurements, such as the surface potential measurements with the Kelvin probe and  $I$ - $V$  hysteresis measurements. With these characteristics, these nanocluster-embedded films are an excellent option for industrial applications such as high-density capacitance devices [59] and future options for memory devices [60], but may not be optimal for CMOS gate applications, where any memory effect in the device is not desirable.

### 3.7 References

1. P.A. Packan, *Science* **285**, 2079 (1999).
2. *International Technology Roadmap for Semiconductors, (Front-end process)*, Semiconductor Industry Association, 2009 Edition.
3. Y. Kado, Y. Arita, *J. Appl. Phys.* **61**, 2398 (1987).
4. C.J. Först, C.R. Ashman, K. Schwarz, P.E. Blöchl, *Nature* **427**, 53 (2003).
5. A. Ohtomo, D.A. Muller, J.L. Grazul, and H.Y. Hwang, *Nature* **419**, 378 (2002).
6. M. Fleetwood et al., *Microelectron. Reliab.* **35**, 403 (1995).
7. M. Alexe, *Appl. Phys. Lett.* **72**, 2283 (1998).
8. D.K. Schroder, *Semiconductor Material and Device Characterization*, Wiley-Interscience, Ed. 3, New Jersey (2006).
9. R. Fujitsuka et al., *J. J. Appl. Phys.* **44**, 2428 (2005).
10. J.-B. Cheng et al., *Appl. Surf. Sci.* **233**, 91 (2004).
11. J.F. Lønnum, J.S. Johannessen, *Electron. Lett.* **22**, 456 (1986)
12. R. Clerc et al., *Microelectronics Reliability* **41**, 1027 (2001).
13. A. Brar, G. D. Wilk, and A. C. Seabaugh, *Appl. Phys. Lett.* **69**, 2728 (1996).
14. F. Crupi et al., *Appl. Phys. Lett.* **80**, 4597 (2002).
15. Y.H. Wu et al., *Electron Device Lett.* **21**, 341 (2000).
16. S.J. Yun et al., *Electrochem. Solid-State Lett.* **10**, H90 (2007).
17. F.G. Allen, G.W. Gobeli, *Phys. Rev. B* **127**, 150 (1962).
18. K. Choi et al., *Thin Solid Films* **486**, 141, (2005).
19. R.L. Puurunen, *J. Appl. Phys.* **97**, 121301 (2005).
20. X. Zhao, and D. Vanderbilt, *Phys. Rev. B* **65**, 075105 (2002).
21. T.-M. Pan et al., *Electrochem. Solid-State Lett.* **10**, H101 (2007).
22. Y.H. Wu et al., *IEEE Electron Device Lett.* **21**, 341 (2000).
23. W.F.A. Besling et al., *J. Non-Cryst. Solids* **303**, 123 (2002).
24. D.H. Triyoso et al., *Appl. Phys. Lett.* **88**, 222901 (2006).
25. S.L. Miller et al., *J. Appl. Phys.* **70**, 4555 (1991).
26. S.M. Sze, *Physics of Semiconductor Devices*, Ed.2, Wiley Publications, New York, 1981.
27. J.H. Klootwijk, *Interpoly dielectrics for Non-volatile Memories*, PhD Thesis,

University of Twente, 1997.

28. J.G. Simmons, *J. Phys. D. Appl. Phys.* **4**, 613 (1971).
29. F.C. Chiu, H.W. Chou, J.Y. Lee, *J. Appl. Phys.* **97**, 103503 (2005).
30. S. Ramanathan, C.-M. Park, P.C. McIntyre, *J. Appl. Phys.* **91**, 4521 (2002).
31. R.H. Fowler, L. Nordheim, *Proceedings of the Royal Society of London*, **119**, 173 (1928).
32. E. Miranda, J. Molina, Y. Kim, H. Iwai, *App. Phys. Lett.* **86**, 232104 (2005).
33. B. Sen et al., *Solid-State Electronics* **51**, 475 (2007).
34. J. Robertson, *Integrated Ferroelectrics* **32**, 251 (2001).
35. E. Miranda, J. Molina, Y. Kim, H. Iwai, *J. Non-Crystalline Solids* **352**, 92 (2006).
36. Y. Yeo, T. King, C. Hu, *Appl. Phys. Lett.* **81**, 2091 (2002).
37. M. Lenzlinger, E.H. Snow, *J. Appl. Phys.* **40**, 278 (1969).
38. M.-T Wang, T.-H Wang, J.Y Lee, *Microelectronics Reliability* **45**, 969 (2005).
39. M.-T. Wang, T.-H. Wang, J.Y. Lee, *J. Electrochem. Soc.* **152**, G182 (2005).
40. P. Jain, E. J. Rymaszewski, *IEEE Transactions on Advanced Packaging*, **25**, 454 (2002).
41. D.J. DiMaria, E. Cartier, D. Arnold, *J. Appl. Phys.* **73**, 3367 (1993).
42. R. Degraeve et al., *IEDM Technical Digest*, 419 (2005).
43. P.E. Nicollian et al., *IEDM Technical Digest*, 743 (2006).
44. T.H. DiStefano, M. Shatzkes, *Appl. Phys. Lett.* **25**, 685 (1974).
45. W.T. Lynch, *J. Appl. Phys.* **46**, 998 (1975).
46. I.C. Chen et al, *Appl. Phys. Lett.* **49**, 669 (1996).
47. E.S. Anolick, G. Nelson, *Proceedings of the IEEE-IRPS* (IEEE, New York, 1979), Vol. 7, page. 8.
48. J.W. McPherson, D.A. Baglee, *Proceedings of the IEEE-IRPS* (IEEE, New York, 1985), Vol. 23, p. 1.
49. J.W. McPherson, D.A. Baglee, *J. Electrochem. Soc.* **132**, 1903 (1985).
50. K.F. Schuegraf, C. Hu, *Proceedings International Reliability Physics Symposium (IRPS)*, P.126, 1994.
51. J.W. McPherson, H.C. Mogul, *J. Appl. Phys.* **84**, 1513 (1998).
52. S-C. Chang, S.-Y. Deng, and J. Ya-M. Lee. *Appl. Phys. Lett.* **89**, 053504 (2006).

53. J.R. Jameson et al. *IEEE Trans. Electron Dev.* **53**, 1858 (2006)
54. A. Dey, S.K. De, *J. Appl. Polymer Sci.* **105**, 2225 (2007).
55. K.B. Jinesh et al., *Appl. Phys. Lett.* **93**, 062903 (2008).
56. G.M. Paulzen, *Microelectronic Engineering* **36**, 321 (1997).
57. P.E. Nicollian, *Physics of Trap generation and Electrical breakdown in Ultra-thin  $\text{SiO}_2$  and  $\text{SiON}$  gate dielectric materials*, PhD Thesis, Univerity of Twente, 2007
58. K.B. Jinesh, M. Matters-Kamerer, F. Rozeboom, J.H. Klootwijk (submitted)
59. K.B. Jinesh et al., *Appl. Phys. Lett.* **93**, 172904 (2008).
60. K.B. Jinesh, et al., *Method for forming a nanoclusters-comprising dielectric layer and device comprising such a layer*. Patent no. WO2009133500 (A1) (2009).



# Chapter 4

## Silicon out-diffusion in atomic-layer-deposited $\text{La}_y\text{Zr}_{1-y}\text{O}_x$ thin films

### 4.1 Introduction

One of the major concerns when the standard silicon oxide is replaced by high- $k$  oxides on silicon is the interface they create with the silicon surface [1]. Large-scale fabrication of the high- $k$  oxide films without an interfacial oxide layer is an enormous technological challenge, because epitaxial growth of such films on silicon is almost impossible due to lattice mismatch. Even when achieved, the proposed atomic structures of such abrupt interface between silicon and the high- $k$  films have been subjected to long discussions [1]. Especially in atomic layer deposition (ALD), the interfacial oxide formation is quite common and sometimes inevitable since the high- $k$  deposition is through a surface reaction. Post-deposition anneals to improve the interface properties of the devices often cause formation of thermodynamically stable silicates with lower  $k$ -values as well [2]. The reaction between the oxide and silicon is related to the thermodynamic stability between them. *Ono* and *Katsumata* suggested that the silicate formation between the high- $k$  rare-earth oxides and silicon is possibly due to the silicon out-diffusion from the substrate to the oxide [3]. Later, *Pan* and coworkers showed that the electrode material has a considerable influence on the silicon out-diffusion phenomenon though  $\text{La}_2\text{O}_3$  [4]. But the extent and the impact of silicon out-diffusion through the high- $k$  layers is not known yet. This Chapter is dedicated to study the silicon out-diffusion phenomena through the  $\text{La}_y\text{Zr}_{1-y}\text{O}_x$  films described in Chapter 2.

### 4.2 Case study on $\text{La}_2\text{O}_3$ with TOFSIMS

The influence of the electrode materials on the device properties of the metal/ $\text{La}_2\text{O}_3$ /Si system was examined using TOFSIMS, which provides compositional information of the films with nanometer resolution. These compositional depth profiles were acquired with TOFSIMS employing an ION-TOF-SIMS IV instrument in dual-beam mode. A major advantage of TOFSIMS is that it uses parallel acquisition; therefore the entire mass spectrum can be stored

at each cycle of the depth-profiling. Depth-profiles can be subsequently reconstructed from the raw data files and allows reconstructing a 3-dimensional stoichiometric map of the layers. This is ideal for detecting unknown contaminants at buried interfaces or for studying many elements simultaneously. TOFSIMS depth-profiling was performed using  $\text{Cs}^+$  ions as sputtering ions in negative mode (detection of negatively charged secondary ions).

Figure 4.1 gives the 3D TOFSIMS stoichiometric map of the as-deposited device, constructed by removing the layers successively by sputtering. For this purpose, 500 nm Al electrodes were sputter-deposited on  $\text{La}_2\text{O}_3$  layer and lithographically patterned to form electrodes. The thickness of the layers is not to the scale with the top electrode area; it is exaggerated due to the sputtering process (the top scan spans a region of  $76 \times 76 \mu\text{m}^2$  area on the capacitors, while the Al is 500 nm and  $\text{La}_2\text{O}_3$  is 14 nm). Fig. 4.1(a) shows the scan of the top aluminum electrode, showing the location of the silicon precipitates that appear as bright spots on the top surface. Fig. 4.1(b) shows the spikes of silicon from the substrate protruding through the oxide layer, that stretch out even through the top of the Al electrode. Fig. 4.1(c) is the La scan of the Al- $\text{La}_2\text{O}_3$  interface after sputtering the Al away. The interface appears to be very non-uniform. The 3D map in Fig. 4.1(d) shows that the interface of  $\text{La}_2\text{O}_3$  with silicon is very rough. Fig. 4.1(e) shows the scan of the top Al electrode surface constructed from the Al signal. 3D map of the device, reconstructed by the aluminum ions as shown in Fig. 4.1(f), demonstrates a bright top surface and a bright interface. The enhanced brightness on top surface and at the interface indicates that the aluminum present at the top and at the Al- $\text{La}_2\text{O}_3$  interface is in the form of aluminum oxide (most probably  $\text{Al}_2\text{O}_3$ ).



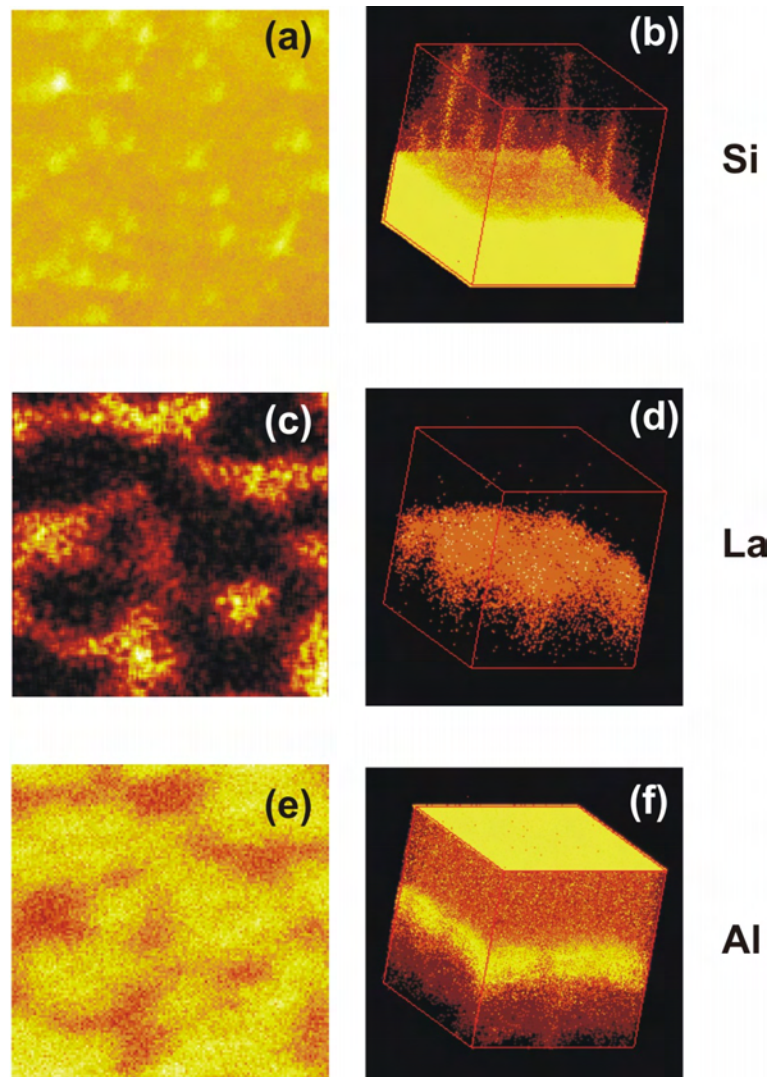


**Fig. 4.1.** TOF-SIMS images of Al/ $\text{La}_2\text{O}_3$ /Si devices. Top panel is Si signal with (a) top view of the Al electrode with  $76 \times 76 \mu\text{m}^2$  area and (b) 3D view of the device on right-hand side. Middle panel is La signal, (c) is top view after Al is completely sputtered away and (d) is the 3D view of  $\text{La}_2\text{O}_3$  thin film. Bottom panel is Al signal, (e) top view of the top Al electrode, (f) 3D image of the device with Al signal.

Figure 4.2 gives the depth profile of the Al/ $\text{La}_2\text{O}_3$ /Si device shown in Fig. 4.1(b), where the stoichiometric profiles of aluminum, silicon, lanthanum and oxygen are shown as a function of the sputter time. Strikingly, the aluminum and silicon signals extend beyond their interface with the  $\text{La}_2\text{O}_3$  layer, which shows that Al is diffusing into the  $\text{La}_2\text{O}_3$  layer, and silicon is diffusing out from the substrate through  $\text{La}_2\text{O}_3$ , towards Al electrode. (As shown in Chapter 2, The HRTEM images of the Al/ $\text{La}_2\text{O}_3$ /Si devices exhibit fuzzy Al/ $\text{La}_2\text{O}_3$  interface, where Al

seems to have diffused into  $\text{La}_2\text{O}_3$  layer). In contrast to the earlier observations by Pan et al. [4], the silicon atoms are not localized at the interface between Al and  $\text{La}_2\text{O}_3$ , but dissolve in Al and reach even the top electrode forming silicon precipitates on the electrode. In addition, the Al signal has a longer but steeper tail extending beyond the  $\text{La}_2\text{O}_3$ -Al interface, possibly indicating the formation of Al oxide at the interface. In addition, it is very likely that the silicon atoms diffused into the oxide have formed  $\text{LaSiO}_x$ .

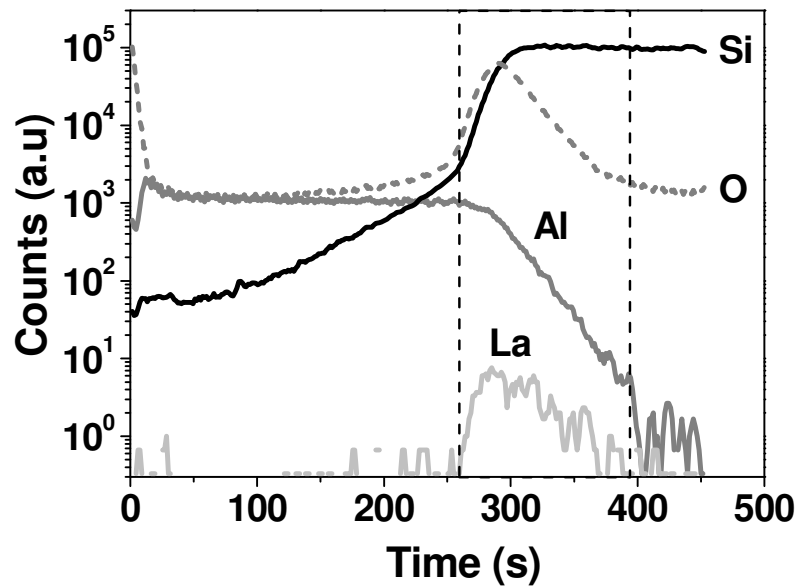


*Fig. 4.2. TOFSIMS depth profile of Al/ $\text{La}_2\text{O}_3$ /Si structures showing the ion counts of Al, La, O and Si. The dashed box roughly indicates the lanthanum oxide film.*

The TOFSIMS experiments demonstrate clearly that silicon diffuses through the  $\text{La}_2\text{O}_3$  oxide layer and 500 nm thick Al electrode. These silicon atoms form precipitates on the aluminum surface even at room temperature. Rare-earth metal oxides, in particular lanthanum oxide, have relatively larger ionic radii and larger coordination number in the solid comparing to other metal oxides. In other words, the film is less dense comparing to, say,  $\text{Al}_2\text{O}_3$ . This allows silicon out-diffusion from the substrate forming lanthanum silicate in the film [3].

When TiN is used as the top electrode instead of Al, the silicon spikes are not visible in these samples as shown in Fig. 4.3. This indicates that silicon out-diffusion is not only due to the large coordination number of  $\text{La}_2\text{O}_3$ , but is enhanced significantly by the presence of the aluminum electrode on top as well.

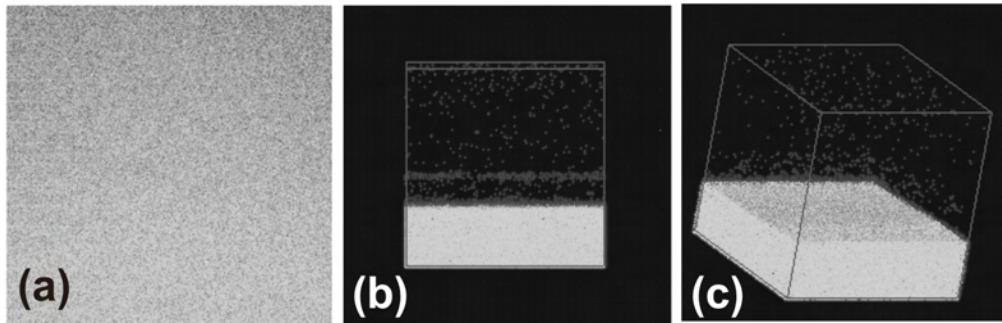


**Fig. 4.3.** TOFSIMS images of TiN/La<sub>2</sub>O<sub>3</sub>/Si devices with Si signal: (a) top view shows no silicon signal; (b) silicon spikes are not protruding from the silicon substrate (the bright bottom part); (c) 3D view of the device shows no silicon present in the oxide or in the TiN electrode. Top surface is  $70 \times 70 \mu\text{m}^2$  in dimension.

The TOFSIMS depth profile of the TiN/La<sub>2</sub>O<sub>3</sub>/Si device is shown in Fig. 4.4. Note that the Si signal in the La<sub>2</sub>O<sub>3</sub> layer is decreasing sooner than in the oxide of Fig.4.2, indicating that the amount of silicon in the oxide is much lower in TiN/La<sub>2</sub>O<sub>3</sub>/Si device than in Al/La<sub>2</sub>O<sub>3</sub>/Si device. The Si signal in TiN is reaching the noise level, as seen in Fig. 4.4.

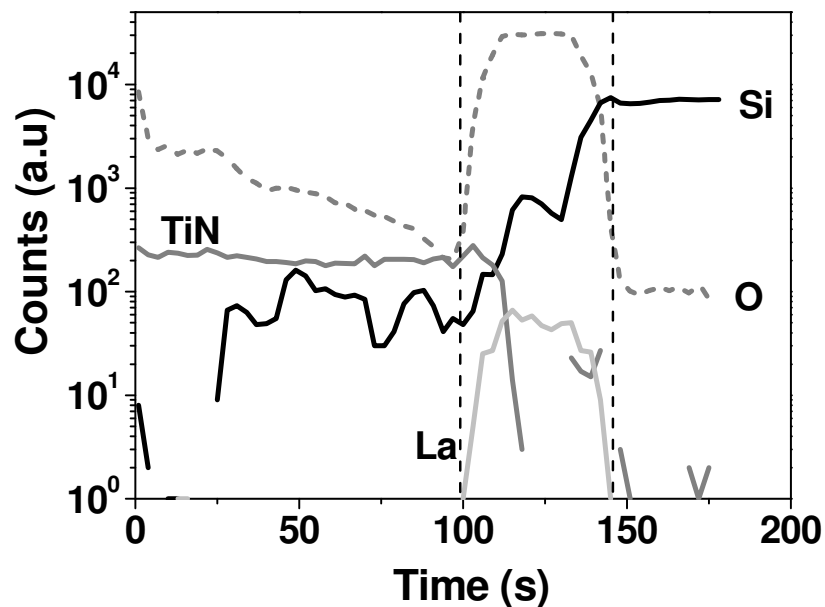


**Fig. 4.4.** TOFSIMS depth profile of TiN/La<sub>2</sub>O<sub>3</sub>/Si device showing the ion counts of Ti, La, Si and O.

### 4.3 Conclusions from TOFSIMS data of $\text{La}_2\text{O}_3$ films

It is known that in a direct Si-Al contact, up to 1 atomic percent of silicon can be dissolved by Si out-diffusion to Al at room temperature [7]. Due to the large solid solubility of Si in Al, Al acts as a sink for Si in this diffusion process, whereas for TiN there is not such a driving force for Si transport. The appearance of the silicon spikes is rather surprising, since the lanthanum oxide film is amorphous and therefore there should not be any preferential path for the silicon out-diffusion. However, the triplet grain boundaries in Al electrode are known to be very favorable paths for silicon diffusion and Si diffuses out to the top layer much faster than it spreads over the Al/ $\text{La}_2\text{O}_3$  interface. Therefore, it could be envisaged that initially the silicon atoms diffuse into  $\text{La}_2\text{O}_3$  layer, which further diffuse towards the Al electrode and they are transported to the top surface much faster than their diffusion in the oxide layer. This creates a Si density variation along the oxide thickness. This causes silicon atoms diffusing more from specific locations underneath the grain boundaries of aluminum.

The effects of these inter-diffusions are reflected in the leakage current through the device as seen in the current density-electric field ( $J$ - $E$ ) plot shown in Fig. 4.5. Upon utilizing an Al electrode the leakage current is orders of magnitude higher in comparison with the TiN electrode (at 4 MV/cm the leakage currents are  $10^{-3}$  and  $10^{-7}$  A/cm<sup>2</sup> respectively). The difference in the leakage current is partially due to the work function difference between Al and TiN to lanthanum oxide as well. After annealing the Al/ $\text{La}_2\text{O}_3$ /Si device at 450°C in forming gas for 30 minutes, the device becomes very leaky and shows no breakdown anymore. Estimation of the energy barrier height between Al and  $\text{La}_2\text{O}_3$  assuming Fowler-Nordheim tunneling through the oxide layer gives 1 eV, which is 2.5 times lower than the theoretical value [8] suggesting again that the interface between Al and  $\text{La}_2\text{O}_3$  is not well defined (or modified with the possible formation of  $\text{LaAlO}_x$ ).

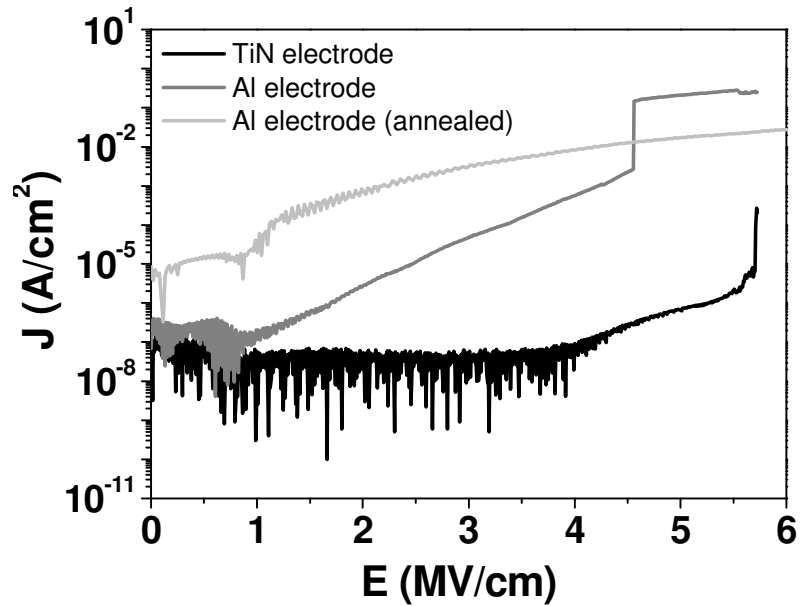


*Fig. 4.5. Leakage current density through Al/La<sub>2</sub>O<sub>3</sub>/Si and TiN/La<sub>2</sub>O<sub>3</sub>/Si devices.*

The Weibull distributions of breakdown fields are shown in Fig. 4.6, which shows that the breakdown with Al electrode is lower than with TiN electrode, which is also attributed to the enhanced silicon out-diffusion in samples with Al electrode.

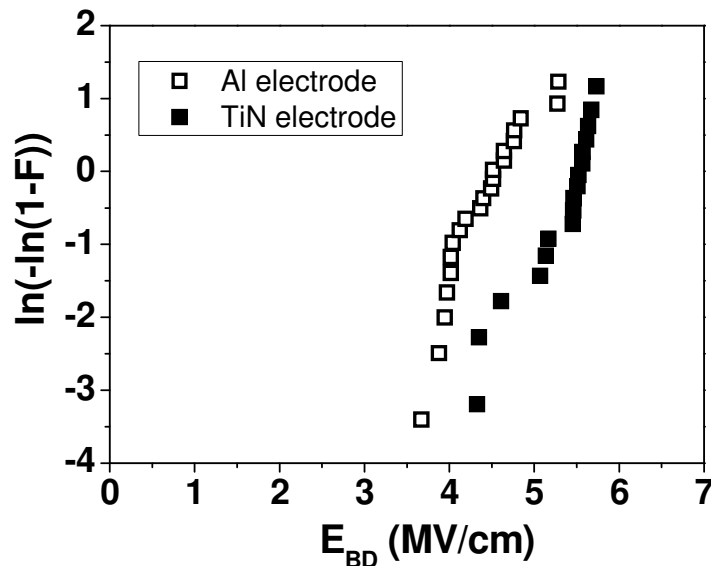


*Fig. 4.6. Weibull distribution of breakdown electric fields of Al/La<sub>2</sub>O<sub>3</sub>/Si and TiN/La<sub>2</sub>O<sub>3</sub>/Si devices.*

In addition, the dielectric permittivity of the  $\text{La}_2\text{O}_3$  layer was reduced by 30 % when Al was used. Since the interfacial silicon oxide formation ( $\sim 1$  nm) is the same in both cases, this

reduction in capacitance should be due to the formation of lower- $k$   $\text{Al}_2\text{O}_3$  formation at the interface ( $k \sim 8.9$ ), which then in series lowers the total effective capacitance of the layer.

#### 4.4 Si out-diffusion in $\text{La}_y\text{Zr}_{1-y}\text{O}_x$ films with Al top electrodes

The hypothesis by Ono et al. is that silicon diffusion is triggered by the thermal instability of the  $\text{La}_2\text{O}_3/\text{Si}$  system and the large coordination number of lanthanum oxide is the reason for larger Si out-diffusion in these films. However, enhanced silicon out-diffusion was also observed in all the LZO films and even in  $\text{Al}_2\text{O}_3$  films as depicted in Fig. 4.7.  $\text{Al}_2\text{O}_3$  is known to be dense when deposited with ALD; therefore, the silicon out-diffusion through this material interrogates the hypothesis that silicon out-diffusion is related to the coordination number of the material molecules.

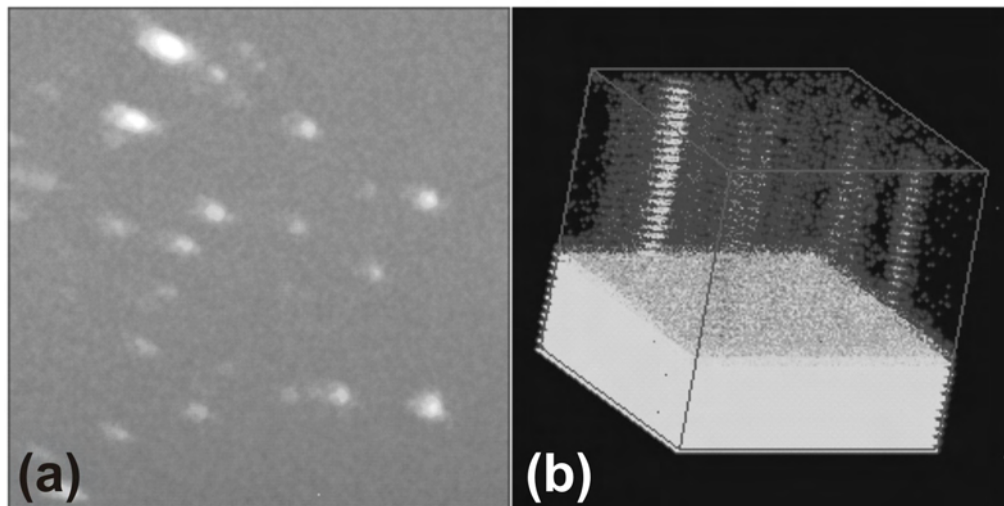


*Fig. 4.7. TOF-SIMS profile of 10 nm  $\text{Al}_2\text{O}_3$  film in the Si detection mode. (a) Top surface of the Al electrode ( $70 \times 70 \mu\text{m}^2$ ) and (b) 3D image showing the localized out-diffusion of silicon.*

Depth-profiles obtained in both the positive and negative mode provide us with different sets of information. The most significant peaks are selected for depth-profiling. The samples have a relatively thick Al layer (500 nm) on top of the thin high- $k$  dielectric layers. This limits the “sharpness” of the interface in the measured depth profiles.

##### Positive mode

In the depth-profiles, the interfaces are readily identified. The location of the Al layer is apparent from the decrease in, the  $\text{Al}^{2+}$  signal for instance, and the location of the  $\text{La}_y\text{Zr}_{1-y}\text{O}_x$

layer from the La and Zr signals. The intensity of the Al signal is enhanced at the  $\text{Al}/\text{La}_y\text{Zr}_{1-y}\text{O}_x$  interface due to oxidation of Al (evident also from the  $\text{Al}_2\text{O}^+$  signal at the interface). Oxidation is most pronounced for the  $\text{La}_2\text{O}_3$  layer.

The  $\text{Al}/\text{La}_y\text{Zr}_{1-y}\text{O}_x$  interface is less defined because of roughness introduced by ion sputtering. An enhanced concentration of Si is visible in the Al top-layer, especially in case of sample with  $\text{La}:\text{Zr} = 1:1$ . No significant amount of Si has been detected in the Al layer of the other samples investigated. The amount of Si is too low ( $< 0.01\%$ ) to be detected if  $\text{Ar}^+$  ions are used during sputtering in the positive mode.

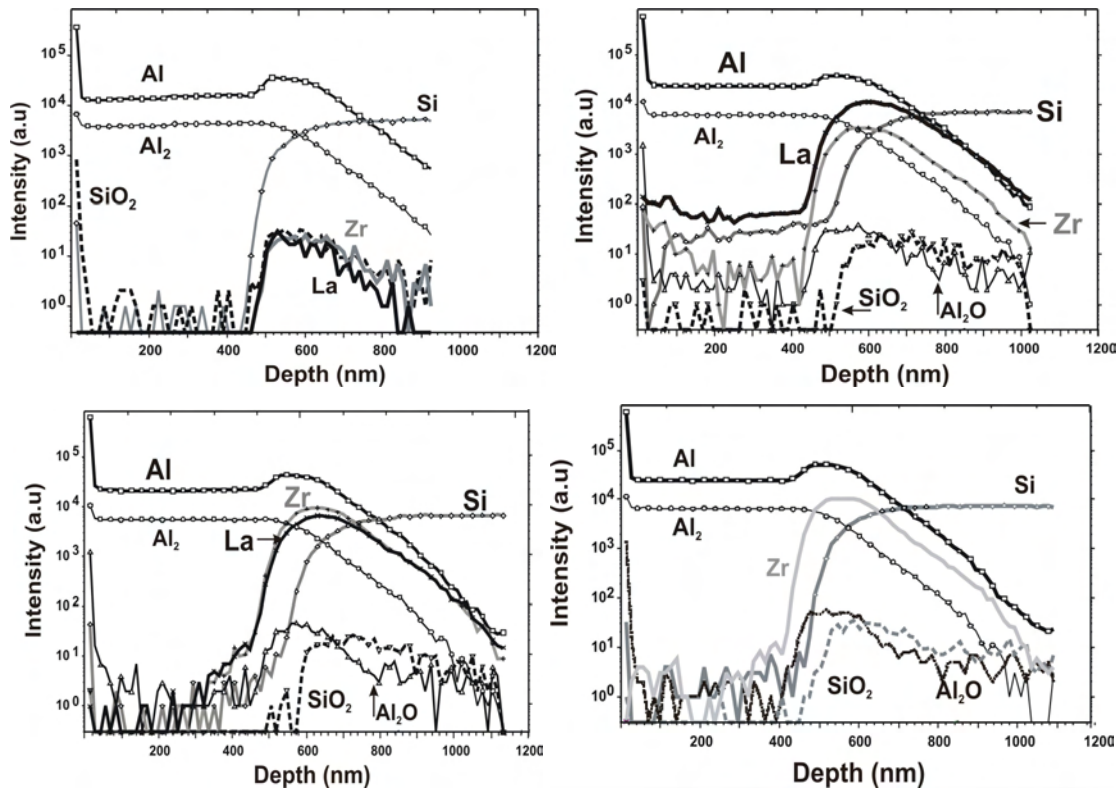


**Fig. 4.8.** TOF-SIMS depth profiles of  $\text{Al}/\text{La}_y\text{Zr}_{1-y}\text{O}_x/\text{Si}$  devices in positive mode (with  $\text{Ar}^+$  ions). Upper panel is the depth profile of the sample with  $\text{La}:\text{Zr} = 4:1$  (left) and  $1:1$  (right); lower panel is that of  $\text{La}:\text{Zr} = 1:4$  (left) and  $\text{ZrO}_2$  (right) respectively.

A steep increase of the  $\text{Si}^+$  signal already starts at the  $\text{Al}/\text{La}_2\text{O}_3$  interface. This also holds for samples with  $\text{La}:\text{Zr} = 4:1$ . The maximum of the  $\text{Si}^+$  signal (Si substrate) is located at a depth at which the Zr and La signals are decreasing. It is also evident that  $\text{SiO}_x$  is present in the  $\text{La}_y\text{Zr}_{1-y}\text{O}_x$  layer. In the case of the sample with  $\text{La}:\text{Zr} = 1:1$ , the  $\text{Si}^+$  signal strongly increases at



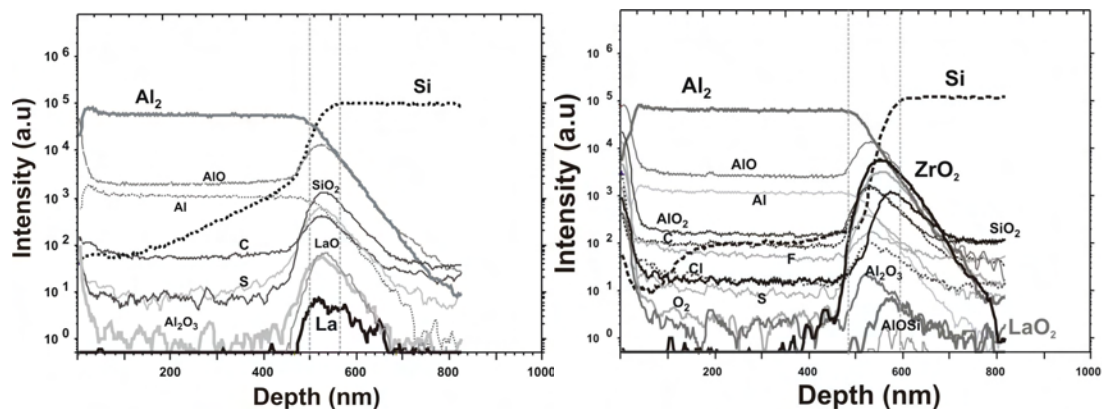
the position of the  $\text{Al}/\text{La}_y\text{Zr}_{1-y}\text{O}_x$  interface. This also holds for the  $\text{La}_2\text{O}_3$  and the sample with  $\text{La}:\text{Zr} = 1:4$ .

### Negative mode

Sputtering in the negative mode with  $\text{Cs}^+$  ions yields strongly enhanced signals for Si, which is therefore more suitable to detect the out-diffusion of small amounts of Si throughout the  $\text{Al}/\text{LZO}$  films.

A collection of the negative depth-profiles given in Fig. 4.9 shows that a high amount of Si is present in the Al layer in all samples investigated. The highest amount of Si in Al is detected in sample with  $\text{La}:\text{Zr} = 1:1$ , which is in fair agreement with the results obtained in the positive mode. It is striking that in devices with  $\text{ZrO}_2$  also a comparatively high Si signal is detected in the Al top layer.

From the depth profile, it can be confirmed that a layer of  $\text{AlSiO}_x$  has been formed at the  $\text{Al}/\text{La}_y\text{Zr}_{1-y}\text{O}_x$  interface in the case of  $\text{Al}/\text{La}_2\text{O}_3/\text{Si}$  devices. The other samples, including the  $\text{ZrO}_2$  sample, exhibits a thin layer of  $\text{AlO}_x$  at the  $\text{Al}/\text{La}_y\text{Zr}_{1-y}\text{O}_x$  interface, and a thin layer of  $\text{SiO}_2$  at the  $\text{La}_y\text{Zr}_{1-y}\text{O}_x/\text{Si}$  interface, which is very consistent with the EDX-HRTEM results described in Chapter 2.





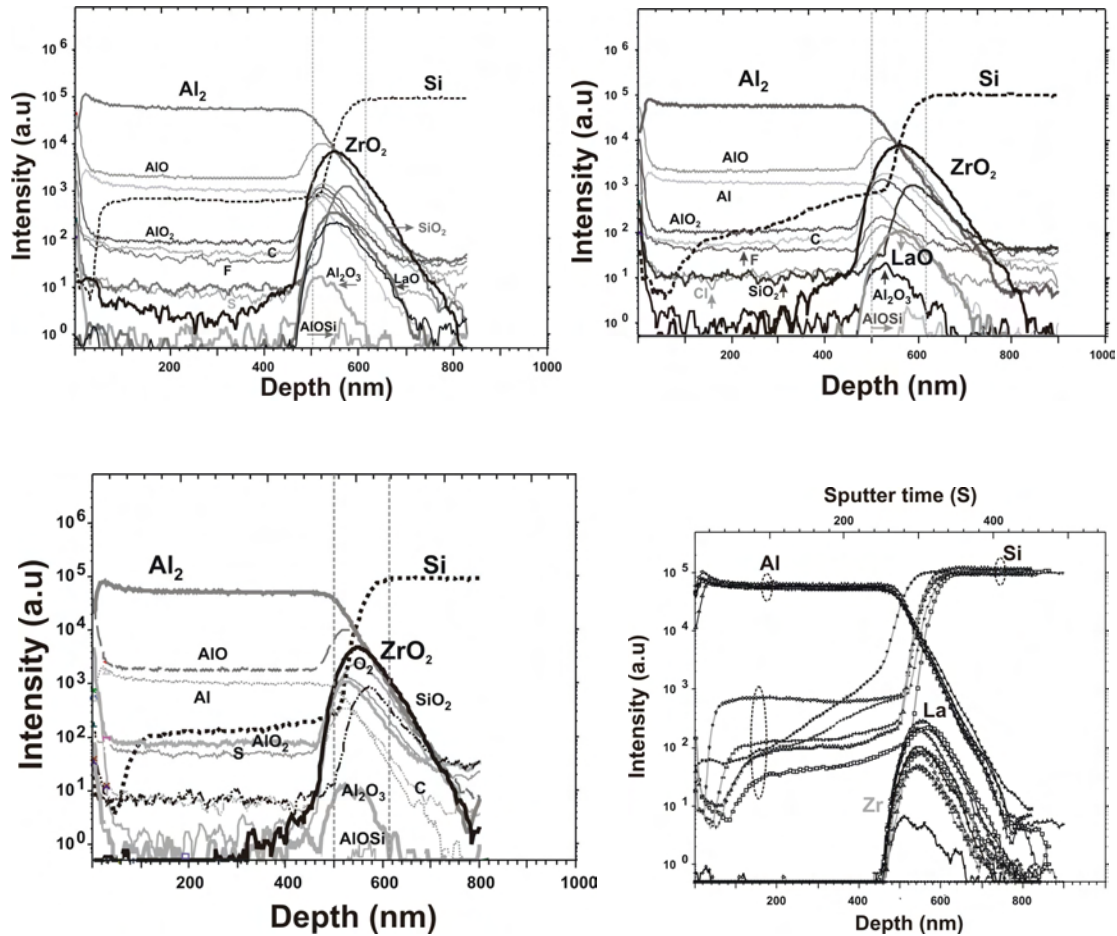


**Fig. 4.9.** TOF-SIMS depth profiles of Al/La<sub>y</sub>Zr<sub>1-y</sub>O<sub>x</sub>/Si devices in negative mode (with Cs<sup>+</sup> ions). Upper panel is the depth profile of the device with La<sub>2</sub>O<sub>3</sub> (left) and La:Zr = 4:1 (right); middle panel is with La:Zr = 1:1 (left) and with La:Zr=1:4 (right). The lower panel is with ZrO<sub>2</sub> (left) and a general overview of Al, Si, La and Zr signals in various samples (right) respectively. The largest silicon out-diffusion was observed in sample with La:Zr = 1:1.

An important observation from the depth profiles of the devices shown in Fig. 4.9 is that all the Al/LZO/Si devices have significant Si out-diffusion through the sample. The out-diffused Si is mostly in the form of SiO<sub>x</sub>, as evident from the SiO<sub>2</sub> signals shown in the depth profiles. A very small percentage of the Si has formed AlSiO<sub>x</sub> inside the oxide with the in-diffused Al, but the signal is rather weak. An enhancement of the SiO<sub>2</sub> signal at the Al/ La<sub>2</sub>O<sub>3</sub> interface indicates that the out-diffused silicon forms a silicon-rich layer at this interface, which is very consistent with the observation of Pan et al. However, this silicon layer is not visible in other La<sub>y</sub>Zr<sub>1-y</sub>O<sub>x</sub> samples with nonzero Zr content. Another observation is that Al/La<sub>y</sub>Zr<sub>1-y</sub>O<sub>x</sub>

interface, aluminum forms  $\text{AlO}_x$ , as seen in the devices with all stoichiometries. It is also seen that the silicon signals increase close to the surface, indicating that instead of dissolving in the Al electrode, silicon siphons out to the top surface. This hypothesis is confirmed by means of 3D stoichiometric maps of elements constructed from the raw TOFSIMS data as shown in Fig. 4. 10, which is an example using  $\text{La}_y\text{Zr}_{1-y}\text{O}_x$  films with  $\text{La}:\text{Zr} = 1:1$ .

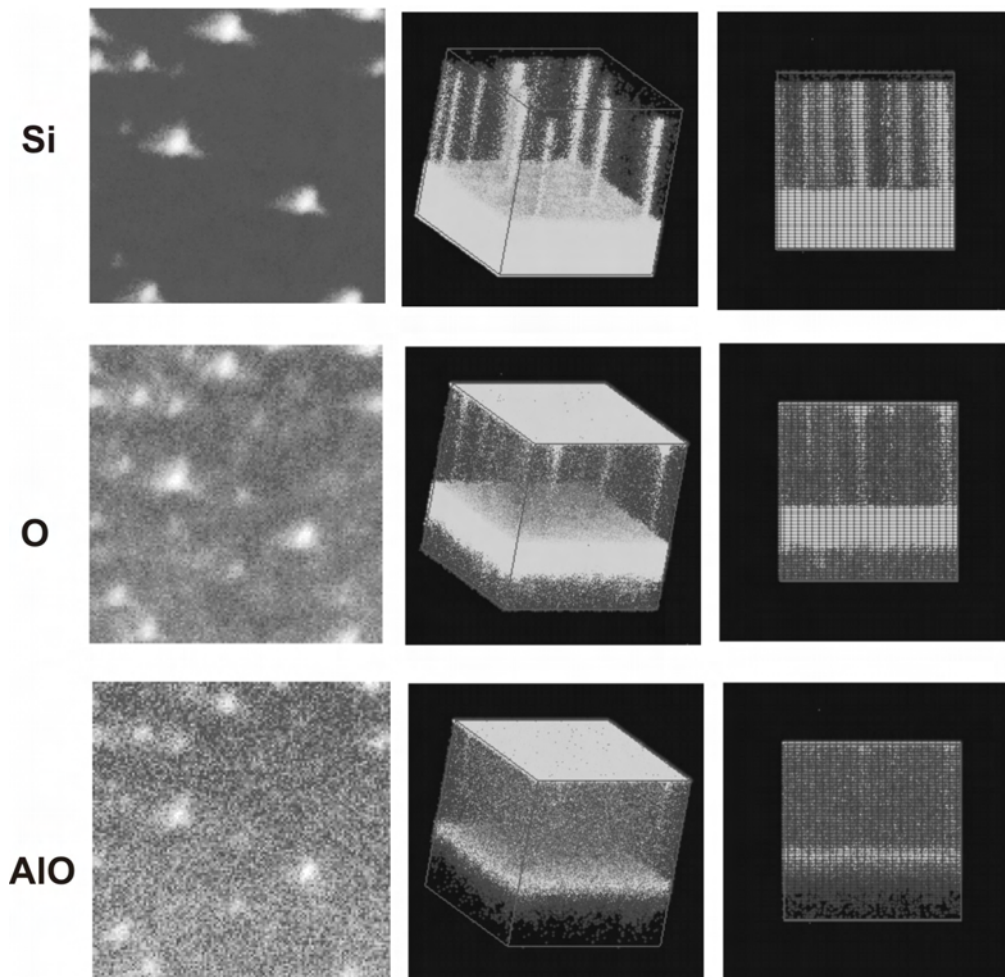


**Fig. 4.10.** TOFSIMS maps of  $\text{Al}/\text{La}_y\text{Zr}_{1-y}\text{O}_x/\text{Si}$  device with  $\text{La}:\text{Zr} = 1:1$ , using three different signals. Images at the left side are stoichiometric top-views on Al electrode; images in the middle column are 3D maps of the devices and the images in the right column are 2D cross-sectional maps of the device. The top row was constructed using Si signal, middle row is with O signal and the lower row is with AlO signal. Top surface is  $70 \times 70 \mu\text{m}^2$  in dimension.

The images in Fig. 4. 10 were constructed using Si, O and AlO signals, from the top Al

electrode layer (500 nm thick). TOFSIMS 3D maps generally demonstrate enhanced signals when the elements are oxidized (for instance, AlO appears brighter than Al). However, the bright spots on the top layer apparently consist of Si and O, which points out possible formation of  $\text{SiO}_x$ . The column-like bright lines seen in the 3D image constructed using Si shows that Si has very preferred diffusion paths through the oxide and Al layers. Considering the fact that the oxide layers are very thin compared to the Al electrode films, the Si diffusion could be determined by the Al top layer.

The depth profiles reveal the presence of several other elements such as carbon, fluorine and sulfur close to the  $\text{Al/La}_y\text{Zr}_{1-y}\text{O}_x$  interfaces. The presence of carbon could be suspected to come from the organic residue of the precursor and generally it is known that  $\text{La}(\text{thd})_3$  gives carbon contamination. In addition to the presence of fluorine and sulfur at the same spots of the Si spots, the oxygen signal in 3D imaging appears brighter at the top surface and diffuses gradually through the same paths where silicon diffusion paths appear. This also is a good indication that the silicon diffusion paths trace the triplet grain boundaries in the polycrystalline Al film. Striking also is that Al forms oxide with La and Zr at the  $\text{Al/La}_y\text{Zr}_{1-y}\text{O}_x$  interface.

## 4.5 Conclusions

The conventional notion is that the silicon out-diffusion is strongly related to the ionic radii of the metal-oxide. With increasing atomic number in the Lanthanide series, the ionic radii reduce. This characteristic is known as *lanthanide contraction* [3]. Lanthanum being a *light* rare-earth metal, has a larger ionic radius of 0.117 nm and has the strongest propensity towards silicon diffusion among other oxides of the rare-earth metals.

This Chapter demonstrates that the electrode material used to fabricate the metal-oxide-insulator (MIS) device is crucial in determining the quality of the devices. Besides the fact that the choice of the electrode is crucial with respect to its workfunction and therefore the barrier height for charge carrier tunneling through the oxide, it influences the silicon out-diffusion as well. Intermixing of silicon with aluminum is well-known in the context of low-temperature *a*-Si crystallization [5] and is triggered by strong diffusion of silicon in aluminum [6]. An additional driving force for the silicon diffusion through  $\text{La}_2\text{O}_3$  is the higher free energy of the  $\text{La}_2\text{O}_3$ -Si system and Al diffuses to the oxide until the oxide becomes metal rich silicide [4].

The influence of top electrode material in determining the silicon out-diffusion through the LZO films is the major theme of this Chapter. In  $\text{La}_2\text{O}_3$  films, silicon appears to have less spike-formation than in  $\text{La}_y\text{Zr}_{1-y}\text{O}_x$  films, which is possibly due to the crystalline  $\text{ZrO}_2$  present in these films. The interfaces between  $\text{La}_y\text{Zr}_{1-y}\text{O}_x$  and  $\text{ZrO}_2$  crystals are very favorable media for the silicon atoms to commute to the top electrode, since grain boundaries have higher surface energy to promote diffusion of atoms [9]. At the same time, certain amount of the diffused silicon alloys with the Al electrode, thus changing its electrical behavior. As a result of this enhanced diffusion through the interfaces, silicon concentration in  $\text{La}_y\text{Zr}_{1-y}\text{O}_x$  films appears highly localized, as seen in Fig. 4.10. On the other hand, the strong silicon out-diffusion observed through ALD processed  $\text{Al}_2\text{O}_3$  shows that the top electrode is more influential than the ionic radius of the metal-oxide. However, concerning the reliability of the devices with high- $k$  layers deposited on silicon, the instability of the Si/high- $k$  interface can lead to faster degradation of the MIS devices.

## 4.6 References

1. C.J. Först, C.R. Ashman, K. Schwarz, P.E. Blöchl, *Nature* **427**, 53 (2003)
2. S. Van Elshocht et al., *J. Vac. Sci. Technol. A* **26**, 274 (2008)
3. H. Ono, T. Katsumata, *Appl. Phys. Lett.* **78**, 1832 (2001)
4. T.M. Pan et al., *Electrochem. Solid-State Lett.* **10**, H101 (2007)
5. G. Radnoczi et al., *J. Appl. Phys.*, **69**, 6394 (1991)
6. Y. Masaki, T. Ogata, H. Ogawa, D. I. Jones, *J. Appl. Phys.* **76**, 5225 (1994).
7. S. Wolf, *Silicon processing for VLSI Era*, Vol. 2 Lattice Press, California (1990) p. 113.
8. E. Miranda, J. Molina, Y. Kim, H. Iwai, *Appl. Phys. Lett.* **86**, 232104 (2005).
9. *Materials Interfaces: atomic-level structures and properties*, Edited By D. Wolf & S. Yip, Chapman & Hall (London) (1992) page 197.



## Chapter 5

# Dielectric properties of $\text{La}_y\text{Zr}_{1-y}\text{O}_x\text{-SiO}_2$ bilayer stacks

### 5.1 Introduction

High- $k$  materials deposited on silicon have several concerns with respect to their electrical behaviour, such as silicate formation at the interface as described in Chapter 2, and silicon out-diffusion due to larger ionic radius and the metal electrodes used to fabricate the devices as discussed in Chapter 4. Interface-stability of the high- $k$  layers with silicon can be improved upon using a few angstrom thick barrier layer (e.g.  $\text{Al}_2\text{O}_3$  or  $\text{HfSiO}_x$ ) on which the high- $k$  layer is usually deposited. Application of a passivation layer has been shown to improve the crystallinity of the polycrystalline dielectric layers as well [1]. In order to suppress the leakage current through the devices, nano-laminated structures of dielectric materials are extensively used [2,3,4]. *Ding* et al. reports that  $\text{HfO}_2/\text{Al}_2\text{O}_3$  nanolaminates outperform individual  $\text{HfO}_2$  or  $\text{Al}_2\text{O}_3$  layers from leakage current point of view since the  $\text{Al}_2\text{O}_3$  layer inhibits the crystallization of  $\text{HfO}_2$  with a high-permittivity crystalline phase (and therefore exhibiting comparatively larger capacitance density) and the intermediate amorphous  $\text{Al}_2\text{O}_3$  layers hinder the continuity of the  $\text{HfO}_2$  grain boundaries [5,6].

An important issue that has been overlooked with respect to the leakage current through the nanolaminated structures is the interfacial polarization or charge trapping effects due to difference between the conductances of the layers. Such intra-dielectric interfacial polarization can lead to larger leakage currents through the system, due to a phenomenon called Maxwell-Wagner instability. This effect will be described in this Chapter at length, by investigating the electrical properties of  $\text{La}_y\text{Zr}_{1-y}\text{O}_x/\text{SiO}_2$  bilayers.

This Chapter is arranged as follows: initially, thickness measurements of the films using High-Resolution Transmission Electron Microscopy (HRTEM) are described. Secondly, the device fabrication is mentioned in detail. Unlike the sputter-deposited TiN electrodes of the devices described in the previous Chapter, the devices studied in this Chapter were fabricated

with ALD-processed TiN electrodes. ALD synthesis of TiN will be required for the fabrication of multiple MIM stacks without introducing the layers to environmental contamination. This Chapter concentrates on different aspects of technological requirements towards a multi-layered MIMIMIM stack to achieve ultra-high capacitance densities. Further on, the electrical measurements such as capacitance-voltage ( $C$ - $V$ ) and current-voltage ( $I$ - $V$ ) measurements carried out on the MIS devices are discussed.  $I$ - $V$  measurements show remarkable asymmetry between the charge injection from the Si substrate and TiN electrode. This effect is explained on the basis of Maxwell-Wagner effect and a model is developed to explain the reliability issues of the nanolaminated dielectrics in general based on their conductance properties. The reliability behaviour of the layers was studied using time-dependent dielectric breakdown and the Arrhenius behaviour of the dielectric breakdown is discussed.

## 5.2 Experimental details

In Chapter 3, we examined the electrical properties of the  $\text{La}_y\text{Zr}_{1-y}\text{O}_x$  films with different La:Zr ratios. With the insights from these results, a thickness series of three compositions of the  $\text{La}_y\text{Zr}_{1-y}\text{O}_x$  films were chosen for the studies reported in this Chapter. These films were deposited with a La:Zr pulse ratio of 4:1, 1:1 and 1:4 deposited on  $n^{++}$  wafers. Among these combinations, devices fabricated using films with La:Zr = 1:4 are investigated in more detail, since this combination gives one of the highest  $k$ -values among the  $\text{La}_y\text{Zr}_{1-y}\text{O}_x$  films with different La:Zr ratio ( $k=36.48$ , see Fig. 3.14). The series of stacks have the same  $\text{SiO}_2$  thickness of 4.2 nm and four different  $\text{La}_y\text{Zr}_{1-y}\text{O}_x$  layer thicknesses, so that the total film thicknesses in the case of the film with La:Zr = 1:4 are 8 nm, 13.3 nm, 22.6 nm, and 33.4 nm. The experimental results described in this Chapter are on devices with as-deposited thin films, i.e., without any post-deposition anneal applied to them. In this series of samples, the TiN electrodes were deposited by ALD. In order to fabricate the devices, highly As doped,  $n^{++}$  wafers were used so that the Si substrate would behave as metal-like electrode. The characterization of the metal-insulator-silicon MIS devices is intended as a first step towards creating high-density capacitors close to the technological requirements. The four steps of the device fabrication are as follows:

- Thermal oxidation of the  $n^{++}$  wafers to achieve 4 nm thick thermal oxide on it.

- Deposition of the  $\text{La}_y\text{Zr}_{1-y}\text{O}_x$  layers on the  $\text{SiO}_2/\text{Si}$  wafers using ALD.
- Deposition of 30 nm thick TiN on  $\text{La}_y\text{Zr}_{1-y}\text{O}_x/\text{SiO}_2/\text{Si}$  using ALD.
- Patterning of TiN into top electrodes using standard lithography and subsequent etching to yield capacitors of areas ranging from  $120 \times 120 \mu\text{m}^2$  to  $3020 \times 3020 \mu\text{m}^2$ .

The benefit of the ALD processed top electrode (TiN here) is that this avoids the plasma damage of the layers and electrode film could be manufactured in 3D trenches with good step coverage (see Chapter 5). It should be noted that thinner electrodes were employed compared to the 100 nm thick sputter-deposited TiN electrodes mentioned in the previous chapters.

### 5.3 Thickness measurements: HRTEM

The HRTEM cross sections of a  $\text{TiN}/\text{La}_y\text{Zr}_{1-y}\text{O}_x/\text{SiO}_2/\text{Si}$  device, where  $\text{La}_y\text{Zr}_{1-y}\text{O}_x$  film was deposited with La:Zr pulse ratio of 1:4, is shown in Fig. 5.1.

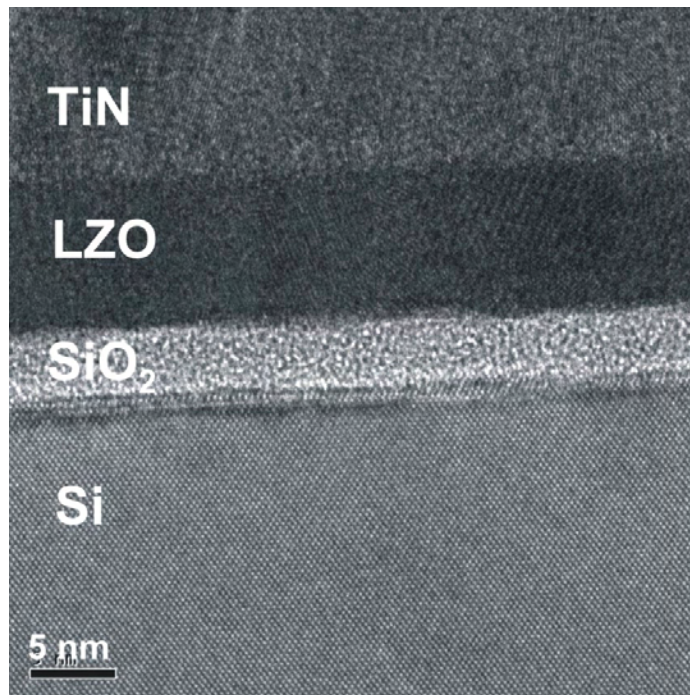


*Fig. 5.1. HRTEM images of the  $\text{TiN}/\text{La}_y\text{Zr}_{1-y}\text{O}_x/\text{SiO}_2/\text{Si}$  device.*

The thickness of  $\text{La}_y\text{Zr}_{1-y}\text{O}_x$  film and  $\text{SiO}_2$  layer measured using HRTEM is  $9.3 \pm 0.82$  nm and  $4.05 \pm 0.35$  nm respectively. This estimation is also in line with the film thickness measured using ellipsometry and XRR. Therefore, the film thickness for thicker samples measured using ellipsometry is assumed to yield correct values.



The measured thicknesses of 9.2 nm high- $k$  and 4.2 nm silicon oxide fit nicely with the total thickness of 13.4 nm that had measured using ellipsometry, subsequent to the deposition of the films.

## 5.4 Electrical properties of $\text{TiN}/\text{La}_y\text{Zr}_{1-y}\text{O}_x/\text{SiO}_2/\text{Si}$ stack

The MIS devices comprising  $\text{TiN}/\text{La}_y\text{Zr}_{1-y}\text{O}_x/\text{SiO}_2/\text{Si}$  stacks were subjected to capacitance-voltage ( $C$ - $V$ ) and current-voltage ( $I$ - $V$ ) measurements. Electrical characterizations of the devices were done using Agilent 4155C parameter analyzer and HP 4194A impedance analyzer.

### 5.4a Capacitance-Voltage ( $C$ - $V$ ) measurements

Figure 5.2 shows the forwards and reverse  $C$ - $V$  characteristics of  $\text{TiN}/\text{SiO}_2\text{-La}_y\text{Zr}_{1-y}\text{O}_x$  ( $\text{La}:\text{Zr} = 1:4$ )/ $\text{Si}$  devices with various stack thicknesses. All measurements were begun with a negative bias to the bottom electrode ( $\text{Si}$ -injection) and performed at 1 kHz.

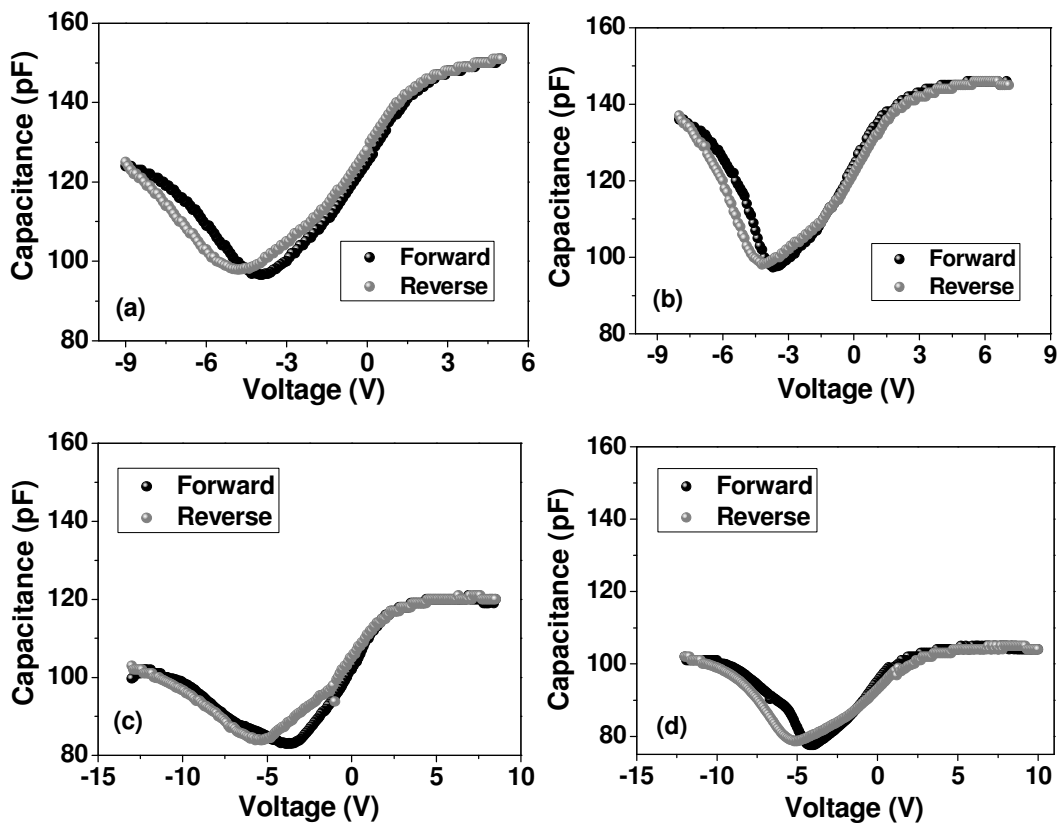
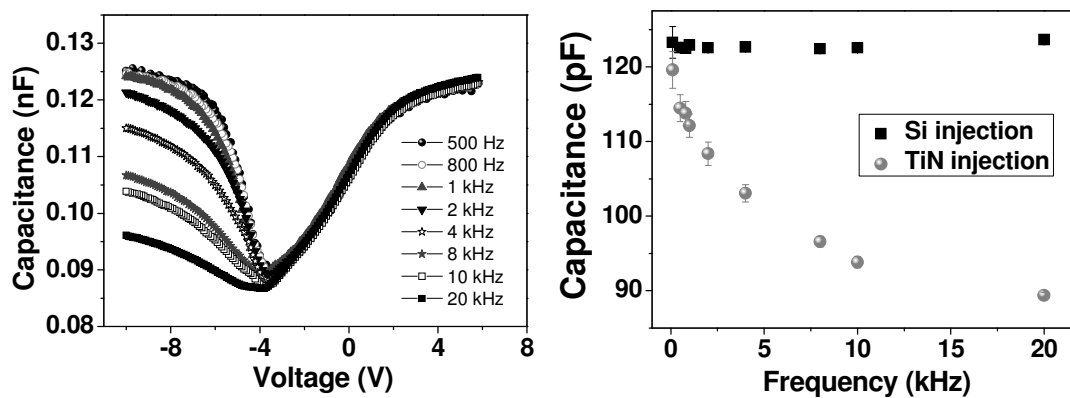


Fig. 5.2.  $C$ - $V$  curves of (a) 8 nm, (b) 13.3 nm, (c) 22.6 nm and (d) 33.4 nm of  $\text{TiN}/\text{La}_y\text{Zr}_{1-y}\text{O}_x/\text{SiO}_2/n^{++}\text{Si}$  (MIS) devices measured at 1 kHz frequency.

The  $C$ - $V$  curves appear asymmetric (though the  $n^{++}$  doped silicon is assumed to be nearly metallic, the dip in the  $C$ - $V$  behaviour indicates the formation of a thin depletion layer in the silicon substrate. This will be explained in section 5.4.4). Noticeably, the saturation capacitance is lower at TiN injection compared to the Si-injection, which is an indication of the lower apparent dielectric thickness under substrate injection than under TiN electron injection.

The frequency dependence of the device with 22.6 nm  $\text{La}_y\text{Zr}_{1-y}\text{O}_x$  is shown in Fig. 5.3. This graph not only shows that the capacitance is lower at TiN injection compared to the Si-injection but also that the capacitance at TiN injection depends significantly on the oscillation frequency. A more detailed explanation will be given in the next paragraphs.



*Fig. 5.3. (Left)  $C$ - $V$  curves of the TiN/  $\text{La}_y\text{Zr}_{1-y}\text{O}_x$  / $\text{SiO}_2$ /Si device with 22.6 nm  $\text{La}_y\text{Zr}_{1-y}\text{O}_x$  film at different frequencies. (Right) Response of the saturation capacitance as a function of the frequency, when the injection is from Si and TiN. The capacitance measured under TiN injection condition is strongly frequency dependent.*

Fig. 5.4 shows the capacitance of the layers as a function of the high- $k$  layer thickness for different injection conditions. The capacitance was measured at +5V and -5V i.e. for respective TiN injection and Si injection conditions and at 1 kHz and 10 kHz frequencies. From this graph it becomes clear that for the different  $\text{La}_y\text{Zr}_{1-y}\text{O}_x/\text{SiO}_2$  bilayer thickness the capacitance is consistently lower at TiN injection compared to the Si-injection and depends significantly on the oscillation frequency. Thus, for all the bilayer thicknesses the effective dielectric thickness under substrate injection remains smaller than under TiN electron injection. From Fig 5.4 also two other effects can be observed: 1) with increasing thickness

the capacitance read-out from TiN injection for the 1 kHz and 10 kHz measurements are approaching each other, 2) the difference between the Si and TiN injection becomes larger especially for the lower frequency (1 kHz) measurements.

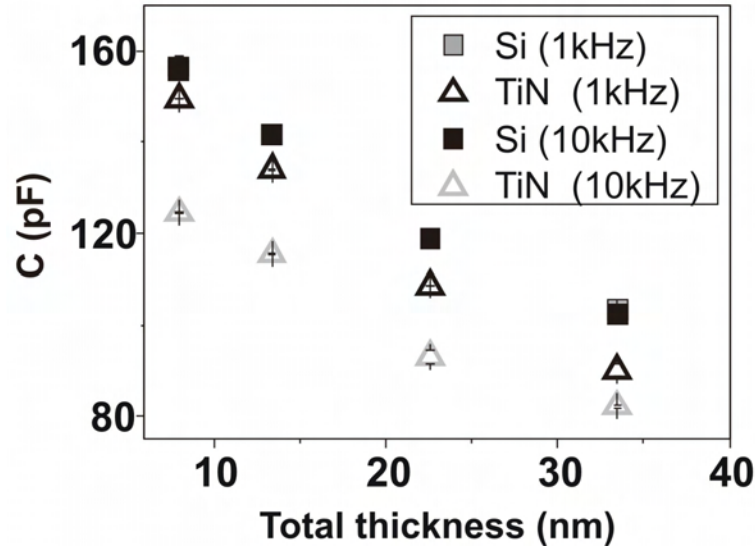


*Fig. 5.4. Capacitance of the stacks as a function of the  $\text{La}_y\text{Zr}_{1-y}\text{O}_x/\text{SiO}_2$  stack thickness, measured with negative bias applied to Si and TiN.*

#### 5.4b Current-Voltage (*I-V*) measurement

If there is asymmetry in the capacitance of the layers depending on the direction of the electron injection through the dielectric stack (from Si or TiN in this case), it should be evident in *I-V* measurements as well. Fig. 5.5 shows the *I-V* characteristics plotted as current density–electric field (*J-E*) characteristics. Here, the electric field is defined as the applied voltage across the electrodes divided by the total thickness of the dielectric stack. This corresponds to the mean electric field in the sample. A very distinct asymmetry is visible between the electron injection behaviour from the silicon bottom electrode and TiN top electrode. Such a *J-E* asymmetry is not observed when the device is fabricated using only one of these dielectric layers [7] indicating little impact of the work function difference between the two electrode materials. Because the Fermi level difference of TiN and  $n^{++}$  doped silicon substrate is less than 0.5 eV, the influence of the work function difference on the leakage current can be ruled out when the asymmetry is observed at voltages far above 0.5V.

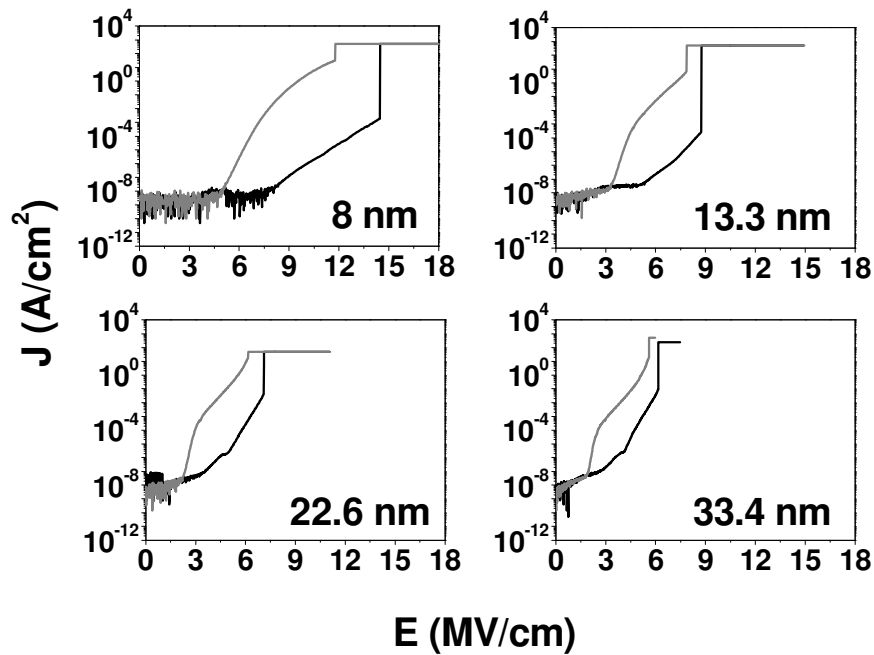


*Fig. 5.5. The J-E characteristics of the devices with different stack-thickness measured at electron injection from Si (grey curves) and from TiN (black curves).*

As evident from Fig. 5.5, the dielectric breakdown electric field of the stacks differ depending on whether the charge injection is from Si or TiN. The breakdown electric field is smaller if the high- $k$  layer is made thicker, as Fig. 5.6 shows. Noticeably, the dielectric breakdown field is consistently lower when the electron injection is from the substrate, which is a first indication that the effective (electric) thickness of the dielectric under substrate injection condition is smaller than under TiN electron injection. At higher thickness, the breakdown electric field is closer to the breakdown of  $\text{La}_y\text{Zr}_{1-y}\text{O}_x$  layers [8] and the breakdown fields under silicon and TiN electron injection become more similar.

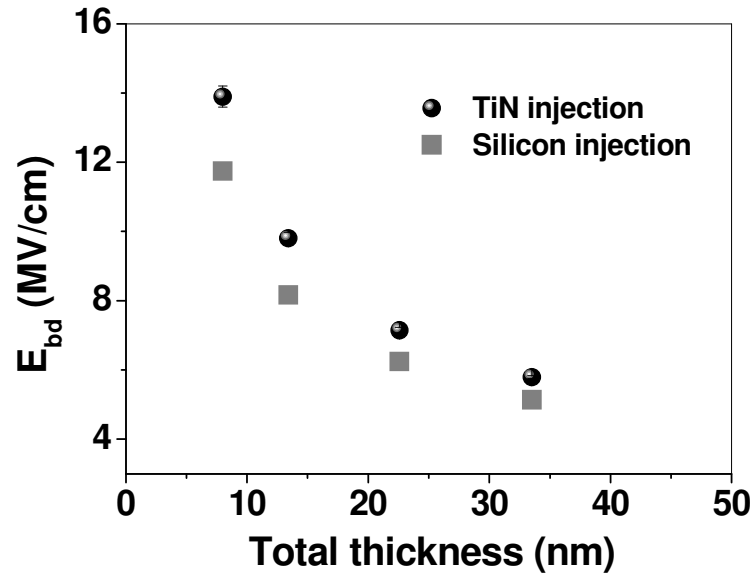


*Fig. 5.6. The dielectric breakdown field of the devices with different stack-thickness measured at electron injection from Si and from TiN.*

The asymmetric capacitance values and  $J$ - $E$  characteristics described above might be explained by the so-called Maxwell-Wagner effect, as elaborated in the next section.

### 5.4c The Maxwell-Wagner effect

#### (a) Modelling

In steady state, i.e. when a dc voltage is applied across the stack of dielectrics with different conductances, the current passing through both layers must be the same under a constant applied electric field across the stack (as per the Poisson's equations). In order to satisfy this condition, the charges (electrons or holes) are transported through the leakier dielectric film (the film dielectric with larger conductance) to the interface between the two dielectrics until the same current is passing through both the films under equilibrium. This enhanced charge migration to the inter-dielectric interfaces due to the difference of conductances is known as the Maxwell-Wagner (MW) effect [9]. (This is however different from the charge disproportionation in superlattice structures [10] that is occurring purely due to interface imperfections). The presence of MW effect in a stack would even invalidate the conventional picture of stacked dielectrics as capacitors connected in series, since the contribution of charge accumulation at the interface is generally ignored. This may lead to controversial

results as well; for instance, recent studies have shown that the ultra-high dielectric permittivity observed in ferroelectric heterostructures [11] could likely be an artefact of the MW effect [12].

In principle, any heterogeneous material system characterized by different sets of dielectric permittivities ( $k_i$ ) and conductances ( $\sigma_i$ ) can exhibit MW effect. I.e., when a potential is applied to such a system, the initial potential distribution corresponds only to the spatial distribution of  $k_i$ , not to that of  $\sigma_i$ , but at the steady state, the potential distribution is characterized only by the spatial distribution of  $\sigma_i$ , rather than by that of the permittivities [13]. If the capacitive and resistive distributions of the system are not the same, the system will change from one to the other in response to an alternative voltage. This relaxation-like process is the MW relaxation. This phenomenon has been studied extensively in the context of impedance of the polycrystalline grain boundaries where charge accumulation effects prevail [14].

The striking asymmetry in  $J$ - $E$  and  $C$ - $V$  curves can be explained using MW effect arguing on the observation that the electron carrier transport across the layers is enhanced when the electron injection is from the silicon. The proposed scenario to explain this effect is illustrated in Fig. 5.7 using the energy band-diagram of these dielectric layers under opposite voltage biasing conditions. As Fig. 5.7 (a) shows, when a negative bias is applied to the silicon substrate, the electrons undergo direct tunnelling through the  $\text{SiO}_2$  and reach the dielectric interface even at low electric field. Depending on the position of the conduction band of the high- $k$  film, these tunnelled electrons will either enter the high- $k$  conduction band already at these low electric fields [15, Page 21] or will be trapped at the dielectric interface. In the latter case, a large number of electrons are transported to the dielectric interface.

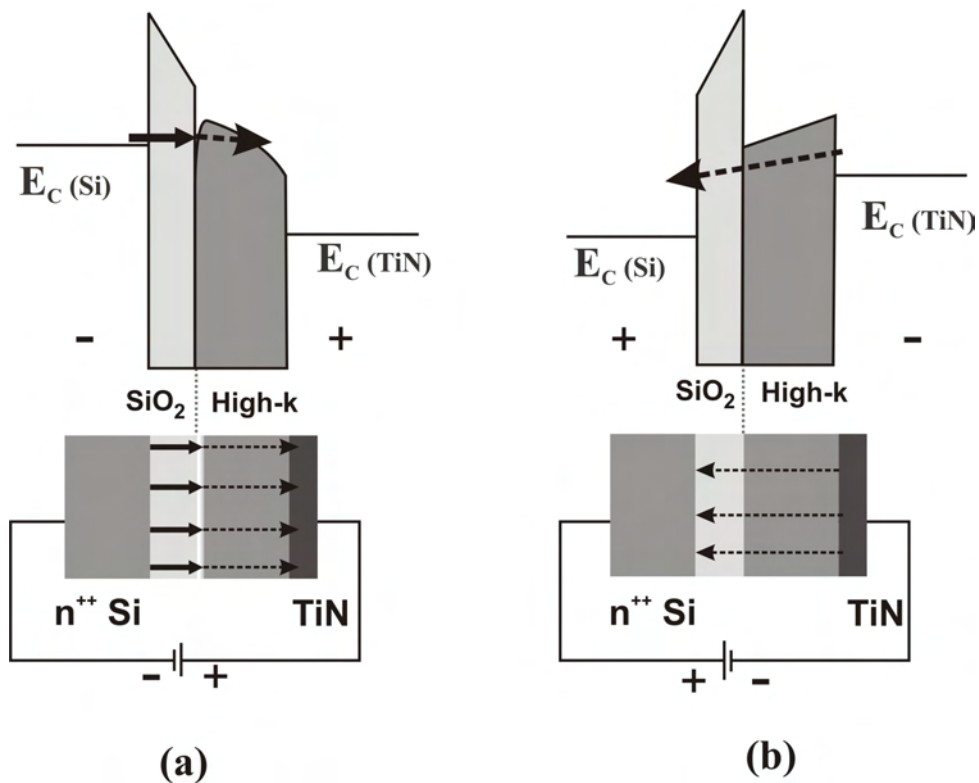


**Fig. 5.7.** Band diagram of the  $\text{SiO}_2/\text{high-k}$  stack under different electron injection directions: (a) when the electron injection from the Si substrate, (b) when the electron injection is from the TiN electrode. The thick arrows represent direct tunnelling of electrons and the dotted arrows represent FN tunnelling.

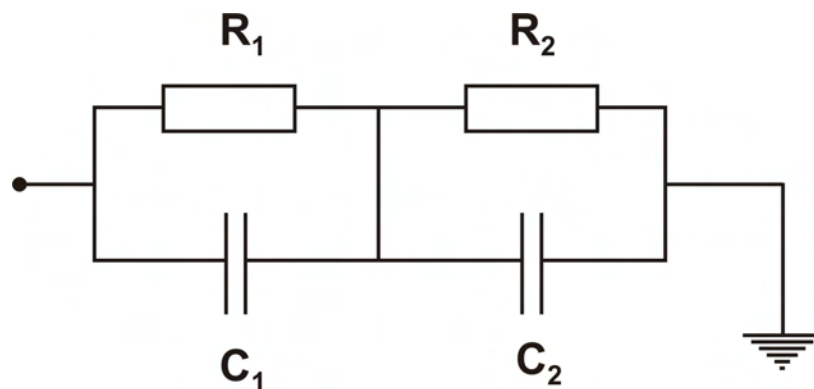


**Fig. 5.8.** Circuit diagram of two capacitors in series, which constitute  $\text{Si}/\text{SiO}_2$  system ( $C_1$ ) with surface charges at the  $\text{SiO}_2/\text{high-k}$  interface and the  $\text{high-k}/\text{TiN}$  system ( $C_2$ ) with the same interfacial charges.  $R_1$  and  $R_2$  express how leaky the layers are (Ref. [9, 13, 14]).

The tunnelling behaviour through the  $\text{SiO}_2$  layer and interface charge trapping can be

modelled using a standard equivalent circuit consisting of two serially connected modules of capacitors with their series resistance in parallel, as shown in Fig. 5.8. In this model,  $C_1$  and  $C_2$  are the capacitances and  $R_1$  and  $R_2$  are the resistances of the individual layers ( $\text{SiO}_2$  and  $\text{La}_y\text{Zr}_{1-y}\text{O}_x$ ). Assuming  $e^{j\omega t}$  time dependence, the impedance of the total system can be written as

$$Z = \frac{R_1}{1 + j\omega C_1 R_1} + \frac{R_2}{1 + j\omega C_2 R_2} \quad (5.1)$$

Where,  $\omega = 2\pi f$  (with  $f$  is the frequency of ac modulation). When the stack is assumed to be a single dielectric layer with an effective dielectric constant  $k_{eff}$ , the effective capacitance can be written as  $C_{eff} = k_{eff} A/d$  with  $d$  is the physical thickness of the stack and  $A$  is the area of the electrode. Then the impedance of the device would be  $Z = 1/j\omega C_{eff}$ . Here,  $k_{eff}$  is defined in complex form as

$$k_{eff} = k' - jk'' \quad (5.2)$$

where  $k'$  and  $k''$  are the real and imaginary dielectric permittivities. By solving Poisson's continuity equations for the electron flow through this equivalent circuit, the dielectric permittivity  $k'$  can be written in terms of the dielectric relaxation timescales  $\tau_1$  and  $\tau_2$  for the individual capacitors (with capacitances  $C_1$  and  $C_2$  respectively; generally  $\tau_i = R_i C_i$  [see Ref. [14]) as

$$\left. \begin{aligned} k' &= \frac{d_{phys}}{A(R_1 + R_2)} \frac{\tau_1 + \tau_2 - \tau + \omega^2 \tau_1 \tau_2 \tau}{1 + \omega^2 \tau^2} \\ &= k_\infty + \frac{k_0 - k_\infty}{1 + \omega^2 \tau^2} \end{aligned} \right\} \quad (5.3)$$

where  $k_\infty$  and  $k_0$  are the dielectric permittivities at infinite and zero frequencies and  $\tau$  is the effective relaxation timescale of the whole stack [13, 14]. Similarly, the effective imaginary permittivity ( $k''$ ) of the dielectric stack with an interface polarization can be expressed in terms of zero and infinite frequency responses as

$$k'' = \frac{d}{\omega A(R_1 + R_2)} + \frac{(k_0 - k_\infty)\omega\tau}{1 + \omega^2 \tau^2} \quad (5.4)$$

where  $(R_1 + R_2)$  is the sum of the resistances of the dielectric layers and  $k_\infty$  and  $k_0$  are the infinite and zero frequency dielectric permittivities of the stack [9]. The second term in Eq.



(5.4) represents the Debye polarization whereas the first term is related to Maxwell-Wagner polarization. Since the MW carrier migration adds up to the dissipation of the capacitor, the imaginary dielectric permittivity  $k''$  would increase significantly when the frequency approaches zero. That is, for the MW case,  $k'' \rightarrow \infty$  as  $\omega \rightarrow 0$  and for Debye polarization,  $k'' \rightarrow 0$  as  $\omega \rightarrow 0$ .

With the conventional view, Fig. 5.7 looks counterintuitive since Maxwell's equation suggests that the slope of the conduction band should be inversely proportional to the dielectric permittivity of the dielectric stacks. Thus the displacement  $D = k_{\text{SiO}_2} E_{\text{SiO}_2} = k_{\text{High-k}} E_{\text{High-k}}$ , where  $\epsilon$  is the permittivity of the corresponding layer and  $E$  is the electric field in respective layer. From this picture,  $E_{\text{SiO}_2} = (k_{\text{High-k}} / k_{\text{SiO}_2}) E_{\text{High-k}}$  and thus  $E_{\text{SiO}_2} \gg E_{\text{High-k}}$ . However, when the (net) charge inside the dielectric is not negligible, this picture is different.

If  $\sigma_{\text{high-k/TiN}}$  is the charge density at the high- $k$ /TiN interface, then the electric field in  $\text{SiO}_2$  and in the high- $k$  layer will be

$$\left. \begin{aligned} E_{\text{SiO}_2} &= (\sigma_{\text{high-k/TiN}} + \sigma_{\text{SiO}_2/\text{high-k}}) / k_{\text{SiO}_2} = -\sigma_{\text{Si/SiO}_2} / k_{\text{SiO}_2} \\ E_{\text{high-k}} &= -(\sigma_{\text{Si/SiO}_2} + \sigma_{\text{SiO}_2/\text{high-k}}) / k_{\text{high-k}} = \sigma_{\text{SiO}_2/\text{high-k}} / k_{\text{high-k}} \end{aligned} \right\} \quad (5.5)$$

Here,  $\sigma_{\text{Si/SiO}_2}$  and  $\sigma_{\text{SiO}_2/\text{high-k}}$  are the surface charge densities close to the Si/SiO<sub>2</sub> and the SiO<sub>2</sub>/high- $k$  interfaces, respectively. Due to tunnelling,  $E_{\text{high-k}} \gg E_{\text{SiO}_2}$  (which is different from the solution for Maxwell's equation for a non-tunnelling situation) and hence the slope of the conduction band bending will be larger for the high- $k$  layer than for the SiO<sub>2</sub> layer. For dielectric stacks the exact slope will be a function of the ratio of the conductance of each of the layers. Under the condition of the electron transport to the interface of both dielectrics, the ratio of the breakdown electric fields from different electron injections should be proportional to the ratio of the thickness of the high- $k$  layer to the total thickness of the layer, i.e.,

$$|E_{BD}|_{\text{Si}} / |E_{BD}|_{\text{TiN}} \propto d_{\text{High-k}} / d_{\text{Total}}.$$

*(b) Theoretical fit to the experimental data*

The experimental results presented in figure 5.4-5.7 can be qualitatively understood in terms of the aforementioned interface charging effects. Fig. 5.6 shows a trend that resembles the relation between breakdown fields as mentioned above, although the thickness ratio does not completely fit the breakdown behaviour. In reality, more important than the average breakdown electric field is the peak electric field at the interfaces and within the bulk at the time of breakdown. The exact ratio depends on the percentage of electrons tunnelling through the barriers. In the case of thicker high- $k$  films the breakdown electric field under silicon injection becomes closer to the breakdown field of pure  $\text{La}_y\text{Zr}_{1-y}\text{O}_x$  layers. In that case, the  $\text{SiO}_2$  layer behaves nearly as if it was an extension of the silicon substrate. In the case of thinner high- $k$  films, the potential drop over the thermal oxide layer becomes larger due to the increased leakage current through the whole stack and therefore the breakdown electric field becomes larger, i.e. it is determined more by the properties of the thermal oxide.

When a negative bias is applied on the gate (leading to electron injection from TiN, figure 5.7 (b)), the electrons tunnelling across the entire stack is weaker comparing to the injection from Si. This can be explained as follows. When the electron injection is from TiN, the whole dielectric stack acts as the barrier to the tunnelling. This is because the tunnelling probability of holes at the Si- $\text{SiO}_2$  interface is much smaller than electrons (though it is not improbable), as the Si- $\text{SiO}_2$  barrier height for electrons is 3.2 eV from the silicon conduction band, whereas that for holes from the silicon valence band is 4.8 eV [16]. Therefore, the holes will mostly accumulate at the Si- $\text{SiO}_2$  interface without tunnelling to the- $\text{La}_y\text{Zr}_{1-y}\text{O}_x$  interface. Due to lower barrier height and lower effective mass, electrons tunnel easily to the  $\text{La}_y\text{Zr}_{1-y}\text{O}_x/\text{SiO}_2$  interface when the charge injection is from silicon. This means that the MW effect happens in this stack only in one direction, i.e. when the electron injection is from the silicon, which accounts for the asymmetry shown in Fig. 5.5.

This model has been experimentally validated using the low frequency response of the imaginary permittivities of the layers, as shown in Fig. 5.9, where the electron injection is from TiN and Fig. 5.10 with electron injection from the Si substrate. The experiments were done at 4V with an ac modulation of 100 mV amplitude.

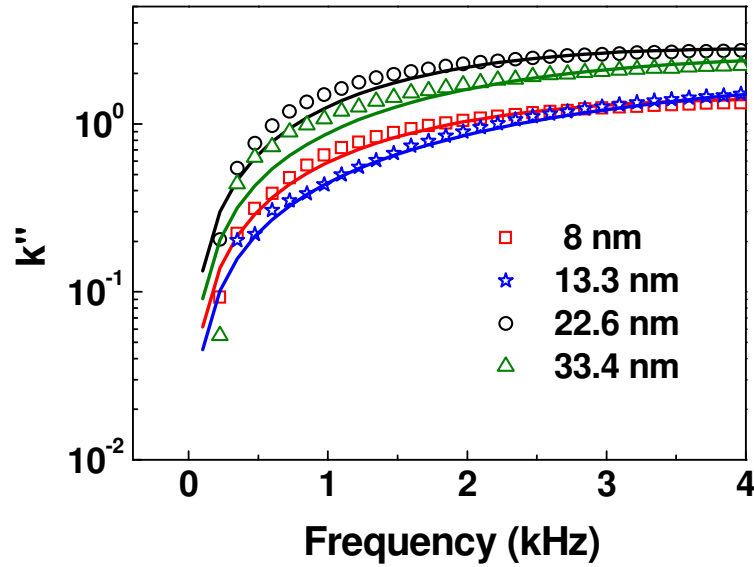


*Fig. 5.9. Imaginary dielectric permittivity  $k''$  of the layers of different stack thickness, plotted against the frequency, when the electron injection is from TiN. The measurement was done at  $-4\text{V}$  on TiN. The open symbols are the experimental data and the lines are theoretical curves plotted using Eqn. (5.4).*

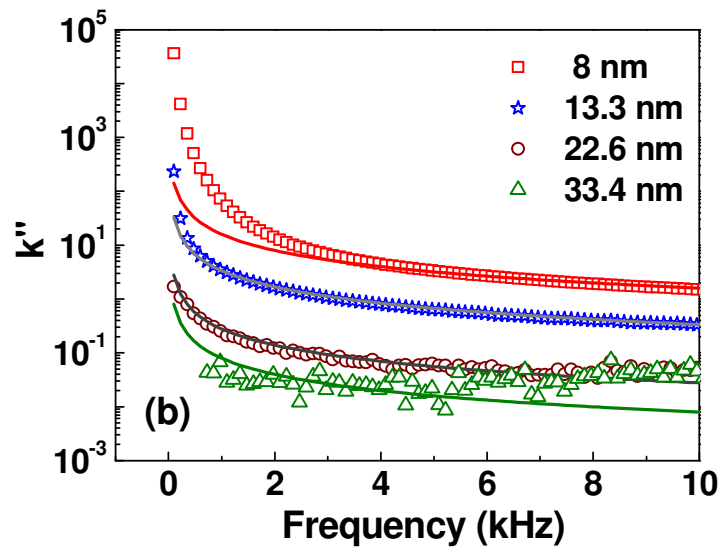


*Fig. 5.10. Low frequency behaviour of imaginary permittivity for Si electron injection showing  $k'' \rightarrow \infty$  as  $\omega \rightarrow 0$ , which indicates Maxwell-Wagner charge migration to  $\text{SiO}_2\text{-La}_y\text{Zr}_{1-y}\text{O}_x$  interface. The measurement was done at  $-4\text{V}$  on Si substrate.*

Under TiN electron injection, as shown in Fig.5.9,  $k'' \rightarrow 0$  when the frequency approaches zero, as expected from Debye polarization of the stack. However, under the electron injection

from silicon, as seen in Fig.5.10,  $k'' \rightarrow \infty$  with reducing frequency, which is a clear signature of MW charge migration. The solid lines in Fig. 5.9 and 5.10 are theoretical fits to the experimental data employing Eqn. (5.4), with a fixed  $(d/\varepsilon_0 A(R_1 + R_2))^{-1}$  value of  $10^{-3}$  Hz, assuming that  $d/(R_1 + R_2)$  remains the same for all stacks (which is a fair assumption, since the resistance usually scales with the thickness of a layer). The relaxation timescale  $\tau$  and  $k_0 - k_\infty$  were the only two fitting parameters for both sets of data. To fit the experimental data,  $k_0 - k_\infty = 5$  was assumed for all thicknesses for the Debye case, while different values of  $k_0 - k_\infty$  had to be used to fit the MW data shown in Fig. 5.10. These values of  $k_0 - k_\infty$  are 450 (8 nm), 200 (13.3 nm), 175 (22. nm) and 100 (33.4 nm), respectively. This thickness dependence of  $k_0 - k_\infty$  only in one polarization direction is strongly indicative of the MW phenomenon, since the interfacial polarization effect has a strong dependence on the conductance of the layers and thus it varies significantly with the thickness of the dielectric layers. Note that the permittivity of single layers of the high- $k$  is independent of the thickness and that this thickness dependence arises due to MW effect.

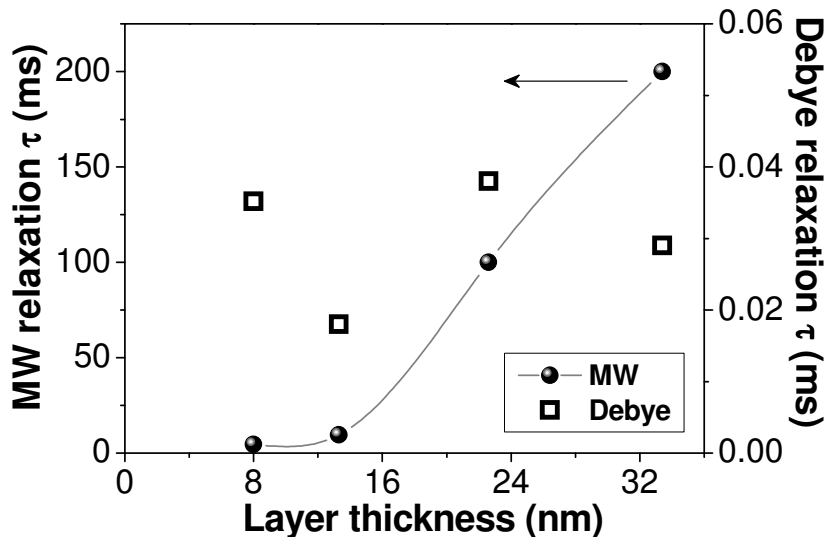


**Fig. 5.11.** Relaxation times obtained from the theoretical fit to the data corresponding to different thickness shown in Fig. 5.9 and 5.10. The timescales corresponding to MW (left axis) and the Debye (right axis) relaxations differ by orders of magnitude from each other.

In addition to the modestly good fit to the data, the theoretical fits provide an important

observation about the characteristic time scales associated with the MW effect and Debye polarization. Here,  $\tau$  represents the decay of MW electrons from the  $\text{SiO}_2\text{-La}_y\text{Zr}_{1-y}\text{O}_x$  interface for silicon electron injection, and the dielectric relaxation timescale of the  $\text{La}_y\text{Zr}_{1-y}\text{O}_x$  film for TiN electron injection. Interestingly, the theoretical fits for both scenarios suggest relaxation times that differ significantly in magnitude as shown in Fig. 5.11.

Under TiN electron injection, the relaxation time related to the Debye polarization is relatively constant around  $30 \pm 8 \mu\text{s}$ , which is independent of the dielectric thickness, whereas the MW relaxation timescales are much larger and increase exponentially with the film thickness. At the moment when the applied electric field is switched off, MW electrons trapped at the interface decay by tunnelling through the  $\text{SiO}_2$  layer, which is a process that depends on the thickness of the tunnel oxide.

#### 5.4d Dielectric properties of the $\text{La}_y\text{Zr}_{1-y}\text{O}_x/\text{SiO}_2$ stacks

##### (a) *EOT versus physical thickness*

Equivalent oxide thickness (EOT) of a dielectric layer/stack can be estimated only when the capacitance-in-series model is valid; i.e., when the electric field is uniform within the stack. In the presence of MW effect, which is an interfacial polarization effect due to different electric fields in the individual dielectric layers, this capacitance-in-series model cannot be simply expressed as the inverse-sum of individual capacitance values. Therefore, an attempt to estimate the EOT values with TiN injection and Si injection would give different values (since the capacitance also varies with the polarity of electron injection). Fig. 5.12 shows the relation between EOT and stack thickness of the  $\text{La}_y\text{Zr}_{1-y}\text{O}_x/\text{SiO}_2$  stacks, measured from TiN injection and Si injection conditions. With the TiN injection, the  $\text{EOT} = 5.72 \pm 0.42 \text{ nm}$ , while for Si injection,  $\text{EOT} = 3.45 \pm 0.49 \text{ nm}$ .

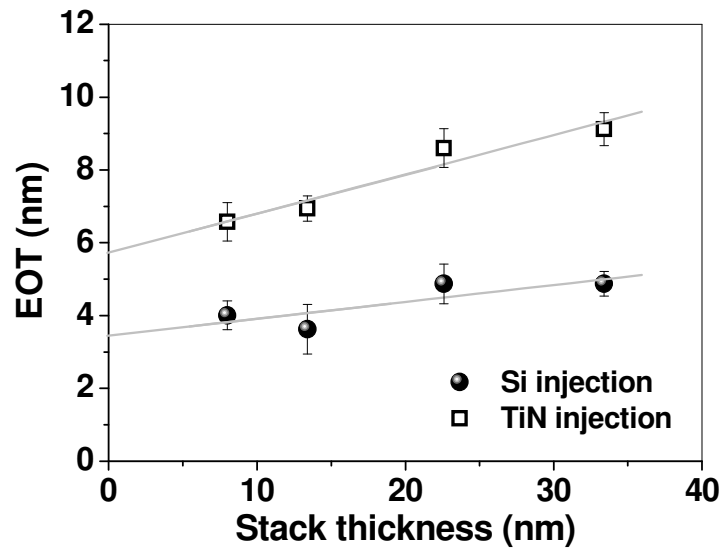


**Fig. 5.12.** EOT versus physical thickness of the  $\text{La}_y\text{Zr}_{1-y}\text{O}_x/\text{SiO}_2$  stacks measured from TiN and Si injection. The extrapolation to the EOT-axis is  $5.72 \pm 0.42$  nm for TiN injection and  $3.45 \pm 0.49$  nm for Si injection.

When TiN is negatively biased (TiN injection condition), one should expect a uniform electric field over the entire dielectric stack following the same reasoning mentioned in the previous section. On the other hand, MW effect appears when the electron injection is from the Si substrate, leading to interface polarizations. As a result, when the measurement frequency is low enough, the charged interface layer acts as a virtual electrode and only one of the two dielectric films is characterized. Therefore, the EOT values measured from Si injection should be horizontal, as seen in Fig. 5.12.

In summary, the measurement-dependent EOT values in Fig. 5.12 show that the capacitor-in-series model is indeed invalid for a stack that exhibits MW effect and therefore, the estimation of such dielectric stacks leads to erroneous results.

#### (b) Time to Breakdown ( $t_{BD}$ ) measurements

As discussed in Chapter 3, the electrical strength of dielectric materials is generally characterized by the total charge passing through the layer (at voltages low enough not to generate avalanche breakdowns) until the layer breaks down electrically. This parameter is called *charge to breakdown*, with the expression described by Eqn. (3.22) which is expressed as:

$$Q_{BD} = \frac{1}{A} \int_0^{t_{BD}} I_{Leak} dt \quad (5.6)$$

where the leakage current through the device is integrated over time, until it breaks down (at time  $t_{BD}$ ).

When a dielectric layer exhibits a clear Fowler-Nordheim tunnelling, constant current stress (CCS) would be an appropriate technique to estimate  $Q_{BD}$  values. However, since the degradation in dielectric films thinner than 4 nm has been found to be voltage-driven, constant voltage stress (CVS) measurements have been accepted as a more accurate technique to estimate  $Q_{BD}$  [17]. Therefore,  $Q_{BD}$  values of the  $\text{La}_y\text{Zr}_{1-y}\text{O}_x/\text{SiO}_2$  stacks were estimated using CVS measurements.

The total charge passing through the stack until it breaks down ( $Q_{BD}$ ) at constant voltage stress varies dramatically according to the direction of the electron injection. Fig. 5.13 shows  $Q_{BD}$  plotted as a function of the leakage current density for electron injection from silicon and TiN for 13 nm  $\text{La}_y\text{Zr}_{1-y}\text{O}_x/\text{SiO}_2$  stack:

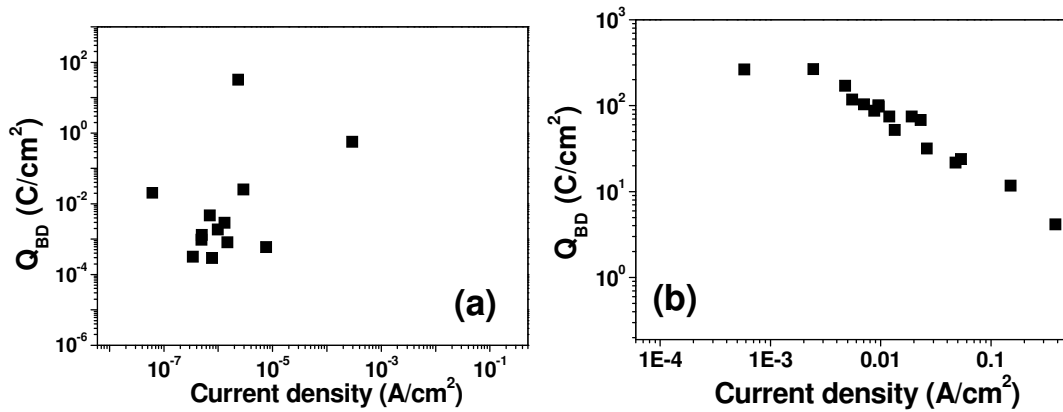


**Fig. 5.13.**  $Q_{BD}$  plotted as a function of the leakage current density through the layers for electron injection from (a) TiN and (b) silicon substrate. The data for each case were measured in the same bias voltage range.

Apparent from Fig. 5.13 is that for the same stress voltage across the Si and TiN injection, the leakage current and corresponding  $Q_{BD}$  values are different for electron injection from Si and TiN. While  $Q_{BD}$  measured under Si injection shows a typical power-law dependence with the current density,  $Q_{BD}$  values under TiN injection are very scattered. Fig. 5.14 shows the constant voltage stress (CVS) measurements of charge injection from Si and TiN electrodes:

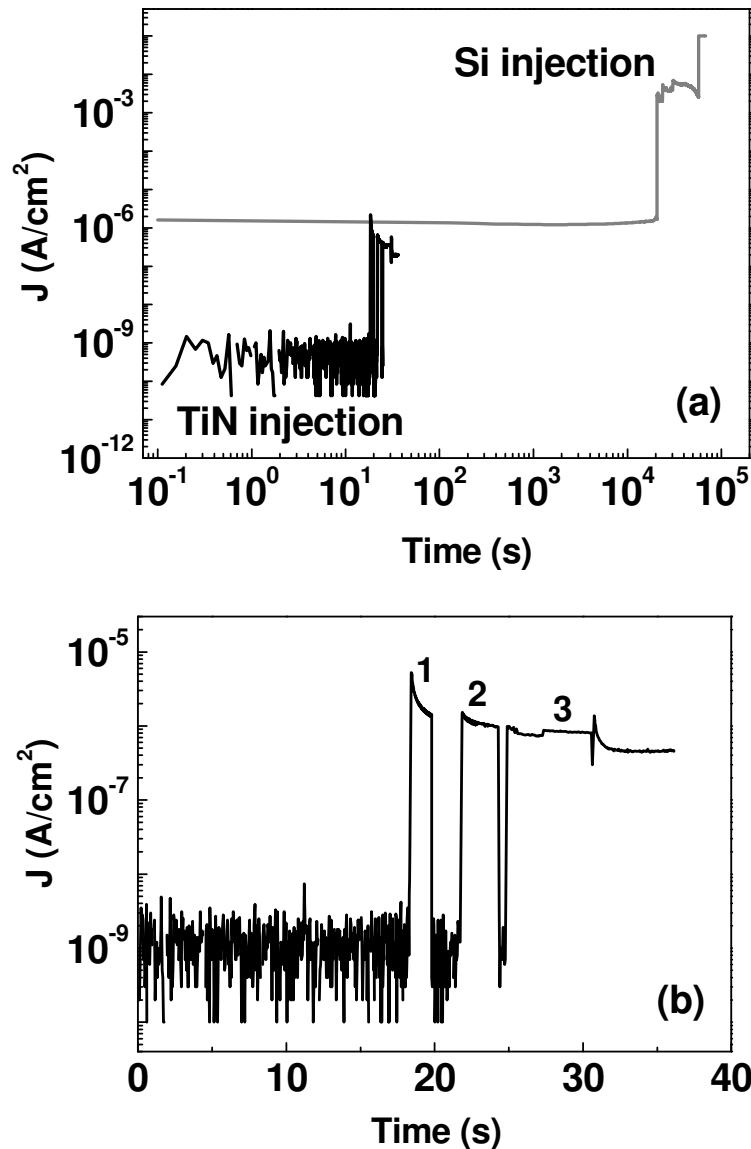


*Fig. 5.14. (a) CVS measurement at 7 V across the electrodes of 13 nm stack. (b) CVS measurement under TiN injection often exhibits jumps in leakage current.*

As Fig. 5.14 (a) shows, at the same stress voltage across the electrodes, the leakage current under Si injection is much larger than that from the TiN electrodes, which is in line with the  $J$ - $E$  measurements shown in Fig. 5. 5. On the other hand, when the electron injection is from TiN, occasional jumps in the leakage currents are observed, as seen in Fig. 5.14 (b). Such jumps in leakage currents usually occur in CVS measurements due to soft breakdowns in the dielectric film due to the formation of nanometric conduction paths connecting the defects. An existing theory explains that charge trapping around such narrow conducting channels can



turn it on and off [18]. However, due to the enhanced charge migration to the interfaces between the dielectric layers under silicon injection, the  $Q_{BD}$  measured under electron injection from silicon will be larger than that from TiN injection.

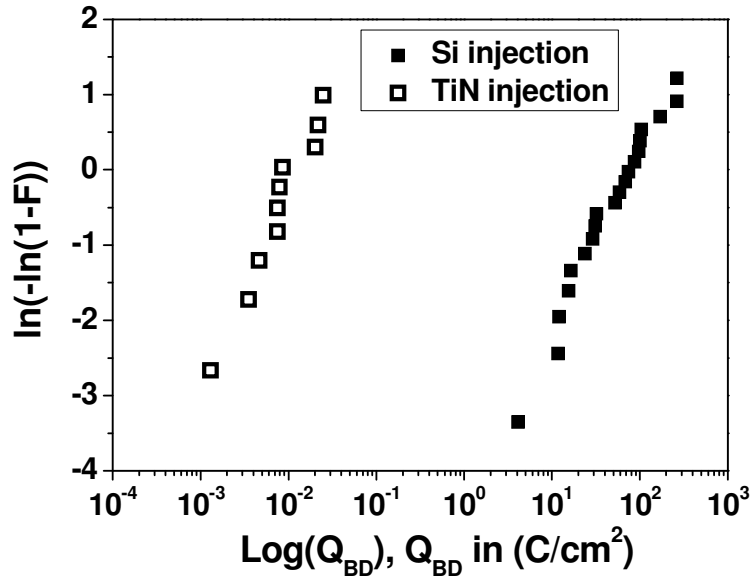


**Fig. 5.15.** Weibull distributions of charge to breakdown ( $Q_{BD}$ ) of 13.3 nm dielectric stack measured at constant stress voltage of 6.5 V during electron injection from the TiN (open squares) and from the silicon (solid squares).  $F$  is the cumulative distribution function of the device at this constant applied voltage.

Fig. 5.15 shows the Weibull distributions of  $Q_{BD}$  during electron injection from TiN and silicon electrodes at 6.5 V, where the average values are  $0.009 \text{ C/cm}^2$  and  $97.7 \text{ C/cm}^2$ , respectively. The distribution of  $Q_{BD}$  values under the Si-injection condition has a much larger slope, indicating less defined breakdown events, probably caused by enhanced charge migration to the  $\text{La}_y\text{Zr}_{1-y}\text{O}_x/\text{SiO}_2$  interface. Thermally grown silicon oxide has a  $Q_{BD}$  of  $\sim 10 \text{ C/cm}^2$  [19] and in the experiments reported in Chapter 3, a  $\text{La}_y\text{Zr}_{1-y}\text{O}_x$  layer deposited with the same composition directly on silicon gives a  $Q_{BD} \sim 8.7 \text{ C/cm}^2$ . These  $Q_{BD}$  values of the stack differ from this value in both injection directions, which may be the result of the Maxwell-Wagner charge transportation to the dielectric interface.

### 5.5 Lifetime measurements of the $\text{La}_y\text{Zr}_{1-y}\text{O}_x/\text{SiO}_2$ stacks

Trap generation is a statistical process, and it is known that the dielectric breakdown is directly linked to the neutral electron trap generation during high field stress [20]. This section investigates the dielectric strength of the  $\text{La}_y\text{Zr}_{1-y}\text{O}_x/\text{SiO}_2$  stacks using lifetime extrapolation measurements. For this, the stacks with  $\text{La}:\text{Zr} = 1:4$  described in the previous section are employed here as well. Since the defect formation in the dielectric stack is related to the applied bias voltage across it (due to the FN tunnelling of the electrons through the conduction band of the high- $k$  layer), the time-to-breakdown ( $t_{BD}$ ) is measured in this technique as a function of the bias voltage. Due to the statistical nature of defect generation under the applied bias across the stack, the measured  $t_{BD}$  values depend on the top electrode area of the capacitor. This is illustrated in Fig. 5.16 by measuring the  $t_{BD}$  values of 13.3 nm  $\text{La}_y\text{Zr}_{1-y}\text{O}_x/\text{SiO}_2$  stack for two different electrode areas.

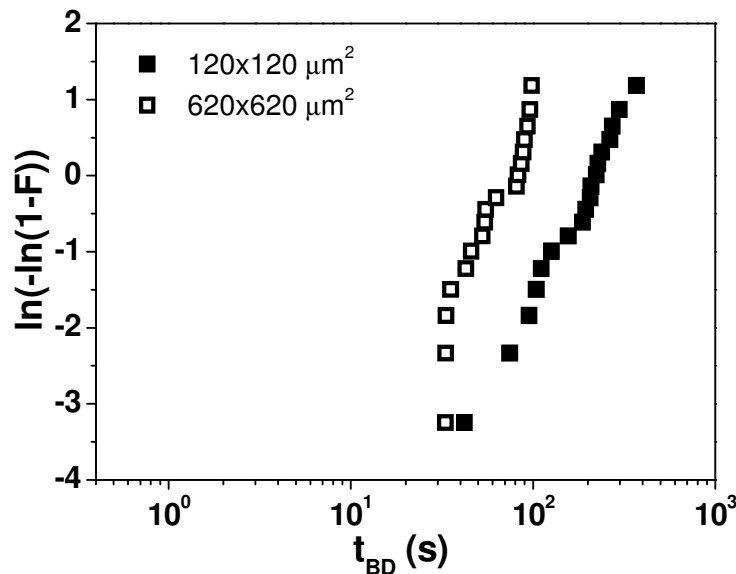


**Fig. 5.16.** Weibull distribution of  $t_{BD}$  values for two different TiN electrode areas, measured for TiN injection condition at 8V. Further measurements reported in this Chapter were carried out on devices with area  $120 \times 120 \mu\text{m}^2$ .

As discussed in Chapter 3,  $t_{BD}$  is determined by the voltage across the dielectric layer, which yields the following relationship [21]:

$$t_{BD} = t_0 \exp(-\gamma V) \quad (5.7)$$

where  $\gamma$  is the voltage acceleration factor and  $V$  is the applied voltage across the oxide. As

per this expression,  $t_{BD}$  has an exponential relation with the voltage. Fig. 5.17 shows the dependence of  $t_{BD}$  with bias voltage, for electron injection from Si and TiN.

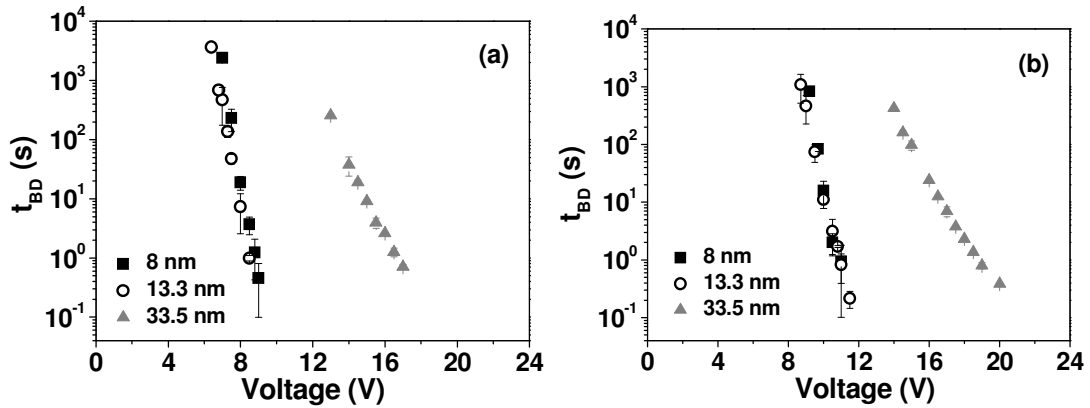


**Fig. 5.17.**  $t_{BD}$  values plotted as a function of voltage for (a) silicon injection and (b) TiN injection for the devices with different thicknesses of  $(\text{La}_y\text{Zr}_{1-y}\text{O}_x/\text{SiO}_2)$  stack. Capacitors with area of  $120 \times 120 \mu\text{m}^2$  were used for these measurements (at room temperature).

Using Eqn. (5.7), the acceleration parameter  $\gamma$  can be calculated for different thickness as plotted in Fig. 5.18.

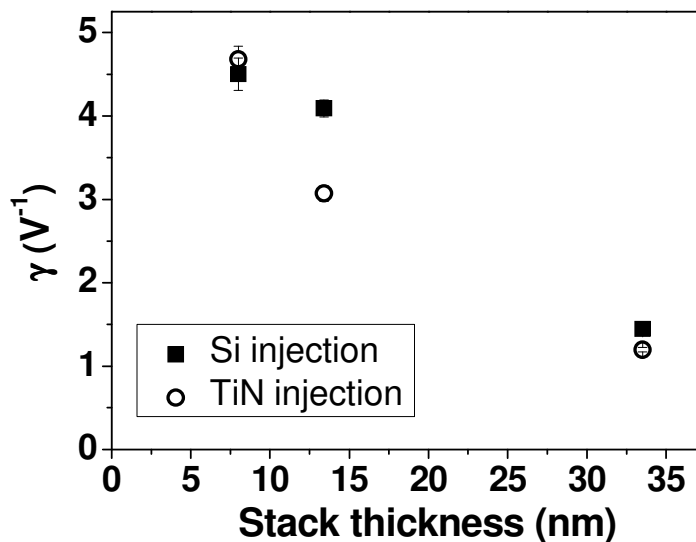


**Fig. 5.18.** The acceleration factor  $\gamma$  as a function of the layer thickness.

For very thin films ( $\sim 1.5$  nm) of HfSiON/poly-Si stack, acceleration factor of  $\gamma \sim 7$  decade/V has been reported (Ref. [15], page 53), which has a much larger degradation rate comparing to

the  $\text{La}_y\text{Zr}_{1-y}\text{O}_x/\text{SiO}_2$  stack reported here. However, the interface reactions are significant for high- $k$  materials with silicon compared to the standard  $\text{SiO}_2$  layers grown on silicon. Therefore, it should be noted that the exponential model given by Eqn. (5.7) is applicable only for thicker films so that the interface defect density will not influence the degradation rate considerably. This explains the linear decrease of the acceleration factor with the film thickness. On the other hand, acceleration parameter  $\gamma$  is a material parameter that is independent of the film thickness, and can be written as [22]

$$\gamma = -\left(\frac{\partial \ln t_{BD}}{\partial E}\right) = \frac{\Delta P}{k_B T} \quad (5.8)$$

where,  $E$  is the electric field and  $\Delta P$  is the change in polarization of the dielectric system from a stable to breakdown transition state. If we normalize  $\gamma$  plotted in Fig. 5.17 for the thickness,  $\gamma = 4.52 \pm 1.01 / (\text{MV}/\text{cm})$  for Si injection and  $\gamma = 3.93 \pm 0.18 / (\text{MV}/\text{cm})$  for TiN injection. This field-direction-dependence of  $\gamma$  is clearly due to the MW effect.

Another method for the lifetime extrapolation of dielectric films for different voltages is the *voltage power law model* given by [23]

$$t_{BD} \propto V^{-n} \quad (5.9)$$

The power law model gives a slightly more optimistic extrapolation compared to the exponential. Fig. 5.19 shows the power-law dependence of  $t_{BD}$  with voltage. The validity of Eqn. 5.9 has been illustrated in Fig. 5.19 (d), where the power  $n$  appears to have a strong dependence on the thickness as well as the bias polarity. The degradation rate for the 33.5 nm film is almost independent of the bias polarity (electron injection from Si or TiN), indicating that the degradation happens mainly in the high- $k$  layer. This illustrates the earlier assumption that a majority of electrons tunnel through the  $\text{SiO}_2$  towards the  $\text{La}_y\text{Zr}_{1-y}\text{O}_x/\text{SiO}_2$  interface and thus the degradation is dominated by defect formation in high- $k$  layers due to non-ballistic charge transport through the conduction band of  $\text{La}_y\text{Zr}_{1-y}\text{O}_x$  layer.

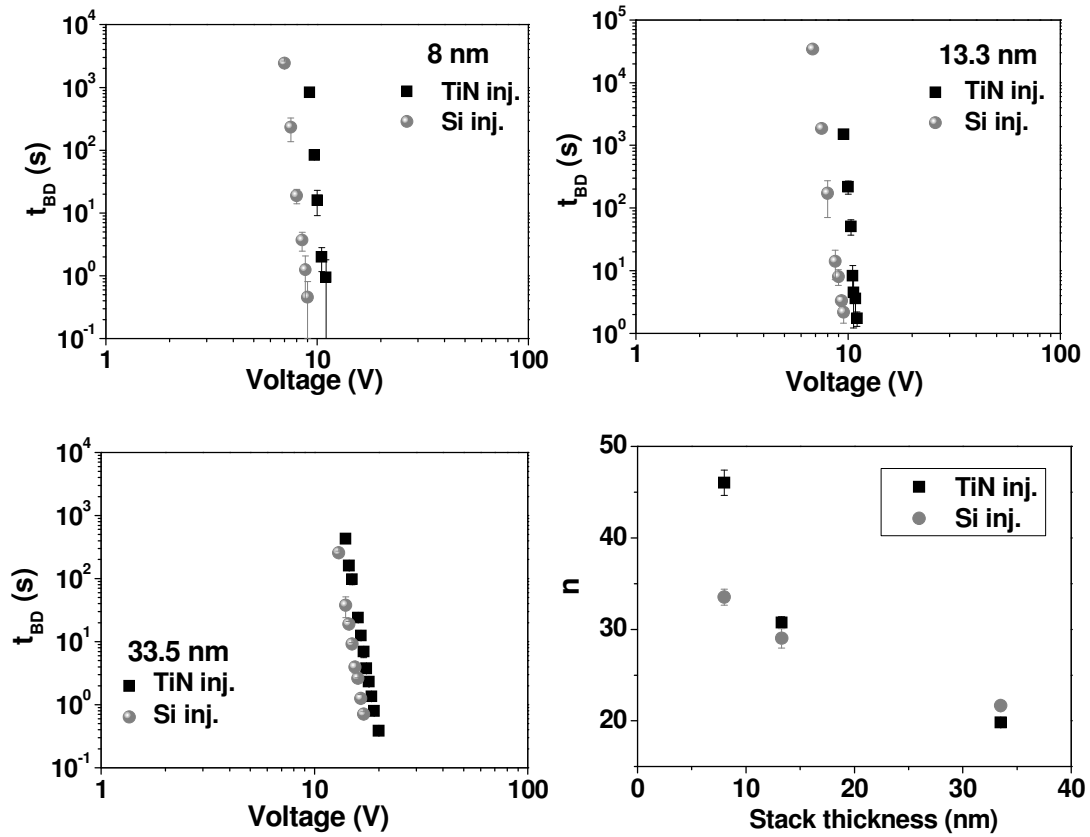


**Fig. 5.19.** Time-dependent breakdown data for the  $\text{La}_y\text{Zr}_{1-y}\text{O}_x$  ( $\text{La}:\text{Zr} = 1:4$ ) capacitors of different  $\text{La}_y\text{Zr}_{1-y}\text{O}_x/\text{SiO}_2$  stack thickness and the slope of the data, which is the power  $n$  in Eqn. (5.9).

For the thinnest stack (8 nm), the 10-year operation voltage measured from Si injection is 1.4 times lower than from TiN injection. This is because the high- $k$  layer is more vulnerable to defect generation than  $\text{SiO}_2$ . When the injection is from TiN, the total stack ( $\text{La}_y\text{Zr}_{1-y}\text{O}_x/\text{SiO}_2$ ) acts as the tunnel barrier and the degradation occurs due to the defect generation partially in  $\text{SiO}_2$  and in  $\text{La}_y\text{Zr}_{1-y}\text{O}_x$  layers. Therefore, it can be concluded that the thickness dependence of the power-law exponent also is an artefact of the asymmetric charge injection, of MW effect.

The power  $n$  plotted in Fig. 5.19 allows us to estimate the safe operational voltage of the device for continuous operation for 10 years. The result of such a lifetime extrapolation is plotted in Fig. 5.20 for various thicknesses of the stacks. The safe voltage for 10-year endurance of the device is larger when under the TiN injection than Si injection, because the effective dielectric stack thickness is larger from TiN injection.

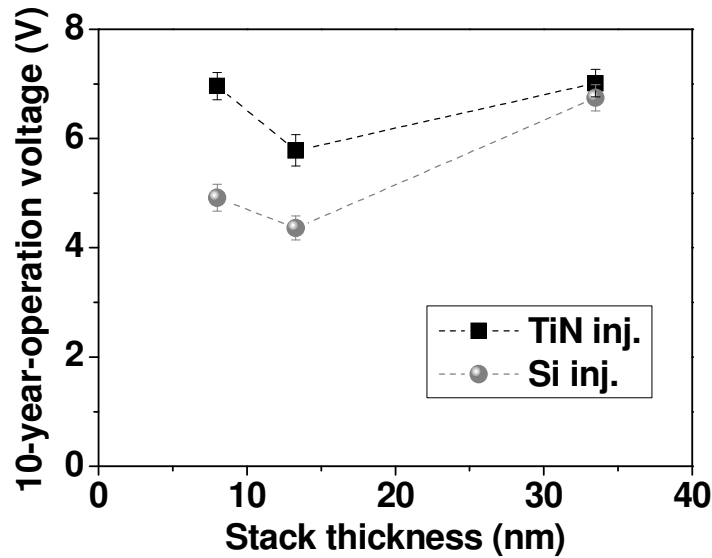


Fig. 5.20. Extrapolation of 10-year operational voltage of the  $\text{La}_y\text{Zr}_{1-y}\text{O}_x/\text{SiO}_2$  stacks as a function of the stack thickness.

### 5.5a Temperature dependence of the defect generation in $\text{La}_y\text{Zr}_{1-y}\text{O}_x/\text{SiO}_2$ stacks

Defect generation in dielectrics under a stress voltage is a thermally driven process [24,25] and has certain activation energy. Thus the rate of defect generation will be larger at elevated temperatures. (For the same reasons, the lifetime extrapolations according to industrial standards are done at 125°C, where the defect generation rate is much larger than at room temperature). Fig.5.21 and 22 show the lifetime measurements and 10-year operation voltage of 13.3 nm  $\text{La}_y\text{Zr}_{1-y}\text{O}_x/\text{SiO}_2$  stack at different temperatures from Si and TiN injection.

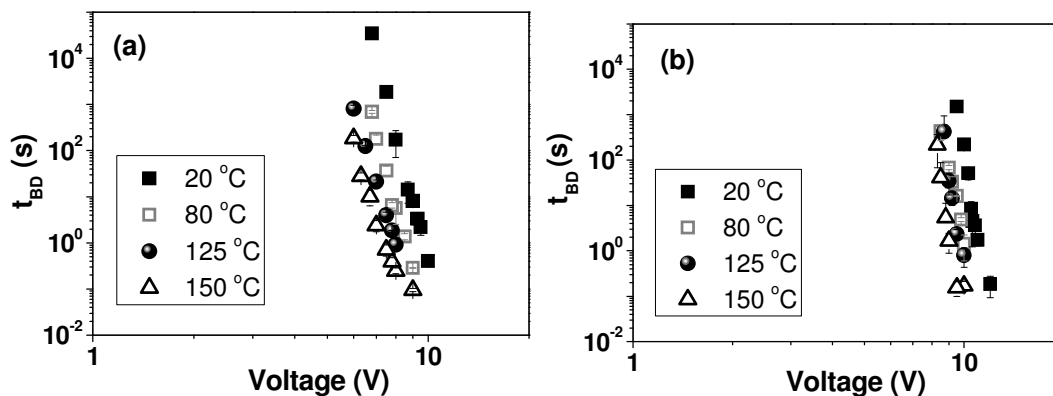


Fig. 5.21.  $\text{Log}(t_{\text{BD}})\text{-log}(V)$  plot for 13.3 nm  $\text{La}_y\text{Zr}_{1-y}\text{O}_x/\text{SiO}_2$  stack measured at different temperatures for (a) electron injection from Si and (b) electron injection from TiN.

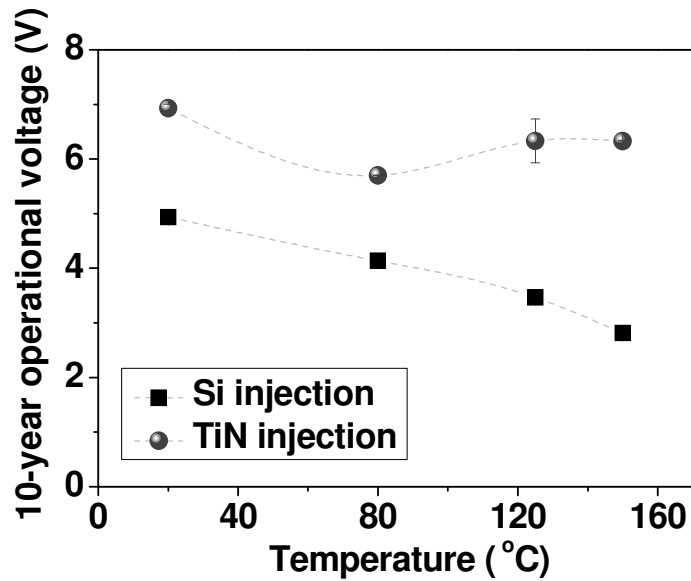


Fig. 5.22. 10-year operational voltage for 13.3 nm  $\text{La}_y\text{Zr}_{1-y}\text{O}_x/\text{SiO}_2$  stack extracted from Fig. 5.21, as a function of temperature.

The degradation rates, which explicitly reflect in the 10-year operational voltage of the stacks, appear to be very different when the electron injection is from Si than from TiN for 13.3 nm stack. Fig. 5.23 shows the  $\log(t_{BD})\text{-}\log(V)$  plot of 33.5 nm stack at different temperatures.

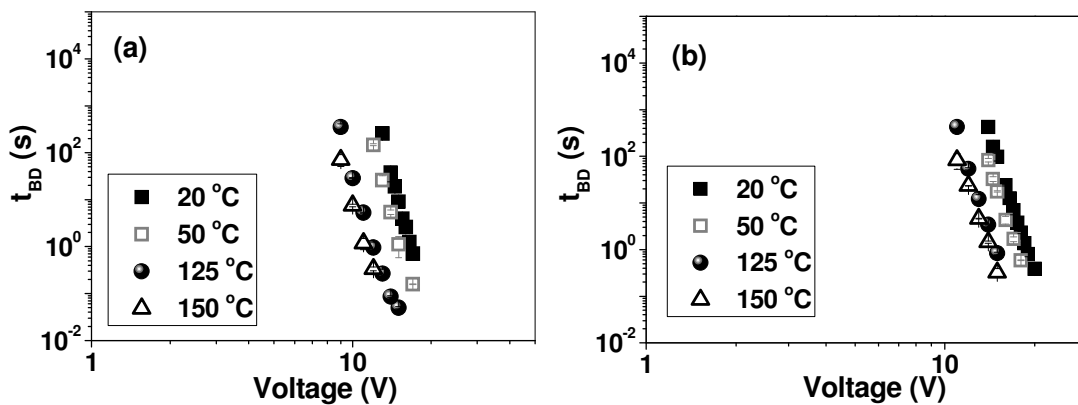
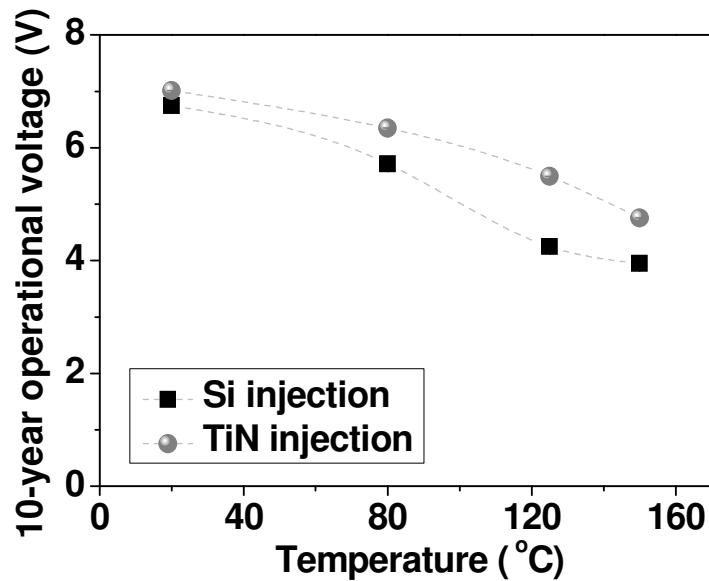


Fig. 5.23.  $\log(t_{BD})\text{-}\log(V)$  plot for 33.5 nm  $\text{La}_y\text{Zr}_{1-y}\text{O}_x/\text{SiO}_2$  stack measured at different temperatures for (a) electron injection from Si and (b) electron injection from TiN.



*Fig. 5.24. 10-year operational voltage for 33.5 nm  $\text{La}_y\text{Zr}_{1-y}\text{O}_x/\text{SiO}_2$  stack extracted from Fig. 5.22, as a function of temperature.*

The 10-year operational voltage extracted from Fig. 5.23 has been plotted in Fig. 5.24, where the degradations from Si and TiN injections have comparable behaviour. Contrasting to the temperature-dependent degradation behaviour of 13.4 nm thick films (Fig. 5.22), the degradation behaviour of the 33.5 nm film is comparable from both Si and TiN injection directions, meaning that the degradation is caused mainly by the  $\text{La}_y\text{Zr}_{1-y}\text{O}_x$  film in this stack. It means that when the thickness of the  $\text{La}_y\text{Zr}_{1-y}\text{O}_x$  film increases, MW effect becomes less and less noticeable (similar to the case of  $\sim 1$  nm interfacial oxide between Si and thicker ( $>10$  nm) high- $k$  layers where the interfacial oxide has hardly any influence of the degradation when the field is inverted). This complies well with the breakdown data shown in Fig. 5.6 where the asymmetry in the breakdown values is larger for thinner stack, and the discussion followed in section 5.4.3.

### 5.5b Arrhenius behaviour of defect generation in $\text{La}_y\text{Zr}_{1-y}\text{O}_x/\text{SiO}_2$ stacks

Figure 5.22 is suggesting that the degradation mechanism of the stack is different under different biasing conditions (due to the MW effect) and therefore, the defect generation in both cases should be triggered by different activation energies. Degradation of the dielectric stack is a thermally activated process. The activation energy of defect generation can be estimated from Arrhenius plots of the lifetime extrapolations, where  $\ln(1/t_{BD})$  is plotted



against  $1/T$ . The slope of the Arrhenius plots gives the activation energy of the defect generation in the stack.

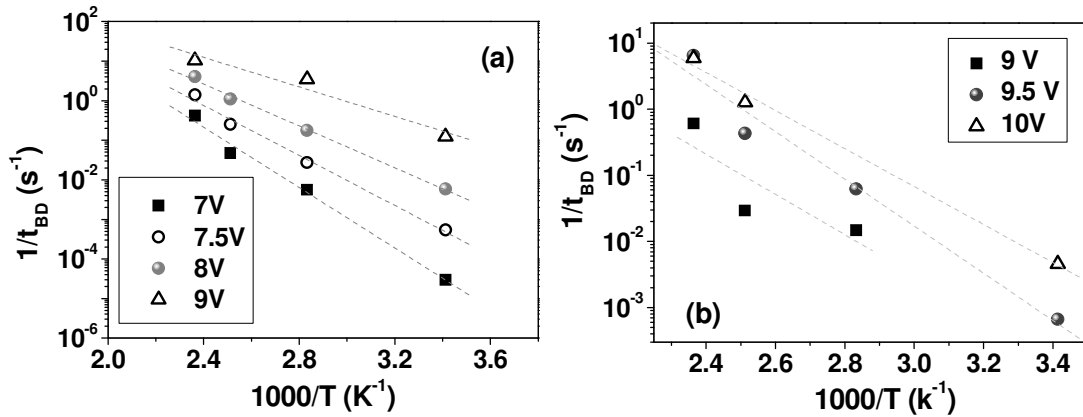


*Fig. 5.25. Arrhenius plot of  $1/t_{BD}$  plotted for 13.3 nm  $\text{La}_y\text{Zr}_{1-y}\text{O}_x/\text{SiO}_2$  stack (a) from Si injection and (b) from TiN injection.*

The Arrhenius plots shown in Fig. 5.25 suggest that the stress voltage influences the activation energy of the defect generation. Fig. 5.26 shows a plot between activation energy ( $\Delta E$ ) as a function of the stress voltage, when the electron injection is from Si and TiN.

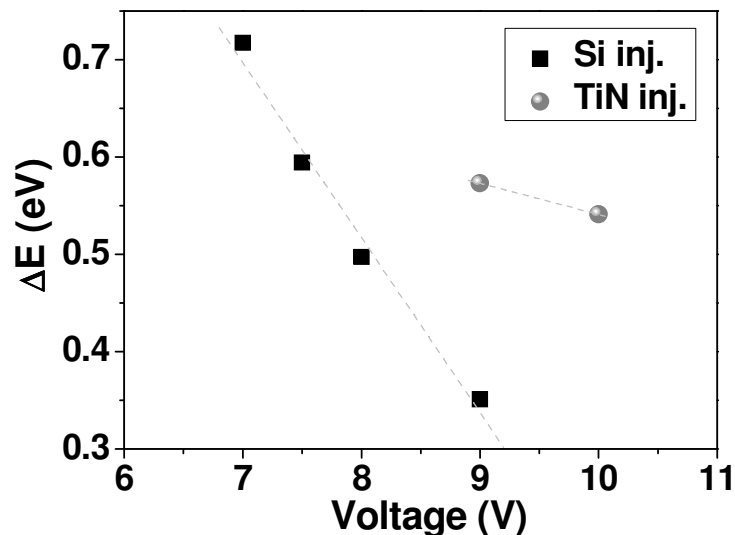


*Fig. 5.26. Activation energy of the defect formation as a function of the stress voltage for 13.3 nm stack, when the electron injection is from Si and TiN.*

Figure 5.26 shows that the activation energy of defect generation has a linear relationship with

the voltage (electric field). This behaviour is expected from the thermochemical E-model, which predicts that the enthalpy of activation (of bond-breaking, vacancy generation etc) in the presence of an electric field is lower due to the coupling of the dipoles with the electric field [26]. Activation energy of defect generation as a function of the electric field has been reported later by Dumin for  $\text{SiO}_2$  [27]. The enthalpy of defect generation  $\Delta H$  is related to the electric field by [28]

$$\Delta H = \Delta H_0 - p.E \quad (5.10)$$

where,  $\Delta H_0$  is the enthalpy of defect generation without an electric field,  $p$  is the permanent dipole moment of the molecules and  $E$  is the electric field. From a linear extrapolation of the data, the (thermal) enthalpy or the activation energy of defect generation at zero field (unbiased condition) can be estimated. Approximately,  $\Delta E_{\text{Si}}|_{V=0} = 1.96 \pm 0.1$  eV with dipole moment  $p \sim 24$  e Å is obtained for Si-injection condition (where the voltage is mostly across the high- $k$  layer) and  $\Delta E_{\text{TiN}}|_{V=0} = 0.86 \pm 0.03$  eV with  $p \sim 4.3$  e Å is obtained for TiN injection condition, where the voltage is across the whole stack.

A similar analysis for 33.5 nm stack is shown in Fig. 5.27, where the Arrhenius behaviour is shown for different stress voltages.

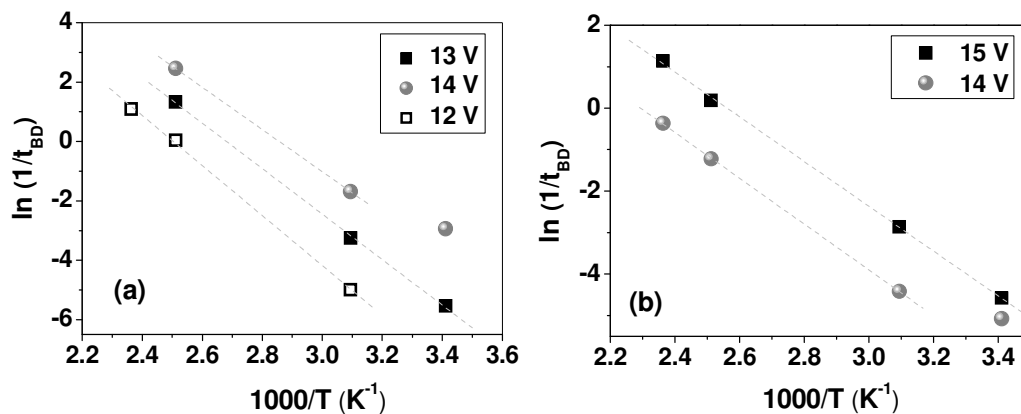
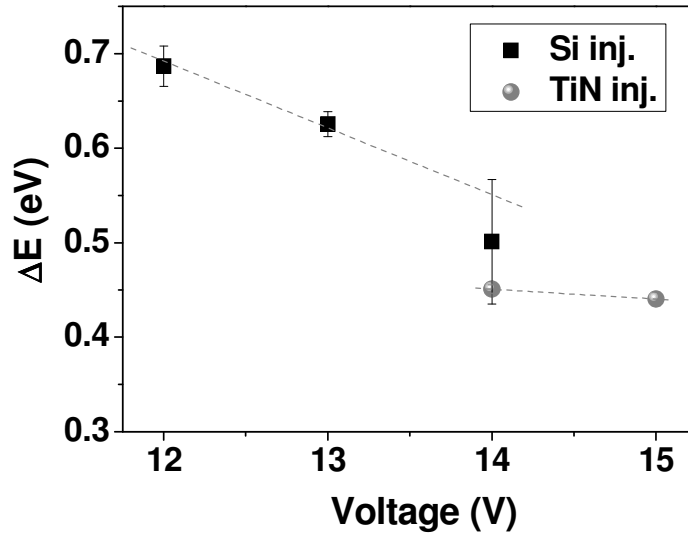


Fig. 5.27. Arrhenius plot of  $1/t_{BD}$  plotted for 33.5 nm  $\text{La}_y\text{Zr}_{1-y}\text{O}_x/\text{SiO}_2$  stack at different stress voltages.  $t_{BD}$  is expressed in seconds.



*Fig. 5.28. Activation energy of the defect formation as a function of the stress voltage for 33.5 nm stack, when the electron injection is from Si and TiN.*

The activation energies of defect generation at 0 V for 33.5 nm stack are estimated to be  $\Delta E_{Si} |_{V=0} = 1.5 \pm 0.3$  eV with  $p \sim 23.6$  e Å for Si injection condition and  $\Delta E_{TiN} |_{V=0} = 0.46 \pm 0.1$  eV with  $p \sim 3.5$  e Å for TiN injection condition.

Complying with the theory, the thermal activation of the defect generation should reduce the device lifetime at elevated temperature as seen in the case of electron injection from Si. When the electron injection is from Si, the electrons tunnel to the  $\text{La}_y\text{Zr}_{1-y}\text{O}_x/\text{SiO}_2$  interface and thus the degradation corresponds predominantly to the defect generation in the  $\text{La}_y\text{Zr}_{1-y}\text{O}_x$  layer. On the contrary, when the electron injection is from TiN, the degradation is due to the defect generation in the entire stack (both in  $\text{SiO}_2$  and in  $\text{La}_y\text{Zr}_{1-y}\text{O}_x$  films). Here the origins of the degradation are entirely of different nature: the degradation of the  $\text{SiO}_2$  layer is usually determined by the dissipative hydrogen ions tunnelling through the film [29], whereas the degradation in  $\text{La}_y\text{Zr}_{1-y}\text{O}_x$  is likely due to oxygen vacancy generation in the oxide. This could explain why the oxide degradation behavior is different when the electron injection is from TiN, compared to the standard degradation behavior exhibited by the film when the electron injection is from Si.

The MW effect can arise even in a single film sandwiched between metallic electrodes, due to the presence of mobile charges creating an additional charged layer at the metal-dielectric interface, as has been shown with  $\text{TiN}/\text{Ta}_2\text{O}_5/\text{TiN}$  MIM capacitors [30]. The MW

effect reported in this case is due to the migration of oxygen vacancies in the film, which has an activation energy of  $\Delta E = 0.98$  eV at 0 V bias. In the case of  $\text{La}_y\text{Zr}_{1-y}\text{O}_x/\text{SiO}_2$  stacks of 13.3 nm and 33.5 nm thicknesses, the activation energy obtained for the defect generation is  $\sim 1.9$  eV when the TiN electrode is negatively biased with respect to the Si substrate, while the activation energy varies when Si is negatively biased with respect to TiN. This asymmetry also is indicative of MW polarization depending on the bias conditions.

## 5.6 Conclusions

Nanolaminated dielectric stacks have been suggested as an efficient alternative to prevent leakage currents in MIS capacitors without drastic compromise with reduction in dielectric permittivity of the whole stack. But in this Chapter, striking gate-polarity asymmetries are observed, in capacitance, EOT, EBD, and TDDB. These asymmetries are qualitatively explained assuming that Maxwell-Wagner instability occurs. The capacitance asymmetry has further been quantitatively described using the MW theory, showing a very good correspondence between modelled and measured dielectric loss.

## 5.7 References

1. C.J. Först, C.R. Ashman, K. Schwarz, P.E. Blöchl, *Nature* **427**, 53 (2003).
2. Y. Liang, N. D. Theodore, J. Curless, C. Tracy, *J. Appl. Phys.* **99**, 066110 (2006).
3. V. Mikhelashvili, et al., *IEEE Electron Device Lett.* **27**, 344 (2006).
4. H. Kim, P.C. McIntyre, K.C. Saraswat, *J. Mater. Res.* **19**, 643 (2004).
5. S.-J. Ding et al., *IEEE Electron Device Lett.* **25**, 681 (2004).
6. S.-J. Ding et al., *J. Vac. Sci. Technol. B* **24**, 2518 (2006).
7. J.H. Klootwijk et al., *IEEE Electron Device Lett.* **29**, 740 (2008).
8. K.B. Jinesh et al., *Appl. Phys. Lett.* **93**, 172904 (2008).
9. J.R. Jameson et al., *IEEE Trans. Electron Dev.* **53**, 1858 (2006).
10. A. Ohtomo, D.A. Muller, J.L. Grazul, H.Y. Hwang, *Nature* **419**, 378 (2002).
11. A. Ebril, Y. Kim, R.A. Gerhardt, *Phys. Rev. Lett.* **77**, 1628 (1996).
12. D. O'Neill, R.M. Bowman, J.M. Gregg, *Appl. Phys. Lett.* **77**, 1520 (2000).
13. *Physics of Dielectrics for the Engineer*; R. Coelho, Elsevier Publications, Amsterdam, Ed.1, 1979, page 88-90.
14. *Physics of Solid Dielectrics (Fizica Dielectricilor Solizi)*, I. Bunget and M. Popescu, Elsevier Publications, Amsterdam, 1978, page 244-246.
15. T. Kauerauf, *Degradation and Breakdown of MOS gate stacks with High permittivity dielectrics*, PhD Thesis, Catholic University, Leuven (2007).
16. *Nonvolatile Semiconductor Memory Technology*, Edited by W.D. Brown, J.E. Brewer, IEEE Press, New York 1998, page 9.
17. P. Nicollian et al., *Proc. Int. Reliability Physics Symp.*, Page 7-15 (2000).
18. A. Crespo-Yepes et al., *Microelectronics Reliability* **49**, 1024 (2009).
19. *Deposited interpoly dielectrics for non-volatile memories*; J.H. Klootwijk, PhD Thesis, University of Twente, 1997.
20. R. Degraeve et al., *IEEE Trans. Electron Devices*, **45**, 904 (1998).
21. T. Nigam, *Growth kinetics, electrical characterization and reliability study of sub-5nm gate dielectrics*, PhD Thesis, Catholic University, Leuven (1999).
22. H. Cui, P.A. Burke, *Appl. Phys. Lett.* **84**, 2629 (2004).
23. E.Y. Wu, et al., *IEDM Technical Digest*, p. 541-544 (2000).
24. J. S. Suehle et al., *IEEE Int. Rel. Phys. Symp. Proc.* Page 95(2004).

25. S. Lombardo et al., *J. Appl. Phys.* **98**, 121301 (2005).
26. J.W. McPherson, D.A. Baglee, *J. Electrochem. Soc.* **132**, 1903 (1985).
27. D.J. Dumin, *J. Electrochem. Soc.* **142**, 1272 (1995).
28. J.W. McPherson, H.C. Mogul, *J. Appl. Phys.* **84**, 1513 (1998).
29. P.E. Blöchl, J.H. Stathis, *Phys. Rev. Lett.* **83**, 372 (1999).
30. J.-P. Manceau et al., Annual Report, *Conference on Electrical Insulation and Dielectric Phenomena*, Page 708 (2006).



# Chapter 6

## Electrical characterization of atomic-layer-deposited $\text{Er}_2\text{O}_3$ and $\text{Er}_y\text{Hf}_{1-y}\text{O}_x$ thin films

### 6.1 Introduction

Last chapters have been concentrating on the material properties of atomic layer deposited  $\text{La}_y\text{Zr}_{1-y}\text{O}_x$  and their peculiar electrical behaviour due to the spontaneous nanoclustering of  $\text{ZrO}_2$  in the films. This chapter concentrates on the electrical properties of a similar system in the Lanthanide series, Erbium oxide ( $\text{Er}_2\text{O}_3$ ) and its combinations with Hafnium to form  $\text{Er}_y\text{Hf}_{1-y}\text{O}_x$  thin films. A striking difference in the electrical properties of  $\text{La}_2\text{O}_3$  and  $\text{Er}_2\text{O}_3$  is that the conduction band offset (CBO) of  $\text{La}_2\text{O}_3$  with Si is smaller than the valence band offset (VBO) [1]. Therefore, the leakage current transport mechanism would be electron tunnelling through the conduction band of the oxide. As it will be discussed in detail in this Chapter,  $\text{Er}_2\text{O}_3$  has a larger CBO than the VBO, and therefore, the conduction mechanism may be hole-tunnelling through the valence band. This Chapter describes the dielectric properties of  $\text{Er}_2\text{O}_3$  films and the influence of adding hafnium in the material and dielectric properties of the films.

### 6.2 Dielectric properties of $\text{Er}_2\text{O}_3$ films

Erbium oxide ( $\text{Er}_2\text{O}_3$ ) has recently been proposed as an interesting future high- $k$  candidate because it has a static dielectric constant higher than 14 and very low interface trap density of  $4.2 \times 10^{10} \text{ cm}^{-2} \text{ eV}^{-1}$  which is comparable to standard silicon oxide gate dielectrics [2]. Moreover,  $\text{Er}_2\text{O}_3$  is one of the rare-earth oxides in the lanthanum series that has little silicon out-diffusion through it when deposited onto silicon substrates [3]. But despite the superior material characteristics of  $\text{Er}_2\text{O}_3$ , not much is known about the charge conduction mechanisms through thin  $\text{Er}_2\text{O}_3$  films, which is crucial in determining the reliability of the device. The basic conduction mechanism through  $\text{Er}_2\text{O}_3$  could be Fowler-Nordheim (FN) tunnelling of holes since the valence band offset is smaller than the conduction band offset with silicon [4]. However, the conduction band offset in epitaxially grown  $\text{Er}_2\text{O}_3$  films on (001) silicon surface

is reported to be 3.5 eV [5], which is comparable to most of the metal- $\text{Er}_2\text{O}_3$  structures. Therefore, the exact charge conduction mechanism through  $\text{Er}_2\text{O}_3$  thin films is still under debate even at low temperatures.

This section of the Chapter reports the electrical behaviour of atomic-layer-deposited  $\text{Er}_2\text{O}_3$  thin films grown on p-type Si (100) substrates, measured at different temperatures. We find that Poole-Frenkel (PF) conduction of electrons is a significant fraction of the total leakage current through TiN/ $\text{Er}_2\text{O}_3$ /Si MIS type capacitors at normal operational temperatures and electric fields. Analyzing various power-law regimes of current density-voltage ( $J$ - $V$ ) characteristics, the density of traps and interface states could be estimated. Further on, the electrical properties of the  $\text{Er}_y\text{Hf}_{1-y}\text{O}_x$  films are analyzed in this Chapter.

### 6.2a Details of deposition of $\text{Er}_2\text{O}_3$ and experimental techniques

Thin films of  $\text{Er}_2\text{O}_3$  with a thickness of 10 nm were deposited on p-type Si (100) substrates (with resistivity of 3-10  $\Omega\cdot\text{cm}$ ) in an ASM hot-wall, cross-flow PULSAR<sup>®</sup> 2000 ALCVD reactor at 325 °C. 2,2,6,6-tetramethylheptane-3,5-dionato erbium,  $\text{Er}(\text{thd})_3$  (from SAFC Hitech) was used as precursors for the  $\text{Er}_2\text{O}_3$  deposition, with ozone as the oxidizing agent. 100 nm TiN was sputter-deposited on the dielectric layers and the TiN/ $\text{Er}_2\text{O}_3$ /Si capacitors of sizes varying from  $120\times 120\ \mu\text{m}^2$  to  $1.02\times 1.02\ \text{mm}^2$  were created using standard lithography together with subsequent selective etching. The capacitor structures were analyzed as-deposited (i.e. without a post deposition anneal). The electrical measurements were performed with Agilent 4155C Semiconductor parameter analyzer and HP multi-frequency LCR meter.

### 6.2b Electrical characterization of as-deposited TiN/ $\text{Er}_2\text{O}_3$ /Si devices

This section describes the electrical properties of  $\text{Er}_2\text{O}_3$ , such as the charge conduction mechanism through the oxide that is related to the band-offsets with silicon, the tunnel barrier heights and the temperature dependence of the leakage current through the layers. The results of the capacitance-voltage measurements of  $\text{Er}_2\text{O}_3$  will be discussed together with the  $\text{Er}_y\text{Hf}_{1-y}\text{O}_x$  thin films in Section 6.3.

Figure 6.1 shows the leakage current density – electric field ( $J$ - $E$ ) characteristics of TiN/ $\text{Er}_2\text{O}_3$ /Si capacitors at different temperatures when the TiN electrode is negatively biased. The electric field ( $E$ ) is defined as the applied voltage across the electrodes divided by the



thickness of the  $\text{Er}_2\text{O}_3$  film determined by ellipsometry and high resolution transmission electron microscope (HRTEM).

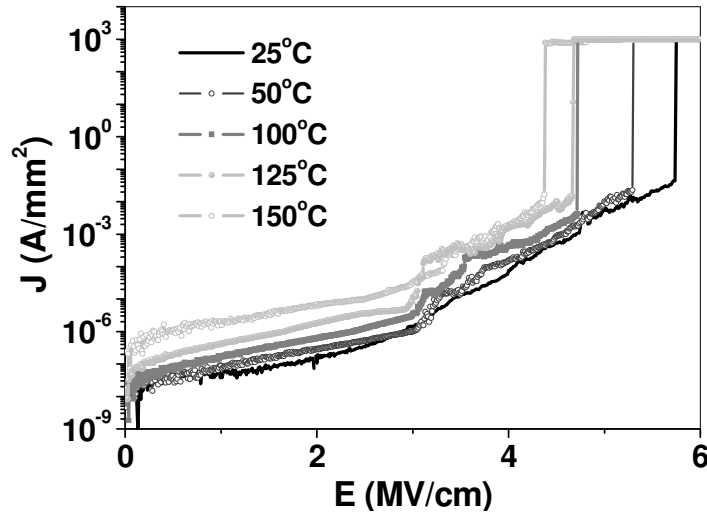


*Fig. 6.1. J-E characteristics of the TiN/ $\text{Er}_2\text{O}_3$ /Si devices at different temperatures.*

The  $J$ - $E$  curves are sensitive to the temperature of the device as is observed in Fig. 6.1. This temperature dependence of the leakage current is indicative of the trap levels in the oxide, which release charges (electrons or holes) by thermal excitation. Therefore, as discussed in Chapter 3, re-plotting the  $J$ - $E$  curves measured at room temperature as a  $\log(J)$ - $\log(V)$  plot given in Fig. 6.2, three regimes of the Ohmic conduction regime (region I), shallow-trap assisted conduction in the space-charge limited conduction (SCLC) regime (region II) and successively, trap-free conduction regime (region III) can be identified.

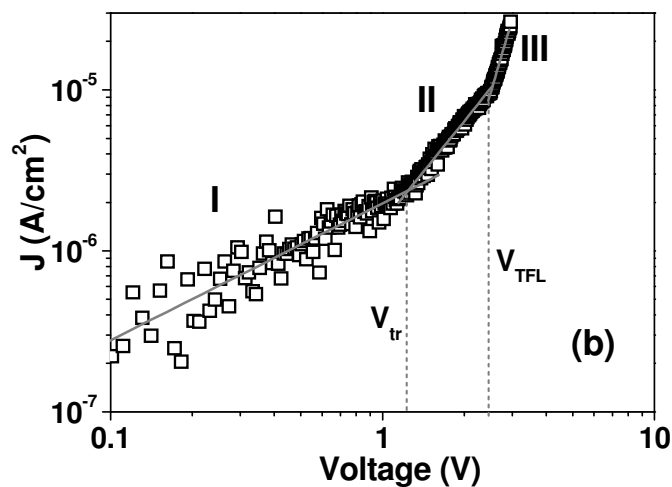


*Fig. 6.2.  $\log(J)$ - $\log(V)$  plot of TiN/ $\text{Er}_2\text{O}_3$ /Si device measured at room temperature. Three regimes of electrical conduction are indicated.*

From the *trap-filled limit voltage* ( $V_{TFL}$ ), i.e. the voltage at which the transition from the SCLC to trap-free conduction occurs, the trap concentration  $N_t$  can be estimated as [6]

$$V_{TFL} = qN_t d^2 / 2\epsilon_0 \epsilon_r \quad (6.1).$$

Here,  $\epsilon_r$  is the dynamic dielectric constant (= 3.85, derived from the refractive index of 1.963 reported for Er<sub>2</sub>O<sub>3</sub> thin films [2]) and  $d$  is the thickness of the film. Thus the trap concentration  $N_t$  was estimated to be  $4.8 \times 10^{18} / \text{cm}^3$ , which is well within the range of values of recently measured high- $k$  materials [7].

The current in the SCLC regime follows Child's law [8] where the current is proportional to  $V^2/d^3$  as given by

$$J_{Child} = 9\mu\epsilon_0\epsilon_r V^2 / 8d^3 \quad (6.2).$$

Therefore, the intersect of the SCLC regime in the  $J$ - $V$  plot in Fig. 6.2 gives the electronic mobility  $\mu$  for polycrystalline Er<sub>2</sub>O<sub>3</sub>, which is calculated to be  $1.05 \times 10^{-8} \text{ cm}^2/\text{Vs}$  at room-temperature. The free carrier density  $n_0$  at room temperature can be calculated from the Ohmic current in the SCLC regime (regime I) as

$$J_{Ohm} = qn_0\mu V / d \quad (6.3)$$

and is determined to be  $4.1 \times 10^{13} / \text{cm}^3$ . This low carrier density implies that the effective density of states in the conduction band ( $N_C$ ) is as low as  $1.6 \times 10^{17} / \text{cm}^3$ , which is more than an order of magnitude lower than the effective density of states for the oxides in the lanthanide series [8] (reported value for La<sub>2</sub>O<sub>3</sub> thin films is  $5.54 \times 10^{18} / \text{cm}^3$ ).

In order to estimate the interface trap density  $D_{it}$ , the parallel conductance  $G_p$  of TiN/Er<sub>2</sub>O<sub>3</sub>/Si capacitors as a function of the frequency was measured in accumulation voltages. Generally, the interface trap density can be estimated from the maximum value of  $G_p$  when measured as a function of frequency [9], and is given by the relation  $D_{it} = (G_p / \omega)_{Max} Z$ , where  $\omega = 2\pi f$ ,  $Z = (2.5 / qA)$  and  $A$  is the area of the capacitor. Fig. 6.3 shows  $Z(G_p / \omega)$  measured as a function of the frequency  $f$ , at 3V and 4V bias voltages (bias voltage higher than  $V_{TFL}$  applied to ensure that all the traps are filled), yielding a maximum that corresponds to the typical trap density of the material.

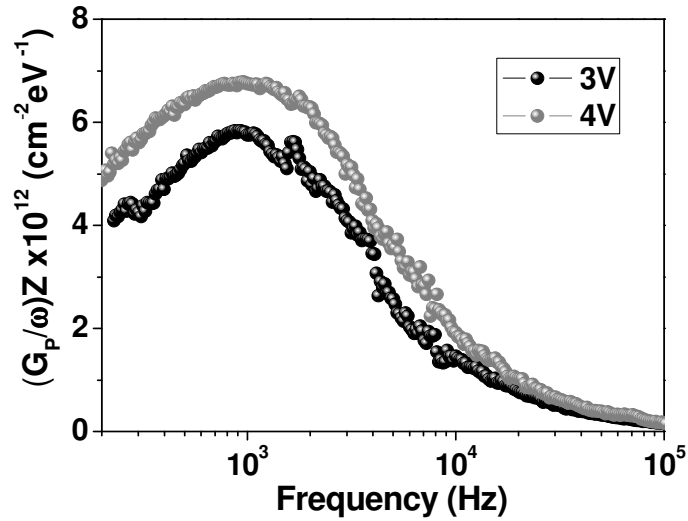


**Fig. 6.3.** The parallel conductance measurements as a function of the frequency. The vertical axis is  $(G_p/\omega) \times Z$  where  $Z = 2.5/2\pi A$ .

The average trap density  $D_{it}$  estimated is  $6.3 \times 10^{12} \text{ cm}^{-2} \text{ eV}^{-1}$ . This is well comparable with the value reported for as-deposited 11.2 nm thick  $\text{Er}_2\text{O}_3$  thin films grown on Si (001) substrates by metal-organic chemical vapour deposition ( $D_{it} = 3.4 \times 10^{12} \text{ cm}^{-2} \text{ eV}^{-1}$ ) [2], meaning that the  $\text{Er}_2\text{O}_3$  makes good interface with the silicon substrate.

Regarding the oxide quality in terms of the defects in the oxides, these imperfections at the interface could play a role, because of the dangling bonds originating from unsaturated  $\text{ErSiO}_x$  formation or due to oxygen vacancies in the oxide layer. As it has been discussed in detail in Chapter 3, the energy levels of these traps distributed closer to the conduction band of the oxide can be estimated from the Arrhenius behaviour of the leakage current at the SCLC regime. The leakage current in the SCLC regime is sensitive to the temperature, because the *shallow* traps liberate free electrons to the conduction band (or free holes to the valence band), which is a thermally activated process that follows Arrhenius law. The leakage currents measured at different temperatures is plotted in Fig. 6.4, where the current density follows an Arrhenius behaviour when  $\ln(J)$  is plotted against  $1/T$ . From the slope of this data, the average activation energy of the *shallow* traps obtained is  $\Delta E = 0.21 \pm 0.01 \text{ eV}$ .

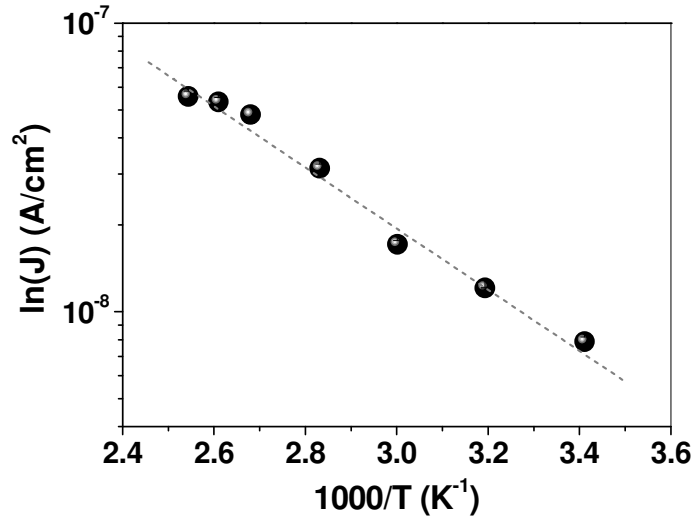


Fig. 6.4. Arrhenius behavior of leakage current through the Er<sub>2</sub>O<sub>3</sub> film at 1 MV/cm.

At electric fields lower than 3 MV/cm, the leakage current is resulting from the electrons that have sufficient energy to cross the TiN-Er<sub>2</sub>O<sub>3</sub> barrier, which can be theoretically estimated using the Schottky emission formula:

$$J_s = AT^2 \exp\left(\frac{-\phi_s + q\sqrt{qE / 4\pi\epsilon_0\epsilon_r}}{kT}\right) \tag{6.4}$$

where  $\phi_s$  is the Schottky barrier height and A is the effective Richardson constant [6]. The Schottky plot is shown in Fig. 6.5 for different temperatures.

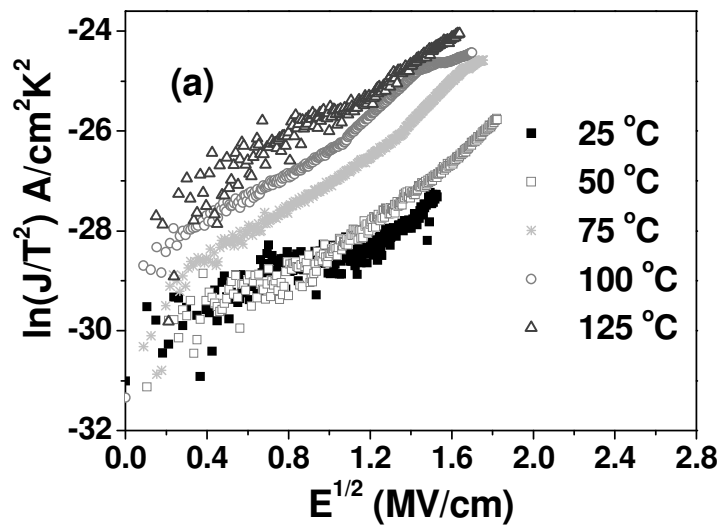


Fig. 6.5. Schottky plot of the leakage currents through TiN/Er<sub>2</sub>O<sub>3</sub>/Si device at different temperatures.

The work-function of silicon is 4.8 eV (as estimated in Chapter 3) and its conduction band offset with  $\text{Er}_2\text{O}_3$  is 3.5 eV [4]. Since the work-function of TiN (4.5 eV), the TiN- $\text{Er}_2\text{O}_3$  conduction band difference (the theoretical tunnel barrier height) should be 3.2 eV and  $\text{Er}_2\text{O}_3$ -Si valance band offset is 3.1 eV [4]. The intersect of the data in Fig. 6.5 on the  $\ln(J_s / AT^2)$  axis is given by  $\phi_s / kT$ . If we estimate the effective mass of charges from the theoretical barrier height, it would be  $0.049 m_0$ . This value is very comparable with the effective mass of the holes in  $\text{Er}_2\text{O}_3$ , which is  $0.068 m_0$  [4], indicating that the Schottky current is probably due to the conduction of holes through the  $\text{Er}_2\text{O}_3$  layer.

Since the leakage current behaviour is strongly temperature dependent at higher electric fields in the oxide, Poole-Frenkel charge injection is very likely to occur. The leakage current induced by PF charge conduction is given by [6,10]

$$J_{PF} = CE \exp\left(\frac{-\phi_t + q\sqrt{qE / \pi\epsilon_0\epsilon_r}}{kT}\right) \quad (6.5).$$

Here,  $C$  is a constant and  $\phi_t$  is the ionization energy of the traps that assist charge tunnelling and thermal hopping through the conduction band of the oxide.

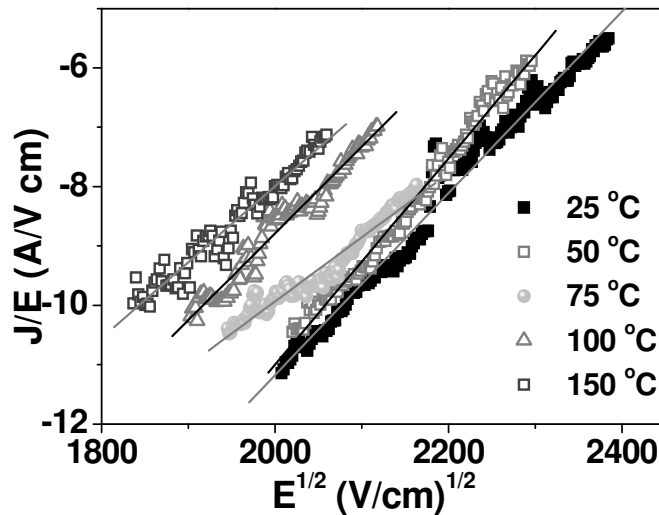


**Fig. 6.6.** Poole-Frenkel plot of the leakage current through TiN/ $\text{Er}_2\text{O}_3$ /Si device at different temperatures.

Figure 6.6 shows the PF plot of the current density of the device, where the data fall on straight lines when  $\ln(J/E)$  is plotted against  $\sqrt{E}$ . The intersect of the data on the  $J/E$  axis is

$\phi_i / kT$  and the slope of the lines is  $q\sqrt{q / \pi\epsilon_0\epsilon_r} / kT$ . From the intersect, the ionization energy of the deep traps is estimated to be  $\phi_i = 1.51 \pm 0.08$  eV. The dynamic dielectric permittivity estimated from the slopes is  $\epsilon_r = 3.88 \pm 0.22$ , from which the refractive index of Er<sub>2</sub>O<sub>3</sub> estimated is 1.97. This is in good agreement with the reported refractive index 1.963 of Er<sub>2</sub>O<sub>3</sub> [2].

The fact that the activation energy obtained from the Arrhenius plot in the given temperature range is much smaller than the trap energy estimated with the PF fitting indicates that the Arrhenius behaviour is due to the shallow interface trap levels, like dangling bonds and other imperfections at the interfaces, distributed closer to conduction band edge of the oxide. Therefore, the PF conduction should be originating from the deep trap levels, for instance, from the oxygen vacancies in the oxide.

At even higher electric fields, the conduction and valence bands of Er<sub>2</sub>O<sub>3</sub> bend in opposite directions and FN tunnelling of either electrons or holes occurs depending upon the band offsets with the electrodes. The current density due to FN tunnelling is given by

$$J_{FN} = \frac{q^3 m}{16\pi^2 \hbar m_{ox} \Phi_B} E^2 \exp\left(-\frac{4}{3} \frac{\sqrt{2m_{ox}}}{q\hbar E} \Phi_B^{3/2}\right) \quad (6.6)$$

where  $\Phi_B$  is the energy barrier height for tunnelling and  $m_{ox}$  is the electron effective mass in the Er<sub>2</sub>O<sub>3</sub>. Figure 6.7 shows the current density plotted as a FN plot ( $\ln(J/E^2)$  versus  $1/E$ ).

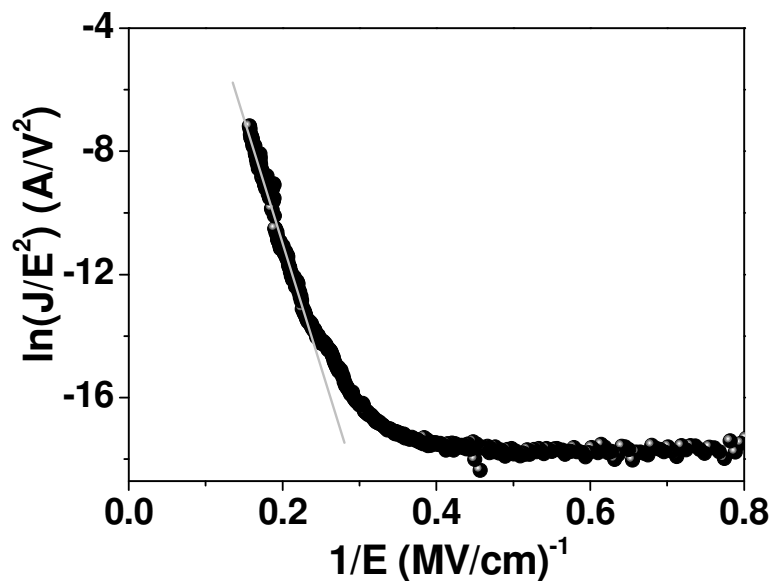


**Fig. 6.7.** Fowler-Nordheim tunnelling through of the leakage current through TiN/Er<sub>2</sub>O<sub>3</sub>/Si device.

Since the valence-band offset of  $\text{Er}_2\text{O}_3$  with silicon (3.1 eV) is smaller than their conduction band offset (3.5 eV), FN tunnelling of holes is likely to happen at higher fields through the valence band of the oxide which is in line with the arguments and results from a dedicated study on band offsets of  $\text{Er}_2\text{O}_3$  [4]. Using the effective mass of  $0.068 m_0$  for holes proposed by Yu et al., a barrier height of 3.13 eV is obtained, which is well comparable to the 3.1 eV of the valence band offset with Si. With the parameters obtained from the PF and FN tunnelling expression, the leakage current through the TiN/ $\text{Er}_2\text{O}_3$ /Si device can be modelled as shown in Fig. 6.8.

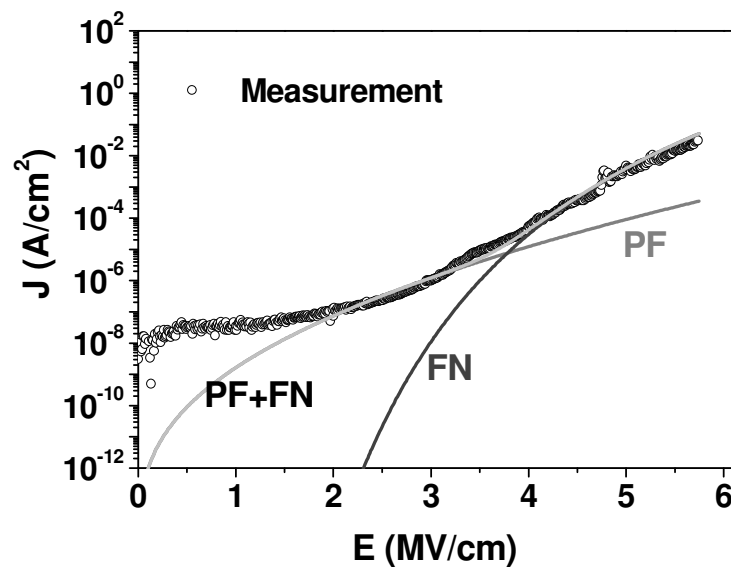
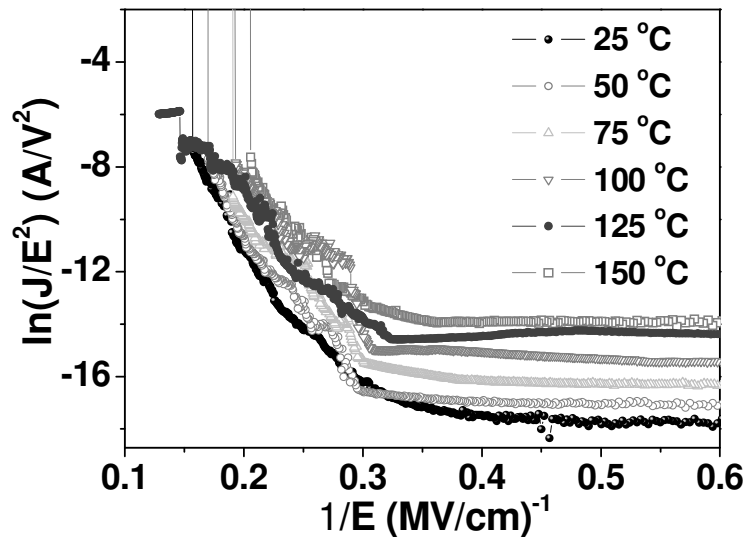


Fig. 6.8.  $J$ - $E$  data measured and theoretical fits with PF and FN tunnelling.

An alternative way of looking at the barrier height is to check the temperature dependence of the Fowler-Nordheim tunnelling. Theoretically, FN tunnelling should not be temperature dependent, because it is a purely quantum mechanical process where the electron (or hole) wavefunction in the conduction band of the TiN extends to the conduction band of the silicon, depending on the *effective* barrier width for tunnelling, which is a function of the electric field in the oxide. FN tunnelling expression given in Eqn. 6.6 is a solution to Schrodinger equation for a triangular energy barrier with a rounded edge. Even though FN tunnelling is theoretically independent of temperature, several experiments on various dielectrics report that the FN current density strongly increases with temperature. This increase in current density with temperature has been attributed mainly to two possibilities: the change in the transverse component of the electron effective mass tangential to the electrode-oxide interface

[11], and to the temperature dependence of the band-gap of the dielectric, which explicitly influences the barrier height  $\phi$  [12]. The observed linear reduction of the barrier height with increasing temperature ( $d\phi/dT$ ) is of the order of  $10^{-3}$  to  $10^{-4}$  eV/K [12,13] and can be related to intrinsic properties of the dielectric materials. Another model explains this phenomenon on the basis of the thermal fluctuation of the local microscopic barrier height [14]. Despite numerous models, the exact picture of the temperature dependence of the barrier height still remains ambiguous.

If the measured tunnel barrier height is a function of temperature, then the whole discussion about the effective mass for the data measured at room temperature would become meaningless. The FN plots of the leakage current through the TiN/ $\text{Er}_2\text{O}_3$ /Si device at different temperatures are shown in Fig. 6.9.



**Fig. 6.9.** Fowler-Nordheim tunnelling through of the leakage current through TiN/ $\text{Er}_2\text{O}_3$ /Si device at different temperatures.

In conclusion,  $\text{Er}_2\text{O}_3$  appears to exhibit both Poole-Frenkel electron injection at lower electric fields (i.e.  $< 3$  MV/cm) and normal temperatures, while undergoing Fowler-Nordheim hole tunnelling at higher electric fields. The major electrical and material parameters of atomic-layer deposited  $\text{Er}_2\text{O}_3$  thin films estimated from  $J$ - $E$  measurements are listed in Table 6.1.

Density of states in the conduction band ( $N_C$ )	$1.6 \times 10^{17}/\text{cm}^3$
Trap density	$6.3 \times 10^{17}/\text{cm}^2 \text{ eV}$



Interface trap density $D_{it}$	$6.3 \times 10^{12} \text{ cm}^{-2} \text{ eV}^{-1}$
Activation energy of traps ( $\Delta E$ )	$0.21 \pm 0.01 \text{ eV}$
Trap concentration ( $N_t$ )	$4.8 \times 10^{18} / \text{cm}^3$
Trap ionization energy ( $\phi_t$ )	$1.514 \pm 0.085 \text{ eV}$
Charge mobility	$1.05 \times 10^{-8} \text{ cm}^2/\text{Vs}$
Dynamic permittivity $\epsilon_r$	$3.88 \pm 0.22$
Si/ $\text{Er}_2\text{O}_3$ barrier height	$3.13 \text{ eV}$

**Table 6.1.** The major electronics parameters of  $\text{Er}_2\text{O}_3$  estimated from this study.

### 6.3 Dielectric properties of $\text{Er}_y\text{Hf}_{1-y}\text{O}_x$ films

Hafnium and zirconium-based high- $k$  materials exhibit striking dielectric properties when alloyed with rare-earth metal oxides [15,16,17]. For instance,  $\text{HfO}_2$  can be stabilized in a high-permittivity tetragonal phase with  $k$ -values up to 25-30, when doped with foreign elements like Si, Y, La, Dy, Sc, and Er [15,17]. Among these dopants, Er was chosen to form  $\text{Er}_y\text{Hf}_{1-y}\text{O}_x$  thin films, due to apparent reasons mentioned in the previous section that erbium oxide ( $\text{Er}_2\text{O}_3$ ) has several properties that make it attractive for high- $k$  applications, like the larger conduction band offset, and thus lower leakage current, though it has a comparatively low dielectric constant of 12-17 [2,18]. It has been reported that amorphous  $\text{HfO}_2$  can be deposited by ALD technique by incorporating La in it and the crystallization temperature increases with the La-content in the film [19]. On the other hand, little is known about the dielectric properties and high- $k$  phase-stabilization of ALD  $\text{HfO}_2$  thin films when mixed with  $\text{Er}_2\text{O}_3$  [20].

This section concentrates on the dielectric properties of atomic-layer deposited  $\text{Er}_y\text{Hf}_{1-y}\text{O}_x$  thin films. The impact of varying erbium concentration on high permittivity phase formation is systematically investigated to achieve optimum permittivity and leakage current properties at low annealing temperatures.

#### 6.3a Dielectric properties of $\text{Er}_y\text{Hf}_{1-y}\text{O}_x$ films

The deposition of  $\text{Er}_y\text{Hf}_{1-y}\text{O}_x$  thin films is similar to the deposition of  $\text{Er}_2\text{O}_3$  mentioned in section 6.2.1. Bis(methylcyclopentadienyl)methylmethoxy hafnium (IV), ‘HfD-04’ (SAFC

Hitech) was used as precursors for the  $\text{HfO}_2$  deposition, with ozone as the oxidizing agent.  $\text{Er}_y\text{Hf}_{1-y}\text{O}_x$  films were grown at  $325^\circ\text{C}$  applying alternating precursor cycles of Er and Hf. 100 nm TiN was sputter-deposited and patterned to form top electrodes. The electrical measurements were done with an Agilent 4155C Semiconductor parameter analyzer and an HP multi-frequency LCR meter. A forming gas rapid thermal anneal (RTA) at  $460^\circ\text{C}$  for 10 minutes was applied to passivate interface states.

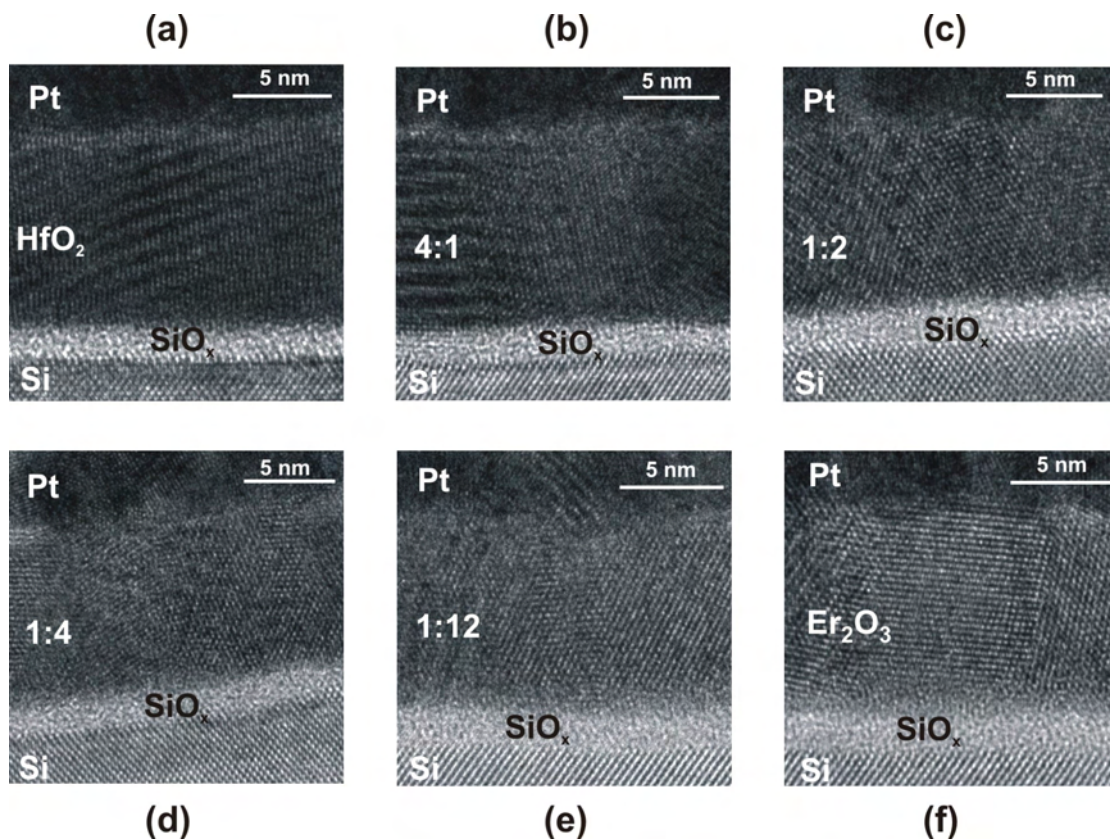


**Fig. 6.10.** HRTEM images of thin films of (a)  $\text{HfO}_2$ , (b) Hf:Er = 4:1, (c) Hf:Er = 1:2, (d) Hf:Er = 1:4, (e) Hf:Er = 1:12, (f)  $\text{Er}_2\text{O}_3$  deposited on Si substrate. Pt was used as the protection layer for the samples.

Figure 6.10 shows the High-Resolution Transmission Electron Microscope (HR-TEM) images of six representative as-deposited films with different stoichiometries: (a)  $\text{HfO}_2$ , (b)  $\text{Er}_y\text{Hf}_{1-y}\text{O}_x$  with Hf:Er pulse ratio = 4:1, (c) Hf:Er = 1:1, (d) Hf:Er=1:2, (e) Hf:Er=1:4, and (f)  $\text{Er}_2\text{O}_3$ . The films were targeted to have the same thickness of 10 nm. All the samples appear to be polycrystalline and show a bright interfacial  $\text{SiO}_x$  layer with a thickness between 1.1 and 1.5 nm. Only the  $\text{Er}_2\text{O}_3$  and the  $\text{Er}_y\text{Hf}_{1-y}\text{O}_x$  film with Hf:Er pulse ratio = 1:12 shows the presence of a 1 nm thick amorphous layer on top of the interfacial oxide whereas all the other

high- $k$  films appear to be polycrystalline throughout. This amorphous layer was included in the thickness of the  $\text{Er}_y\text{Hf}_{1-y}\text{O}_x$  films as tabulated in Table 6.2. The composition of the interfacial oxide was measured by High Angle Annular Dark Field Scanning Transmission Electron Microscopy (HAADF STEM) in combination with Energy Dispersive X-ray spectrometry (EDX). The HAADF–EDX line scans of the films with different Hf:Er ratio are depicted in Fig. 6.11.

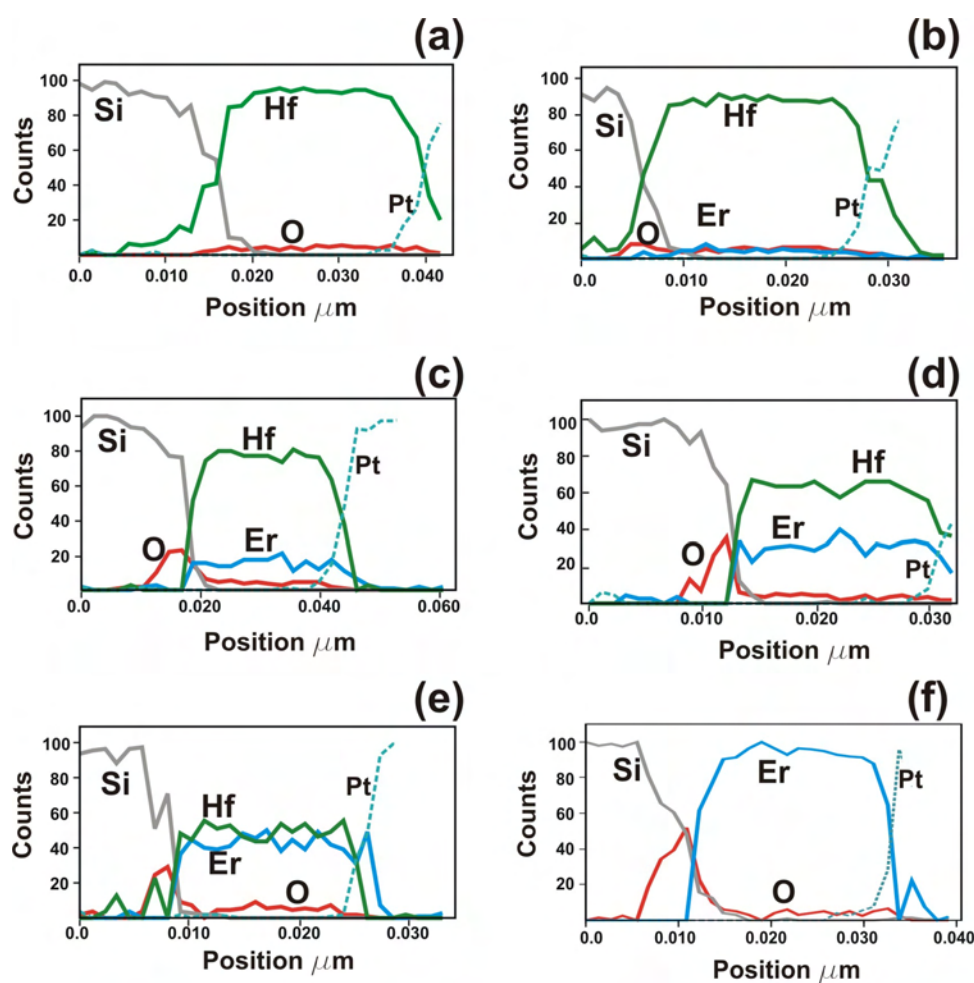


**Fig. 6.11.** HAADF–EDX line scan of the films with different Hf:Er ratio: (a)  $\text{HfO}_2$ , (b)  $\text{Er}_y\text{Hf}_{1-y}\text{O}_x$  film with pulse ratio of Hf:Er = 4:1, (c) Hf:Er = 1:1, (d) Hf:Er = 1:2, (e) Hf:Er = 1:4 and (f)  $\text{Er}_2\text{O}_3$ , please note that the line scans were not taken perpendicularly to the Si-substrate but under an angle of  $45^\circ$  to allow more resolution over the different interfaces.

The  $\text{HfO}_2$  and Hf-rich (4:1) samples seem to contain a hafnium silicate layer which would indicate Hf diffusion into the  $\text{SiO}_2$  interface during ALD film growth. In contrast, the  $\text{Er}_2\text{O}_3$

and the Er<sub>y</sub>Hf<sub>1-y</sub>O<sub>x</sub> samples containing more than 27 at. % Er show a sharp SiO<sub>2</sub>-high-*k* interface. However, the EDX profile of the HfO<sub>2</sub> and Hf-rich (4:1) samples suffered from sample drift that could not be corrected during sampling. This might also be the reason why the interfacial SiO<sub>2</sub> layer is not observed with HDAAF-EDX while it is clearly visible in the HRTEM images. Moreover, the apparent presence of Hf and also Er in the Si substrate is a quantification artifact due to normalisation of concentrations in regions with low X-ray count rate such as the Si-substrate. In order to elucidate whether the interface oxide contained hafnium Energy Filtered TEM (EFTEM) was performed. In this case the EFTEM image was filtered for the typical SiO<sub>2</sub> plasmon loss and shows a bright SiO<sub>2</sub> layer with equally sharp interfaces to Si as to the high-*k* layer indicating that Hf diffusion could be ruled out.

Hf/Er pulse ratio	Number of cycles	Growth rate (Å/cycle)	Hf in at. % (XRF)	Thickness high- <i>k</i> (nm) (XRR)	Thickness high- <i>k</i> (nm) (HRTEM)	Thickness interfacial SiO <sub>x</sub> (nm) (HRTEM)
1:0	200×(1+0)	0.56	100	9.7	10.2	1.1
4:1	45×(4+1)	2.46	86.9	10.4	10.9	1.3
1:1	128×(1+1)	0.81	72.4	10	10.3	1.5
1:2	95×(1+2)	1.10	57.5	9.1	9.0	1.4
1:4	68×(1+4)	1.52	43.9	9.7	10.2	1.2
1:12	31×(1+12)	2.53	20.5	9.1	9.8	1.1
0:1	458×(0+1)	0.21	0	9.3	10.8	1.3

**Table 6.2.** The ALD deposition parameters of the films, Hf at.% in the films measured using XRF, the high-*k* thickness measured using XRR and HRTEM together with the thickness of the native oxide measured using HRTEM. The variation of the growth rates in the films is due to the different -OH ligand density on the surfaces terminated with -Hf-OH and Er-OH groups (that comes from steric hindrance, ion size, and their coordination). The interfacial oxide thickness has been determined with HRTEM. Targeted film thickness was 10 nm.

The pure  $\text{Er}_2\text{O}_3$  sample shows a relative sharp Si gradient into the  $\text{Er}_2\text{O}_3$  film which indicates that silicon out-diffusion into the high- $k$  layer did not occur. This implies that the amorphous layer in the HRTEM image in between the  $\text{SiO}_2$  and the polycrystalline  $\text{Er}_2\text{O}_3$  film is due to an amorphous  $\text{Er}_2\text{O}_3$  layer. Table 6.2 summarizes the employed pulse ratio of the Er and Hf precursors, the composition of the films determined with X-ray fluorescence spectroscopy (XRF), and the high- $k$  and interfacial oxide film thicknesses measured by X-ray reflectivity (XRR) and HR-TEM. As is evident from Table 6.2 a good correlation is found between the XRR and HR-TEM thickness measurements.

### 6.3b C-V characteristics of $\text{TiN}/\text{Er}_y\text{Hf}_{1-y}\text{O}_x/\text{Si}$ devices

Capacitance-voltage ( $C$ - $V$ ) measurements were performed on the as-deposited and annealed films at 500 Hz (50 mV) frequency. The  $C$ - $V$  plots are depicted in Fig. 6.12 (a) and 6.12 (b), respectively. The  $C$ - $V$  characteristics are remarkably improved after RTA, with less dispersion due to interface states at the accumulation capacitance and better capacitance saturation in accumulation voltages.

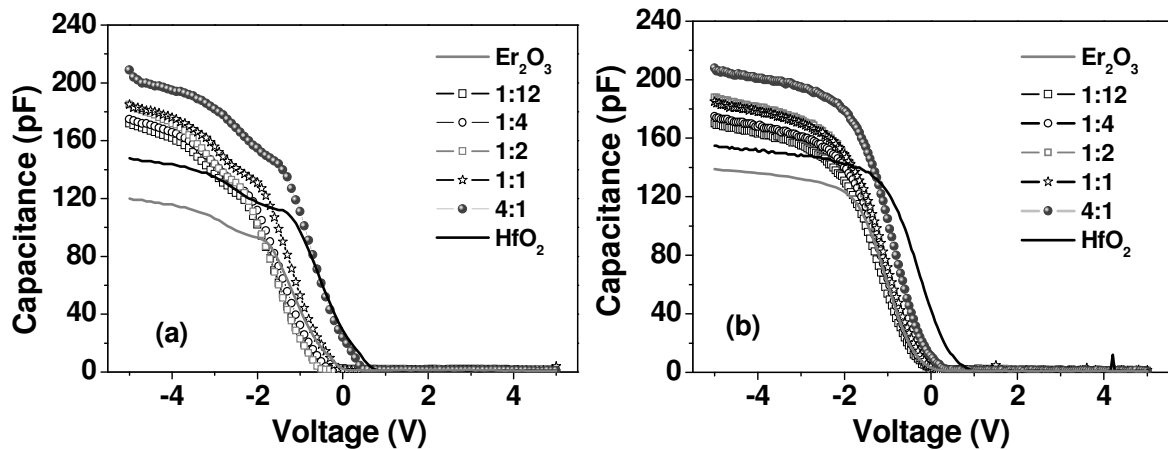


**Fig. 6.12.**  $C$ - $V$  curves of (a) as-deposited and (b) rapid-thermal-annealed (RTA)  $\text{Er}_y\text{Hf}_{1-y}\text{O}_x$  films.

The permittivities of the films were derived from the accumulation capacitance employing the individual thickness of high- $k$  layer and interface oxide as measured with HR-TEM, given in Table 6.2. The dielectric constants plotted in Fig. 6.13 (a) shows a consistent increase in the dielectric constant with increasing Hf percentage in the film. There is hardly any change in

the dielectric constants after RTA. However, while the estimated  $k$ -value of  $\text{Er}_2\text{O}_3$  is 14.5 and of  $\text{HfO}_2$  is 17.8, the mixed oxide films have dielectric constants peaking up to 37.6 for films that contain 87 % Hf. For comparison, the reported  $k$ -values of ALD-synthesized  $\text{Er}_2\text{O}_3$  is 10-17 [2,18] and that of  $\text{HfO}_2$  is 18 [20].

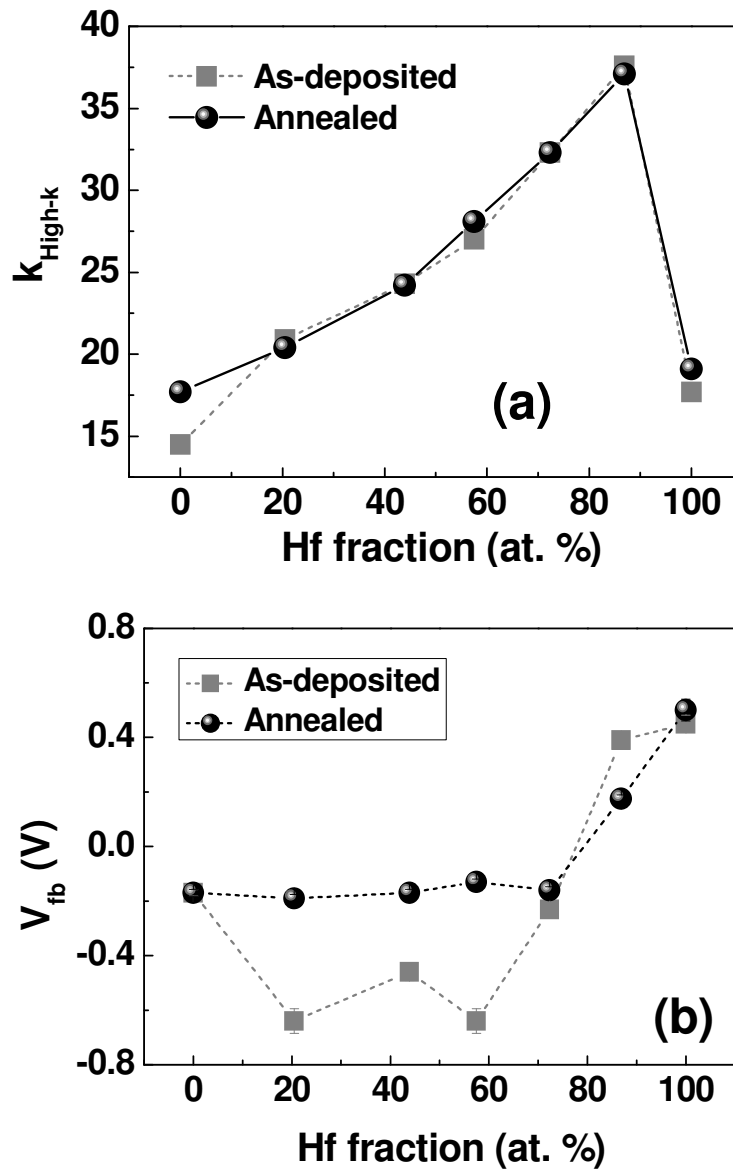


**Fig. 6.13.** (a) The dielectric constant of the  $\text{Er}_y\text{Hf}_{1-y}\text{O}_x$  film as a function of the hafnium content for as-deposited and annealed samples; (b) the flat-band voltage as a function of the Hf content in the film, for as-deposited and annealed films.

The flat-band voltage ( $V_{fb}$ ) and hysteresis of the  $C$ - $V$  curves are signatures of trapped oxide charges both at the interface and in the bulk of the layer.  $V_{fb}$  originates from the work-function

difference of the electrodes ( $\phi_{MS}$ ) and the presence of oxide charges as given by [21].

$$V_{fb} = \phi_{MS} - (Q_f + Q_{it}) \frac{d}{\epsilon_0 k} - \frac{1}{\epsilon_0 k} \int_0^d [\rho_m(x) + \rho_{ot}(x)] x dx \quad (6.6),$$

where  $Q_f$  and  $Q_{it}$  are the fixed oxide and the interface trapped charge densities. The integral term sums over the charge densities due to mobile charges ( $\rho_m$ ) and oxide trap charges ( $\rho_{ot}$ ). Since the  $C$ - $V$  curves exhibit low hysteresis and the capacitors were not stressed to generate defects, the integral is negligibly smaller than  $(Q_f + Q_{it})d / \epsilon_0 k$  and  $(Q_f + Q_{it})$  can be derived from Eqn. 6.6. The flat-band voltage variation is plotted in Fig. 6.12 (b) and shows that  $V_{fb}$  is positive for pure HfO<sub>2</sub> and films with 87% of Hf, while for lower Hf contents, the devices exhibit negative  $V_{fb}$  values. This suggests the introduction of more positive fixed charges or dipole formation with increasing Er concentration, which is consistent with observations of Govindarajan et al. [15]. Fig. 6.14 shows that the total oxide charge becomes more negative upon RTA.

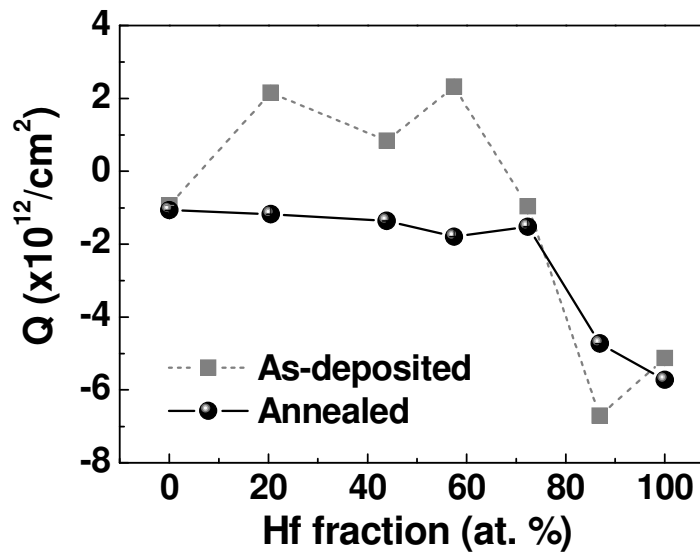


Fig. 6.14. Oxide charges of the as-deposited and annealed TiN/Er<sub>y</sub>Hf<sub>1-y</sub>O<sub>x</sub>/Si devices.

As we discussed in Chapter 3, in an as-deposited device, the flat-band shift can be resulting from fixed oxide charges, oxide trap charges or interface traps. To understand the influence of the interface trap charges in these devices, parallel conductance ( $G_P$ ) measurements were performed on these samples as a function of frequency. Fig.6.15 shows  $G_P$  plotted as  $G_P/\omega$ , (where  $\omega=2\pi f$ ) measured as a function of the frequency  $f$ , at the flat-band condition.

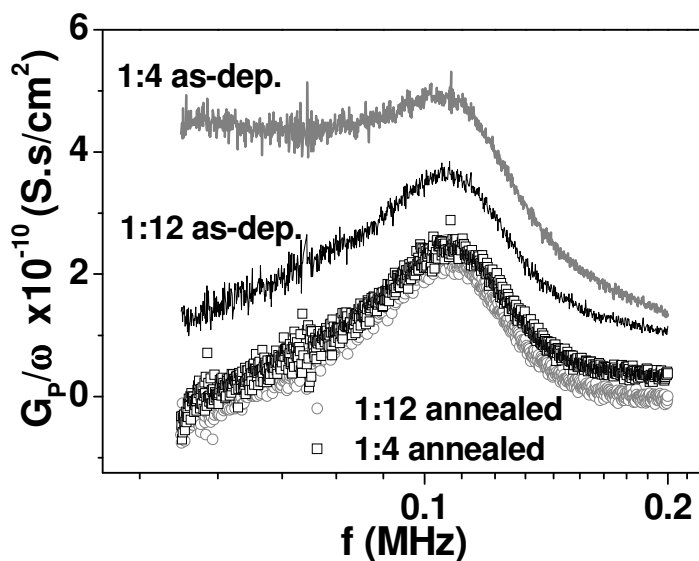


Fig. 6.15. Parallel conductance  $G_p/\omega$  measured as a function of frequency  $f$ .

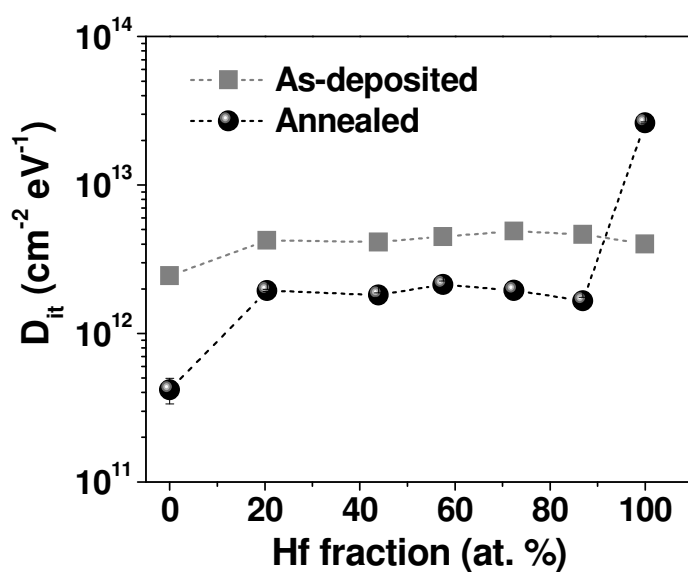


Fig. 6.16. The interface state density ( $D_{it}$ ) as a function of the hafnium content in the  $\text{Er}_y\text{Hf}_{1-y}\text{O}_x$  films.

The density of interface states ( $D_{it}$ ) distributed over the silicon band-gap can be determined from the maximum of the curve by  $(G_p / \omega)_{Max} \times 2.5 / qA$ . The  $D_{it}$  values are shown in Fig. 6.16 as a function of the Hf content, and show comparable  $D_{it}$  for the mixed oxides around  $4 \times 10^{12} \text{ cm}^{-2} \text{eV}^{-1}$ . Upon RTA, the  $D_{it}$  values were systematically reduced by a factor of 2 to  $2 \times 10^{12} \text{ cm}^{-2} \text{eV}^{-1}$ , indicating improved oxide-Si interface quality. Lowest  $D_{it}$  values were



obtained for  $\text{Er}_2\text{O}_3$  where  $D_{it}$  reduced from  $2.5 \times 10^{12} \text{ cm}^{-2}\text{eV}^{-1}$  to  $4.2 \times 10^{11} \text{ cm}^{-2}\text{eV}^{-1}$  after annealing. However,  $\text{HfO}_2$  appears to have an increasing interface density from  $4.0 \times 10^{12} \text{ cm}^{-2}\text{eV}^{-1}$  to  $2.6 \times 10^{13} \text{ cm}^{-2}\text{eV}^{-1}$ , the origin of which is not yet clear.

### 6.3c *I-V* characteristics of $\text{TiN}/\text{Er}_y\text{Hf}_{1-y}\text{O}_x/\text{Si}$ devices

#### a. As-deposited $\text{Er}_y\text{Hf}_{1-y}\text{O}_x$ thin films

In order to check the quality of the films, the electrical behaviour of the devices fabricated with the as-deposited films were studied in detail. The current density – electric field (*J-E*) behaviour of the as deposited  $\text{TiN}/\text{Er}_y\text{Hf}_{1-y}\text{O}_x/\text{Si}$  devices are depicted in Fig. 6.17.

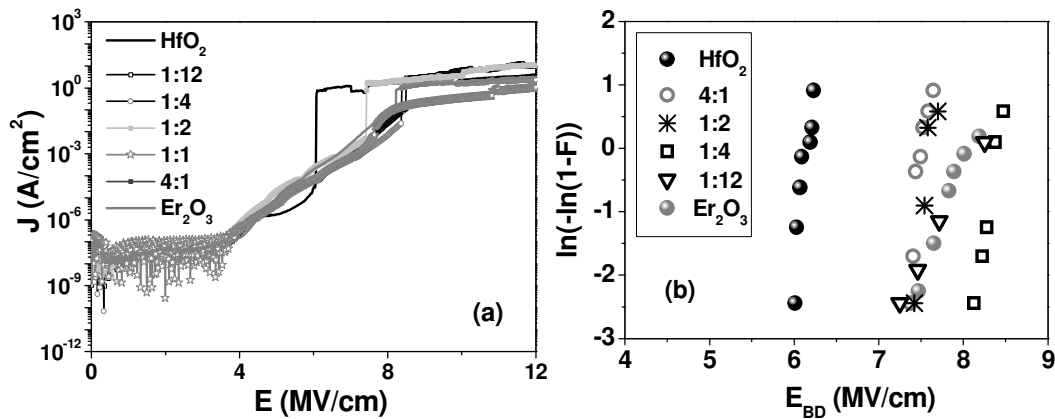


**Fig. 6.17.** (a) The *J-E* behaviour of  $\text{TiN}/\text{Er}_y\text{Hf}_{1-y}\text{O}_x/\text{Si}$  devices with as-deposited dielectric films; (b) the Weibull distributions of dielectric breakdown fields of the devices.

The breakdown behaviour of the as-deposited  $\text{TiN}/\text{Er}_y\text{Hf}_{1-y}\text{O}_x/\text{Si}$  devices plotted in Fig. 6.17 (b) as Weibull distributions suggests that the processing of the films was good enough to carry on with further electrical analysis. The steep slopes of the distributions show that the breakdown of the devices is intrinsic in nature, as a result of the good quality films.

Similar to the case of the  $\text{La}_y\text{Zr}_{1-y}\text{O}_x$  films, the defect levels in the films due to the incorporation of the Hf were investigated by the temperature dependent leakage current measurements and plotting Arrhenius plots as shown in Fig. 6.18.

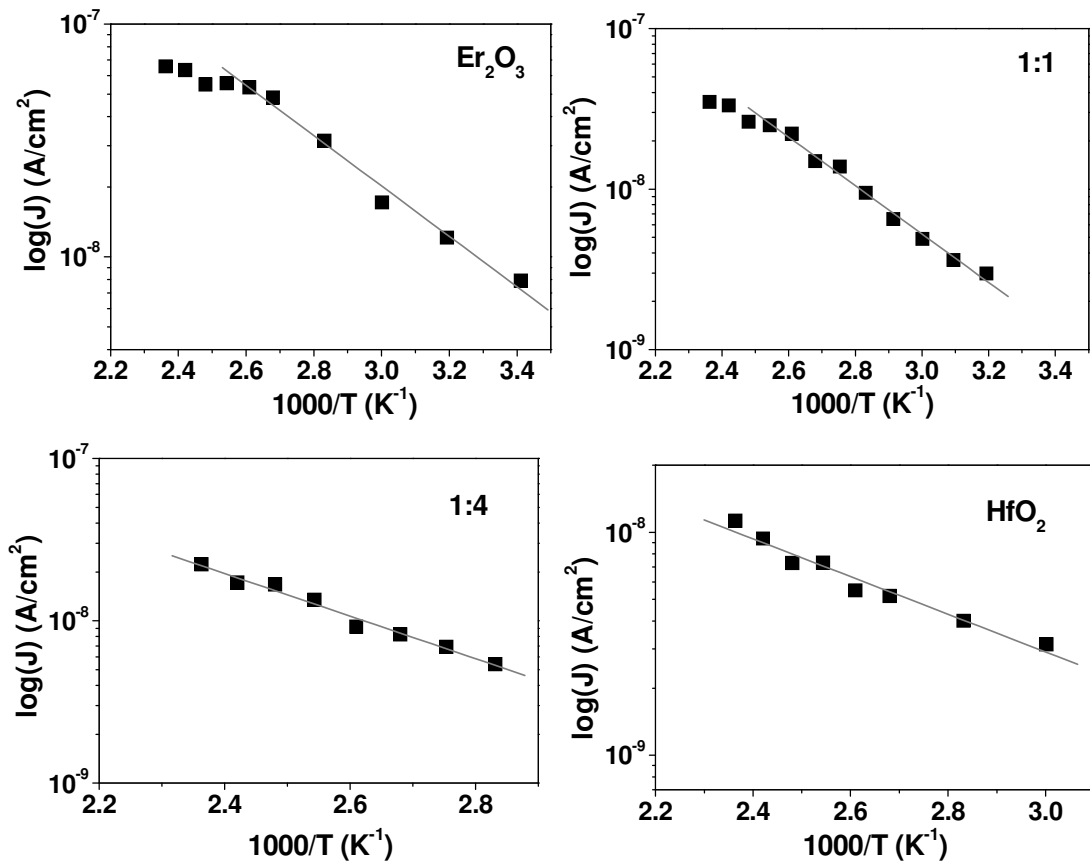


Fig. 6.18. Arrhenius behaviour of the current density  $J$  at an electric field of 1 MV/cm for devices with as-deposited films of  $\text{Er}_2\text{O}_3$ , Hf:Er=1:1, Hf:Er=1:4 and  $\text{HfO}_2$ .

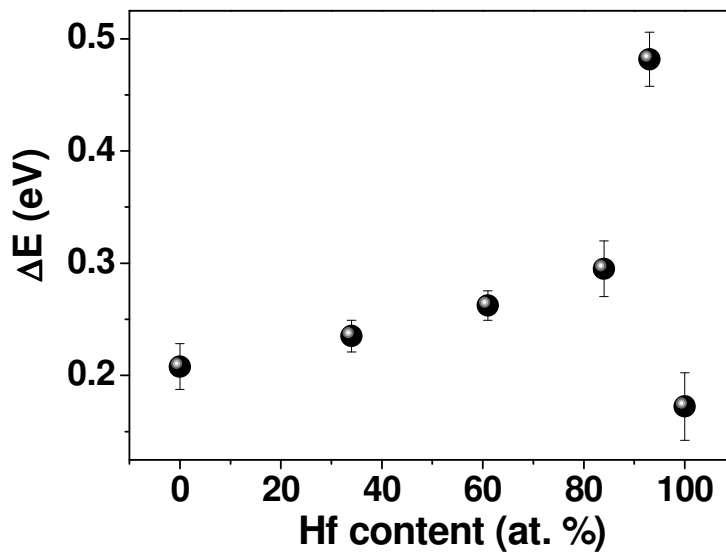
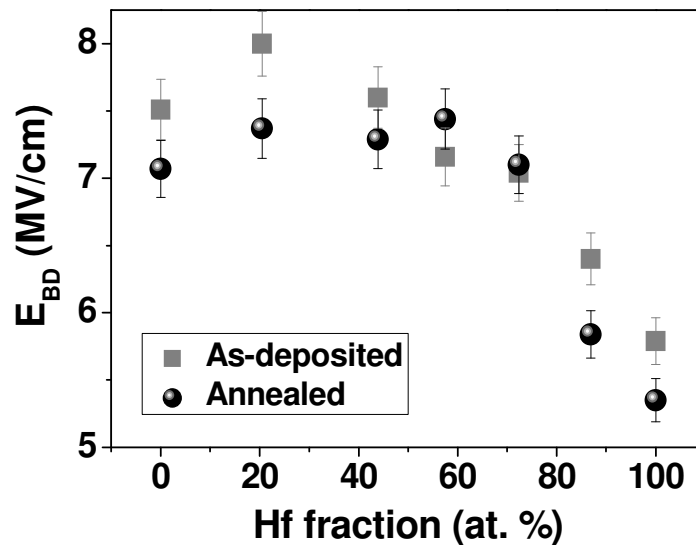


Fig. 6.19. Activation energy of the as-deposited  $\text{Er}_y\text{Hf}_{1-y}\text{O}_x$  films estimated from the Arrhenius plots.

The activation energy of the as-deposited films appears to increase with the amount of Hf in the films. Since the defects levels could be generated by oxygen vacancies by incorporating Hf in it, but Fig. 6.19 is not conclusive enough to attribute compositional changes to the change in activation energy. This will be investigated later in this chapter with material analysis studies.

### b. Comparison of breakdown fields between as-deposited and annealed $\text{Er}_y\text{Hf}_{1-y}\text{O}_x$ thin films

The dielectric electric breakdown field ( $E_{BD}$ ) of the  $\text{Er}_y\text{Hf}_{1-y}\text{O}_x$  films as a function of the Hf content is shown in Fig. 6.20. The breakdown fields were slightly lower after annealing. This might be due to slight reduction in the thickness, which was, however, not apparent from the HRTEM measurements. However, most of the mixed oxides have good breakdown fields around 7.5 MV/cm.



*Fig. 6.20. Breakdown characteristics of the as-deposited and annealed  $\text{TiN}/ \text{Er}_y\text{Hf}_{1-y}\text{O}_x/\text{p-Si}$  capacitors.*

Very low leakage currents ( $<60 \text{ nA}/\text{cm}^2$ ) were measured at 1 MV/cm electric field as depicted in Fig. 6.21. With increasing Hf content a gradual increase of the leakage current is observed. Normally, the leakage current for metal- $\text{HfO}_2$ -Si devices is expected to be higher than that of metal- $\text{Er}_2\text{O}_3$ -Si devices because of their band-gap differences (5.8 eV for  $\text{HfO}_2$  and 7.5 eV for  $\text{Er}_2\text{O}_3$ ). In addition, the  $\text{HfO}_2$ -Si conduction band offset (1.5 eV) is lower compared to that of

the 3.5 eV offset of  $\text{Er}_2\text{O}_3$ -Si structure [22].

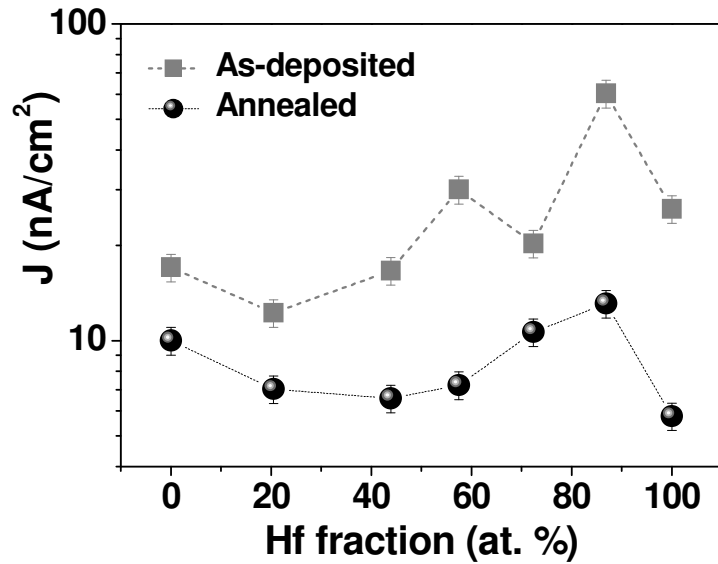


*Fig. 6.21. Leakage current of the  $\text{TiN}/\text{Er}_y\text{Hf}_{1-y}\text{O}_x/\text{p-Si}$  capacitors as a function of the hafnium content of the film, measured at an electric field of 1 MV/cm.*

### 6.3d X-ray diffraction analyses

Grazing incidence x-ray diffraction (GIXRD) experiments were performed on the as-deposited  $\text{Er}_y\text{Hf}_{1-y}\text{O}_x$  films with a Philips X'Pert MPD diffractometer, equipped with a Cu x-ray source (Cu K $\alpha$ , wavelength: 1.542 Å). All the films are polycrystalline and slightly textured. It has been verified that the crystallinity and peak positions did not alter upon RTA at 460°C. Fig. 6.22 (a) shows the GIXRD spectra of the samples in the whole range and (b) shows a zoomed-in version of the main peaks.

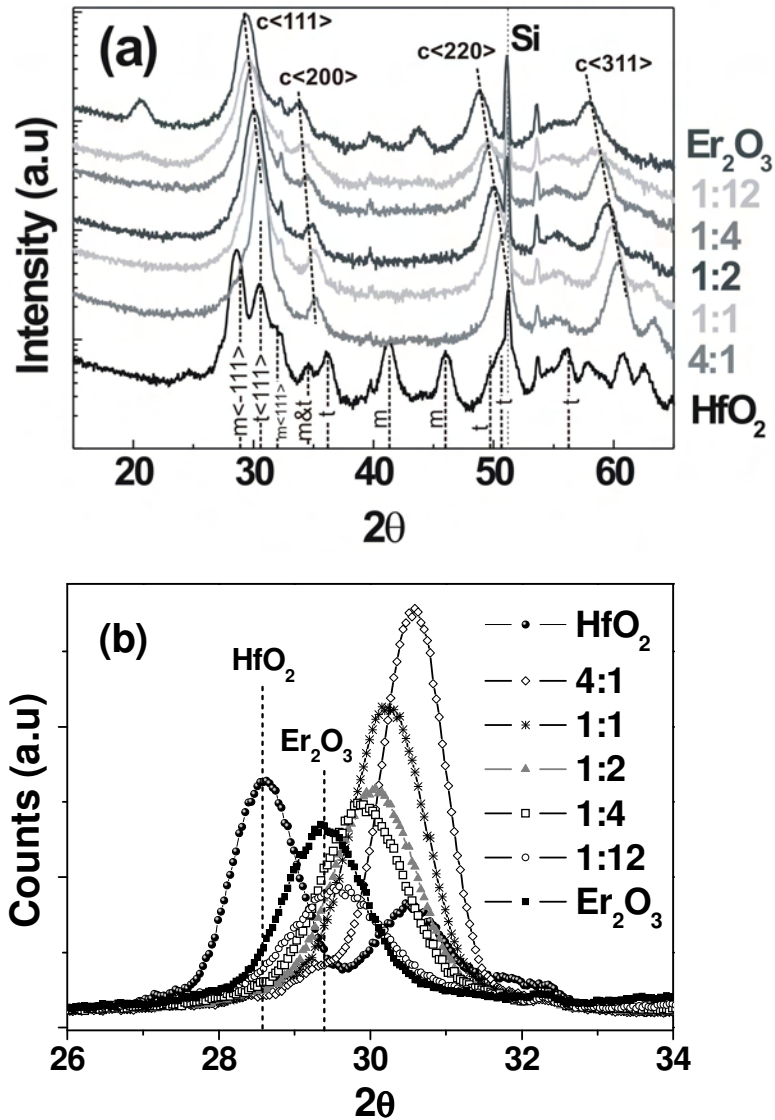


**Fig. 6.22.** (a) XRD graph for as-deposited  $\text{Er}_y\text{Hf}_{1-y}\text{O}_x$  films showing that all the films are crystalline. Cubic  $\text{HfO}_2$  peaks are found at  $2\theta$  values of  $30.6^\circ$   $\langle 111 \rangle$ ,  $35^\circ$   $\langle 220 \rangle$ ,  $51^\circ$   $\langle 220 \rangle$ , and  $60.5^\circ$   $\langle 311 \rangle$ ; (b) Section of the XRD graph showing main crystallographic peaks of  $\text{Er}_y\text{Hf}_{1-y}\text{O}_x$  films with different stoichiometry: Pure  $\text{HfO}_2$  is monoclinic with a small percentage of tetragonal phase, whereas all the mixed oxide films and the  $\text{Er}_2\text{O}_3$  film are present in their cubic phase.

A careful analysis shows that the pure  $\text{Er}_2\text{O}_3$  thin film has body-centred-cubic structure (BCC -  $\text{Mn}_2\text{O}_3$  type) with main peak at  $29.4^\circ$ . This corresponds with a lattice parameter of  $10.51 \text{ \AA}$  ( $10.55 \text{ \AA}$  from ICSD database, file no. 39185). The  $\text{Er}_y\text{Hf}_{1-y}\text{O}_x$  films have a face-centered-cubic structure (fcc—defect fluoride type) as evidenced by the XRD peak positions and

additional out-of-plane diffraction measurements. For instance, the Hf:Er 4:1 pulse ratio films show diffraction peaks at 2 theta values of  $30.6^\circ$   $\langle 111 \rangle$ ,  $35^\circ$   $\langle 200 \rangle$ ,  $51^\circ$   $\langle 220 \rangle$ , and  $60.5^\circ$   $\langle 311 \rangle$ , indicating a cubic unit cell of  $5.08 \text{ \AA}$ . The absence of tetragonal  $\text{HfO}_2$  peaks in these measurements suggests that the Hf and Er atoms are randomly distributed over identical atom-positions in the cubic fluorite structure. As comparison, Rauwel et al. have reported cubic diffraction peaks for MOCVD  $\text{HfYO}_x$  films with 9.9 at.% Y, at  $2\theta = 30.38^\circ$ ,  $35.22^\circ$ ,  $50.65^\circ$ ,  $60.15^\circ$ , and  $74.42^\circ$  (which would have a unit cell of  $5.10 \text{ \AA}$ ). Furthermore, Adelman et al. demonstrated by GIXRD the formation of a cubic crystal structure in Dy- and Sc-doped atomic vapor deposited (AVD)  $\text{HfO}_2$  films, whereas their pure  $\text{HfO}_2$  films were monoclinic [17].

At higher erbium concentrations, the characteristic peak for the cubic  $\text{HfO}_2$  phase at  $30.6^\circ$  gradually shifts towards the cubic signature peak of  $\text{Er}_2\text{O}_3$  at  $29.3^\circ$ . This gradual shift of the diffraction peak to smaller diffraction angles indicates the formation of a larger unit cell size. A clear correlation is observed between the lattice constant  $a$  estimated from the XRD peaks and the dielectric constant of the films as is shown in Fig.6.23. This observation suggests that the dielectric polarization of the oxide is directly linked to the size of the  $\text{HfO}_2$  cubic lattice by incorporating Er atoms. Such a shift in diffraction angle has also been observed by He *et al.* in cubic La-doped  $\text{HfO}_2$  films deposited by ALD [23].

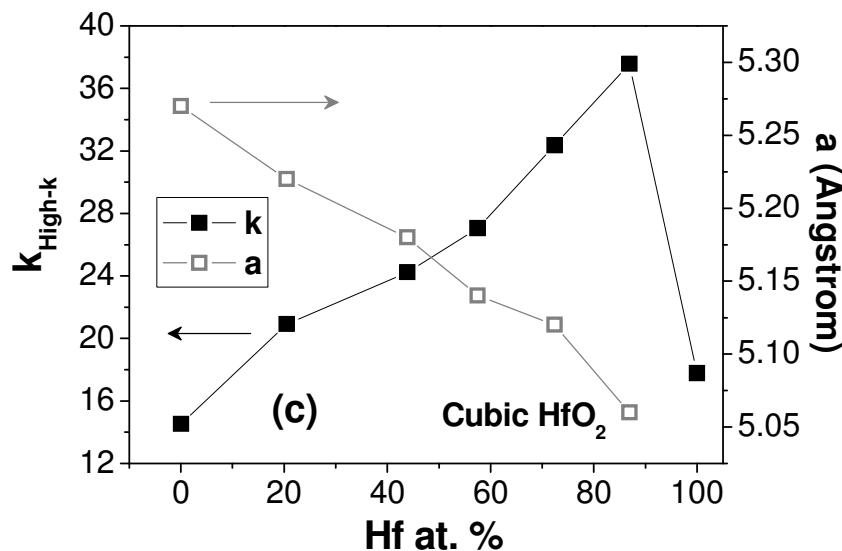


**Fig. 6.23.** The  $k$ -values and the lattice constants estimated from the XRD peaks of the films as a function of the Hf % of the film.

The pure  $\text{HfO}_2$  thin film is monoclinic ( $2\theta = 28.5^\circ$ ); the peak at  $30.5^\circ$  shows the presence of a second, tetragonal phase. The relative peak intensities indicate that the monoclinic phase is dominating in the pure  $\text{HfO}_2$  films.  $\text{HfO}_2$  is typically monoclinic at room temperature. It forms a tetragonal phase only at temperatures above  $1700^\circ\text{C}$ , and a cubic phase (fluorite type) at even higher temperatures ( $T > 2200^\circ\text{C}$ ). It is known that the high-temperature tetragonal phase can be stabilized in very thin films due to the large contribution of the surface energy to the Gibbs free energy [24,25,26]. Interestingly, the presence of 13% erbium in the  $\text{Er}_y\text{Hf}_{1-y}\text{O}_x$  film (Hf:Er pulse ratio of 4:1) stabilizes the high-temperature cubic phase and not the tetragonal phase. These findings are in clear contrast with the results of Wu et al. [27]. They obtained an amorphous  $\text{ErHfO}_x$  film in the as-deposited and annealed state (30 s RTA at  $800^\circ\text{C}$ ). Only after annealing at  $1000^\circ\text{C}$  a monoclinic  $\text{HfO}_2$  film was formed, although the used chemistry and deposition conditions were similar to ours. An explanation for this behavior could be the slightly smaller (i.e., 7 at.%) erbium concentration compared to our films and the lower film thickness (i.e., 4 nm). Cho et al. [28] have found clear indications that the crystallinity of the  $\text{HfO}_2$  films is strongly dependent on the film thickness. The films below 5 nm are amorphous and films thicker than 10 nm are polycrystalline with either a monoclinic or a tetragonal crystal structure.

At higher erbium concentration, the peak at  $30.6^\circ$  gradually shifts towards the signature peak of  $\text{Er}_2\text{O}_3$  at  $29.3^\circ$ . This gradual shift of the diffraction peak to smaller diffraction angles indicates the formation of a larger unit cell size. A clear correlation between the shift of XRD peak position with the dielectric constant of the films is observed as in Fig. 6.20, which indicates that the dielectric polarization of the oxide is directly linked to the size of the  $\text{HfO}_2$  cubic lattice by incorporating Er atoms. Such a shift in diffraction angle has also been observed by He et al. in cubic La-doped  $\text{HfO}_2$  films deposited by ALD [23].

Calculations show that the monoclinic phase has a strongly anisotropic lattice dielectric tensor resulting in a small orientationally averaged dielectric constant [29]. The low-temperature monoclinic phase of  $\text{HfO}_2$  has a dielectric constant of  $\sim 20$  [29]. The cubic and tetragonal phases have much larger dielectric response than the monoclinic phase which explains the improved dielectric permittivity of the  $\text{Er}_y\text{Hf}_{1-y}\text{O}_x$  films. Although the stabilization of the tetragonal  $\text{HfO}_2$  phase (with high  $k$ -value of 25-35) has been recently reported at lower temperatures upon introducing cationic dopants in the  $\text{HfO}_2$  matrix [30,31],

we see here that the addition of  $\text{Er}_2\text{O}_3$  is stabilizing the high-temperature *cubic*  $\text{HfO}_2$  phase in a large compositional range i.e. with at least 13 at.% up to 80 at.% of erbium in the film. In addition, Fig. 6.20 indicates that the highest  $k$ -value of  $\text{HfO}_2$  is achieved for the smallest volume of the cubic structure as the XRD peak shift towards lower incident angle with decreasing erbium concentration in the film. At erbium concentrations below 13 at.% monoclinic  $\text{HfO}_2$  peaks start to appear resulting in a sharp reduction of the  $k$ -value. The Clausius–Mosotti theory suggests that incorporating cationic dopants with high polarizability, the dielectric response of the medium can be enhanced [32]. Rare-earth metals have been commonly used as such cationic dopants and specially, Yt has been shown to stabilize the low-temperature cubic phase of  $\text{HfO}_2$  at temperatures of 500–600 °C [33]. Our observations clearly show that high-temperature cubic  $\text{HfO}_2$  phase can be stabilized even at lower thermal budgets as low as 325°C of the ALD deposition temperature.

## 6.4 Conclusions

Though  $\text{Er}_2\text{O}_3$  has been proposed as a promising high- $k$  material due to its low interface states and low oxide charge densities, the lower valence band offset with silicon and resulting hole tunnelling in this material could be disadvantageous in terms of the reliability of the devices. Moreover, the dielectric constant of this material also is not high enough to propose as a good candidate for advanced CMOS technology. On the other hand, the enhancements in the dielectric properties of ALD  $\text{Er}_y\text{Hf}_{1-y}\text{O}_x$  thin films are shown to have strong correlation with the formation of cubic  $\text{HfO}_2$  phase when  $\text{Er}_2\text{O}_3$  is co-deposited during ALD processing. The stabilization of this high temperature cubic phase by the presence of Er is quite unique, which results in high permittivity, excellent breakdown field and low leakage current films. All these qualities together make erbium doped hafnium oxide a promising future dielectric material.



## 6.5 References

1. J. Robertson, *Integrated Ferroelectrics*, **32**, 251 (2001).
2. M. Losurdo et al., *Appl. Phys. Lett.* **91**, 091914 (2007).
3. H. Ono, T. Katsumata, *Appl. Phys. Lett.* **78**, 1832 (2001).
4. Y.Y. Zhu et al., *Appl. Phys. Lett.* **91**, 122914 (2007).
5. S. Chen et al., *Appl. Phys. Lett.* **88**, 222902 (2006).
6. J.G. Simmons, *J. Phys. D. Appl. Phys.* **4**, 613 (1971).
7. I.Y.K. Chang, J.Y.M. Lee, *Appl. Phys. Lett.* **93**, 223503 (2008).
8. F.C. Chiu, H.W. Chou, J.Y. Lee, *J. Appl. Phys.* **97**, 103503 (2005).
9. E.H. Nicollian, J.R. Brews, *MOS (Metal Oxide Semiconductor) Physics and Technology*, Ed. 2. (Wiley, New Jersey, 2003).
10. S.M. Sze, *Physics of Semiconductor Devices*, Ed. 2 (Wiley, New York, 1981).
11. L.F. Mao, *Appl. Phys. Lett.* **90**, 183511 (2007).
12. A. Hadjadj, G. Salace, C. Petit, *J. Appl. Phys.* **89**, 7994 (2001).
13. G. Pananakakis, G. Ghibaudo, R. Kies, C. Papadas, *J. Appl. Phys.* **78**, 2635 (1995).
14. D. Schroeder, A. Avellàn, *Appl. Phys. Lett.* **82**, 4510 (2003).
15. S. Govindarajan et al., *Appl. Phys. Lett.* **91**, 62906 (2007).
16. K.B. Jinesh et al., *Appl. Phys. Lett.* **93**, 172904 (2008).
17. C. Adelman et al., *Appl. Phys. Lett.* **91**, 162902 (2007).
18. K.B. Jinesh, Y. Lamy, E. Tois, W.F.A. Besling, *Appl. Phys. Lett.* **94**, 252906 (2009).
19. T. Wang, J.G. Ekerdt, *Chemistry of Materials*, **21**, 3096 (2009).
20. H. Yang et al., *Electron Device Lett.* **27**, 435 (2006).
21. D.K. Schroder, *Semiconductor Material and device Characterization*, 3<sup>rd</sup> Ed., Wiley-Interscience, New York, 2006.
22. Y.Y. Zhu et al., *Appl. Phys. Lett.* **91**, 122914 (2007).
23. W. He, L. Zhang, D.S.H. Chan, B.J. Cho, *IEEE Electron Device Lett.* **30**, 623 (2009).
24. M.W. Pitcher et al., *J. Am. Ceram. Soc.* **88**, 160 (2005).
25. C. Wang, M. Zinkevich, F. Aldinger, *J. Am. Ceram. Soc.* **89**, 3751 (2006).
26. A. Navrotsky, *J. Mater. Chem.* **15** 1883 (2005).
27. L. Wu et al., *Electrochem. and Solid-State Lett.* **13**, G21 (2010).
28. M.-H. Cho et al., *Appl. Phys. Lett.* **81**, 472 (2002).

29. X. Zhao, D. Vanderbilt, *Phys. Rev. B* **65**, 075105 (2002).
30. G.-M. Rignanese et al., *Phys. Rev. B* **69**, 184301 (2004).
31. D. Fischer, A. Kersch, *J. Appl. Phys.* **104**, 084104 (2008).
32. R. D. Shannon, *J. Appl. Phys.* **73**, 348 (1993).
33. E. Rauwel et al., *Appl. Phys. Lett.* **89**, 012902 (2006).



# Chapter 7

## High-density capacitors using high-*k* dielectric thin films – Towards industrial needs

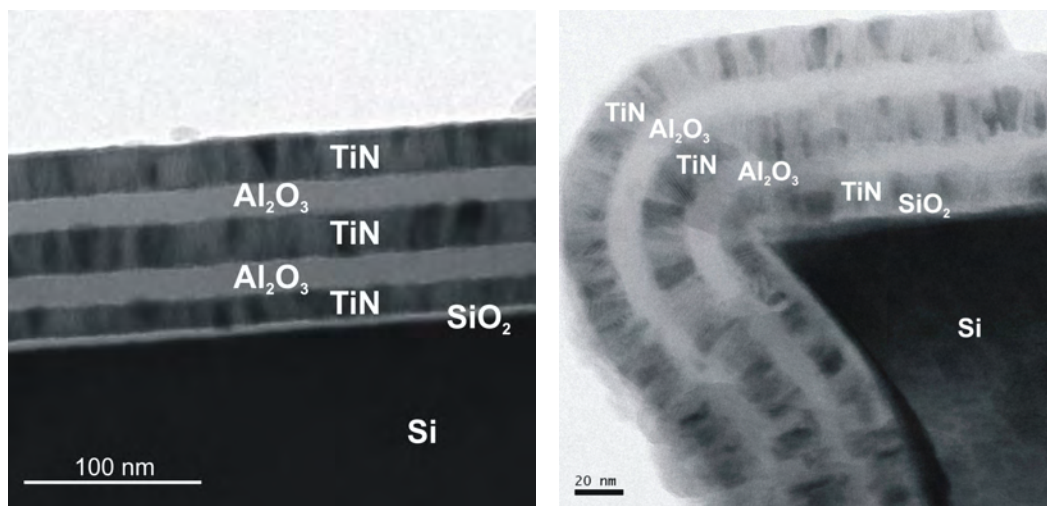
### 7.1 Introduction: Passive Integration Connecting Substrates

As the first step to integrating passive elements such as resistors, capacitors and inductors, micro-pore capacitors are commercially available in NXP Semiconductors' Passive Integration Connecting Substrate (PICS) process to realize high-density capacitor integration in one chip [1]. For this purpose, micro-pore arrays were dry-etched using deep reactive ion etching (DRIE), which yielded pores with smooth walls, a rounded bottom and high aspect ratio up to 20 [2]. Thus a capacitance density of 20 nF/mm<sup>2</sup> could be achieved, with an electrical breakdown voltage of 18 V for a ~20 nm Oxide-Nitride-Oxide (ONO) dielectric stack. Further on, 80 nF/mm<sup>2</sup> has been demonstrated with micro-pore capacitors using a thinner ON stack (where the breakdown voltage reduced to 8V) [3]. Although thinner dielectric films give larger capacitance densities, their breakdown voltages are lower, which limits their application scope. Moreover, such dielectrics are more vulnerable according to industrial standards, in terms of the durability of the devices. Therefore, multiple stacks of capacitors were contrived on top of each other and connecting in parallel, they yielded >200 nF/mm<sup>2</sup> with breakdown voltages of 11 V using multiple ONO stacks [4].

Further increase in capacitance density would be possible only by the application of high-*k* layers in micro-pore structures. The International Technology Roadmap for Semiconductors (ITRS) mentions the challenges of the process integration of these high-*k* materials in detail [5]. Integration of high-*k* materials in high-aspect ratio structures apparently necessitates the usage of atomic layer deposition (ALD), which gives excellent step coverage over demanding substrate topographies. As an added advantage, ALD can deposit thin and very uniform electrode materials (such as TiN) also in such high aspect ratio structures [6,7].

## 7.2 High-density capacitors realized with Al<sub>2</sub>O<sub>3</sub>: illustration of the feasibility

In order to demonstrate the feasibility of ALD to deposit thin dielectric layers together with electrode films, 10 nm thick Al<sub>2</sub>O<sub>3</sub> was chosen as the starting dielectric material. This is because, the deposition of good quality Al<sub>2</sub>O<sub>3</sub> films by ALD is known in literature [8]. ALD synthesized Al<sub>2</sub>O<sub>3</sub> in combination with TiN electrode layer has been studied in detail focusing on the high-aspect ratio micro-pore devices and a capacitance density of 180 nF/mm<sup>2</sup> has been attained using MIMIM stacks with 10 nm Al<sub>2</sub>O<sub>3</sub> layers [6,8,9,10]. As shown in Chapter 1 (Fig. 1.1), the micro-pores were etched 30 μm deep into the n<sup>++</sup> Si substrate, with 1.5 μm diameter and 3.5 μm pitch in footprint area varying from 120×120 μm<sup>2</sup> to 6000×6000 μm<sup>2</sup>. After Al<sub>2</sub>O<sub>3</sub> deposition, some wafers were annealed *in situ* in O<sub>3</sub> (for 300 s at 400°C) to improve the dielectric isolation and breakdown properties. The first layer was 5 nm SiO<sub>2</sub> over the Si substrate, on which 30 nm TiN was deposited by means of ALD. Two stacks of 10 nm Al<sub>2</sub>O<sub>3</sub>/30nm TiN were deposited successively on this to form 2 stacks of metal-insulator-metal (MIM) structures, which formed a MIMIMIM device configuration. Fig. 7.1 shows the TEM image of the step-coverage of these films over different regions of the micro-pore devices.



(a)

(b)

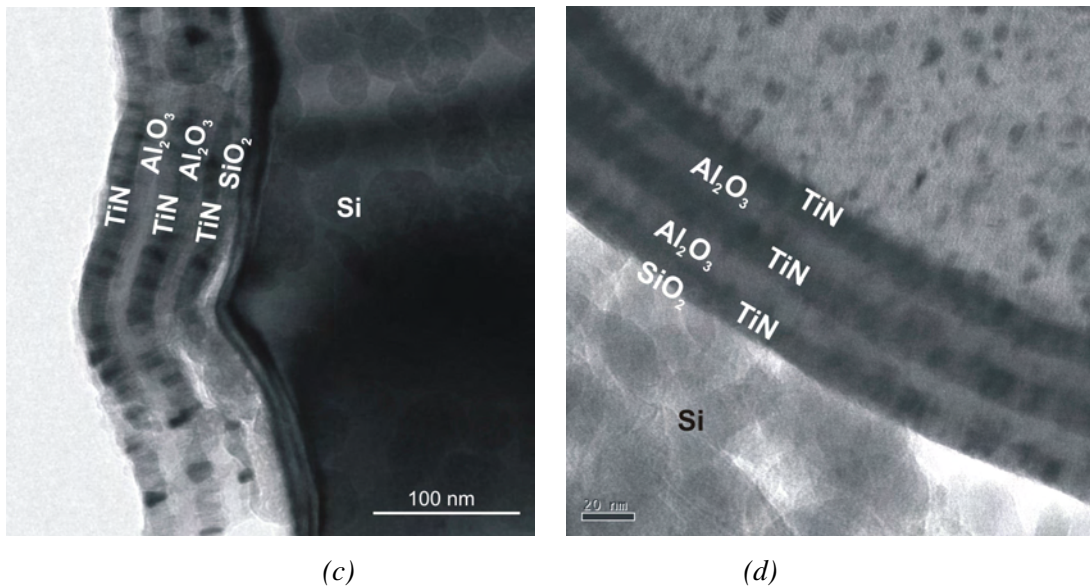


**Fig. 7.1.** High resolution TEM of MIMIMIM stack deposited over micro-pore structures in silicon substrate. (a) On planar surface on top (between the pores); (b) at the corner of the pore; (c) at side walls ( $\sim 10 \mu\text{m}$  below the surface); (d) at the bottom ( $30 \mu\text{m}$  below the surface) where the first MIM is  $n^{++}$  Si/SiO<sub>2</sub>/TiN, second MIM is TiN/Al<sub>2</sub>O<sub>3</sub>/TiN and the third MIM is again TiN/Al<sub>2</sub>O<sub>3</sub>/TiN. SiO<sub>2</sub> was thermally grown on Si substrate while TiN and Al<sub>2</sub>O<sub>3</sub> were deposited by means of ALD. These images illustrate the uniform step coverage over the whole Si-area exposed to ALD.

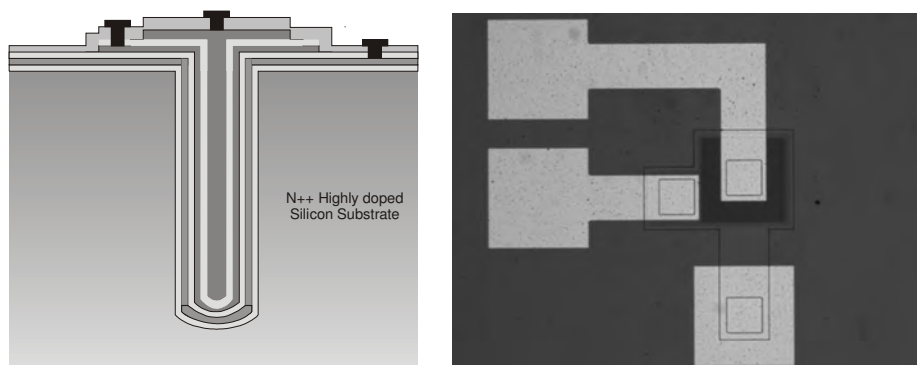


**Fig. 7.2.** (Left) The capacitor configuration in reality; the bright lines are the dielectric layers, the grey lines are TiN films, which are connected to connecting plugs when the whole layers are buried in a protective oxide film. (Right) The top view of the device with stack of three capacitors. Including the  $n^{++}$  Si substrate, there are four connections, so that the three capacitors can be connected in parallel.

In terms of the device processing, the complication of the device increase with the number of layers to be connected in parallel. The device configuration of the MIMIMIM capacitor stack is shown in Fig. 7.2.

### 7.2a Conclusions from the MIMIMIM devices using $\text{Al}_2\text{O}_3$

With the optimized processing, the MIMIMIM stacks comprising one  $\text{SiO}_2$  and two  $\text{Al}_2\text{O}_3$  stacks could provide an ultra-high capacitance density of  $450 \text{ nF/mm}^2$ , which was the world record capacitance density in 2008, and more than twice the value achieved using ONO stacks in the previous PICS program [11]. A capacitance density of  $1 \text{ }\mu\text{F/mm}^2$  would be therefore plausible by replacing  $\text{Al}_2\text{O}_3$  with a high- $k$  material of  $k \sim 20$ , by replicating the same process for the high- $k$  layers. However, despite the challenges of depositing the high- $k$  layers in high-aspect ratio micro-pores, there are several technical challenges to be solved. The deposition of  $\text{Al}_2\text{O}_3$  in deep pores appears to be possible with appreciable step-coverage even at the bottom of the pores, but the area enhancement factor is reducing with increasing thickness of the films.

The area enhancement factor for  $120 \times 120 \text{ }\mu\text{m}^2$  footprint area (the 2D area on the surface of Si) should be  $\sim 12$  for the micro-pore capacitors comparing to the planar devices. However, the maximum capacitance enhancement obtained is 10 for the annealed samples, which indicates that the quality of the film is not the same on the surface and in deep pores. This conclusion is supported by the observation that in deep trenches, the TiN deposited by ALD appears amorphous unlike crystalline appears on planar parts of the devices, as reported by Hoogeland et al. [7].

## 7.3 High-density capacitors using $\text{La}_y\text{Zr}_{1-y}\text{O}_x$ layers

Subsequent to the success of MIMIMIM stacks with  $\text{Al}_2\text{O}_3$  films, the deposition of  $\text{La}_y\text{Zr}_{1-y}\text{O}_x$  films in deep pores were performed to study the step-coverage and the electrical properties of MIS capacitors. The first step in the manufacturing of the 3D capacitors is the etching of the large-aspect-ratio pores into the silicon substrate upon using the Bosch process. The actual area enhancement that can be achieved depends on the 3D geometry i.e. the depth, diameter, and the pitch of the pores. At mask level the holes were  $1.5 \text{ }\mu\text{m}$  in diameter with  $2.6 \text{ }\mu\text{m}$  pitch creating a theoretical area enlargement of 7.3 to 8.0 times depending on the capacitor area.

The same mask was employed to etch deep pores in n<sup>++</sup> Si substrate, and the pore depth was 10 μm. These pre-patterned silicon substrates were then subjected to thermal oxidation to create the required SiO<sub>2</sub> layer, on which La<sub>y</sub>Zr<sub>1-y</sub>O<sub>x</sub> and TiN films were deposited by ALD. The same La<sub>y</sub>Zr<sub>1-y</sub>O<sub>x</sub>/SiO<sub>2</sub> stack discussed in Chapter 5 with 4.2 nm of SiO<sub>2</sub> and 9.2 nm thick La<sub>y</sub>Zr<sub>1-y</sub>O<sub>x</sub> films (with La:Zr pulse ratio of 1:4) and the nominal thickness of the TiN layer was 36 nm. HRTEM images of top, sidewalls and bottom of the pores shown in Fig. 7.3 illustrates very conformal deposition of the layers over the pore surface.

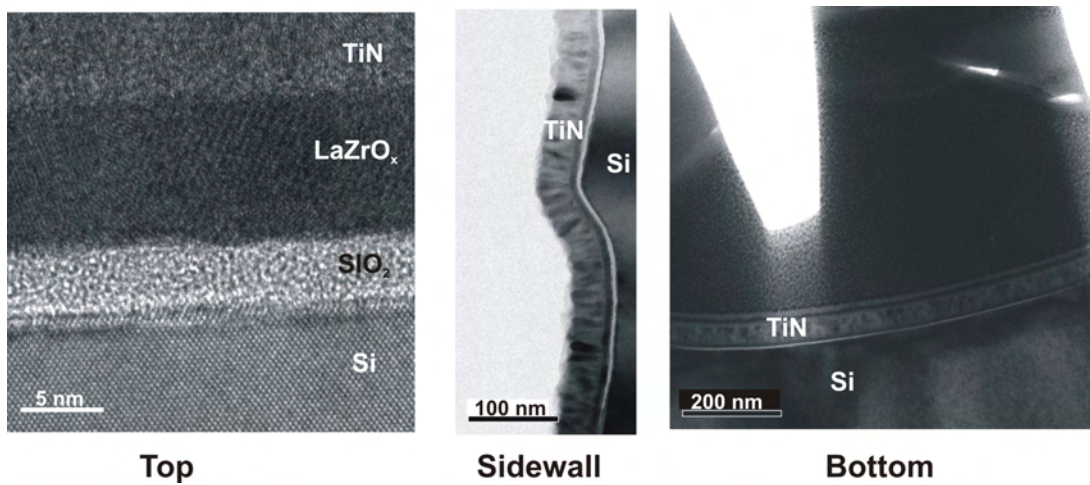


**Fig. 7.3.** HRTEM images of the LaZrO<sub>x</sub> film deposition on top, sidewall of the pore and bottom of the pore.

Location	SiO <sub>2</sub> (nm)	La <sub>y</sub> Zr <sub>1-y</sub> O <sub>x</sub> (nm)	TiN (nm)
Top surface	3.8 – 4.3	9.3 – 9.6	35 – 39
Sidewall (1μm below the top surface)	4.9 – 6.8	7.2 – 8.3	35 – 42
Bottom of the pore	4.3 – 5.6	7.0 – 7.1	33 – 40

**Table 7.1.** Thickness of the SiO<sub>2</sub>, La<sub>y</sub>Zr<sub>1-y</sub>O<sub>x</sub> and TiN layers on the top surface, sidewalls and the bottom of the pores (as measured using HRTEM images).

The deposited layers have excellent step-coverage and TiN is polycrystalline throughout the surface of the pores, which indicates that the layers are of the same quality both on the surface and in deep pores. Table 7.1 gives the layer thickness on the top surface, sidewalls and bottom

of the trenches measured using HRTEM.

Although no dedicated pulse and purge time optimization was carried out, satisfactory step coverage could be obtained for  $\text{La}_y\text{Zr}_{1-y}\text{O}_x$  atomic-layer depositions in 12.5 high aspect ratio pores. ALD processed TiN yielded a step-coverage better than 95% step coverage, which shows the feasibility of conformal growth in deep trenches. However, a further increase in pore depth results in a further reduction of the conformality of the ALD. Although films with better step conformality can be achieved upon further optimization of deposition conditions (like longer pulse and purge times of the precursors), this is likely to result in a dramatic decrease in wafer throughput and increase in Cost of Ownership (CoO).

### 7.3a Capacitance measurements of the pore capacitors with $\text{SiO}_2/\text{LaZrO}_x$ stacks

The capacitances measured as the function of real area of the devices (planar and micro-pore) for devices with different stack thicknesses are shown in Fig. 7.4.

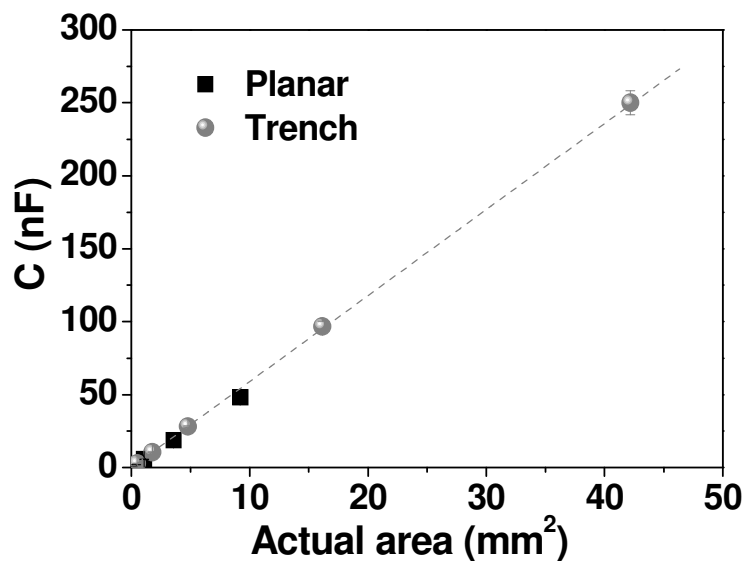


*Fig. 7.4. Capacitance of the planar and micro-pore  $\text{TiN}/\text{La}_y\text{Zr}_{1-y}\text{O}_x/\text{SiO}_2/\text{Si}$  devices (with 8 nm stack) plotted against the actual electrode area showing a linear relationship.*

The capacitance scales linearly with the area of the electrode, even for the micro-pore devices, indicating that the TiN layer deposited was of low resistivity. Fig. 7.5 is the capacitance measured over the footprint area of the devices, where the capacitance enhancement can be seen for different film thickness. Fig. 7.6 gives an overview of the capacitance density of devices with different  $\text{La}_y\text{Zr}_{1-y}\text{O}_x/\text{SiO}_2$  stack thickness.



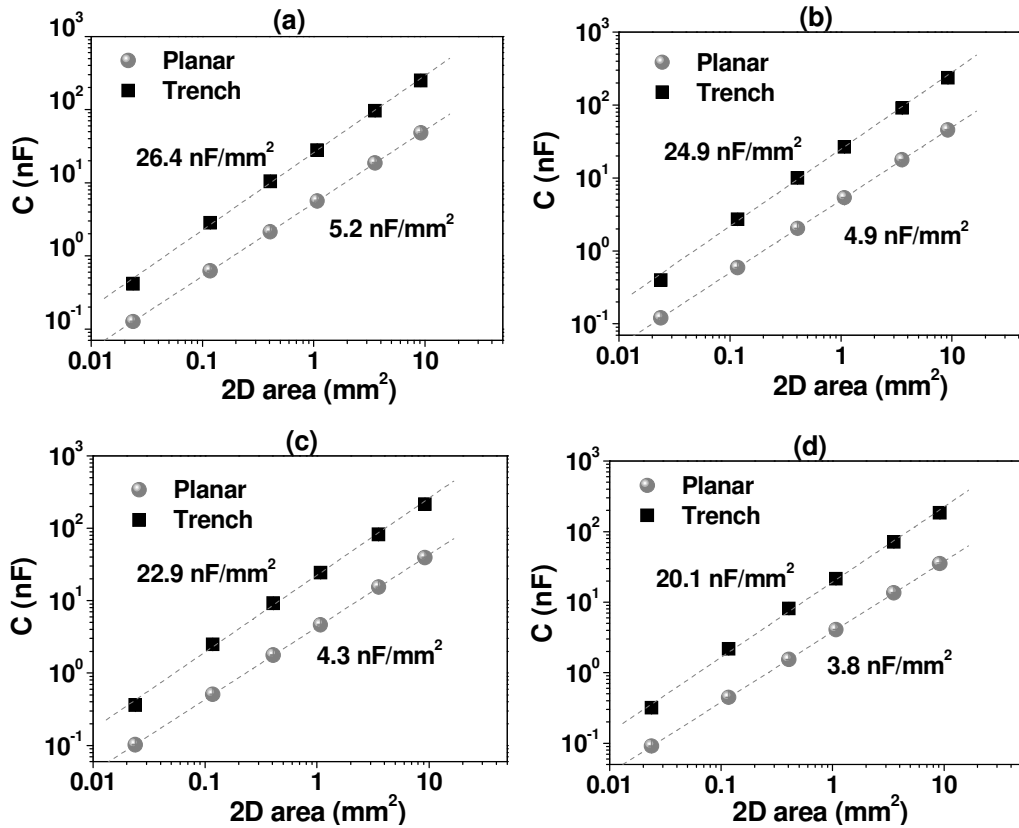


Fig. 7.5. Capacitance of the planar and micro-pore  $\text{TiN}/\text{La}_y\text{Zr}_{1-y}\text{O}_x/\text{SiO}_2/\text{Si}$  devices plotted against the electrode footprint area for different dielectric stack thicknesses (a) 8 nm, (b) 13.4 nm, (c) 22.6 nm and (d) 33.5 nm.

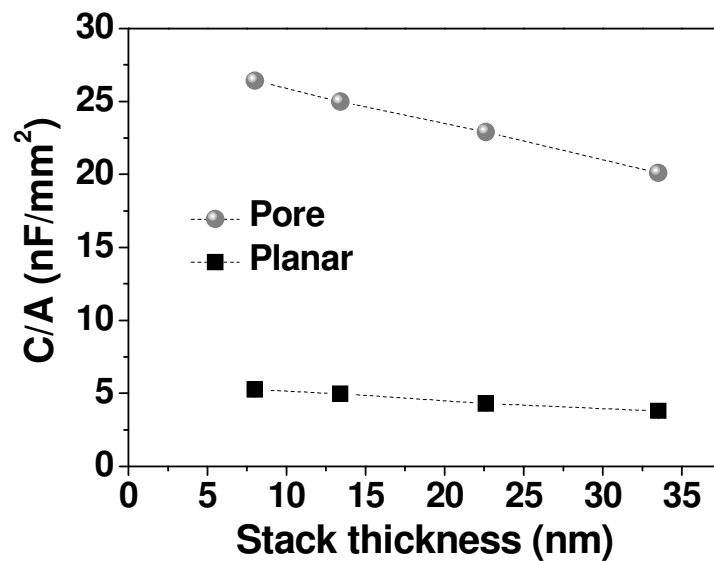
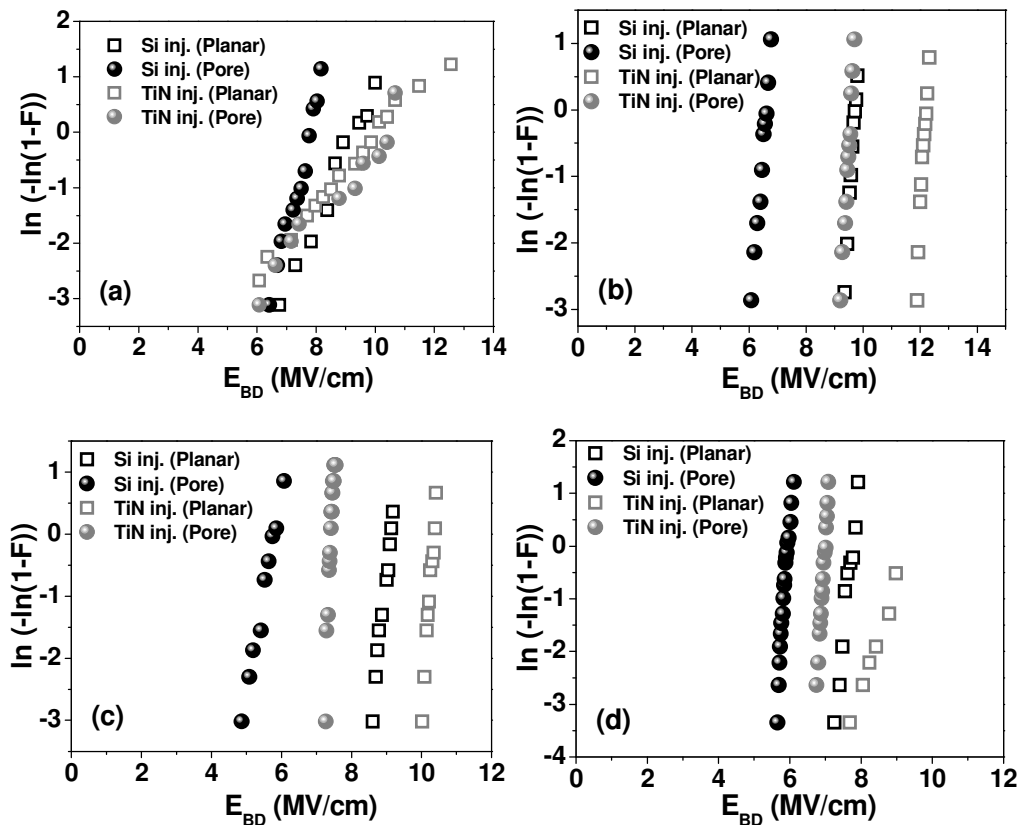


Fig. 7.6. Capacitance density of the planar and micro-pore  $\text{TiN}/\text{La}_y\text{Zr}_{1-y}\text{O}_x/\text{SiO}_2/\text{Si}$  devices plotted against the thickness of the  $\text{La}_y\text{Zr}_{1-y}\text{O}_x/\text{SiO}_2$  stack.

### 7.3b Electrical breakdown of the micro-pore devices

The dielectric breakdown behaviour of the planar TiN/SiO<sub>2</sub>/La<sub>y</sub>Zr<sub>1-y</sub>O<sub>x</sub>/Si devices with La:Zr pulse ratio of 4:1 has been extensively described in Chapter 5. This section describes the breakdown characteristics of the micro-pore devices with the same device configuration. Fig. 7.7 shows the Weibull plots of breakdown electric fields for different stack thickness for planar and micro-pore devices.



*Fig. 7.7. Weibull distributions of the breakdown electric field ( $E_{BD}$ ) measured for the TiN /La<sub>y</sub>Zr<sub>1-y</sub>O<sub>x</sub>/SiO<sub>2</sub>/Si micro-pore devices for different stack thicknesses of (a) 8 nm, (b) 13.4 nm, (c) 22.6 nm and (d) 33.5 nm. Open symbols are the data of planar capacitors and the closed symbols are of the micro-pore devices.*

As discussed in Chapter 5, the asymmetry between electron injection from Si and TiN in the breakdown fields of the devices due to Maxwell-Wagner effect is observed in micro-pore devices as well. Moreover, comparing to the charge injection from the same direction, say TiN injection, the breakdown electric field is consistently lower for the micro-pore capacitors compared to the planar capacitors, except for the 8 nm thick stacks. This observation suggests

that micro-pore capacitors have a shorter lifetime at the same bias voltage than the planar devices. Since the slopes of the Weibull distribution of the micro-pore devices are comparable to those of the planar devices, it can be understood that the earlier breakdown of the micro-pore devices are not due to extrinsic failure resulting from processing non-uniformities of the devices, but are intrinsic failures related to the dielectric breakdown of the films.

For the same applied voltage, the sharp edges of the pores generate enhanced electric field that give rise to larger leakage currents and earlier onset of Fowler-Nordheim tunnelling [12] suggesting that the electric field causing the dielectric breakdown is larger for micro-pore devices than for the planar devices. When the layer thickness is smaller than the radius of curvature of the corner (or any other sharp edges), there is a uniform electric field inside the high- $k$  layers. But when the thickness of the layer is larger than the radius of curvature of the corners, the electric flux density is larger at the sharp edges (as per Gauss' theorem). This field enhancement at the sharp edges results in earlier FN tunnelling at same applied voltages than the planar devices, causing earlier device breakdown.

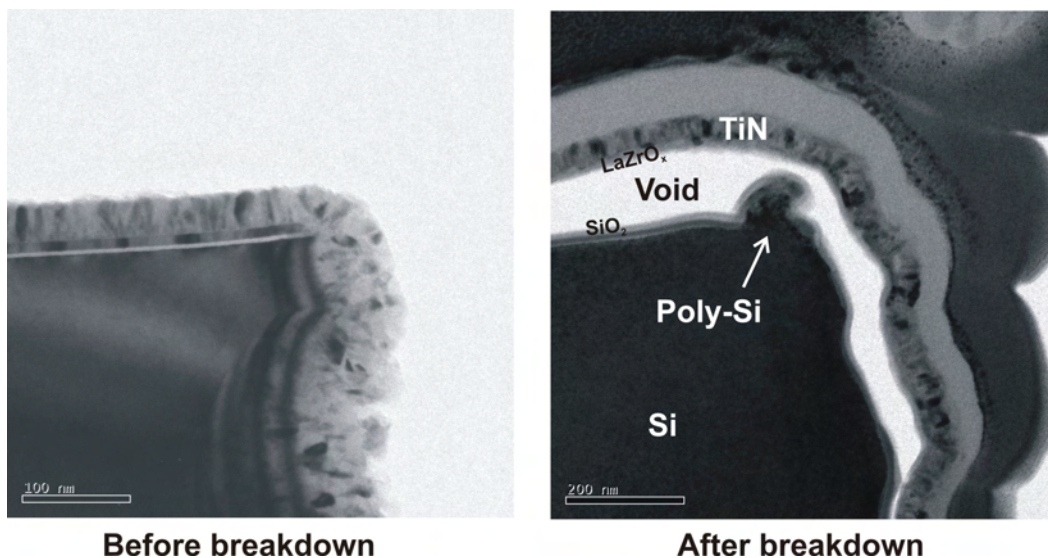


**Fig. 7.8.** HRTEM images of the corners of micro-pore devices before and after dielectric breakdown, showing the rupture of the layers at the corner. The  $\text{La}_y\text{Zr}_{1-y}\text{O}_x$  layer together with the TiN film is completely delaminated at the corner, leaving out a void (white region in the picture on right), while the  $\text{SiO}_x$  reduced to 0.6 nm. Monocrystalline Si substrate turned to polycrystalline Si at the corner where the breakdown occurred.

When the dielectric breakdown happens, a mark due to the rupture of the layers appears on the top TiN electrode. A dedicated high resolution TEM (HRTEM) experiment was performed to discover the origin of the breakdown spot in micro-pore devices. These analyses show that the breakdown is indeed at the corner of the micro-pores, where the  $\text{La}_y\text{Zr}_{1-y}\text{O}_x$  film together with TiN layer appears to be delaminated from the Si surface, while the  $\text{SiO}_2$  layer reduced from 4.2 nm to 0.6 nm on Si substrate (as seen in the right-side image in Fig. 7.8), creating a void between the dielectric layers. A SIMS analysis at the breakdown spot reveals several phenomena underwent soon after the breakdown of the spot. These observations can be summarized as:

1.  $\text{La}_y\text{Zr}_{1-y}\text{O}_x/\text{TiN}$  layers delaminated from the rest of the device at the corner.
2.  $\text{SiO}_2$  layer disappeared (reduced to 0.6 nm from 4.2 nm)
3. Single crystalline Si became polycrystalline towards ~100 nm down to the surface at the corner, indicating the immense heat produced at breakdown spot which caused melting and re-crystallization of the silicon (silicon melts at 1414 °C).
4. Zr diffusing into the Si where the Si turned into polycrystalline Si.
5. Ti diffuses into the  $\text{La}_y\text{Zr}_{1-y}\text{O}_x$  layer.

The rupture of the top electrode upon electric breakdown has been reported earlier [13]. Our TEM analyses demonstrate that rupture of the film occurs all across the films and even in the silicon substrate. Technologically challenging feature is that the breakdown always happens at the pore-edges. Increasing the radius of curvature of the pore-corners by rounding the edges with an additional etching prior to the deposition of the high-*k* films would increase the breakdown voltage to similar to that of the planar devices.

## 7.4 Conclusions and outlook

Thinning the dielectric layer increases the capacitance density, but the breakdown voltage will have to be sacrificed together with high power consumption due to increased leakage currents. Therefore, stacking multiple MIM devices on top of each other is a promising way to increase the capacitance over a given footprint area without compromising the breakdown voltage of the device. However, it should be taken into account that the process complexity of the devices increases with increasing MIM stack on top of each other. The mask designs and etching recipes have to be optimized such that while etching the MIM stacks, the electrode

layers do not short each other and they have sufficient space to place the contact lines.

TiN/La<sub>y</sub>Zr<sub>1-y</sub>O<sub>x</sub>/SiO<sub>2</sub> stacks with different La<sub>y</sub>Zr<sub>1-y</sub>O<sub>x</sub> layer thicknesses were deposited in 10 μm deep pores. HRTEM analyses demonstrate very uniform step coverage over the entire exposed area. Hence the capacitance density over the entire device area scales linearly, indicating that the La<sub>y</sub>Zr<sub>1-y</sub>O<sub>x</sub> step-conformality of these layers is excellent. The breakdown voltages of the micro-pore devices are lower than the planar devices. HRTEM analysis of the breakdown spot reveals that breakdowns of the trench devices occurs at the sharp edges of the pores, which is likely to be due to the local field enhancement at the sharp corners of the devices.

Subsequent to the success of MIS stack comprising of TiN/La<sub>y</sub>Zr<sub>1-y</sub>O<sub>x</sub>/SiO<sub>2</sub> layers in trenches, a MIMIS stack with layers comprising electrode/dielectric stacks with TiN/La<sub>y</sub>Zr<sub>1-y</sub>O<sub>x</sub>/TiN/La<sub>y</sub>Zr<sub>1-y</sub>O<sub>x</sub>/SiO<sub>2</sub>/n<sup>++</sup> Si configuration have been fabricated and a capacitance density as high as 200 nF/mm<sup>2</sup> has been achieved, with a breakdown voltage of 7 V.

The specifications that were proposed at the beginning of the REALISE project state that for future application of novel high-*k* dielectrics in decoupling capacitors the following targets should be met by the films:

- Equivalent oxide thickness (EOT) of ~3 nm with a typical thickness ~15 nm,
- leakage current  $J < 10^{-7}$  A/cm<sup>2</sup> at a voltage of 6-8 V (which means  $J < 10^{-7}$  A/cm<sup>2</sup> at an electrical field of ~4 MV/cm),
- The films should be robust during post-deposition processing.

The role of the interfacial oxide is crucial in determining the EOT of the high-*k* films. If we take a minimum EOT of 3 nm as example, a *k*-value of 30 is required for planar capacitors with 15 nm thick high-*k* film and an interfacial oxide thickness of 1.0 nm. But a *k*-value of 20 is sufficient for planar MIM capacitors since there is no interfacial oxide (assuming that there is no electrode oxidation). If we translate the EOT into the minimum capacitance density, an EOT of 3 nm corresponds to a capacitance density of 11.5 nF/mm<sup>2</sup>. As we have seen in Chapter 6, the leakage current target can be met at 4 MV/cm with Er<sub>y</sub>Hf<sub>1-y</sub>O<sub>x</sub> films, together with a *k*-value larger than 30. Therefore, Er<sub>y</sub>Hf<sub>1-y</sub>O<sub>x</sub> films would be an ideal choice to meet the target specifications.

As discussed in Chapter 3, the highest permittivity in  $\text{La}_y\text{Zr}_{1-y}\text{O}_x$  thin film capacitors have been obtained in as-deposited MIS-type capacitors for a La:Zr pulse ratio of 1:9. Unfortunately, the  $k$ -value drops considerably after forming gas anneal at even moderate annealing temperatures (450°C). In that respect the  $\text{Er}_y\text{Hf}_{1-y}\text{O}_x$  high- $k$  material is preferred over the  $\text{La}_y\text{Zr}_{1-y}\text{O}_x$  films in MIS type capacitors because of its higher robustness and better stability against Si-out diffusion. For MIM capacitors, however,  $\text{La}_y\text{Zr}_{1-y}\text{O}_x$  and  $\text{Er}_y\text{Hf}_{1-y}\text{O}_x$  show comparable effective  $k$ -values, leakage current, and breakdown behavior.

Decoupling capacitors are vital components that minimise cross-talk in radio frequency (RF) communications products, *e.g.* mobile phones, but contribute substantially to manufacturing costs. At present it is difficult to calculate these costs for the different integration options and compare them with current production costs. But we can conclude that the specification targets as per the technological needs can be met for both MIS and MIM type 3D capacitors choosing  $\text{La}_y\text{Zr}_{1-y}\text{O}_x$  and  $\text{Er}_y\text{Hf}_{1-y}\text{O}_x$  as the high- $k$  layers. At the stage when this Thesis is summarized,  $\text{La}_y\text{Zr}_{1-y}\text{O}_x$  layers (without  $\text{SiO}_2$ ) deposited over surfaces with 30  $\mu\text{m}$  deep micro-pores and TiN electrode layer have been processed and the device processing is progressing. As an advanced step, ALD processed STO (strontium titanium oxide) layers which have  $k > 100$  are also being currently investigated for future high-density capacitor applications.

## 7.5 References

1. F. Roozeboom, et al., *Thin Solid Films* **504**, 391 (2006).
2. F. Roozeboom, et al., *Int. J. Microcircuits and Electronic Packaging*, **24**, 182 (2001).
3. F. Murray et al., *Mater. Res. Soc. Symp.* **969**, 27 (2007).
4. F. Roozeboom et al., *ECS Transactions* **173**, (2007).
5. ITRS 2009 Edition: Process Integration, Devices and Structures, page 12.
6. D.J. Hoogeland et al., *ECS Transactions* **25**, 389 (2009).
7. D.J. Hoogeland et al., *J. Appl. Phys.* **106**, 114107 (2009).
8. J. L. van Hemmen et al., *J. Electrochem. Soc.* **154**, G165 (2007).
9. S. B. S. Heil et al., *J. Vac. Sci. Technol. A* **25**, 1357 (2007).
10. D.J. Hoogeland, *Plasma-assisted ALD of TiN/Al<sub>2</sub>O<sub>3</sub> stacks for MOS trench capacitor applications*, Master's Thesis, University of Eindhoven, Netherlands, (2008).
11. J.H. Klootwijk et al., *IEEE Electron Device Lett.* **29**, 740 (2008).
12. P.H. Cutler, J. He, N.M. Miskovsky, T.E. Sullivan, B. Weiss, *J. Vac. Sci. Technol. B* **11**, 387 (1993).
13. D.R. Wolters, *Growth, conduction, trapping and breakdown of SiO<sub>2</sub> layers on silicon*, PhD Thesis, University of Groningen, Netherlands (1985).



## Chapter 8

### Summary of this Thesis

This Thesis contributes to the development of high density capacitors using ultra-thin high dielectric permittivity (high- $k$ ) materials deposited by means of atomic layer deposition (ALD) techniques. As discussed in Chapter 1, an extensive background work is necessary for integrating high- $k$  layers into 3D silicon structures to realize high-density capacitors. Therefore this Thesis concentrates on evaluating the specific material and electrical properties of combinations of four promising binary high- $k$  materials namely  $\text{La}_2\text{O}_3$ ,  $\text{ZrO}_2$ ,  $\text{Er}_2\text{O}_3$  and  $\text{HfO}_2$  as  $\text{La}_y\text{Zr}_{1-y}\text{O}_x$  and  $\text{Er}_y\text{Hf}_{1-y}\text{O}_x$ . A capacitance density of  $450 \text{ nF/mm}^2$  had been demonstrated already using  $\text{Al}_2\text{O}_3$  as the dielectric material. The major goal was to achieve a capacitance density  $>1\mu\text{F/mm}^2$  by replicating the  $\text{Al}_2\text{O}_3$  devices using high- $k$  materials. It is also important to note that as mentioned in Chapter 1, the focus of this thesis is on the high-density capacitors, which is a different application domain from the CMOS gate-oxide research, though both technologies share several characteristics of high- $k$  layers and therefore the outcome of this thesis is applicable to both domains.

The work done in this Thesis has been benefited from the expertise of several individuals and groups in various subjects. Atomic layer depositions of the thin films mentioned in Thesis were carried out by the experts at ASM Microchemistry, Finland. Therefore, this Thesis does not mention the details of the optimization of deposition parameters. The material analyses of these films have been performed by the experts at MiPlaza Materials Analysis of Philips Research, Eindhoven. The extensive discussions with those experts were helpful in interpreting the data correctly, and to avoid misinterpretations such as the e-beam induced crystallization of the  $\text{La}_2\text{O}_3$  films in Transmission electron microscopy (TEM) experiments. Contribution of the author to this Thesis lies in the experimental design, electrical characterization of the devices, interpretation of the results together with the insights from material analyses, literature survey and the composition of this Thesis.

Chapters 2-7 of this Thesis present new insights on the material system studied in the



respective Chapters. Thus, Chapter 2 presents the results of phase segregation of  $\text{ZrO}_2$  nanocrystals from the  $\text{La}_y\text{Zr}_{1-y}\text{O}_x$  thin films and its explanation, Chapter 3 presents the advantages of these nano-clustering for dielectric applications, Chapter 4 presents the Si out-diffusion through the high- $k$  films, Chapter 5 describes the Maxwell-Wagner effects in bilayer dielectric stacks and its consequences in the reliability measurements, Chapter 6 presents a promising ternary oxide namely  $\text{Er}_y\text{Hf}_{1-y}\text{O}_x$  for high- $k$  applications, together with the explanation of the origin of the large  $k$ -values of this system and Chapter 7 presents the steps towards achieving ultra-high capacitance densities required for the future technological demands and their technological challenges. A chapter-wise summary of the Thesis is given below.

**Chapter 2:** The stoichiometric and morphological properties of atomic layer deposited  $\text{La}_y\text{Zr}_{1-y}\text{O}_x$  thin films have been investigated in this Chapter, using material analysis techniques such as X-ray diffraction (XRD), High resolution Transmission Electron Microscopy (HRTEM), Rutherford back scattering spectroscopy (RBS) and X-ray photoelectron spectroscopy (XPS), High Angle Annular Dark Field (HAADF) detector and Energy dispersive X-ray spectrometry (EDX). The results show that when the film contains  $\geq 30\%$  of Zr,  $\text{ZrO}_2$  tends to form  $\text{ZrO}_2$  nanocrystals into its high-temperature high- $k$  tetragonal phase. This tetragonal phase segregation of  $\text{ZrO}_2$  is explained on the basis of the excess free surface energy of nanocrystals with diminishing size.

**Chapter 3:** With the  $\text{La}_y\text{Zr}_{1-y}\text{O}_x$  thin films studied in Chapter 2, metal-insulator-semiconductor (MIS) capacitor devices were fabricated and their electrical properties have been evaluated in this Chapter. Electrical investigations include the interface states ( $D_{it}$ ) in silicon as a function of the La:Zr ratio, flat-band shift ( $V_{fb}$ ) and corresponding fixed oxide charge densities in the films, dielectric constant ( $k$ -values) of the films and their corresponding equivalent oxide thickness ( $EOT$ ), activation energy of the traps ( $\Delta E$ ), identification of different conduction regimes of the films, from which the trap density ( $N_t$ ) in the films, leakage current densities ( $J_{leak}$ ), Poole-Frenkel analysis, from which the dynamic dielectric constants ( $\epsilon_r$ ) and the trap ionization energies ( $\phi_t$ ), Fowler-Nordheim analysis and breakdown fields ( $E_{BD}$ ) of the films. The major result of this Chapter is that these mixed oxide

films exhibit remarkably high dielectric constants with increasing Zr content in the films, compared to either  $\text{La}_2\text{O}_3$  or  $\text{ZrO}_2$  films. This is attributed to the tetragonal phase-stabilized  $\text{ZrO}_2$  present in the layers. A model to explain the origin of the low leakage current densities of the films and large breakdown values also is presented in this Chapter, which employs the electric field simulation of the high- $k$  layer consisting of the nano-clustered  $\text{ZrO}_2$  in the film. The electrical quality of these films is more than twice better than the maximum quality of the dielectric layers predicted by the empirical law.

**Chapter 4:** A novel technical challenge is introduced in this Chapter, which is the silicon out-diffusion through the  $\text{La}_y\text{Zr}_{1-y}\text{O}_x$  thin films at room temperature. A gradual siphoning of silicon from the substrate through the high- $k$  layers is observed. This effect is explained as due to the triplet grain boundaries in Al top electrode, through which the diffusion of Si ions is faster. TiN electrodes suppress the siphoning of Si and thus enhance the electric strength and reliability of the devices.

**Chapter 5:** The asymmetric charge injection through  $\text{La}_y\text{Zr}_{1-y}\text{O}_x/\text{SiO}_2$  stack depending on the polarity of the electrode is described in this chapter. This effect is explained on the basis of Maxwell-Wagner instability due to difference in conductance of the individual dielectric layers. A model based on MW effect is described, which accounts for the low-frequency capacitance responses of the devices. An interesting outcome of the theoretical fit to the experimental data is the relaxation timescales of Maxwell-Wagner and Debye effects, which differ by orders of magnitude. Subsequently, the experimental artefacts in evaluating the charge-to-breakdown ( $Q_{BD}$ ) arising due to MW effect is described in this Chapter. Further, the lifetime extrapolations of these dielectric stacks according to the industrial standards are detailed. The Arrhenius behaviour of the defect generation which is responsible for the breakdown of the layers has been studied. These measurements suggest that the extrapolated 10-year operational voltage of the device also exhibits strong polarity dependence, and their activation energies of degradation also are strongly influenced by the direction of the electron injection.

**Chapter 6:** This Chapter studies the dielectric properties of atomic-layer-deposited thin

$\text{Er}_y\text{Hf}_{1-y}\text{O}_x$  films. Unlike  $\text{La}_y\text{Zr}_{1-y}\text{O}_x$  films, these layers are polycrystalline and alloyed.  $\text{Er}_2\text{O}_3$  being a comparatively new dielectric material, has been studied electrically in detail in this Chapter. While  $\text{Er}_2\text{O}_3$  has a  $k$ -value of 14.5 and  $\text{HfO}_2$  has  $k = 17.8$ ,  $\text{Er}_y\text{Hf}_{1-y}\text{O}_x$  films that contains 87% of Hf has a  $k$ -value of 37.6. The excellent dielectric properties of these  $\text{Er}_y\text{Hf}_{1-y}\text{O}_x$  films is explained as the tetragonal phase stabilization of  $\text{HfO}_2$  by the presence of Er in the film, as revealed by the X-ray diffraction experiments.

**Chapter 7:** This Chapter describes the first step towards realizing the industrial needs implementing multiple-capacitor-stack (MIMIMIM) comprising  $\text{SiO}_2$  as the first dielectric layer and ALD processed  $\text{Al}_2\text{O}_3$  layers as the dielectric layers of the second and third MIM devices. A concise description of the electrical properties of the  $\text{TiN}/\text{Al}_2\text{O}_3/\text{TiN}$  capacitors is given in this Chapter. With this capacitor stack, a very high capacitance density of  $450 \text{ nF}/\text{mm}^2$  was achieved. Aiming at  $1 \mu\text{F}/\text{mm}^2$ , the  $\text{La}_y\text{Zr}_{1-y}\text{O}_x$  films were deposited in high aspect ratio pores with excellent step coverage and their electrical properties were studied. The early breakdown of the micro-pore devices is found to be due to the sharp edges of the pores, as evidenced from HRTEM analysis of the breakdown spots. This Chapter concludes with further outlook to improve the capacitance density using other ternary dielectric materials such as strontium titanium oxide (STO).



## Samenvatting

Dit proefschrift beschrijft de ontwikkeling en karakterisatie van capaciteiten met een hoge capaciteitsdichtheid op basis van ultra dunne dielectrische lagen met een hoge permittiviteit (high- $k$ ) die zijn vervaardigd met behulp van Atomic Layer Deposition (ALD). In hoofdstuk 1 wordt de achtergrond van dit werk besproken waarbij wordt ingegaan op de noodzaak om high- $k$  lagen te deponeren in drie dimensionale silicium structuren met als doel de capaciteitsdichtheid verder te vergroten. Dit proefschrift concentreert zich op de evaluatie van specifieke materiaaleigenschappen en haar relatie tot elektrische eigenschappen van vier veelbelovende binaire high- $k$  materialen namelijk:  $\text{La}_2\text{O}_3$ ,  $\text{ZrO}_2$ ,  $\text{Er}_2\text{O}_3$ ,  $\text{HfO}_2$ , en twee ternaire combinaties daarvan, namelijk:  $\text{La}_y\text{Zr}_{1-y}\text{O}_x$  en  $\text{Er}_y\text{Hf}_{1-y}\text{O}_x$ . In voorgaand werk is reeds een capaciteitsdichtheid van  $450 \text{ nF/mm}^2$  aangetoond waarbij  $\text{Al}_2\text{O}_3$  als dielectrisch materiaal werd toegepast. Het ultieme doel is om een capaciteitsdichtheid van  $>1\mu\text{F/mm}^2$  te bereiken door een nanogelamineerde stack te vervaardigen in 3D poriën en  $\text{Al}_2\text{O}_3$  te vervangen voor een diëlectricum met een nog hogere diëlectrische constante. Belangrijk om te vermelden is dat dit proefschrift zich richt op de karakterisatie van zogenaamde hoge dichtheid capaciteiten wat een ander applicatiedomein is dan de ontwikkeling van nieuwe high- $k$  diëlectrica voor CMOS gate oxide toepassingen. Desalniettemin maken beide toepassingen gebruik van dezelfde materialen en depositie technieken waardoor de resultaten die in dit proefschrift worden beschreven toepasbaar zullen zijn in beide gebieden.

Het werk dat wordt beschreven in dit proefschrift is gebaseerd op uitgebreide expertise van verscheidene personen en onderzoeksgroepen verdeeld over verschillende disciplines. De Atomic Layer Deposition van de dunne lagen is uitgevoerd door experts werkzaam bij ASM Microchemistry, Finland. Daarom wordt in dit proefschrift ook niet ingegaan op de details met betrekking tot de optimalisatie van de depositie parameters. De dunne film materiaal analyse is uitgevoerd door experts werkzaam bij MiPlaza Materials Analysis van Philips Research, Eindhoven. De uitgebreide discussies met deze experts waren nuttig om de data correct te interpreteren en om foutieve conclusies te vermijden bijvoorbeeld als gevolg van elektronen bundel geïnduceerde kristallisatie van  $\text{La}_2\text{O}_3$  lagen in de Transmissie Electronen Microscopie (TEM) experimenten. De bijdrage van de auteur aan dit proefschrift bestaat uit het planmatig

opzetten van de experimenten, de elektrische karakterisatie van de capaciteiten, de interpretatie van deze resultaten in relatie tot de materiaaleigenschappen, samenstelling, en de resultaten beschreven in de literatuur.

Hoofdstuk 2-7 van dit proefschrift beschrijft de nieuwe inzichten die zijn verworven in nieuwe, ternaire en diëlectrische multilaag systemen op basis van “vreemde aarde” elementen. Hoofdstuk 2 presenteert de resultaten van de fase scheiding van  $ZrO_2$  nanokristallen uit  $La_yZr_{1-y}O_x$  dunne lagen en de verklaring daarvan; Hoofdstuk 3 bespreekt de elektrische eigenschappen van deze nanogelusterde systemen en het voordeel dat dit oplevert voor diëlectrische toepassingen; Hoofdstuk 4 behandelt de Si-diffusie vanuit het substraat door de high- $k$  lagen; Hoofdstuk 5 beschrijft het zogenaamde Maxwell-Wagner effect in dubbellaagige diëlectrische materialen en de implicaties hiervan op betrouwbaarheids- en levensduur bepalingen; Hoofdstuk 6 presenteert een ander veelbelovend ternair oxide voor high- $k$  applicaties, namelijk  $Er_yHf_{1-y}O_x$ , samen met een verklaring voor reden voor de hoge  $k$ -waarde voor dit systeem, en Hoofdstuk 7 laat de stappen zien die gemaakt moeten worden om ultra hoge capaciteitsdichtheden te verwezenlijken voor toekomstige technologieën en om te voldoen aan de toekomstige vraag. Een korte samenvatting per hoofdstuk wordt hieronder gegeven:

**Hoofdstuk 2:** De stoichiometrie en morfologie van dunne  $La_yZr_{1-y}O_x$  lagen die gedeponerd zijn met ALD worden in dit hoofdstuk beschreven waarbij gebruik wordt gemaakt van materiaal analyse technieken zoals Röntgen diffractie (XRD), Hoge Resolutie Transmissie Electronen Microscopie (HRTEM), Rutherford Back Scattering spectroscopie (RBS) en X-ray Photoelectron Spectroscopie (XPS), High Angle Annular Dark Field (HAADF) detector en Energie Dispersieve X-ray spectrometrie (EDX). De resultaten laten zien dat tetragonale  $ZrO_2$  nanokristallen worden gevormd indien de  $La_yZr_{1-y}O_x$  laag meer dan 30% Zr bevat. De segregatie van deze tetragonale fase die normaal slechts bij hoge temperatuur wordt gevormd, kan worden verklaard door de toename aan vrije oppervlakte energie van deze nanodeeltjes met afnemende grootte.

**Hoofdstuk 3:** Gebruikmakend van de  $La_yZr_{1-y}O_x$  dunne lagen die in hoofdstuk 2 zijn beschreven, zijn metal-insulator-semiconductor (MIS) capaciteiten vervaardigd. In dit

hoofdstuk worden de elektrische eigenschappen beschreven. De elektrische karakterisatie bestaat uit de bepaling van de interface states ( $D_{it}$ ) in silicium als functie van de La:Zr ratio, de flat-band verschuiving ( $V_{fb}$ ) en de bijbehorende fixed oxide ladings dichtheid in de lagen zelf, de diëlectrische constante ( $k$ -value) van de lagen en hun bijbehorende equivalente oxide dikte ( $EOT$ ), en de activatie energie van de traps ( $\Delta E$ ). Op basis van een identificatie van verschillende geleidingsregimes in de lagen is de trap dichtheid ( $N_t$ ), de ladings mobiliteit ( $\mu$ ), en de lekstroom dichtheid ( $J_{leak}$ ) bepaald. Hierbij is Poole-Frenkel analyse uitgevoerd waaruit de dynamische dielectrische constante ( $\epsilon_r$ ) en de trap ionisatie energie ( $\phi_t$ ) is afgeleid, en een Fowler-Nordheim analyse waarmee onder andere het elektrische breakdown veld ( $E_{BD}$ ) van de lagen is bepaald. Het belangrijkste resultaat van dit hoofdstuk is dat deze gemengde oxides een aanzienlijk hogere diëlectrische constante laten zien die afhankelijk is van het Zr gehalte in de laag vergeleken met de binaire  $\text{La}_2\text{O}_3$  of  $\text{ZrO}_2$  lagen. Dit wordt toegeschreven aan de aanwezigheid van tetragonaal gestabiliseerd  $\text{ZrO}_2$  welke een hoge diëlectrische constante heeft. Er is ook een model gepresenteerd om de lage lekstroom dichtheid en de hoge breakdown spanning te verklaren. Dit model simuleert de variaties in het elektrische veld die ontstaan doordat de high- $k$  laag bestaat uit ultra kleine  $\text{ZrO}_2$  nano clusters. De elektrische eigenschappen van deze lagen zijn namelijk meer dan twee keer beter dan de maximale kwaliteit van binaire diëlectrische lagen zoals voorspeld op basis van een empirische wet.

**Hoofdstuk 4:** In dit hoofdstuk wordt het gedrag beschreven van silicium diffusie bij kamer temperatuur door een dunne  $\text{La}_y\text{Zr}_{1-y}\text{O}_x$  laag heen. Het voorkomen van diffusie is een nieuwe uitdaging in de vervaardiging van hoge permittiviteit diëlectrica op silicium. Het silicium diffundeert vanuit het substraat door de high- $k$  laag heen als gevolg van een soort sifon werking. Dit effect kan worden verklaard door de aanwezigheid van triplet korrel grenzen in de Al top electrode waarlangs de diffusie van Si sneller verloopt. Het gebruik van TiN elektroden onderdrukt het effect van het vormen van Si sifons en verbetert dus de elektrische eigenschappen en de betrouwbaarheid van de capaciteiten.

**Hoofdstuk 5:** Afhankelijk van de electrode polariteit treedt er een asymmetrische ladings injectie op door een dubbellaags  $\text{SiO}_2/\text{La}_y\text{Zr}_{1-y}\text{O}_x$  stack. In dit hoofdstuk wordt dit effect verklaard op basis van Maxwell-Wagner (MW) instabiliteit als gevolg van een verschil in

conductiviteit van de afzonderlijke, individuele diëlectrische lagen. Een elektrisch equivalent model gebaseerd op het MW effect kan goed het gedrag beschrijven voor de capaciteitsrespons bij lage frequenties. De relaxatie tijdsschaal van het Maxwell-Wagner effect en het Debye effect verschilt ordes van grootte: een vergelijking van de experimentele resultaten met een theoretische fit laat zien dat het Maxwell-Wagner effect daadwerkelijk optreedt in één bepaalde polarisatie richting.

Vervolgens worden in dit hoofdstuk de experimentele moeilijkheden in de beoordeling van het charge-to-breakdown ( $Q_{BD}$ ) gedrag besproken indien het MW effect optreedt. Met dit in het achterhoofd, zijn levensduur extrapolaties volgens de industriële standaard specificaties gemaakt. Tevens is het Arrhenius gedrag van de breakdown bestudeerd die verantwoordelijk is voor de defect generatie. Deze metingen laten zien dat het geëxtrapoleerde voltage voor 10 jaar operationeel gebruik eveneens een sterke afhankelijkheid van de polariteit laat zien waarbij de activatie energie voor degradatie sterk wordt beïnvloed door de richting van de elektronen injectie.

**Hoofdstuk 6:** Dit hoofdstuk bestudeert de diëlectrische eigenschappen van dunne, met ALD gedeponeerde  $\text{Er}_y\text{Hf}_{1-y}\text{O}_x$  lagen. In tegenstelling tot de  $\text{La}_y\text{Zr}_{1-y}\text{O}_x$  lagen bestaan deze lagen uit een polykristallijn gemengd oxide of ternair alloy.  $\text{Er}_2\text{O}_3$  is een relatief onbekend diëlectrisch materiaal en is daarom in detail bestudeerd in dit hoofdstuk. Terwijl  $\text{Er}_2\text{O}_3$  een  $k$ -waarde van 14.5 heeft en  $\text{HfO}_2$  een  $k$ -waarde van 17.8, vertoont een  $\text{Er}_y\text{Hf}_{1-y}\text{O}_x$  laag met een Hf atoom concentratie van 87% een  $k$ -waarde van 37.6. De excellente diëlectrische eigenschappen van deze ternaire  $\text{Er}_y\text{Hf}_{1-y}\text{O}_x$  lagen kunnen worden verklaard door de vorming van een tetragonale  $\text{HfO}_2$  fase die wordt gestabiliseerd door de aanwezigheid van erbium zoals is aangetoond met Röntgen diffractie analyse (XRD).

**Hoofdstuk 7:** Dit hoofdstuk beschrijft de eerste stappen naar industrialisatie waarbij verscheidene capaciteiten bovenop elkaar zijn gedeponerd in een zogenaamde MIMIMIM configuratie waarbij de eerste diëlectrische laag bestaat uit  $\text{SiO}_2$  en de tweede en de derde diëlectrische laag van de MIM capaciteit bestaat uit  $\text{Al}_2\text{O}_3$  gegroeid met behulp van ALD. Een beknopte beschrijving van de elektrische eigenschappen van deze  $\text{TiN}/\text{Al}_2\text{O}_3/\text{TiN}$  capaciteiten wordt in dit hoofdstuk gegeven. Met deze gestapelde capaciteit is een ultra-hoge

capaciteitsdichtheid gerealiseerd van  $450 \text{ nF/mm}^2$ . Met als doel capaciteitsdichtheden van boven de  $1 \text{ }\mu\text{F/mm}^2$  te bereiken zijn multilagen van  $\text{La}_y\text{Zr}_{1-y}\text{O}_x$  gedeponeerd in poriën met hoge aspect ratio. Nadat de diëlectrische laag in de gaten was aangebracht met een excellente stap bedekking, zijn de elektrische eigenschappen bestudeerd. De relatief lage breakdown spanning van deze capaciteiten wordt veroorzaakt door de scherpe kanten van de poriën zoals aangetoond kon worden met HRTEM analyse in het gebied van de elektrische doorslag. Dit hoofdstuk besluit met een vooruitzicht en aanbevelingen om de capaciteitsdichtheid nog verder te verbeteren door gebruik te maken van andere ternaire dielectrische materialen zoals strontium titanium oxide (STO).





## List of publications

### This Thesis is based on the following publications:

1. *Cubic phase stabilization of atomic layer deposited ErHfO<sub>x</sub> thin films*; K.B. Jinesh, Y. Lamy, E. Tois, R. Forti, M. Kaiser, F. Roozeboom, W.F.A. Besling, **J. Mater. Res.** 25, 1629 (2010).
2. *Plasma-Assisted Atomic layer deposition of TiN/Al<sub>2</sub>O<sub>3</sub> stacks for Metal-Oxide-Semiconductor capacitor applications*. D. Hoogeland, K.B. Jinesh, F.C. Voogt, W.F.A. Besling, Y. Lamy, F. Roozeboom, M.C.M. van de Sanden and W.M.M. Kessels. **J. Appl. Phys.** 106, 114107 (2009).
3. *Plasma-Assisted ALD TiN/Al<sub>2</sub>O<sub>3</sub> stacks for MIMIM Trench Capacitor Applications*; D. Hoogeland, K.B. Jinesh, F.C. Voogt, W.F.A. Besling, Y. Lamy, F. Roozeboom, M.C.M. van de Sanden and W.M.M. Kessels. **Electrochem. Soc. Trans.** 25, (2009) 389.
4. *Maxwell-Wagner instability in bilayer dielectric stacks*; K.B. Jinesh, Y. Lamy, J.H. Klootwijk, W.F.A. Besling, **Appl. Phys. Lett.** 95, 122903 (2009).
5. *Charge conduction mechanisms of atomic-layer deposited Er<sub>2</sub>O<sub>3</sub> thin films*; K.B. Jinesh, Y. Lamy, E. Tois, W.F.A. Besling, **Appl. Phys. Lett.** 94, 252906 (2009).
6. *Silicon out-diffusion and aluminum in-diffusion in atomic-layer deposited La<sub>2</sub>O<sub>3</sub> thin films*; K.B. Jinesh, Y. Lamy, R. Wolters, W.F.A. Besling, **Appl. Phys. Lett.** 93, 192912 (2008).
7. *Enhanced electrical properties of atomic layer deposited La<sub>y</sub>Zr<sub>1-y</sub>O<sub>x</sub> thin films with embedded ZrO<sub>2</sub> nanoclusters*: K.B. Jinesh, W.F.A. Besling, E. Tois, J.H. Klootwijk, R. Wolters, W. Dekkers, M. Kaiser, F. Bakker, M. Tuominen, F. Roozeboom, **Appl. Phys. Lett.** 93, 172904 (2008).

8. *Spontaneous nanoclustering of ZrO<sub>2</sub> in atomic layer deposited La<sub>y</sub>Zr<sub>1-y</sub>O<sub>x</sub> thin films*: K.B. Jinesh, J.H. Klootwijk, Y. Lamy, R. Wolters, E. Tois, M. Tuominen, F. Roozeboom, W.F.A. Besling, *Appl. Phys. Lett.* 93, 062903 (2008).
9. *Ultra-high capacitance density for multiple ALD-grown MIM capacitor stacks in 3D silicon*: J. H. Klootwijk, K. B. Jinesh, W. Dekkers, J. F. Verhoeven, F. C. van den Heuvel, H.-D. Kim, D. Blin, M. A. Verheijen, R. G. R. Weemaes, M. Kaiser, J. J. M. Ruigrok, F. Roozeboom, *IEEE Electron Device Lett.* 29 (7) 2008.
10. *Characterization and modeling of high-k ALD trench capacitors in Silicon*; K.B. Jinesh, M.K. Matters-Kammerer, F. Roozeboom, J.H. Klootwijk (Submitted).
11. *Comparison of Thermal and Plasma-assisted ALD Al<sub>2</sub>O<sub>3</sub> thin films*; K.B. Jinesh et al. (Submitted)
12. *Reliability issues of high-aspect-ratio capacitors with atomic-layer-deposited La<sub>y</sub>Zr<sub>1-y</sub>O<sub>x</sub> thin films*. K.B. Jinesh et al., (in preparation).
13. *Si out-diffusion in atomic-layer deposited high-k materials*; K.B. Jinesh et al., (in preparation).
14. *Electrical properties of atomic layer deposited LaZrO<sub>x</sub>/SiO<sub>2</sub> stacks*; K.B. Jinesh et al., (in preparation).
15. *Atomic-layer-deposited LaZrO<sub>x</sub> thin films: material and electrical properties*; K.B. Jinesh et al., (in preparation).

#### Other publications (Journal)

16. *RF characterization and analytical modelling of through silicon vias and coplanar waveguide for 3D integration*. Y.P.R. Lamy, K. B. Jinesh, F. Roozeboom, D.J.

- Gravesteijn and W.F.A. Besling, *IEEE Transactions on Advanced Packaging* (in print) 2010.
17. *CO<sub>2</sub> detection at room temperature using atomic-layer-deposited La<sub>2</sub>O<sub>3</sub> thin films*; K.B. Jinesh, V.A. Dam, M. Crego-Calama, S.H. Brongersma (*in preparation*).
18. *Experimental evidence for ice formation at room temperature*; K.B. Jinesh, J. W. M. Frenken, *Phys. Rev. Lett.* 101, 036101 (2008).
19. *Thermolubricity in atomic-scale friction*; K.B. Jinesh, S. Yu Krylov, H. Valk, M. Dienwiebel, J.W.M. Frenken; *Phys. Rev. B* 78, 155440 (2008).
20. *Capillary condensation in atomic-scale friction: how water acts like glue*; K.B. Jinesh, J.W.M. Frenken, *Phys. Rev. Lett.* 96, 166103 (2006).
21. *Thermally induced reduction of friction at atomic-scale*; S. Yu Krylov, K.B. Jinesh, H. Valk, M. Dienwiebel, J.W.M. Frenken; *Phys. Rev. E* 71, 65101R, (2005).
22. *Role of excess Cadmium in the electrical properties of devices made of chemically deposited nano-CdS*; K.B. Jinesh, C. Sudha Kartha, K.P. Vijayakumar; *Appl. Surf. Sci.*, 207, 26 (2003).
23. *How Quantum confinements comes in chemically deposited CdS? – A detailed XPS investigation*; K.B. Jinesh, C. Sudha Kartha, K.P. Vijayakumar; *Physica E* 19, 303 (2003).
24. *Effects of Size-quantization in the I-V characteristics of CdS Bulk- nano junctions*; K.B. Jinesh, C. Sudha Kartha, K.P. Vijayakumar, *Appl. Surf. Sci.*, 195, 263 (2002).

25. *Capillary condensation in atomic-scale friction measurements*: K.B. Jinesh, J.W.M. Frenken (*in preparation*).
26. *Influence of externally excited lateral resonances in atomic-scale friction*; K.B. Jinesh, J.W.M. Frenken. (*in preparation*).

### Patents published:

1. *Phase-change memory cells and fabrication thereof*: **WO2010038216 (A1)**: K.B. Jinesh, R. Wolters, M. Zandt (2010).
2. *A capacitor and the method of manufacturing the same*; **WO2010023575 (A1)** Y. Furukawa, K.B. Jinesh, F. Pasveer, J.H. Klootwijk. (2010)
3. *A photovoltaic cell and the method to construct the same*; **O2010018490 (A2)**; Y. Furukawa, F. Pasveer, J.H. Klootwijk, K.B. Jinesh. (2010).
4. *Integrated Seebeck device*; **WO2010010520 (A2)**: K.B. Jinesh, J.H. Klootwijk (2010).
5. *Through wafer Via filling method*; **WO2009153728 (A1)**; K.B. Jinesh, Y. Lamy (2009).
6. *Enhanced surface area structure*; **WO2009150600 (A1)**: K.B. Jinesh, F. Roozeboom, J.H. Klootwijk, W. Dekkers. (2009)
7. *Method of forming a nanoclusters-comprising dielectric layer and device comprising such a layer*; **WO2009133500 (A1)**: K.B. Jinesh, W. Besling, R. Wolters, J.H. Klootwijk, F. Roozeboom. (2009).

### Contributions at Conferences & Symposia

#### Invited talks:

1. *Atomic-scale friction: effects of Capillary condensation*: IBM Zurich, **Switzerland** (2006).
2. *Capillary condensation in atomic-friction*: Micro and Nanotribology International Conference, Warsaw, **Poland** (2005).
3. *Nanoparticles – basics and perspectives*: Cochin University of Science and Technology, **India** (2004).

Other Talks:

4. *Ice-formation at room temperature in atomic-scale friction*: Nanotribology conference, Antalya, **Turkey** (2006).
5. *Capillary condensation in atomic friction*: Physical Preview Lunch meeting, Leiden, **The Netherlands** (2006).
6. *Capillary Condensation in atomic friction*: FOM annual meeting, Veldhoven, **The Netherlands** (2005).
7. *Capillary condensation in atomic friction*: NEVAC Day, Eindhoven, **The Netherlands** (2005).
8. *Effects of capillary condensation in nanoscopic sliding*: Tribology Day, Leiden, **The Netherlands** (2005).
9. *Thermolubricity in atomic-scale friction*: ESF Nanotribology conference, **France** (2005).
10. *Ice formation at room temperature in atomic-scale friction experiments*: Nanotribology conference, Vienna, **Austria** (2005).
11. *Capillary condensation and ice-formation in atomic-scale friction experiments*: American Physical Society meeting, Los Angeles, CA, **USA** (2005).
12. *Studies on Tunneling Properties of CdS Bulk-Nano Junctions*: National conference on Material Science, Trichi, **India** (2000)
13. *Effects of Increasing pH on the Morphology of Chemically deposited CdS films* - National conference on Advanced Materials, M.G University, Kerala, **India** (2000).





### *Acknowledgements*

This Thesis elaborates on the results of my two-year research (2007-2009) at NXP Semiconductors within the *REALISE* consortium. For the completion of this Thesis, the outstanding support of the former *Vias & Integrated Passives (VIP)* team of Microsystems Technology group at NXP Semiconductors, Eindhoven is gratefully acknowledged. The research described in this Thesis in its entirety was financially supported by NXP Semiconductors and the *REALISE* consortium.

The completion of this Thesis was benefitted from several outstanding personalities. Among them, first of all I would like to thank *Dr. Wim Besling*, principal scientist and the leader of the former VIP project, for the extraordinary support that led me to the accomplishment of this Thesis from the initial idea to its final level. *Dr. Reinout Woltjer*, the leader of Microsystems Technology group at NXP is thankfully acknowledged for the support and official permission to write this Thesis and for directing me to *Prof. Dr. Jurriaan Schmitz*.

I would like to acknowledge my Promotor, *Prof. Dr. Jurriaan Schmitz*, leader of the Semiconductor Components group in Department of Electrical Engineering, University of Twente, for accepting the work as the base for the PhD Thesis and for giving fast and constructive feedbacks to strengthen the Thesis. His detailed suggestions were of great help to improve this Thesis. My sincere thanks to Ms. *Annemiek Janssen*, secretary of Prof. Schmitz, for timely arranging the official formalities of the Thesis submission procedures.

I would like to extend my gratitude to *Dr. Yann Lamy*, my colleague in the *VIP* team (currently at CEA-LETI, Grenoble) for his friendly encouragements. I sincerely acknowledge *Dr. Johan Klootwijk*, senior scientist at Philips Research, who introduced me to the world of high-*k* physics. *Prof. Dr. Fred Roozeboom* (now at Technical University, Eindhoven) is thankfully acknowledged for his support in the project.

The proximity of several scholars was remarkably helpful in developing my new career turns at NXP Semiconductors. Among them, *Prof. Dr. Rob Wolters* is specially acknowledged. I would like to thank my former colleagues at NXP, especially, *Dr. Martijn Goossens*, *Dr. Peter Steeneken*, *Mr. Tonny Coppens*, *Mr. Wouter Dekkers* (now at Philips Research), *Dr. Klaus Reimann* and *Dr. Hans Tuinhout*.

The author likes to thank *Dr. Eva Tois* and *Marko Tuominen* of ASM Microchemistry, Finland, who carried out the deposition of the thin films studied in this Thesis. *Dr. Simon*

*Elliot*, (Tyndall National Institute, Ireland) is specially acknowledged as the coordinator of the REALISE project. The fruitful collaboration and discussion sessions with all the members of the *REALISE* project are thankfully acknowledged.

*Dr. Erwin Kessels*, Plasma and Materials Processing group of Technical University Eindhoven (TU/e) is specially acknowledged for the successful collaborative works in *INNOVia* project framework. Thanks to *Mr. Hans van Hemmen* for the collaborative works and *Mr. Dirk-Jan Hoogeland* (TU/e) for the excellent Master's thesis done partly with the *VIP* group.

This project benefitted a lot from the professional support of the material analysis experts in MiPlaza Materials Analysis, Eindhoven. Among them, *Dr. Monja Kaiser* (TEM, EDX), *Dr. Corrie Bulle Lieuwma* (TOFSIMS), *Mr. Rene Bakker*, *Mr. Harry Wondergem* (XRD) and *Dr. Peter Graat* (AFM) are specially acknowledged for their extended reports on data analysis and discussions.

The graduation committee who carefully evaluated this work is gratefully acknowledged for their valuable suggestions to strengthen the Thesis.

The motivation in accomplishing this second PhD degree comes from the blessings of my mother *E.V. Jagadamma*, father *K.G. Balakrishna Pillai*, brother *Jayan* and sister-in-law *Lekshmi*, and the affection of my little nieces *Ammu* and *Kathu*. The encouragements of my parents-in-law – *S. Jagadamba* and *E.M. Ramachandra Panicker*, and *Manju* also are gratefully acknowledged.

The energy and enthusiasm that lead me to pursue with this hard work come constantly from the affection and encouragements of my beloved wife *Devi*. Acknowledging her is beyond what words can convey.





## Curriculum Vitae

Jinesh Kochupurackal Balakrishna Pillai (Jinesh, K.B) was born on 1<sup>st</sup> June, 1978 in Kerala, India. Following his Bachelor's degree in Physics from Mahatma Gandhi University, Kerala in 1998, he received his Masters in Physics with distinction from Cochin University of Science & Technology, Kerala, in 2000. In the same year, he joined Jawaharlal Nehru Center for Advanced Scientific Research (JNCASR), Bangalore as a researcher. In 2001, he joined as a researcher at Delft Institute of Microelectronics and Submicrontechnology (DIMES) in Delft University of Technology, The Netherlands, working in crystallization of amorphous silicon thin films using Excimer-laser. In 2002, he joined Kammerlingh Onnes Laboratory in Leiden University, Leiden for PhD research. In 2006, he received PhD in Physics with the thesis entitled "*Atomic-scale friction: thermal effects and capillary condensation*" from Interface Physics group of Prof. Dr. J.W.M. Frenken.

After his PhD from Leiden, he joined NXP Semiconductors in 2006 November as a research scientist, working in the field of high-density capacitors for the purpose of passive integration. The results culminated into this Thesis are from the work carried out at NXP during his stay there (2007-2009). During 2009-2010 October, he is working as a research scientist at Holst Centre (IMEC) in Eindhoven. From October 2010 onwards, he will be working as a senior research fellow at the Energy Research Institute at Nanyang Technological University (ERI@N) in Singapore.

